METHODS ON THE ASSESSMENT OF HUMAN BAROREFLEX FUNCTION

EDITED BY: Yue-Der Lin and André Diedrich

PUBLISHED IN: Frontiers in Neuroscience and Frontiers in Physiology

frontiers Research Topics

frontiers

ISSN 1664-8714
ISBN 978-2-88976-617-8
DOI 10.3389/978-2-88976-617-8

About Frontiers

Frontiers is more than just an open-access publisher of scholarly articles: it is a pioneering approach to the world of academia, radically improving the way scholarly research is managed. The grand vision of Frontiers is a world where all people have an equal opportunity to seek, share and generate knowledge. Frontiers provides immediate and permanent online open access to all its publications, but this alone is not enough to realize our grand goals.

Frontiers Journal Series

The Frontiers Journal Series is a multi-tier and interdisciplinary set of open-access, online journals, promising a paradigm shift from the current review, selection and dissemination processes in academic publishing. All Frontiers journals are driven by researchers for researchers; therefore, they constitute a service to the scholarly community. At the same time, the Frontiers Journal Series operates on a revolutionary invention, the tiered publishing system, initially addressing specific communities of scholars, and gradually climbing up to broader public understanding, thus serving the interests of the lay society, too.

Dedication to Quality

Each Frontiers article is a landmark of the highest quality, thanks to genuinely collaborative interactions between authors and review editors, who include some of the world's best academicians. Research must be certified by peers before entering a stream of knowledge that may eventually reach the public - and shape society; therefore, Frontiers only applies the most rigorous and unbiased reviews.
Frontiers revolutionizes research publishing by freely delivering the most outstanding research, evaluated with no bias from both the academic and social point of view. By applying the most advanced information technologies, Frontiers is catapulting scholarly publishing into a new generation.

What are Frontiers Research Topics?

Frontiers Research Topics are very popular trademarks of the Frontiers Journals Series: they are collections of at least ten articles, all centered on a particular subject. With their unique mix of varied contributions from Original Research to Review Articles, Frontiers Research Topics unify the most influential researchers, the latest key findings and historical advances in a hot research area! Find out more on how to host your own Frontiers Research Topic or contribute to one as an author by contacting the Frontiers Editorial Office: frontiersin.org/about/contact

METHODS ON THE ASSESSMENT OF HUMAN BAROREFLEX FUNCTION

Topic Editors:
Yue-Der Lin, Feng Chia University, Taiwan
André Diedrich, Vanderbilt University, United States

Citation: Lin, Y.-D., Diedrich, A., eds. (2022). Methods on the Assessment of Human Baroreflex Function. Lausanne: Frontiers Media SA. doi: 10.3389/978-2-88976-617-8

Table of Contents

frontiers | Frontiers in Neuroscience

EDITORIAL
published: 28 June 2022
doi: 10.3389/fnins.2022.965406

Editorial: Methods on the Assessment of Human Baroreflex Function

Yue-Der Lin[1,2] *and André Diedrich*[3,4]*

[1] Department of Autonomic Control Engineering, Feng Chia University, Taichung, Taiwan, [2] Master's Program of Biomedical Informatics and Biomedical Engineering, Feng Chia University, Taichung, Taiwan, [3] Vanderbilt Autonomic Dysfunction Center, Vanderbilt University Medical Center, Nashville, TN, United States, [4] Department of Biomedical Engineering, Vanderbilt University, Nashville, TN, United States

Keywords: blood pressure, heart rate, autonomic nervous system, baroreflex, sympathetic activity, vagal activity

Editorial on the Research Topic

Methods on the Assessment of Human Baroreflex Function

The human baroreflex represents a crucial integrative neuronal negative feedback system which confines excessive blood pressure fluctuations into physiologically normal ranges (Robertson et al., 2012). Arterial baroreceptors within carotid sinuses, the aortic arch, and receptors in cardiopulmonary veins and right atrium sense pressure changes and transmit input through the glossopharyngeal nerve and vagus nerve to *nucleus tractus solitarii* (NTS) in the brainstem. During high blood pressure, baroreceptors respond to vascular wall stretch, which inhibits sympathetic pacemaker neuron in the rostral ventrolateral medulla (RVLM) via an inhibotry neuron in the caudal-ventrolateral medulla (CVLM). At the same time, excitatory projections from NTS increases cardiac parasympathetic drive from nucleus ambiguus (NA) and the dorsal motor nucleus of the vagus (DMNV), in turn increasing release of acetylcholine at the sinoatrial node and decreasing heart rate (details in **Figure 1**). During upright, blood pressure falls and unloads vascular wall, thereby reducing the activity of the baroreceptor afferent nerves which leads to decrease in cardiac vagal tone and increase in sympathetic activity. Sympathetic vasoconstrictor drive initiates release of norepinephrine from the sympathetic nerve terminals on the blood vessels. It causes both arterial vasoconstriction and venoconstriction and an increase in cardiac contractility and heart rate, all of which contribute to normalization of arterial pressure and cerebral perfusion (**Figure 1**).

Baroreflex lesions can affect the afferent limb, the peripheral limb, or the central integration centers. The clinical picture of patients with afferent baroreflex failure is characterized by unpredictable hypertensive crises, symptomatic hypotensive episodes, and orthostatic hypotension, demonstrating the importance of the baroreflex (Biaggioni et al., 2019). Patients with pure autonomic failure with postganglionic lesions experience disabling orthostatic hypotension. The correct assessment of human baroreflex is important not only for targeted treatment of autonomic dysfunction but also for prediction of cardiovascular risk in heart failure, hypertension, diabetes, and other cardiovascular diseases.

This Research Topic focuses on baroreflex measurements in humans. Baroreflex methods can be divided in pharmacological and non-pharmacological testing. Non-pharmacological testing includes measurements of baroreflex responses during neck suction, Valsalva maneuver, controlled breathing, exercise, and orthostatic stress. In addition, baroreflex sensitivity (BRS) can be assessed using analysis of blood pressure and heart rate variability, neural sympathetic activity, and modeling (**Figure 1**). Traditional baroreflex methods assume that the baroreflex system is an open loop system, but that is not the case for living human subjects. In animal studies, the closed loop

OPEN ACCESS

Edited and reviewed by:
Vaughan G. Macefield, Baker Heart and Diabetes Institute, Australia

***Correspondence:**
André Diedrich
andre.diedrich@vumc.org

Specialty section:
This article was submitted to Autonomic Neuroscience, a section of the journal Frontiers in Neuroscience

Received: *09 June 2022*
Accepted: *15 June 2022*
Published: *28 June 2022*

Citation:
Lin Y-D and Diedrich A (2022) Editorial: Methods on the Assessment of Human Baroreflex Function. Front. Neurosci. 16:965406. doi: 10.3389/fnins.2022.965406

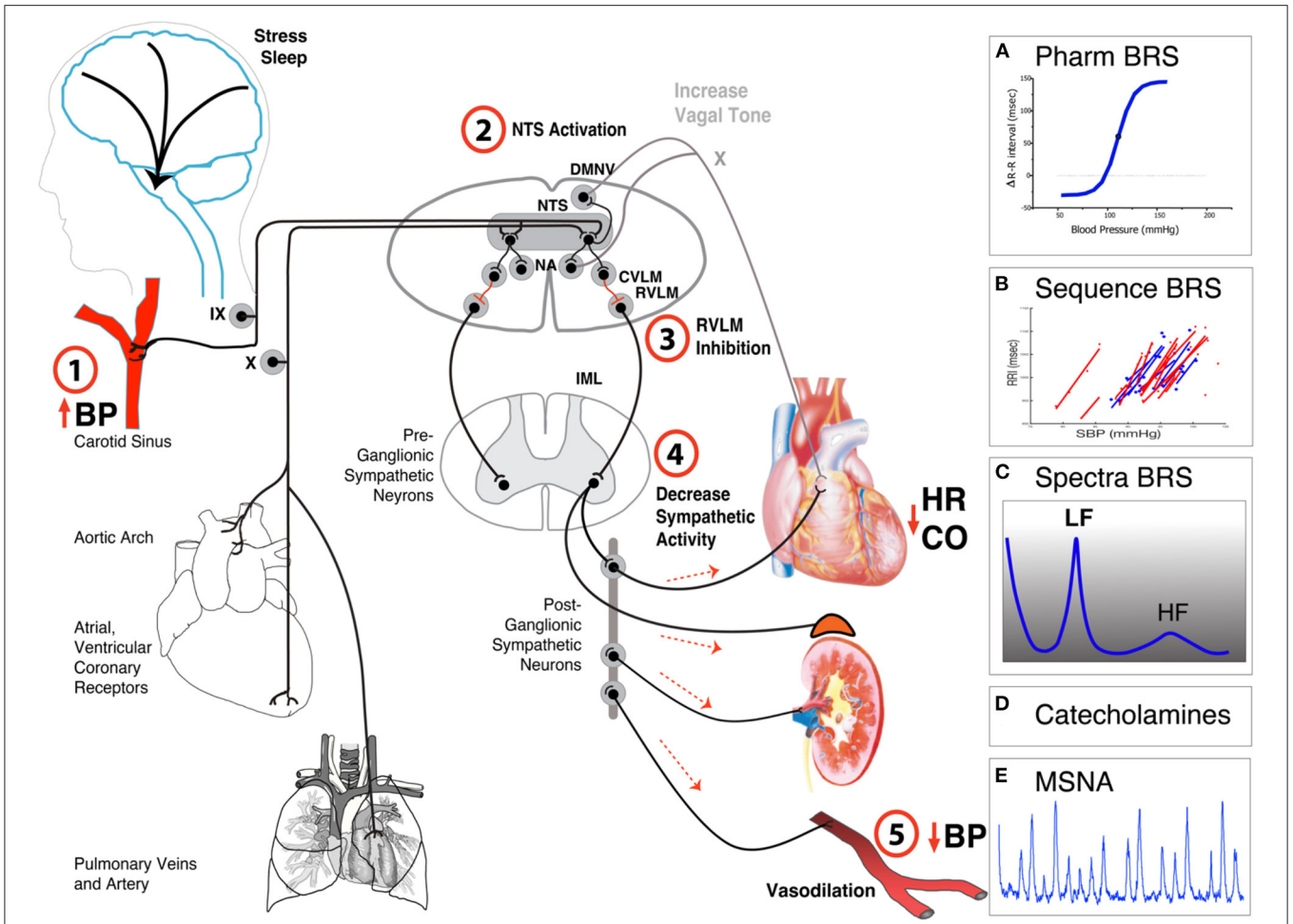

FIGURE 1 | Simplified anatomical and functional scheme of baroreflex function. Baroreceptors in the carotid sinus, aortic arch, right atrium and in the cardiopulmonary veins are activated-by (1) stretching and passing this information through the Vagus (X) or glossopharyngeal (IX) nerves to (2) the nucleus tractus solitarii (NTS) of the brain stem. The NTS projects to neurons in caudal ventrolateral medulla (CVLM) which (3) inhibits sympathetic pacemaker neurons in the rostral ventrolateral medulla (RVLM) and (4) reduces sympathetic outflow. This decreases heart rate, cardiac output, and (5) blood pressure. Activation of the NTS projects also to the nucleus ambiguous (NA) and dorsal motor nucleus of the Vagus (DMNV) and increases parasympathetic activity. Common methods to evaluate baroreflex function include **(A)** pharmacological challenge with vasoactive drugs, **(B)** spontaneous sequence analysis, **(C)** spectral analysis, **(D)** measurements of catecholamines, or **(E)** muscle sympathetic activity (MSNA) during orthostatic challenges.

can be opened surgically and pharmacologically. In humans, measurements in closed loop system are difficult. Pharmacological testing using vasoactive substances underestimate the effects, as the overall effect is determined by a combination of the direct peripheral effect on vascular tone and the indirect central baroreflex buffering (Jordan et al., 2002).

In this Research Topic, new methods for closed loop identification of baroreflex properties have been discussed. Kawada et al. described a method using white noise perturbation to measure central and peripheral arc properties. Yamasaki et al. proposed a novel analytical framework using equilibrium diagram to overcome the close loop open loop problem.

Measurement of baroreflex function using stimuli is the preferred approach, and it has some advantages in comparison to analysis of spontaneous fluctuations caused by biological noise. Neck suction is a direct non-pharmacological way to stimulate carotid baroreceptor and measure the physiological response. This complex technique is not available in the clinic. Pinheiro et al. developed an improved noiseless neck suction chamber device for use in clinic. Huang et al. used the Valsalva maneuver, and they compared it with spontaneous sequences method and BRS estimation using spectral methods. Dutra-Marques et al. used exercise as a stimulation to measure baroreflex response.

This Research Topic also includes improvement of traditional methods of baroreflex slope estimation in addition to novel approaches, such as analysis of baroreflex hysteresis, cross-correlations, and analysis of synchronization between heart rate and blood pressure. Heusser et al. derived a modified curve fitting model of the sigmoidal baroreflex curve, directly obtaining the baroreflex curve slope and other meaningful

physiological parameters. Dabiri et al. used a novel ellipse analysis to characterize hysteresis of the spontaneous respiration-related cardiovagal baroreflex for orthostatic test. The proposed method, by considering gain and set-point changes during respiration, offers instructive insight into the resulting hysteresis of the spontaneous cardiovagal baroreflex with respiration as stimuli.

The influence of higher nervous activity on the cardiovascular system via autonomic control and baroreflex regulation has been neglected for a long time. This is especially the case in sleep, as baroreflex properties change during different sleep stages. Karavaev et al. proposed a quantitative measure representing the total percentage of phase synchronization between the low-frequency oscillations in heart rate and blood pressure. They showed that the degree of synchronization of the studied rhythms is higher in slow-wave sleep compared to the awake state but lower compared to the rapid eye movement sleep.

This Research Topic also presents new methods in detecting cardiovascular autonomic neuropathy in patients with Parkinson's disease, diabetes, and metabolic syndrome. Huang et al. compared spontaneous sequence and spectral BRS with baroreflex slope determined using the Valsalva maneuver in Parkinson's Disease. Yeh et al. proposed an advanced cross-correlation function method with adjustable threshold which was superior for early detection of autonomic neuropathy in diabetes mellitus. Dutra-Marques et al. compared spontaneous sequential baroreflex measures with the exercise responses in patient with metabolic syndrome to study baroreflex mechanisms and risks factors of metabolic syndrome.

Our hope is that readers will gain new insight of novel concepts and measures of baroreflex function. We thank all authors for their contribution to this area of research, as it demonstrates the importance of developing novel methods of baroreflex measures for the early detection of dysfunction and the improvement of treatment of our patients.

AUTHOR CONTRIBUTIONS

The draft was written by AD and proofread and approved by Y-DL. Both authors contributed to the article and approved the submitted version.

FUNDING

This research was funded by Ministry of Science and Technology, Taiwan (contract number: MOST 110-2221-E-035-006-MY3). AD was partly supported by NIH R01 HL142583.

ACKNOWLEDGMENTS

In our capacity as topic editors, we would like to express our sincere appreciation to the authors of this Research Topic and our fellows who supported this work.

REFERENCES

Biaggioni, I., Shibao, C. A., Diedrich, A., Muldowney, J. A. S., Laffer, C. L., and Jordan, J. (2019). Blood Pressure Management in Afferent Baroreflex Failure. *J. Am. College Cardiol.* 74, 2939–2947. doi: 10.1016/j.jacc.2019.10.027

Jordan, J., Tank, J., Shannon, J. R., Diedrich, A., Lipp, A., Schröder, C., et al. (2002). Baroreflex buffering and susceptibility to vasoactive drugs. *Circulation*. 105, 1459–1464. doi: 10.1161/01.CIR.0000012126.56352.FD

Robertson, D., Diedrich, A., and Chapleau, M. W. (2012). Editorial on arterial baroreflex issue. *Auton. Neurosci.* 172, 1–3. doi: 10.1016/j.autneu.2012.10.010

Conflict of Interest: The authors declare that the research was conducted in the absence of any commercial or financial relationships that could be construed as a potential conflict of interest.

Publisher's Note: All claims expressed in this article are solely those of the authors and do not necessarily represent those of their affiliated organizations, or those of the publisher, the editors and the reviewers. Any product that may be evaluated in this article, or claim that may be made by its manufacturer, is not guaranteed or endorsed by the publisher.

frontiers in Physiology

METHODS
published: 20 January 2021
doi: 10.3389/fphys.2020.613311

Noiseless Variable-Pressure Neck Chamber Device to Assess the Carotid Baroreflex Function

Alessandro Pinheiro[1,2], Lauro C. Vianna[3,4] and Jake C. Carmo[5]*

[1]Faculty of Technology, University of Brasília, Brasília, Brazil, [2]Federal Institute of Education, Science, and Technology of Brasília, Brasília, Brazil, [3]NeuroVASQ – Integrative Physiology Laboratory, Faculty of Physical Education, University of Brasília, Brasília, Brazil, [4]Graduate Program in Medical Sciences, Faculty of Medicine, University of Brasília, Brasília, Brazil, [5]Biological Signals Processing Laboratory, Faculty of Physical Education, University of Brasília, Brasília, Brazil

OPEN ACCESS

Edited by:
Yue-Der Lin,
Feng Chia University, Taiwan

Reviewed by:
Eugenio Mattei,
Italian National Institute of Health, Italy
Fiona D. McBryde,
The University of Auckland, New Zealand

***Correspondence:**
Alessandro Pinheiro
alessandro@ieee.org

Specialty section:
This article was submitted to Autonomic Neuroscience, a section of the journal Frontiers in Physiology

Received: *02 October 2020*
Accepted: *16 December 2020*
Published: *20 January 2021*

Citation:
Pinheiro A, Vianna LC and Carmo JC (2021) Noiseless Variable-Pressure Neck Chamber Device to Assess the Carotid Baroreflex Function. Front. Physiol. 11:613311. doi: 10.3389/fphys.2020.613311

Background: The blood pressure responses to baroreflex perturbations can be assessed only using the variable-pressure neck chamber technique. However, the application of this approach in hospital environments is limited owing to the loud noise emitted during its operation. This study was aimed at developing a noiseless neck suction chamber device (NCD) that could stimulate the baroreceptors located in the carotid sinus in humans.

Methods: A non-invasive device was developed to pressurize the carotid arteries externally. A microcontroller with a computer interface and neck chamber (3D-printed) was used. The anatomical neck chamber was fitted on six healthy, young, asymptomatic participants (five men; 32 ± 6 year), who were normotensive, nonsmoking, in sinus rhythm, free of known cardiovascular or metabolic diseases, and not consuming any acute or chronic medications. A suction of −60 mmHg was applied for 5 s, and the corresponding data were recorded. Before each study visit, the participants were instructed to abstain from caffeine, alcohol, and strenuous exercise for 12–24 h.

Results: In all the trials, a significant reflex bradycardia (−10 ± 2 bpm) and depressor response (−15 ± 4 mmHg) to neck suction were observed, consistent with the results in the literature. The neck chamber device operated noiselessly [sound pressure level (SPL) of 34.3 dB] compared to a regular vacuum-cleaner-based system (74.6 dB).

Conclusion: Using the proposed approach, consistent blood pressure and heart rate responses to carotid baroreflex hypertensive stimuli could be recorded, as in previous studies conducted using neck collar devices. Furthermore, the neck chamber device operated noiselessly and can thus be applied in hospital environments.

Keywords: blood pressure, baroreflex, neck suction, hypertensive stimulus, neck collar

INTRODUCTION

The arterial baroreflex system plays a pivotal role in the short-term regulation of blood pressure and cardiovascular variability (Eckberg and Sleight, 1992). Nevertheless, several factors (related to the sex, age, health, and environment of an individual; Cooper et al., 2007; Kim et al., 2011; Credeur et al., 2014; Kaufmann et al., 2020) may influence the gain and effectiveness of the baroreflex, along with the cardiovascular variability. Furthermore, many central neural structures help regulate the cardiovascular system and thus contribute to the integrity of the baroreflex (Chapleau et al., 1989). Notably, abnormalities in the arterial baroreflex function have been linked to a degradation of the cardiovascular variability, deterioration of the cardiovascular outcomes, and mortality in several diseases (La Rovere et al., 1998). Therefore, assessing the baroreflex function is of significance in both healthy and diseased individuals, especially in the context of the prognostic evaluation and assessment of the effect of the treatment.

Several methods have been developed to examine the baroreflex physiology in humans (Parati et al., 2000). In general, the baroreflex function is quantified by measuring the change in the heart rate and/or muscle sympathetic nerve activity in response to provoked and/or spontaneous changes in the blood pressure. However, the blood pressure responses to baroreflex perturbations cannot be evaluated using these approaches. The variable-pressure neck chamber technique offers a unique solution to this problem and exhibits several advantages including, but not limited to, the precise control of the rate, intensity, timing, and duration of the pressure stimulus, and realization of the selective activation or deactivation of the carotid baroreceptors by applying a measurable positive or negative pneumatic pressure to the neck region (Eckberg, 1977a; Fadel et al., 2003). Although these advantages highlight the utility of the variable-pressure neck chamber in assessing the carotid baroreflex function in human experimental investigations, the existing neck chamber devices produce a loud noise during their operation, similar to the suction sound of vacuum cleaners (Ludbrook et al., 1977; Cooper and Hainsworth, 2001). Moreover, noise annoyance is often associated with acute and chronic alterations in the cardiovascular system (Münzel et al., 2018), and hence, this confounding influence should be avoided in human cardiovascular physiology examinations. Consequently, it is essential to develop a noiseless variable-pressure neck chamber device.

Considering this background, this study was aimed at developing a noiseless neck suction chamber device (NCD) that could stimulate the baroreceptors located in the carotid sinus in humans. Furthermore, the neck chamber was developing using a 3D printer as a novel technique, with a focus on enhancing the subject comfort and pressure sealing.

MATERIALS AND METHODS

Ethics

All the study procedures were approved by the institutional research ethics committee (CAAE: 26228819400005103) in accordance with the Declaration of Helsinki. Written informed consent was obtained from the individuals for the publication of any potentially identifiable images or data included in this article.

Subjects

Data were collected from six healthy, young, asymptomatic participants (five men; mean ± SD; age: 32 ± 6 year; height: 1.7 ± 0.1 m; weight: 69 ± 7 kg; and body mass index: 24 ± 2 kg/m^2), who were normotensive, nonsmoking, in sinus rhythm, free of known cardiovascular or metabolic diseases, and not consuming any acute or chronic medications. Before each study visit, the participants abstained from caffeine, alcohol, and strenuous exercise for 12–24 h.

Neck Chamber

The neck chamber device was built based on the principles described by Eckberg et al. (1975) and Raine and Cable (1999). The proposed device involved mechanical and electronic components controlled by software through a portable display. The device was designed to apply controllable pressure within a given range (from 0 to −80 mmHg) to stimulate the carotid baroreceptor.

The development of the neck collar was a very challenging step. After several "trial-and-error" experiences, we realized that the mandibular shape is a key element affecting chamber fit, independent of weight, height, and/or musculature. Our proposed equation is based on the idea of a V-shaped mandible and it was derived from six subjects. The average coordinates were obtained, representing the average natural curves of the specific body region. Three different sizes were designed to ensure that the device could fit people with different body structures. The coordinates were uploaded to software (Inventor Professional 2020, Autodesk, California, United States) to design the best curve to fit each size. **Figure 1** shows the coordinates of the median size neck. The model with nine degrees of the

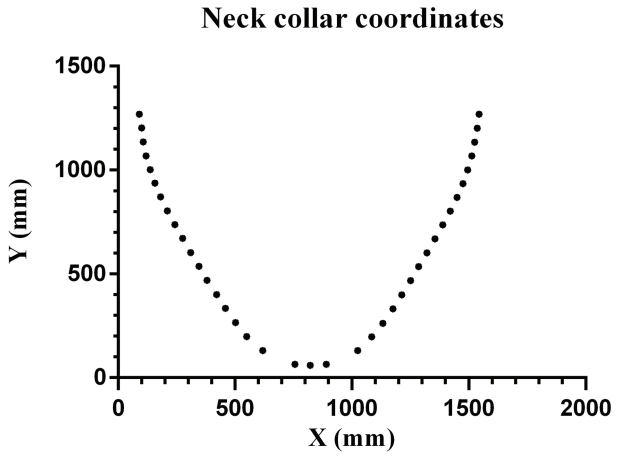

FIGURE 1 | Points representing the coordinates to model a medium-sized human neck.

curve (MATLAB R2018a, MathWorks, Massachusetts, United States) can be expressed as

$$f(x) = -3.4e\text{-}26 * x9 + 1.9e\text{-}21 * x8 + 3.9e\text{-}17 * x7 + 4.4e\text{-}13 * x6 - 2.9e\text{-}09 * x5 + 1.285e\text{-}05 * x4 - 0.035 * x3 + 62.78 * x2 - 6.27e{+}04 * x + 2.73e{+}07.$$

The neck chamber (**Figure 2**) was printed using a 3D printer (i3, RepRap, Bath University, United Kingdom), using a flexible filament (TPU 95A, National 3D, São Paulo, Brazil).

Mechanical

The functional components in the mechanical part include a silent vacuum pump (Airmed D400 220 V/60 Hz, Sao Bernardo do Campo, Brazil) combined with a vacuum tank (10 L, Gasnag, São Paulo, Brazil) to ensure that the pressure can be varied sharply and rapidly. Owing to the vacuum tank, the pump does not need to operate during the entire test, thereby leading to a quiet operation. As shown in **Figure 3**, two valves (Tcontrol, AC220V2L3505, São Paulo, Brazil) are used. The release valve opens to provide negative pressure, and after this suction operation, the equalization valve opens, returning the pressure in the neck chamber to the ambient pressure. Two pressure sensors (NXP Semiconductor, MXP5010dp, Eindhoven, Netherlands) are installed, one in the tank and the other in the neck chamber. All the sensors were calibrated using an external pressure monitor (HT-1890, Rise, China) and a multimeter (MD-6130, ICEL, Manaus, Brazil). Through five calibration points, the respective voltage values were found for each pressure value manually adjusted by the syringe, according to the calibration scheme shown in **Figure 4**. All the mechanical processes are computer-controlled, as described in the subsequent section.

Tests were performed to evaluate the noise produced by the proposed system. The REW software (Room EQ Wizard V15.9, John Mulcahy, United States) was used to analyze the sound pressure level (SPL). The SPL of the mechanical system was measured using a USB microphone (Kolke, KPI-271, Espírito Santo, Brazil) placed 1.5 m from the system.

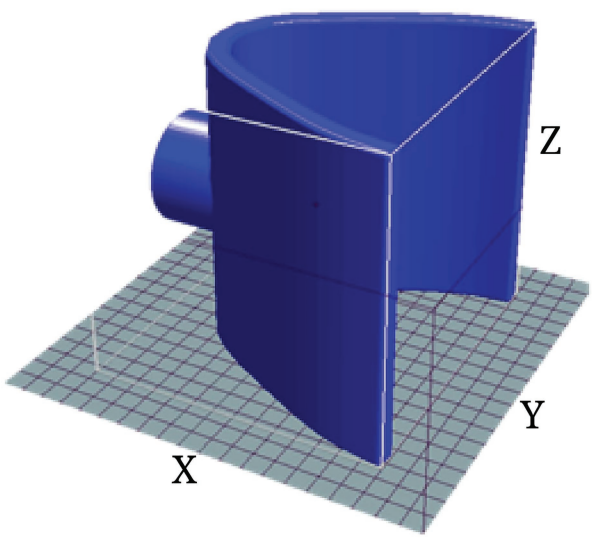

FIGURE 2 | 3D design of the neck chamber, according to the coordinates.

Electronic

As shown in **Figure 5**, the NCD has three solid-state relays with optical coupling (k1, k2, and k3). Each relay is activated through the digital ports (PB0, PB1, and PB2) of the microcontroller ATmega328P-PU (MC). The MC, display, and relays are powered by a compact 5 V power supply (HLK-PM01, Hilink, Guangdong, China). The neck and tank pressure are continually updated at 115,200 bounds by a serial interface through the PD0 and PD1 digital ports (J7 and J8, respectively). The neck and tank pressure sensors are read the analog ports PC0 and PC1, respectively.

One ECG device (CardioMatic, MSC-6111, New York, United States) is connected to the system *via* the J10 analog MC port to provide suction when the R-wave peak occurs, directly to the peak detector circuit (**Figure 5**). Any ECG device can be used as long as it has an analog signal pertaining to the DII lead. The analog ECG signal is rectified in a half-wave using an operational amplifier (LM324). In general, the ECG signal can have different amplitudes, and each peak can be appropriately detected by the diodes that only lead to positive signals in direct polarization. In the last operational amplifier (IC1A), pin 3 has an original signal input, and pin 2 receives an attenuated signal through the voltage divider (R9 and R10). If the electric tension level in pin 3 is higher than that in pin 2, the output changes to high, thereby detecting the peak. The software continuously stores the duration of six consecutive RR intervals in the MC.

When the operator presses the "start" button, the MC checks whether there is a stable condition (i.e., variability less than 5% among six RR intervals). If it is stable, the exact moment to trigger the valves will be calculated based on the predicted RR interval duration (based on the stability of the previous six RR intervals), subtracted by the delay of the valves (~27 ms). Therefore, the valves are opened in ~27 ms before the next R-wave peak. This algorithm ensures that the suction is applied close to the R-wave peak. **Figure 6** shows when neck suction starts in the QRS complex, considering the delay of the valves. The triggering system performance was evaluated using a variable ECG simulator (30, 60, and 120 bpm, **Figure 7**).

A user interface (**Figure 8**) was developed for a display (NX8048K070_011C, Nextion, Shenzhen, China). The display was touch-sensitive and capacitive and could ensure real-time serial communication (115,000 bps) with the MC. The time and pressure indicate the duration and intensity of the suction, respectively. Values such as the neck and tank pressure and R-R interval were transmitted to the display continuously. This interface could adjust the pressure (ranging from 0 to −80 mmHg) and time stimulus (0–60 s).

The neck suction was applied at <50 ms after the R-wave peak (Credeur et al., 2014; Barbosa et al., 2016; Ogoh et al., 2018). This timing (i.e., <50 ms) allows synchronicity between the pressure wave from the cardiac cycle (i.e., systole – the phase

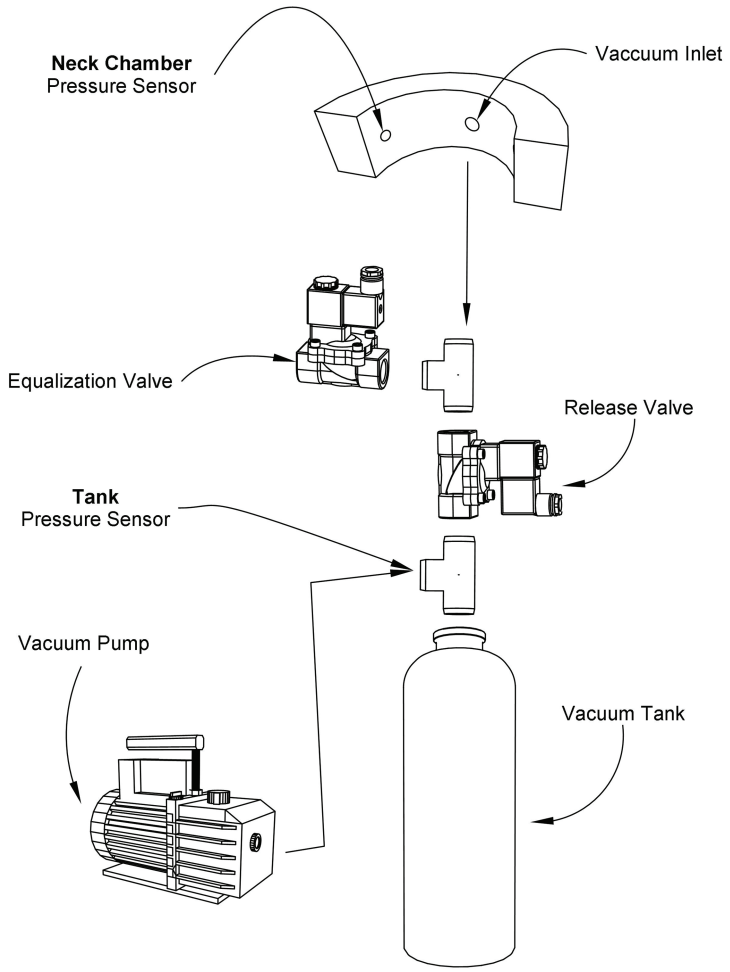

FIGURE 3 | Diagram of the mechanical part of the neck chamber device.

of the cardiac cycle when blood is being pumped out of the heart, which begins approximately 50 ms after the R-wave peak) and the neck suction pressure pulse at the carotid sinus (Eckberg, 1977b).

Protocol

After an explanation of the protocol to the participants, written informed consent was obtained, then a carotid ultrasound scanning was performed in all participants in order to check for the presence of atherosclerotic plaques. Then, the system operator set the protocol on the display. First, the operator set the duration of the stimulus (seconds) and suction intensity (mmHg). To maintain the selectivity of the neck suction to isolate the carotid-baroreflex-mediated responses, the stimulus was required to be brief to avoid any adaptation of the carotid baroreceptors or counteraction from the extracarotid baroreceptors (Fadel et al., 2003). The duration adopted in this study was 5 s, as it is the optimum duration for the stimulation to obtain peak heart rate and blood pressure responses (Eckberg, 1977a,b; Fadel et al., 2003).

The participants remained seated at least for 5 min to stabilize the cardiovascular components (Vianna et al., 2018). The respiratory movements were monitored using a belt placed around the abdomen (MLT 1132 Piezo Respiratory Belt Transducer, ADInstruments, Sydney, Australia). The blood pressure was continuously measured (beat-to-beat) through a photoplethysmography device (Human NIBP Controller, ADInstruments) placed on the middle finger of the non-dominant hand of the participants. All the signals were collected through an integrator (PowerLab 16/35, ADInstruments), at a sampling rate of 1 kHz.

After stabilizing the signals, the neck chamber was comfortably positioned to involve the anterior two-thirds of the neck (Querry et al., 2001; Krnjajic et al., 2016). Under resting conditions, each pressure stimulus was delivered to the carotid sinus during a 10–15 s breath-hold at the end-expiration phase to minimize the respiratory-related modulation of the heart rate and mean arterial pressure (Eckberg et al., 1980).

Four to five trials of neck suction were performed with a minimum of 45 s of recovery allotted between trials to

FIGURE 4 | Method of calibrating the pressure sensors. A syringe is used to vary the pressure of the sensor. The multimeter measures the voltage values at the sensor's output.

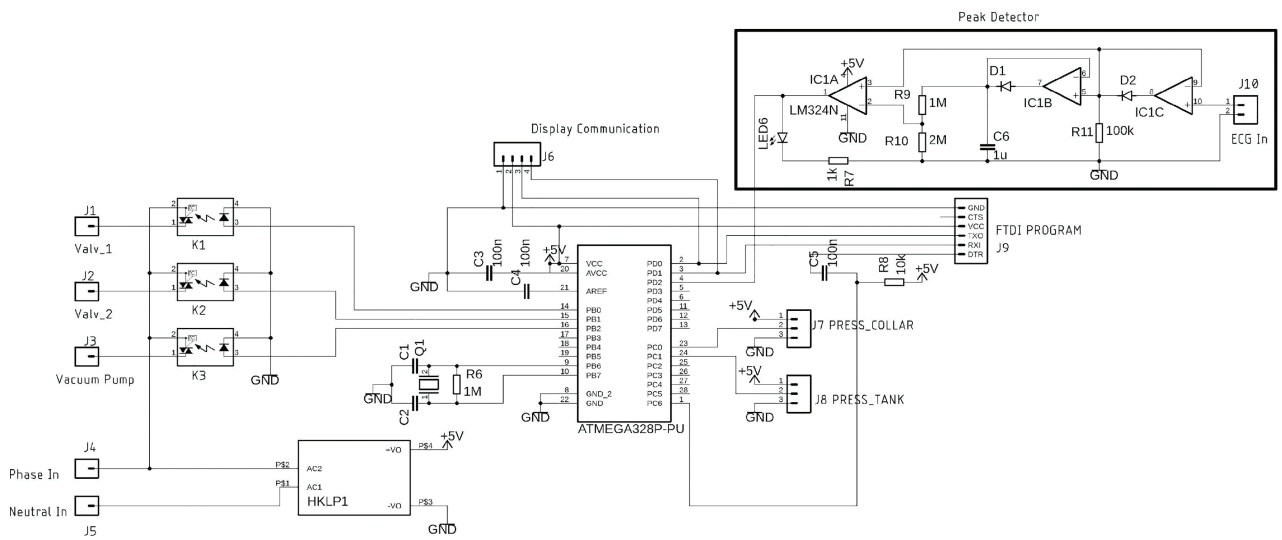

FIGURE 5 | Schematic of the electronics of the neck chamber device, including the R-peak detector.

allow all physiological variables to return to pre-stimulus values (i.e., three cardiac cycles average immediately preceding neck suction). Carotid baroreflex-mediated changes in cardiovascular variables were calculated from the pre-stimulus values and plotted on a beat-to-beat scale. The responses were calculated through the lowest value (nadir) obtained during neck suction and the respective pre-stimulus baseline. Changes in all cardiovascular variables in response to individual

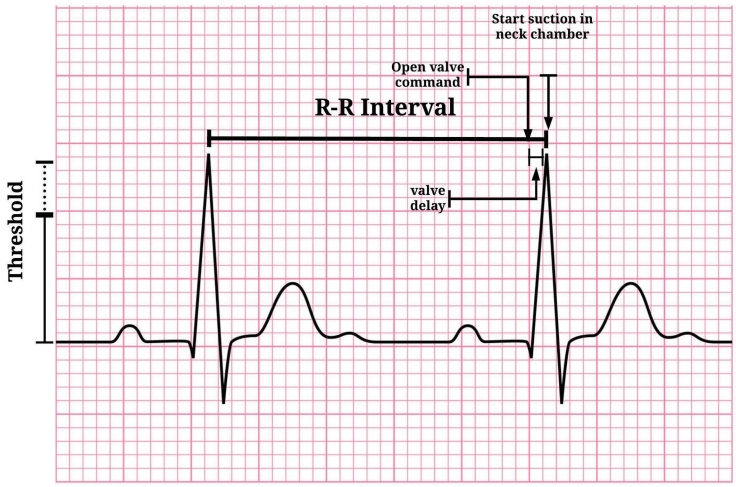

FIGURE 6 | Neck suction start point is advancing due to valve delay.

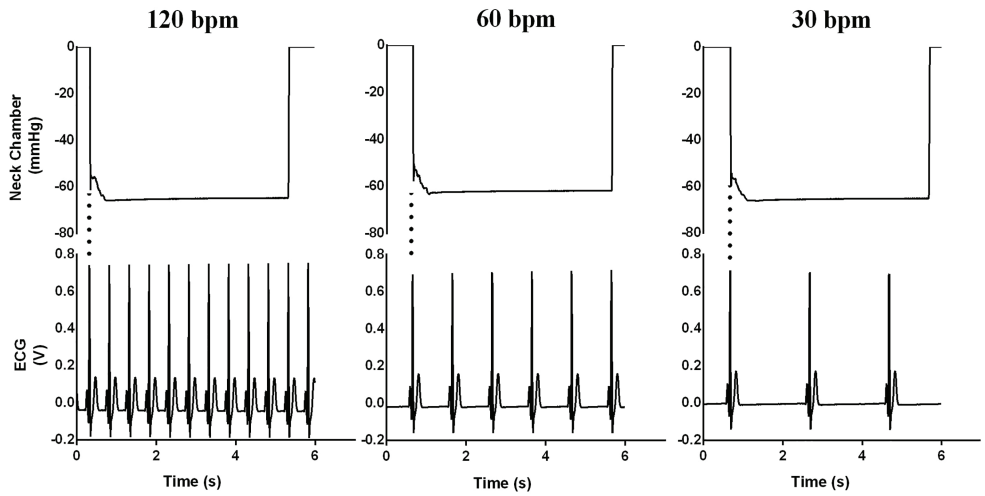

FIGURE 7 | Evaluation of ECG trigger at frequencies of 30, 60, and 120 bpm.

trials neck suction were averaged for each subject and then combined to provide a group mean (A. Kim et al., 2011). Of note, since the present system only operates to assess cardiovascular changes to neck suction, we were unable to model our data using the logistic model to determine a baroreflex sigmoidal curve fit.

All the data were presented as means. All variables showed normal distribution in the Shapiro–Wilk test. One-way repeated-measures ANOVA was used to compare pre-stimulus, neck suction, and post-stimulus. The Greenhouse–Geisser correction was used to adjust ANOVA results whenever sphericity was violated in the Mauchly test. The Bonferroni *post hoc* was used when significant F values were found. All analyses were two-tailed, and statistical significance was accepted for $p < 0.05$. Statistical analyses were performed using Statistical Package for the Social Sciences, version 20.0 for Windows (SPSS, Chicago, IL).

RESULTS

In all the trials of a representative subject, consistent reflex bradycardia (−10 ± 2 bpm) and depressor response (−15 ± 4 mmHg) to the neck suction were observed (**Figure 9**), and these responses are similar to those reported in the literature (Ernsting and Parry, 1957; Huang et al., 2016). The absolute (pre-stimulus: 87 ± 9 bpm; neck suction: 71 ± 7 bpm; post-stimulus: 81 ± 8 bpm; $p < 0.01$; **Figure 10A**) and relative (pre-stimulus: 0%; neck suction: −18 ± 2%; post-stimulus: −6 ± 2%; $p < 0.01$; **Figure 10B**) heart rate

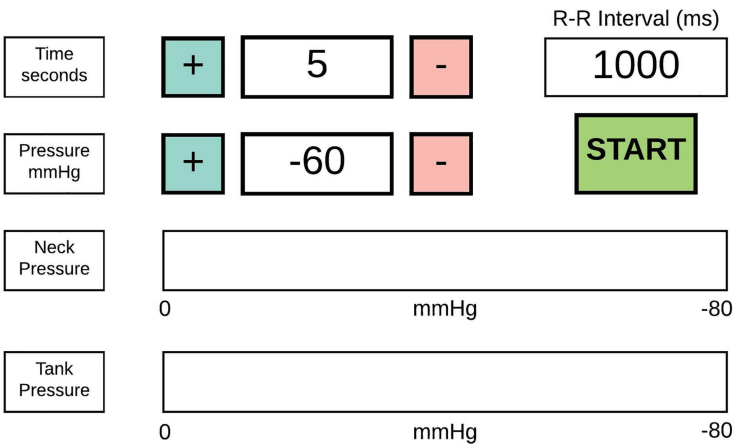

FIGURE 8 | Graphical interface of the neck chamber device.

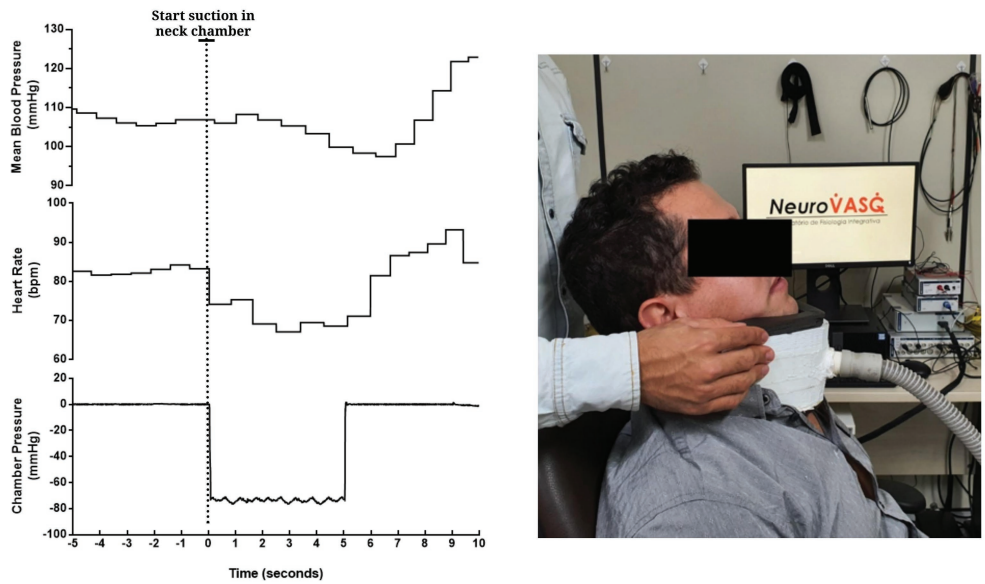

FIGURE 9 | Beat-to-beat tracings from a young man showing the temporal pattern of mean blood pressure (top), heart rate (mid), and chamber pressure (bottom) during acute carotid baroreceptor hypertensive stimuli (i.e., neck suction, −60 mmHg). Neck chamber placed on a participant (right panel).

responses to neck suction were significantly different compared to pre-stimulus values.

The ECG trigger had a delay of less than 50 ms in all attempts, as shown in **Figure 7**. Four attempts of neck suction trials (−60 mmHg) were performed for each participant. The rate of pressure change was ~3,000 mmHg/s.

The proposed device had an average SPL of 34.3 dB, as shown in **Figure 11**, considerably smaller than that of the vacuum-cleaner-based device (74.6 dB). Note that, the SPL of a silent room is usually approximately 30–34 dB.

After a five-point calibration of the sensors, the equation was obtained, which shows linearity between pressure and electrical voltage:

$$V = -0.037p + 0.798$$

Where V is the voltage at the output pin of the pressure sensor, and p is the pressure (mmHg).

DISCUSSION

Several trials were performed on the participants to examine the efficacy of the proposed neck suction technique in terms of generating the reflex responses, in a similar manner as those reported in previous studies. Before each trial, the system operator set the values of pressure (−60 mmHg) and duration

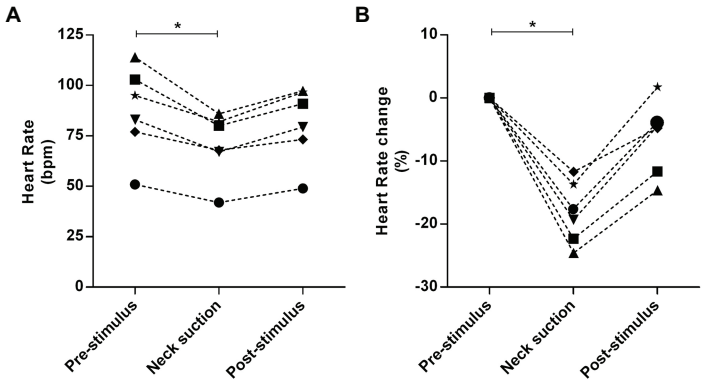

FIGURE 10 | Absolute and relative responses are shown in panels **A**, and **B**, respectively. The responses were calculated through the lowest value (nadir) obtained during neck suction and the respective pre-stimulus baseline, i.e., 3-bpm average immediately preceding neck suction. *$p < 0.01$.

(5 s) for the carotid stimulus. In this study, a noiseless neck suction device was developed to activate the carotid baroreceptors in humans. In accordance with the main objective of the study, the developed device can perform noiselessly, thereby enhancing the participant comfort during the execution of the protocol and providing a suitable environment to examine the baroreflex physiology. The uniqueness of the proposed system pertains to the use of a vacuum tank in which the vacuum is stored, which enables the realization of a rapid and silent pressure change inside the neck collar whenever the neck suction is implemented. In comparison, the noise level of the conventional system used in the existing studies is significantly higher as the motor pump must be operated (vacuum cleaner motor) to provide a continuous vacuum source (Cooper and Hainsworth, 2001). Alternatively, a previous fMRI study has placed the neck suction engine outside the examination room (Makovac et al., 2018) aiming to reduce the noise, although no data were presented in terms of noise during its operation. In contrast, the advantages of the present system lie in the detailed open-source descriptions of the hardware, and electronics, and the development of a "silent" and reasonably portable neck suction device.

In the evaluation, the vacuum reservoir was noted to considerably influence the release and stability of the vacuum. Although the collar was pressurized instantaneously, extremely small fluctuations occurred on the negative plateau, although these were considered to be irrelevant taking into account their possible physiological impact on the carotid baroreflex-mediated reflex responses. The timing of the suction onset was satisfactory, as the peak of the R-wave was observed to exactly coincide with the beginning of the collar pressurization. Nevertheless, it is important to state that our proposed system works only in steady-state conditions. As such, the present algorithm/system does not work in the presence of cardiac arrhythmias or during the transition from rest to exercise (exercise onset). For carotid baroreflex testing in such conditions, the algorithm could be modified. Future studies should investigate its feasibility. In addition to the tank, the role of the malleable neck chamber was significant, as the flexible material allowed a better adaptation to the neck around the anterior two-thirds of the neck and enhanced the participant comfort. Furthermore, the applied silicone coating helped avoid any vacuum leakage.

To activate the carotid baroreceptors through the neck chamber technique, certain parameters must be suitably set. For example, the rate of pressure change in the neck chamber must be extremely high to provide an uniform stimulation throughout the 5 s suction window. Accordingly, in this study, the rate of change was set higher than ~3,000 mmHg/s, which is considered to be sufficient to extend the baroreceptors located in the carotid sinus (Eckberg, 1977a,b).

In the proposed device, the analog circuit for R-wave detection is an essential component because the circuit adapts the gain of the signal to the analog port of the MC, to supply a constant voltage. It is expected that the systems pertaining to a vacuum cleaner motor likely cannot adequately control the amount of suction compared to in the proposed device; nevertheless, further work is necessary to validate this aspect.

The neck collar could generate reproducible responses in the case of all the participants, and consistent carotid baroreflex-mediated responses to neck suction were observed, similar to those reported in the previous publications. The key advantage of the proposed NCD pertained to its quiet operation. The noise produced during a 1 min trial was slightly more than 30 dB (equivalent to that of a whisper); in contrast, the vacuum-cleaner-based system produces a noise of 70–80 dB (equivalent to a passenger car or a telephone ringing). Although we did not test how the acute exposure to noise could directly affect the reflex responses to the neck suction, it has been reported that intermittent exposure of monkeys to noise (85 dB) for 9 months significantly increased the blood pressure by 30 mmHg, even though the auditory system was not notably influenced (Münzel et al., 2018). Furthermore, according to the United States Environmental Protection Agency (1974), the noise levels in hospital environments should not exceed 45 and 35 dB during the day and night, respectively. The World Health Organization recommends a sound level of 30–40 dB in internal hospital environments (Berglund et al., 2000).

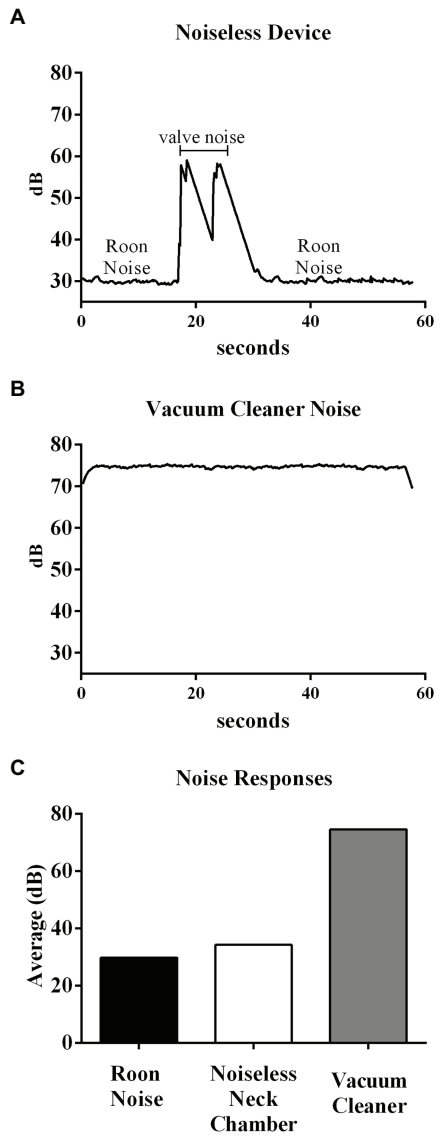

FIGURE 11 | Top and middle panels show the original recording of the noise from the noiseless device and Vacuum cleaner-based system, respectively. Bottom panel shows the average noise responses within different environments.

The proposed neck chamber device, with its unique low noise operation, can thus be widely applied in hospital environments.

CONCLUSION

In the tests using the proposed device, consistent blood pressure and heart rate responses to carotid baroreflex hypertensive stimuli were observed, consistent with the results of previous studies involving the use of neck collar devices. Moreover, the proposed device could realize noiseless operation, thereby providing a *sine qua non* environment for the baroreflex assessment in human physiology laboratories.

DATA AVAILABILTITY STATEMENT

The datasets and/or codes generated during and/or analyzed during the current study are available from the corresponding author on reasonable request.

ETHICS STATEMENT

The studies involving human participants were reviewed and approved by Faculdade de Ciências Médicas e da Saúde de Juiz de Fora/FCMS/FJ/SUPREMA – CAAE: 26228819400005103. The patients/participants provided their written informed consent to participate in this study.

AUTHOR CONTRIBUTIONS

AP, LV, and JC wrote the manuscript and performed the data analysis. All authors contributed to the article and approved the submitted version.

FUNDING

AP was supported by the Federal Institute of Brasília. LV received research support from the National Council for Scientific and Technological Development (CNPq; grants 307293/2019-0 and 431740/2018-6).

ACKNOWLEDGMENTS

The time and effort of all the volunteer participants are appreciated. We thank Jeann L. Sabino-Carvalho for excellent support with the experiments.

REFERENCES

Barbosa, T. C., Vianna, L. C., Hashimoto, T., Petersen, L. G., Olesen, N. D., Tsukamoto, H., et al. (2016). Carotid baroreflex function at the onset of cycling in men. *Am. J. Physiol. Integr. Comp. Physiol.* 311, R870–R878. doi: 10.1152/ajpregu.00173.2016

Berglund, B., Lindvall, T., and Schwela, D. H. (2000). New WHO guidelines for community noise. *Noise Vib. Worldw.* 31, 24–29. doi: 10.1260/0957456001497535

Chapleau, M. W., Hajduczok, G., and Abboud, F. M. (1989). Peripheral central mechanisms of baroreflex resetting. *Clin. Exp. Pharmacol. Physiol.* 16, 31–43. doi: 10.1111/j.1440-1681.1989.tb02994.x

Cooper, V. L., Elliott, M. W., Pearson, S. B., Taylor, C. M., and Hainsworth, R. (2007). Daytime variability in carotid baroreflex function in healthy human subjects. *Clin. Auton. Res.* 17, 26–32. doi: 10.1007/s10286-006-0390-z

Cooper, V. L., and Hainsworth, R. (2001). Carotid baroreceptor reflexes in humans during orthostatic stress. *Exp. Physiol.* 86, 677–681. doi: 10.1113/eph8602213

Credeur, D. P., Holwerda, S. W., Boyle, L. J., Vianna, L. C., Jensen, A. K., and Fadel, P. J. (2014). Effect of aging on carotid baroreflex control of blood pressure and leg vascular conductance in women. *Am. J. Physiol. Heart Circ. Physiol.* 306, H1417–H1425. doi: 10.1152/ajpheart.00036.2014

Eckberg, D. L. (1977a). Baroreflex inhibition of the human sinus node: importance of stimulus intensity, duration, and rate of pressure change. *J. Physiol.* 269, 561–577. doi: 10.1113/jphysiol.1977.sp011915

Eckberg, D. L. (1977b). Adaptation of the human carotid baroreceptor-cardiac reflex. *J. Physiol.* 269, 579–589. doi: 10.1113/jphysiol.1977.sp011916

Eckberg, D. L., Cavanaugh, M. S., Mark, A. L., and Abboud, F. M. (1975). A simplified neck suction device for activation of carotid baroreceptors. *J. Lab. Clin. Med.* 85, 167–173.

Eckberg, D. L., Kifle, Y. T., and Roberts, V. L. (1980). Phase relationship between normal human respiration and baroreflex responsiveness. *J. Physiol.* 304, 489–502. doi: 10.1113/jphysiol.1980.sp013338

Eckberg, D. L., and Sleight, P. (1992). *Human baroreflexes in health and disease (no. 43)*. Oxford: University Press.

Ernsting, J., and Parry, D. J. (1957). Some observations on the effects of stimulating the stretch receptors in the carotid artery of man. *J. Physiol.* 137, P45–P46.

Fadel, P. J., Ogoh, S., Keller, D. M., and Raven, P. B. (2003). Recent insights into carotid baroreflex function in humans using the variable pressure neck chamber. *Exp. Physiol.* 88, 671–680. doi: 10.1113/eph8802650

Huang, M., Allen, D. R., Keller, D. M., Fadel, P. J., Frohman, E. M., and Davis, S. L. (2016). Impaired carotid baroreflex control of arterial blood pressure in multiple sclerosis. *J. Neurophysiol.* 116, 81–87. doi: 10.1152/jn.00003.2016

Kaufmann, H., Norcliffe-Kaufmann, L., and Palma, J. A. (2020). Baroreflex dysfunction. *New Engl. J. Med.* 382, 163–178. doi: 10.1056/NEJMra1509723

Kim, A., Deo, S. H., Vianna, L. C., Balanos, G. M., Hartwich, D., Fisher, J. P., et al. (2011). Sex differences in carotid baroreflex control of arterial blood pressure in humans: relative contribution of cardiac output and total vascular conductance. *Am. J. Physiol. Heart Circ. Physiol.* 301, 2454–2465. doi: 10.1152/ajpheart.00772.2011

Krnjajic, D., Allen, D. R., Butts, C. L., and Keller, D. M. (2016). Carotid baroreflex control of heart rate is enhanced, while control of mean arterial pressure is preserved during whole body heat stress in young healthy men. *Am. J. Phys. Regul. Integr. Comp. Phys.* 311, R735–R741. doi: 10.1152/ajpregu.00152.2016

La Rovere, M. T., Bigger, J. T., Marcus, A., Mortara, A., and Schwartz, P. J. (1998). Baroreflex sensitivity and heart-rate variability in prediction of total cardiac mortality after myocardial infarction. ATRAMI (Autonomic Tone and Reflexes After Myocardial Infarction) Investigators. *Lancet.* 351, 478–484. doi: 10.1016/s0140-6736(97)11144-8

Ludbrook, J., Mancia, G., Ferrari, A., and Zanchetti, A. (1977). The variable-pressure neck-chamber method for studying the carotid baroreflex in man. *Clin. Sci. Mol. Med.* 53, 165–171. doi: 10.1042/cs0530165

Makovac, E., Garfinkel, S., Bassi, A., Basile, B., Macaluso, E., Cercignani, M., et al. (2018). Fear processing is differentially affected by lateralized stimulation of carotid baroreceptors. *Cortex* 99, 200–212. doi: 10.1016/j.cortex.2017.07.002

Münzel, T., Schmidt, F. P., Steven, S., Herzog, J., Daiber, A., and Sørensen, M. (2018). Environmental noise and the cardiovascular system. *J. Am. Coll. Cardiol.* 71, 688–697. doi: 10.1016/j.jacc.2017.12.015

Ogoh, S., Marais, M., Lericollais, R., Denise, P., Raven, P. B., and Normand, H. (2018). Interaction between graviception and carotid baroreflex function in humans during parabolic flight-induced microgravity. *J. Appl. Physiol.* 125, 634–641. doi: 10.1152/japplphysiol.00198.2018

Parati, G., Di Rienzo, M., and Mancia, G. (2000). How to measure baroreflex sensitivity: from the cardiovascular laboratory to daily life. *J. Hypertens.* 18, 7–19. doi: 10.1097/00004872-200018010-00003

Querry, R. G., Smith, S. A., Strømstad, M., Ide, K., Secher, N. H., and Raven, P. B. (2001). Anatomical and functional characteristics of carotid sinus stimulation in humans. *Am. J. Physiol. Heart Circ. Physiol.* 280, H2390–H2398. doi: 10.1152/ajpheart.2001.280.5.H2390

Raine, N. M., and Cable, N. T. (1999). A simplified paired neck chamber for the demonstration of baroreflex blood pressure regulation. *Am. J. Phys.* 277, S60–S66. doi: 10.1152/advances.1999.277.6.s60

United States Environmental Protection Agency (1974). Information on levels of environmental noise requisite to protect public health and welfare with an adequate margin of safety. Washington, DC.: Government Printing Office.

Vianna, L. C., Fernandes, I. A., Martinez, D. G., Teixeira, A. L., Silva, B. M., Fadel, P. J., et al. (2018). Water drinking enhances the gain of arterial baroreflex control of muscle sympathetic nerve activity in healthy young humans. *Exp. Physiol.* 103, 1318–1325. doi: 10.1113/EP087095

Conflict of Interest: The authors declare that the research was conducted in the absence of any commercial or financial relationships that could be construed as a potential conflict of interest.

frontiers in Neuroscience

ORIGINAL RESEARCH
published: 09 June 2021
doi: 10.3389/fnins.2021.680195

Exaggerated Exercise Blood Pressure as a Marker of Baroreflex Dysfunction in Normotensive Metabolic Syndrome Patients

*Akothirene C. Dutra-Marques[1], Sara Rodrigues[1], Felipe X. Cepeda[1], Edgar Toschi-Dias[1,2], Eduardo Rondon[1], Jefferson C. Carvalho[1], Maria Janieire N. N. Alves[1], Ana Maria F. W. Braga[1], Maria Urbana P. B. Rondon[3] and Ivani C. Trombetta[1]**

[1] Instituto do Coracao, Hospital das Clinicas HCFMUSP, Faculdade de Medicina, Universidade de São Paulo, São Paulo, Brazil, [2] Universidade Metodista de São Paulo, São Paulo, Brazil, [3] School of Physical Education and Sport, University of São Paulo, São Paulo, Brazil

OPEN ACCESS

Edited by:
Yue-Der Lin,
Feng Chia University, Taiwan

Reviewed by:
Paolo Castiglioni,
Fondazione Don Carlo Gnocchi Onlus (IRCCS), Italy
Evan L. Matthews,
Montclair State University, United States

***Correspondence:**
Ivani C. Trombetta
ivani.trombetta@gmail.com

Specialty section:
This article was submitted to Autonomic Neuroscience, a section of the journal Frontiers in Neuroscience

Received: 13 March 2021
Accepted: 03 May 2021
Published: 09 June 2021

Citation:
Dutra-Marques AC, Rodrigues S, Cepeda FX, Toschi-Dias E, Rondon E, Carvalho JC, Alves MJNN, Braga AMFW, Rondon MUPB and Trombetta IC (2021) Exaggerated Exercise Blood Pressure as a Marker of Baroreflex Dysfunction in Normotensive Metabolic Syndrome Patients. Front. Neurosci. 15:680195. doi: 10.3389/fnins.2021.680195

Introduction: Exaggerated blood pressure response to exercise (EEBP = SBP ≥ 190 mmHg for women and ≥210 mmHg for men) during cardiopulmonary exercise test (CPET) is a predictor of cardiovascular risk. Sympathetic hyperactivation and decreased baroreflex sensitivity (BRS) seem to be involved in the progression of metabolic syndrome (MetS) to cardiovascular disease.

Objective: To test the hypotheses: (1) MetS patients within normal clinical blood pressure (BP) may present EEBP response to maximal exercise and (2) increased muscle sympathetic nerve activity (MSNA) and reduced BRS are associated with this impairment.

Methods: We selected MetS (ATP III) patients with normal BP (MetS_NT, $n = 27$, 59.3% males, 46.1 ± 7.2 years) and a control group without MetS (C, $n = 19$, 48.4 ± 7.4 years). We evaluated BRS for increases (BRS+) and decreases (BRS−) in spontaneous BP and HR fluctuations, MSNA (microneurography), BP from ambulatory blood pressure monitoring (ABPM), and auscultatory BP during CPET.

Results: Normotensive MetS (MetS_NT) had higher body mass index and impairment in all MetS risk factors when compared to the C group. MetS_NT had higher peak systolic BP (SBP) (195 ± 17 vs. 177 ± 24 mmHg, $P = 0.007$) and diastolic BP (91 ± 11 vs. 79 ± 10 mmHg, $P = 0.001$) during CPET than C. Additionally, we found that MetS patients with normal BP had lower spontaneous BRS− (9.6 ± 3.3 vs. 12.2 ± 4.9 ms/mmHg, $P = 0.044$) and higher levels of MSNA (29 ± 6 vs. 18 ± 4 bursts/min, $P < 0.001$) compared to C. Interestingly, 10 out of 27 MetS_NT (37%) showed EEBP (MetS_NT+), whereas 2 out of 19 C (10.5%) presented ($P = 0.044$). The subgroup of MetS_NT with EEBP (MetS_NT+, $n = 10$) had similar MSNA ($P = 0.437$), but lower BRS+ ($P = 0.039$) and BRS− ($P = 0.039$) compared with the subgroup

without EEBP (MetS_NT−, $n = 17$). Either office BP or BP from ABPM was similar between subgroups MetS_NT+ and MetS_NT−, regardless of EEBP response. In the MetS_NT+ subgroup, there was an association of peak SBP with BRS− ($R = -0.70$; $P = 0.02$), triglycerides with peak SBP during CPET ($R = 0.66$; $P = 0.039$), and of triglycerides with BRS− ($R = 0.71$; $P = 0.022$).

Conclusion: Normotensive MetS patients already presented higher peak systolic and diastolic BP during maximal exercise, in addition to sympathetic hyperactivation and decreased baroreflex sensitivity. The EEBP in MetS_NT with apparent well-controlled BP may indicate a potential depressed neural baroreflex function, predisposing these patients to increased cardiovascular risk.

Keywords: metabolic syndrome, cardiovascular risk, baroreflex sensitivity, muscle sympathetic nerve activity, cardiopulmonary exercise test, exercise blood pressure response

INTRODUCTION

Metabolic syndrome (MetS) is the overlap of cardiovascular risk factors (i.e., dyslipidemia, hypertension, insulin resistance, and visceral obesity) (Grundy et al., 2005) and has been found to increase the incidence of cardiovascular events and death up to 78% (Gami et al., 2007). Among these factors, visceral obesity is the most prevalent (90–100%) (Drager et al., 2009; Cepeda et al., 2015). High amount of visceral adiposity is associated with endothelial dysfunction (Romero-Corral et al., 2010) and impaired autonomic control (Triggiani et al., 2019), mechanisms related to blood pressure (BP) control, and regulation of cardiovascular function during exercise (Tzemos et al., 2015).

In hypertensive patients, arterial baroreflex sensitivity (BRS) is reduced, and this impairment has been found to be associated with increased sympathetic drive and higher BP (Laterza et al., 2007; Wustmann et al., 2009). Regardless of the presence of hypertension, the pathophysiological substrates of visceral obesity, dyslipidemia, and insulin resistance may alter autonomic control, predisposing MetS patients to increased cardiovascular risk (Gami et al., 2007). In fact, MetS is characterized by sympathetic hyperactivation, even in patients with MetS who do not have hypertension (Grassi et al., 2005). Undoubtedly, sympathetic hyperactivation and decreased BRS are involved in the progression of the MetS to cardiovascular disease (Trombetta et al., 2010).

The BRS is an important sophisticated autonomic mechanism in the regulation of the cardiovascular system, designated to buffer beat-to-beat fluctuations in arterial BP. Arterial baroreceptors are mechanosensitive nerves, located in the adventitia of the carotid sinus and aortic arch. An increase in BP causes vascular distension, and the baroreceptor deformation exerts reflex bradycardia and sympathoinhibition, which results in a vasodilation reflex. On the other hand, the baroreflex deactivation causes tachycardia reflex and elicits sympathetic-mediated vasoconstriction reflex. The main role of baroreflex is to maintain BP at physiological levels (Chapleau et al., 2001; Laterza et al., 2007). In humans, arterial baroreflex has been evaluated using several laboratory techniques, mainly by quantifying the reflex responses induced by the injection of vasoactive drugs or selective external stimuli of the carotid baroreceptors. A more recent non-invasive method, based on the computational analysis of spontaneous fluctuations in systolic BP and RR intervals, consists of a sensitive, simple, and inexpensive procedure that allows the quantification of spontaneous BRS in real-life conditions (Parati et al., 2000; La Rovere et al., 2008).

Since exercise induces physiological stress, the analysis of HR and BP responses during maximal progressive exercise may be used as a simple tool to test the integrity of autonomic control to adjust cardiac output. In this context, in a previous study we observed that MetS patients with the comorbidity obstructive sleep apnea (OSA) had impaired HR recovery after maximal exercise, and this seemed to be partly due to the sympathetic hyperactivity in these patients (Cepeda et al., 2015).

There are a large number of studies suggesting that the response (EEBP) during cardiopulmonary exercise test (CPET) that occurs in individuals with normal resting BP is predictive of risk for new-onset hypertension (Miyai et al., 2000; Farah et al., 2009; Tzemos et al., 2015) and cardiovascular disease (Schultz et al., 2013; Keller et al., 2017). Endothelial dysfunction, decreased proximal aortic compliance, and increased exercise-related neurohormonal activation seem to be the main mechanisms underlying this prognosis (Tzemos et al., 2015). The intrinsic risk posed by EEBP may be still higher in MetS patients, as they have pathophysiological substrates that have been consistently associated with autonomic and vascular dysfunction (Trombetta et al., 2010; Shimabukuro et al., 2016; Rodrigues et al., 2017).

Abbreviations: MetS, metabolic syndrome; C, control group without MetS; MetS_NT, normotensive MetS patients; CPET, cardiopulmonary exercise test; EEBP, exaggerated exercise blood pressure response during maximal cardiopulmonary exercise test, i.e., SBP ≥ 190 mmHg for women and ≥210 mmHg for men; MetS_NT+, normotensive MetS subgroup with EEBP response during CPET; MetS_NT−, normotensive MetS subgroup without EEBP response during CPET; BP, blood pressure; SBP, systolic BP; DBP, diastolic BP; HR, heart rate; BRS, spontaneous baroreflex sensitivity; BRS+, BRS for increases in spontaneous BP and HR fluctuations; BRS−, BRS for decreases in spontaneous BP and HR fluctuations; MSNA, muscle sympathetic nerve activity; ABPM, ambulatory blood pressure monitoring; OSA, obstructive sleep apnea; AHI, apnea/hypopnea index; BMI, body mass index; WC, waist circumference; ECG, electrocardiogram; VO_2, oxygen uptake.

Albeit the clinical relevance of EEBP is related to an increased risk of onset hypertension (Miyai et al., 2000), the underlying pathophysiological mechanisms have yet to be fully elucidated. Therefore, this study aimed to assess both whether normotensive patients with MetS have EEBP during maximal CPET and whether autonomic dysfunction, represented by impaired BRS and increased muscle sympathetic nerve activity (MSNA), is involved in this response.

MATERIALS AND METHODS

Study Population

In this prospective study, we recruited 72 newly diagnosed and unmedicated MetS patients from the Outpatient Unit of the Heart Institute (InCor), University of São Paulo Medical School, aged between 40 and 60 years, non-smokers, sedentary, with no history of alcohol consumption, and with no evidence of cardiopulmonary or skeletal muscle disorders. From the initial sample, the ones invited to participate in this study were only those 27 MetS (37.5%) without hypertension based on the office BP (SBP $\leq$ 139 and DBP $\leq$ 89 mmHg) (Mancia et al., 2013; Williams et al., 2019), and with normal BP confirmed by Ambulatory Blood Pressure Monitoring (ABPM: 24 h mean SBP/DBP $<$ 130/80 mmHg; daytime $<$ 135/85 mmHg; and nighttime $<$ 120/70 mmHg) (Mancia et al., 2013; Williams et al., 2019), and we named this group as normotensive MetS (MetS_NT). Likewise, 19 age-matched subjects with normal BP (Williams et al., 2019), who presented only one or none of the other MetS risk factors, were enrolled in the study as a Control group (C). Part of these patients had also previously participated in other studies (Cepeda et al., 2015; Maki-Nunes et al., 2015; Rodrigues et al., 2017).

The study was approved by the Scientific Commission of the Instituto do Coracao (InCor), and by the Ethics in Research Commission of the Hospital das Clinicas HCFMUSP, Faculdade de Medicina, Universidade de São Paulo (#1222/05). All participants signed a written informed consent form.

Procedures and Measures

Experimental Design

All evaluations were carried out in about 2–3 weeks on subsequent visits. The subjects were instructed to abstain from caffeine and physical activity for the 48 h leading up to the evaluations. Initially, venous blood was collected after 12 h of overnight fasting to measure total serum cholesterol, triglycerides, HDL cholesterol (enzymatic method), and plasma glucose (standard glucose oxidase method). After a light meal, all subjects underwent three standard BP measurements, and assessment of body weight, height, body mass index (BMI), and waist circumference (WC). Then, the 24-h ambulatory blood pressure monitoring (ABPM) was placed. The next day, ABPM was removed and the autonomic evaluation was performed in a quiet room with controlled temperature (22°C). In a lying position, the patient's leg was positioned for microneurography, and a microelectrode was placed on the peroneal nerve. After instrumentation and a 15-min rest period, the biological signals of MSNA, heart rate (HR) on the electrocardiogram (ECG), and BP on a beat-to-beat basis were recorded for 10 min at rest in a lying position using a software program (WinDaq Software, Transonic Systems, DATAQ Instruments Inc., Akron, OH, United States). When we did not succeed in assessing MSNA, a second attempt was made on another date. On another visit, a CPET was performed.

Also, individuals underwent a night polysomnography to assess the apnea/hypopnea index (AHI).

Metabolic Syndrome Diagnosis

Metabolic syndrome patients were diagnosed according to Adult Treatment Panel III (ATP-III) (Grundy et al., 2005), which requires meeting at least three of the five following diagnostic criteria: (1) elevated WC $\geq$ 102 cm in men ($\geq$40 inches) and $\geq$88 cm in women ($\geq$35 inches); (2) elevated triglyceride $\geq$ 150 mg/dl (1.7 mmol/L); (3) reduced HDL-c $<$ 40 mg/dl (1.03 mmol/L) in men and $<$50 mg/dl (1.3 mmol/L) in women; (4) elevated systolic BP (SBP) $\geq$ 130 mmHg and/or diastolic BP (DBP) $\geq$ 85 mmHg; and (5) elevated fasting glucose $\geq$ 100 mg/dl (5.6 mmol/L).

In the present study, we selected MetS patients without hypertension (Williams et al., 2019).

Office Blood Pressure

Systolic BP and DBP were measured following the recommended procedure for routine office BP measurement and with appropriate cuff size (Williams et al., 2019; Barroso et al., 2020).

Ambulatory Blood Pressure Monitoring

The 24-h BP measurements were recorded using a continuous blood pressure monitor (model 90207, Spacelabs Inc., Redmond, WA, United States). The device was placed on the non-dominant upper limb of the patient early in the morning and was removed 24 h later. The device was programed to record BP readings every 10 min during wake (daytime) and every 20 min during sleep (nighttime). To validate the ABPM, at least 70% of expected measurements should be conducted in 24 h recording (Williams et al., 2019). Daytime and nighttime intervals were defined using sleeping times reported by the patients in diary cards (awake and asleep periods) (O'Brien et al., 2013). The subjects were instructed to maintain their habitual activities and to relax and straighten out the arm during waking hour measurements. Thresholds for hypertension diagnosis based on ABPM were 24 h mean $\geq$ 130 and or $\geq$80 mmHg; awake (daytime) mean $\geq$ 135 and or $\geq$85 mmHg; and asleep (nighttime) mean $\geq$ 120 and or $\geq$70 mmHg (O'Brien et al., 2013; Williams et al., 2019).

Muscle Sympathetic Nerve Activity

Muscle Sympathetic Nerve Activity was directly measured through a multiunit postganglionic efferent from the peroneal nerve using the microneurography technique, which consists of the impaction of a tungsten microelectrode to the peroneal nerve, as previously described (Fagius and Wallin, 1993; Trombetta et al., 2010).

Beat-To-Beat Arterial Blood Pressure and Heart Rate

During 10 min at rest in a lying position, mean BP was continuously and non-invasively monitored by Finometer, a finger photoplethysmography device (Finapres 2300; Ohmeda, Englewood, Co., United States) on a beat-to-beat basis (WinDaq Software, Transonic Systems, DATAQ Instruments Inc., Akron, OH, United States) at a frequency of 500 Hz. Simultaneously, HR was continuously monitored through the lead II of the ECG. The respiratory rate was monitored with a piezoelectric thoracic belt (Pneumotrace II, model 1132) placed around the upper abdomen.

Spontaneous Baroreflex Sensitivity

A computer-based technique was used to evaluate the BRS by measuring spontaneous fluctuations beat by beat of BP and HR (see above) in the time domain. This method consists of the identification of three or more sequential beats, characterized by either a progressive rise in SBP and enlargement of the *R–R* interval (reflex bradycardia) or by a progressive decrease in SBP and shortening of the *R–R* interval (reflex tachycardia). The consecutive and simultaneous increases in SBP and increases in *R–R* intervals represent spontaneous activation of baroreceptors (BRS+), and consecutive and simultaneous decreases in SBP and decreases in *R–R* intervals represent spontaneous deactivation of baroreceptors (BRS−) (Parati et al., 2000; La Rovere et al., 2008). Basically, the values generated by the WinDaq Software were plotted on an excel spreadsheet, with the beat-to-beat SBP values (mmHg), and *R–R* intervals (from ECG) in milliseconds (ms). After plotting the values side by side, we observed each consecutive sequence of the SBP (from 1 mmHg) and *R–R* interval (from 3 ms), and a slope by a linear regression was generated. Finally, all slopes were averaged, resulting in an index of the sensitivity of arterial baroreflex modulation of heart rate (BRS). The cuff used was adapted according to the size of the patient's finger and arm (Parati et al., 2000; La Rovere et al., 2008).

Blood Pressure Response to Exercise and Functional Capacity

Blood pressure response to exercise and functional capacity were measured using a maximal CPET on cycle ergometer fitted with an electromagnetic brake (Medifit 400L, Medical Fitness Equipment, Maarn, Netherlands) using a ramp protocol. The workload increments of 10 or 15 W were added every minute at constant cadence (60–70 rpm) until exhaustion. Oxygen uptake (VO_2) and carbon dioxide production (CO_2) were determined by gas exchange on a breath-by-breath basis in a computerized system (SensorMedics, model Vmax 229, BuenaVista, CA, United States). Peak VO_2 was defined as the maximum VO_2 reached at the end of the exercise (Beaver et al., 1986). We used the following criteria to define maximal effort achievement: (1) when the subject no longer maintained a cadence of 60 rpm and was unable to continue exercising, thus demonstrating exhaustion, and (2) when the maximal respiratory exchange ratio (RER) was greater than 1.10 (Balady et al., 2010). HR was continuously monitored during all tests by 12-lead electrocardiogram. Both SBP and DBP (auscultatory method) were measured at baseline, every 2 min of the exercise protocol, at peak, and at the first, second, and fourth minutes of recovery. The peak exercise SBP was considered the highest SBP value achieved during the CPET, and, consequently, the EEBP was defined as a peak exercise SBP $\geq$ 210 mmHg in men and $\geq$190 mmHg in women, according to the Framingham criteria (Tsioufis et al., 2008, 2012).

Statistical Analysis

Statistical analysis was carried out using SPSS software (SPSS 20, Inc., Chicago, IL, United States). The data are presented as mean and standard deviation for parametric measurements and median and [interquartile range] for non-parametric measurements. The Kolmogorov–Smirnov and Levine tests were used to assess the normality and homogeneity of distribution of each variable studied. A Chi-square (χ^2) test was used to assess categorical data differences. Comparisons between MetS_NT and C groups as well as between normotensive MetS with EEBP (MetS_NT+) and without EEBP (MetS_NT−) during CPET were carried out using Student's *t*-test. The bivariate correlation (Pearson correlation) was conducted to test the association of peak SBP response during maximal CPET with baroreflex sensitivity (BRS−), association of triglycerides with peak SBP response during maximal CPET and association of triglycerides and BRS−. $P < 0.05$ values were considered statistically significant.

RESULTS

Figure 1 depicts participants' flowchart of the study, which has two different parts. First, we compared MetS_NT patients with the C group. Then, we compared the subgroup of MetS_NT that presented EEBP (MetS_NT+) with those without EEBP (MetS_NT−) during CPET.

Normotensive MetS Patients vs. Control Group

Table 1 displays physical characteristics, MetS risk factors, and AHI from polysomnography of the MetS_NT and C groups. Sex distribution, age, and functional capacity (peak VO_2) were similar between groups. As expected, MetS_NT patients had higher weight and BMI and all MetS risk factors were impaired compared to C (**Table 1**). Regarding autonomic measurements, MetS_NT had lower BRS− (**Figure 2A**) and higher MSNA (**Figure 2B**) when compared to C. No difference was found in BRS+ (**Figure 2A**).

Table 2 shows BP of the ABPM recordings and BP response during CPET in the MetS_NT and C groups. It should be noted that the 24-h, daytime, and nighttime means of SBP and DBP were similar in the MetS_NT and C groups, excepted for nighttime DBP, which was higher in MetS_NT. During CPET, MetS_NT had higher SBP and DBP at peak and at the first minute of recovery than C (**Table 2**).

Figure 3 demonstrates the absolute and relative frequency of EEBP response during maximal CPET in MetS_NT and C. Ten (37%) of the patients with MetS_NT (four men and six women) presented EEBP during CPET (i.e., peak exercise

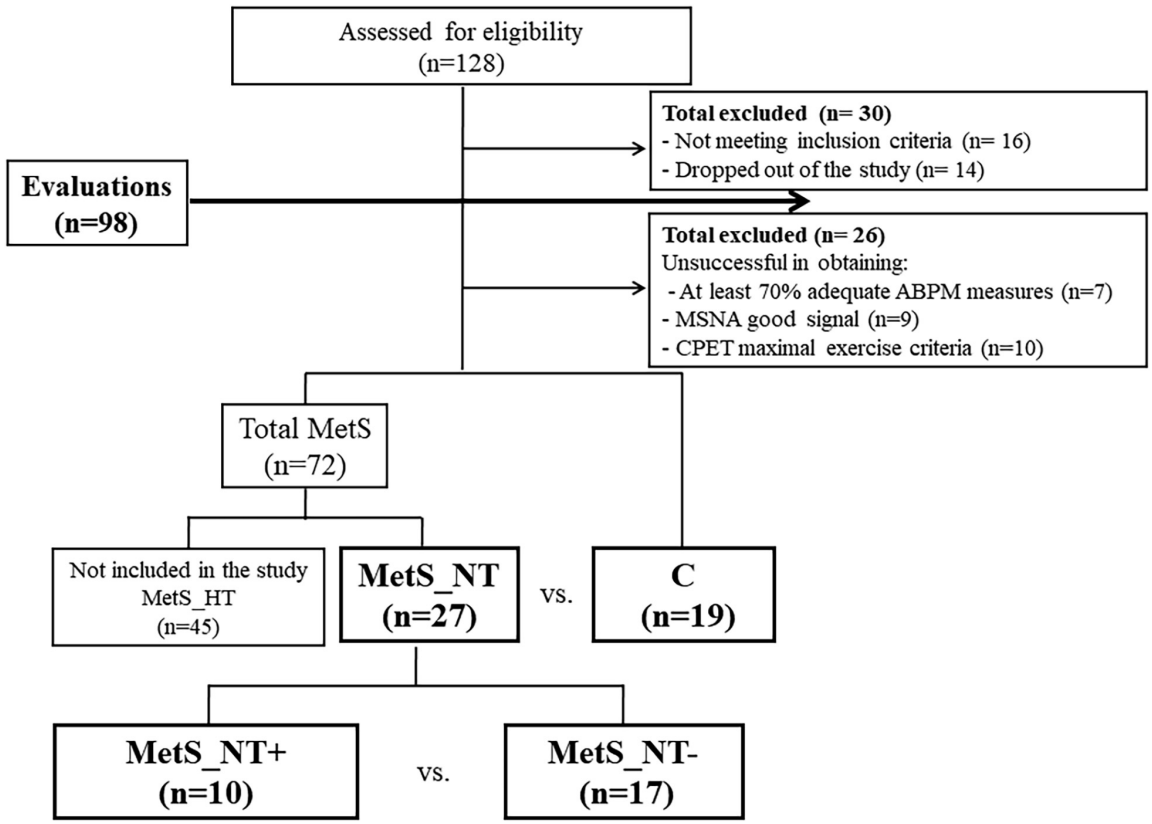

FIGURE 1 | Participants flowchart. Note that there are two different parts in the study. First, we compared normotensive MetS patients (MetS_NT) with the control (C) group. Then, we compared the subgroup of MetS_NT that presented exaggerated exercise BP (MetS_NT+) with those without exaggerated exercise blood pressure response (MetS_NT−) during cardiopulmonary exercise test (CPET). ABPM, ambulatory blood pressure monitoring; MSNA, muscle sympathetic nerve activity.

SBP ≥ 210 mmHg in men and ≥190 mmHg in women), and we named this subgroup as MetS_NT+. On the other hand, the prevalence of EEBP in the C group was significantly lower ($P = 0.044$), with only two in 19 individuals (two men), i.e., 10.5% presented EEBP response (**Figure 3**).

MetS With EEBP (MetS_NT+) Versus MetS Without EEBP (MetS_NT−)

In **Table 3**, we presented comparisons between MetS_NT+ ($n = 10$) and MetS_NT− ($n = 17$, without EEBP) regarding physical characteristics, office BP, BP of the ABPM recordings (24-h, daytime, and nighttime averages of SBP and DBP), and BP response during CPET. The subgroups MetS_NT+ and MetS_NT− were similar in sex distribution, age, weight, BMI, and peak VO_2 (**Table 3**) and AHI ($P = 0.127$).

Despite similar office BP (SBP and DBP), similar 24-h, daytime, and nighttime averages of SBP and DBP measured by the ABPM, these 10 MetS_NT+ who presented EEBP during CPET had higher SBP and DBP levels at peak of maximal exercise and higher SBP levels at the first minute of recovery (**Table 3**).

The MetS_NT+ subgroup had lower BRS+ and BRS− when compared to the MetS_NT− subgroup (**Figure 4A**), whereas MSNA was similar in the two subgroups (**Figure 4B**).

The univariate linear regression between peak SBP and BRS−, BRS+, and MSNA and between SBP at the first min of recovery and BRS−, BRS+, and MSNA in the MetS_NT subgroups with (MetS_NT+) and without (MetS_NT−) EEBP response during maximal CPET is shown in **Table 4**.

Interestingly, only in the MetS_NT+ subgroup, we found a strong negative correlation between peak SBP and BRS− (**Table 4** and **Figure 5**). Similarly, in MetS_NT+ we found a negative correlation between SBP at the first minute at recovery and BRS− (**Table 4**).

In order to determine potential metabolic alterations related to impaired peak SBP during CPET, we analyzed the univariate and multivariate linear regression of all metabolic risk factors with peak SBP during CPET and with BRS− in the MetS_NT+ subgroup (**Table 5**). The univariate linear regression analysis showed a significant correlation between triglycerides with peak SBP and with BRS− (**Table 5**). For multivariate linear regression, we included all metabolic variables regardless of the previous "*P*" value in the univariate linear regression. In multivariate linear regression with peak SBP, no variable was found to be significant. On the other hand, with BRS− the triglycerides remained significant.

TABLE 1 | Physical characteristics, metabolic syndrome (MetS) risk factors, and polysomnography measurements in normotensive metabolic syndrome patients (MetS_NT) and in control (C) group.

	MetS_NT($n = 27$)	C($n = 19$)	*P*
Physical characteristics			
Sex (M/F)	16/11	9/10	0.463
Age (years)	46 ± 7	48 ± 7	0.320
Weight (kg)	88.3 ± 12.6	70.2 ± 11.0	**<0.001**
BMI (kg/m^2)	31.6 ± 3.9	25.3 ± 2.5	**<0.001**
Peak VO_2 (ml/kg/min)	25.9 ± 6.4	25.6 ± 7.1	0.884
MetS risk factors			
WC (cm)	106 ± 8	90 ± 9	**<0.001**
Glucose (mg/dl)	102 ± 12	93 ± 8	**0.004**
Triglycerides (mg/dl)	199 [142–256]	98 [71–124]	**0.005**
HDL-c (mg/dl)	39 ± 9	51 ± 11	**<0.001**
Office SBP (mmHg)	117 [115–120]	111 [108–114]	**0.004**
Office DBP (mmHg)	80 ± 8	70 ± 9	**<0.001**
AHI (events/h)	14.5 [10–19]	8.0 [1–15]	0.091

Data expressed as mean ± SD.
BMI, body mass index; peak VO_2, maximal oxygen uptake; WC, waist circumference; HDL-c, high-density lipoprotein cholesterol; SBP, systolic blood pressure; DBP, diastolic blood pressure; AHI, apnea/hypopnea index. Bold indicates the values that were significant (P < 0.05).

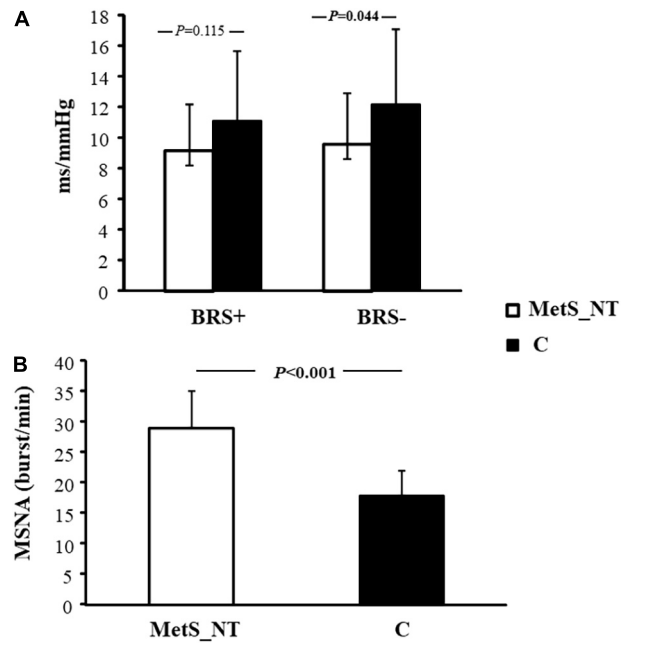

FIGURE 2 | Baroreflex sensitivity for increases (BRS+) and decreases (BRS−) in spontaneous BP fluctuations **(A)**, and muscle sympathetic nerve activity [MSNA, **(B)**] in normotensive MetS patients (MetS_NT, $n = 27$) and control group (C, $n = 19$).

TABLE 2 | Ambulatory Blood Pressure Monitoring recordings (ABPM) and BP response during cardiopulmonary exercise test (CPET) in MetS_NT and in C group.

		MetS_NT($n = 27$)	C($n = 19$)	*P*
Ambulatory blood pressure monitoring (ABPM)				
SBP	24 h (mmHg)	117 ± 8	116 ± 9	0.670
	Daytime (mmHg)	123 ± 8	120 ± 9	0.366
	Nighttime (mmHg)	104 ± 8	107 ± 12	0.405
DBP	24 h (mmHg)	76 ± 7	78 ± 9	0.322
	Daytime (mmHg)	81 ± 8	82 ± 9	0.756
	Nighttime (mmHg)	71 ± 10	64 ± 7	**0.014**
BP response during CPET				
SBP	Peak (mmHg)	195 ± 17	177 ± 24	**0.007**
	1st min rec (mmHg)	188 ± 16	167 ± 21	**0.001**
DBP	Peak (mmHg)	91 ± 11	79 ± 10	**0.001**
	1st min rec (mmHg)	87[82–91]	78[73–83]	**0.007**

Data expressed as Mean ± SD.
SBP, systolic blood pressure; DBP, diastolic blood pressure. Bold indicates the values that were significant (P < 0.05).

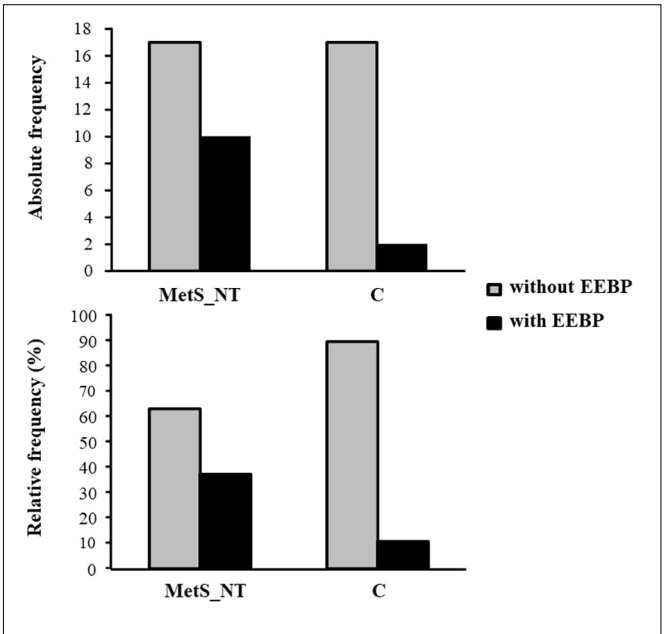

FIGURE 3 | Absolute and relative frequency of exaggerated exercise blood pressure (EEBP = peak exercise SBP ≥ 210 mmHg in men and ≥190 mmHg in women) response during maximal CPET in the MetS_NT and in C. Note that the prevalence was significantly lower in the C group ($P = 0.044$). Ten (37%) of 27 MetS_NT presented EEBP during CPET, whereas only two in 19 individuals (10.5%) presented EEBP in the C group.

DISCUSSION

In the present study, we found that normotensive MetS patients exhibited higher values of peak systolic and diastolic BP during CPET when compared to normotensive controls, regardless of similar sex distribution, age, peak VO_2, and AHI. In addition, they already presented sympathetic hyperactivation and decreased BRS−. Interestingly, some of these normotensive MetS patients (37%) had an EEBP response during maximal exercise (peak SBP ≥ 210 mmHg for men and ≥190 mmHg for women), in spite of similar office BP and similar averages of SBP and DBP at ABPM (24 h, daytime, and nighttime) when compared with normotensive MetS patients without EEBP response. Moreover, this prevalence of EEBP is higher in MetS_NT compared to C.

TABLE 3 | Physical characteristics, office BP, BP of the ABPM recordings, and BP response during CPET in normotensive MetS with (MetS_NT+) and without (MetS_NT−) exaggerated exercise BP response (EEBP) during maximal CPET.

		MetS_NT+($n = 10$)	MetS_NT-($n = 17$)	*P*
Physical characteristics				
Sex (F/M)		6/4	5/12	0.249
Age (years)		48 ± 6	45 ± 8	0.305
Weight (kg)		88.6 ± 10.4	88.1 ± 14.0	0.923
BMI (kg/m^2)		33.1 ± 3.7	30.7 ± 3.8	0.114
Peak VO_2 (ml/kg/min)		24.0 ± 6.8	27.0 ± 6.2	0.256
Office BP measurements				
Office SBP (mmHg)		120 ± 5	116 ± 7	0.089
Office DBP (mmHg)		81 ± 7	80 ± 6	0.620
Ambulatory blood pressure monitoring (ABPM)				
SBP	24 h (mmHg)	119 ± 7	115 ± 8	0.215
	Daytime (mmHg)	124 ± 7	122 ± 9	0.530
	Nighttime (mmHg)	107 ± 5	102 ± 9	0.153
DBP	24 h (mmHg)	76 ± 8	75 ± 7	0.906
	Daytime (mmHg)	81 ± 8	81 ± 8	0.811
	Nighttime (mmHg)	64 ± 7	64 ± 8	0.979
BP response during CPET				
SBP	Peak (mmHg)	210 ± 12	186 ± 14	**<0.001**
	1st-min rec (mmHg)	198 ± 14	182 ± 15	**0.025**
DBP	Peak (mmHg)	98 ± 11	87 ± 9	**0.007**
	1st-min rec (mmHg)	90[80–110]	85[70–105]	0.217

Data expressed as mean ± SD.
BMI, body mass index; peak VO_2, maximal oxygen uptake; SBP, systolic blood pressure; DBP, diastolic blood pressure. Bold indicates the values that were significant ($P < 0.05$).

We would like to point out that our MetS_NT subgroups, with or without EEBP response, were similar in age, sex, and functional capacity, factors that are known to impact EEBP (Schultz et al., 2015). However, the MetS_N subgroup that responds with EEBP (MetS_NT+) had lower BRS+ and lower BRS− than the subgroup without EEBP (MetS_NT−) (see **Figure 4**).

Our data corroborates a previous study conducted by Grassi et al. (2005). They found that sympathetic hyperactivation was not limited when MetS comprise hypertension as one of risk factors. However, unlike this previous study (Grassi et al., 2005), we found that patients with MetS with normal BP had attenuated BRS.

The major finding is that in the subgroup of normotensive MetS with EEBP response, the peak SBP was strong and negatively associated with BRS deactivation (see **Figure 5**). Therefore, the current study provides new and important findings on the autonomic mechanism involved in the EEBP response to exercise in these patients. Although office BP and BP in ABPM were similar (see **Table 3**), in this specific population with several metabolic risk factors the EEBP response denotes an arterial baroreflex dysfunction that seems to play a role in controlling BP during physiological stress, as it seems to do during exercise.

Notwithstanding using submaximal exercise and different measurement techniques as well as different SBP cutoff values to characterize EEBP, a recent community-based analysis from the Paris Prospective Study III (Sharman et al., 2018) has found similar results, observing that impaired BRS was independently associated with EEBP even among those with well-controlled resting BP. Nevertheless, this study that included 8,976 participants differs from ours in that the information pertaining to lifestyle and personal and family medical history (e.g., physical activity, disease status, and medication use) was achieved by self-administered questionnaires. Even so, this study reinforces that in normotensive subjects, decreased BRS seems to be a mechanistic pathway which may account for abnormal BP response to exercise.

It is well-established that adrenergic activation and baroreflex dysfunction are present in all hypertensive states (Grassi et al., 2007; Laterza et al., 2007; Seravalle et al., 2015). Likewise, exacerbation of BP during CPET is common in hypertensive patients (Schultz et al., 2015; Kader Abdel Wahab, 2016). Moreover, hypertensive patients with MetS had more than a twofold risk of exhibiting EEBP response than those without MetS (Tsioufis et al., 2012). Our aim in this study was to investigate whether this exacerbated BP response and autonomic changes were also detectable in the initial clinical phases of MetS, particularly in those patients without the presence of the hypertension component. Albeit it is consensus that decreased BRS is associated with increased sympathetic drive (Laterza, 2007) and higher BP (Wustmann et al., 2009), in our study only the BRS remained different between subgroups when we divided the normotensive MetS group (MetS_NT) by subgroups with

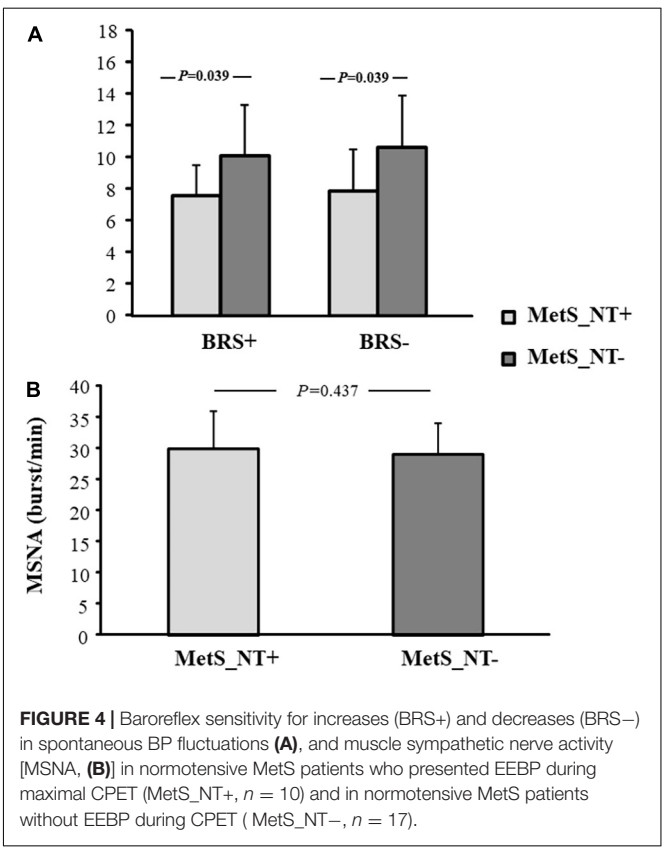

FIGURE 4 | Baroreflex sensitivity for increases (BRS+) and decreases (BRS−) in spontaneous BP fluctuations **(A)**, and muscle sympathetic nerve activity [MSNA, **(B)**] in normotensive MetS patients who presented EEBP during maximal CPET (MetS_NT+, $n = 10$) and in normotensive MetS patients without EEBP during CPET (MetS_NT−, $n = 17$).

(MetS_NT+) or without EEBP (MetS_NT−) response during maximal CPET, whereas MSNA did not. We cannot rule out that there was sympathetic hyperactivation at the peak of exercise in these patients with EEBP, since the measurement of MSNA was performed at rest, with the patients in a lying position. On the other hand, even in a small normotensive MetS group with EEBP response ($n = 10$), there was a strong negative association of peak SBP with BRS−, lending strength to the hypothesis that this autonomic reflex is an important pathophysiological mechanism underlying EEBP.

The mechanisms underlying an exacerbated BP response during exercise have yet to be fully understood and seem indeed to be multifactorial. So far, studies have pointed to endothelial dysfunction and changes in the intima-media thickness as the mechanisms underlying the exacerbation of BP during CPET in hypertension (Kader Abdel Wahab, 2016), perhaps caused by systemic vascular inflammation (Hamer and Steptoe, 2012). We may speculate that these alterations in turn may generate vascular resistance, causing arterial stiffness, and as such may be related to EEBP response in our sample. Indeed, in a previous study multivariate regression models clearly indicated that MetS, when compared to individual metabolic components, predicts impairment of endothelial dysfunction (Shimabukuro et al., 2016). To lend further support to this finding, a previous study conducted by our group involving MetS patients has demonstrated that impaired fasting glucose does play a role in vascular damage associated with sympathetic hyperactivation (Rodrigues et al., 2017). In another study with MetS patients, we found that the higher number of risk factors increase vascular dysfunction, as measured by pulse wave velocity (Lopes-Vicente et al., 2017). Additionally, besides age and increased SBP, altered triglycerides in the clustering worsened the stiffness of large vessels (Lopes-Vicente et al., 2017).

When hypertension is eliminated, controversy remains regarding the pathophysiological change and the EEBP response. In addition, only a few studies have focused on the effects of MetS on BRS (Grassi et al., 2005; Trombetta et al., 2010; Assoumou et al., 2012; Sharman et al., 2018). Sharman et al. (2018) demonstrated that impaired BRS, but not carotid stiffness, was independently associated with exaggerated exercise BP among those with well-controlled resting BP.

Our MetS population sample comprised recently diagnosed and unmedicated MetS patients without hypertension, a very common condition in middle-aged individuals who often do not consider themselves to be diseased. Our study brings a new perspective in that it lends prominence to the role of BRS as a key mechanism which may underlie the response of BP to CPET.

While elucidating the risk factors that impair autonomic control of BP during exercise in normotensive patients with MetS is indeed complex, given that these factors share pathophysiological pathways and seem to potentiate each other, the association of triglycerides with peak SBP may suggest the potential of this risk factor over some pathophysiological changes involved in hemodynamic control. However, the overlap of metabolic risk factors seems to be the main cause of the autonomic alteration in normotensive MetS patients.

TABLE 4 | Univariate linear regression between peak SBP and BRS−, BRS+, and MSNA and between SBP at 1st-min rec and BRS−, BRS+, and MSNA in normotensive MetS with (MetS_NT+) and without (MetS_NT−) EEBP response during maximal CPET.

		Peak SBP		SBP 1st min rec	
		R	***P***	***R***	***P***
MetS_NT+ ($n = 10$)	BRS+	−0.10	0.786	−0.41	0.312
	BRS−	−0.70	**0.024**	−0.73	**0.041**
	MSNA	0.40	0.283	0.56	0.148
MetS_NT− ($n = 17$)	BRS+	0.16	0.552	0.37	0.209
	BRS−	−0.02	0.933	0.28	0.361
	MSNA	0.19	0.558	−0.25	0.519

BRS+, spontaneous baroreflex sensitivity for increases in BP; BRS−, spontaneous baroreflex sensitivity for decreases in BP; MSNA, muscle sympathetic nerve activity; SBP, systolic blood pressure; DBP, diastolic blood pressure. Bold indicates the values that were significant ($P < 0.05$).

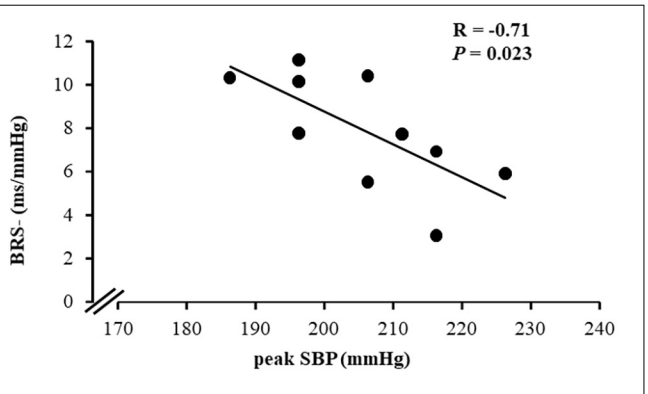

FIGURE 5 | Correlation between peak systolic BP (peak SBP) during CPET and spontaneous baroreflex sensitivity for decreases in blood pressure (BRS−) in the subgroup of normotensive patients with MetS who presented exaggerated SBP during CPET (MetS_NT+, $n = 10$).

In general, the overlap of several risk factors seems to be stronger in predicting the pathophysiological alterations related to attenuation of BRS as well as to EEBP response. Assoumou et al. (2012) have shown that decreased BRS slope was significantly correlated with MetS. Nevertheless, this association also independently was found for triglycerides and waist circumference in elderly patients with MetS (Assoumou et al., 2012).

Indeed, the overlap of several metabolic risk factors is the probable trigger to higher values of peak systolic BP during exercise, as shown by a previous study conducted by Tsioufis et al. (2012). They found that MetS in newly diagnosed hypertensive patients was associated with increased peak exercise BP and a higher frequency of EEBP, regardless of ambulatory BP levels and anthropometric characteristics. Our results extend this knowledge to the change in BRS in MetS without hypertension, which leads to the EEBP response that occurs beyond hypertension, predisposing these normotensive MetS with EEBP response to higher cardiovascular risk.

We have previously observed that OSA, a common comorbidity in patients with MetS, leads to a further impairment

in autonomic control (Trombetta et al., 2010, 2013; Toschi-Dias et al., 2013; Cepeda et al., 2015). However, in the present investigation patients with hypertension as one of MetS risk factors were excluded, and our studied groups were similar in the AHI. Thus, OSA apparently did not affect BP response during exercise in these normotensive MetS patients, not even those with EEBP response.

Although several methods have been developed to study baroreflex function in humans, most of these techniques are of limited value for a daily practice in the clinical setting (La Rovere et al., 2008). Given that the BP measurement is a standard evaluation procedure during the graded exercise test, a routinely in-clinic exam, we may suggest the use of the Framingham criteria cutoff for peak SBP (≥210 mmHg in men and ≥190 mmHg in women) (Tsioufis et al., 2008, 2012) as a surrogate method to indicate probable baroreflex dysfunction in normotensive MetS patients.

In conclusion, the present study offers a new insight on the mechanisms underlying EEBP response to exercise and more particularly on the key role of BRS impairment in the increased BP response during exercise in normotensive patients with MetS. Our findings emphasize the importance of identifying EEBP response to exercise in MetS patients, even in those within the normal range of clinical BP, since exaggerated BP during CPET was associated with the baroreflex in MetS patients, which put these patients at a greater cardiovascular risk. Thus, an awareness of EEBP during maximal CPET in normotensive MetS patients should be part of any clinical interventions.

Limitations

There are some limitations in our study that merit discussion. Previous studies addressing the mechanisms underlying EEBP have been carried out with healthy volunteers. The association of risk factors (at least 3) in our sample of normotensive patients with MetS can cause interpretation bias, since any of the factors, according to their prevalence, may be involved in the EEBP during CPET (Thanassoulis et al., 2012).

We would like to point out that it has already been demonstrated that women have distinct pathophysiological pathways from men (Lambert et al., 2007; Lew et al., 2017), as well as increased adiposity along with differences in endothelial function and recruitment of inflammatory cells. Even though our sample is composed of male and female patients, this should not affect our results, since we did not find any differences in gender distribution between the studied groups.

In this study, the office BP was measured in a single visit. According to the "Brazilian Guidelines of Hypertension–2020" (Barroso et al., 2020), true hypertension is defined when systematically abnormal BP values are measured in the office, or more assertively by using out-of-office measurements by ABPM. Following the guidelines, in order to confirm hypertension, our patients underwent an ABPM.

Regarding the method used for determining the BRS, the venous vasoactive drug infusion technique has been largely used. However, the lack of selectivity in the response has been considered as one important limitation of the use of vasoactive drugs (La Rovere et al., 2008). Thus, we opted for the spontaneous method, since it reflects spontaneous beat-to-beat baroreflex at rest while providing a safe and reliable non-invasive assessment of human BRS. However, the sequence method used in the present study is just one of the spontaneous BRS methods in literature and other methods may quantify different aspects of the autonomic BRS control (Silva et al., 2019). Another limitation is that a spontaneous method used to study the arterial baroreflex estimates the feedback effects of SBP changes on pulse interval (PI) and reciprocal of heart rate, neglecting the simultaneously occurring feedforward effects of PI on SBP, induced through changes in cardiac output (Parati et al., 2019).

Assessing auscultatory BP during treadmill maximal exercise is sometimes difficult. We took great care to have reliable peak BP measurement, using a stationary electromagnetic brake cycle ergometer.

TABLE 5 | Univariate and multivariate linear regression between peak SBP and metabolic risk factors and between BRS− and metabolic risk factors in the MetS_NT subgroups with EEBP (MetS_NT+) during maximal CPET.

Peak SBP	Univariate linear regression		Multivariate linear regression		
	R	*P*	β	(95% CI)	*P*
WC	0.10	0.794	0.06	(102–111)	0.877
Glucose	0.02	0.964	0.16	(94–107)	0.654
Triglycerides	0.66	**0.039**	0.68	(84–156)	0.195
HDL-c	−0.42	0.221	−0.04	(39–51)	0.934
BRS−	**Univariate linear regression**		**Multivariate linear regression**		
	R	*P*	β	(95% CI)	*P*
WC	0.45	0.188	0.218	(102–111)	0.367
Glucose	−0.36	0.301	−0.477	(94–107)	0.064
Triglycerides	0.71	**0.022**	−0.775	(84–156)	**0.034**
HDL-c	−0.31	0.382	−0.030	(39–55)	0.913

BRS−, baroreflex sensitivity for decreases in spontaneous blood pressure; WC, waist circumference; HDL-c, high-density lipoprotein cholesterol. Bold indicates the values that were significant (P < 0.05).

DATA AVAILABILITY STATEMENT

The original contributions presented in the study are included in the article/**Supplementary Material**, further inquiries can be directed to the corresponding author.

ETHICS STATEMENT

The studies involving human participants were reviewed and approved by Scientific Commission of the Instituto do Coracao (InCor), and by the Ethics in Research Commission of the Hospital das Clinicas HCFMUSP, Faculdade de Medicina, Universidade de São Paulo (#1222/05). The patients/participants provided their written informed consent to participate in this study.

AUTHOR CONTRIBUTIONS

ACD-M, SR, FXC, and ICT: conception and design of the work, data acquisition, analysis, interpretation of data, drafting of the work, and critical revision for important intellectual content. ET-D, ER, JCC, MJNNA, AMFWB, and MUPBR: data acquisition, interpretation of data for the work, and critical revision for important intellectual content. All authors read and approved the final version to be published, and all authors agreed with all aspects of the work in order to ensure the accuracy and integrity of the work.

FUNDING

This work was performed at the Instituto do Coracao, Hospital das Clinicas HCFMUSP, Faculdade de Medicina, Universidade de São Paulo, Brazil and supported by Fundação de Amparo à Pesquisa do Estado de São Paulo (FAPESP #2011/17533-6). ACD-M and JCC were supported by Coordenação de Aconselhamento de Pessoal de Nível Superior (CAPES); SR was supported by FAPESP (#2013/15323-0) and Conselho Nacional de Pesquisa (CNPq#165778/2017-2); FXC was supported by FAPESP (#2015/03274-0) and CAPES (#2016/16831-7); ET-D was supported by FAPESP (#2013/07651-7); MUPBR (#313152/2020-9) and ICT (#302809/2018-0) were supported by CNPq. The funders had no role in study design, data collection and analysis, decision to publish, or preparation of the manuscript.

SUPPLEMENTARY MATERIAL

The Supplementary Material for this article can be found online at: https://www.frontiersin.org/articles/10.3389/fnins.2021.680195/full#supplementary-material

Supplementary Table 1 | Univariate linear regression between peak SBP and metabolic syndrome (MetS) risk factors in all studied groups.

REFERENCES

Assoumou, H. G., Bertholon, F., Barthélémy, J. C., Pichot, V., Celle, S., Gosse, P., et al. (2012). Alteration of baroreflex sensitivity in the elderly: the relationship with metabolic syndrome components. *Int. J. Cardiol.* 155, 333–335. doi: 10.1016/j.ijcard.2011.12.050

Balady, G. J., Arena, R., Sietsema, K., Myers, J., Coke, L., Fletcher, G. F., et al. (2010). Clinician's Guide to cardiopulmonary exercise testing in adults: a scientific statement from the American Heart Association. *Circulation* 122, 191–225. doi: 10.1161/CIR.0b013e3181e52e69

Barroso, W. K. S., Rodrigues, C. I. S., Bortolotto, L. A., Gomes, M. A. M., Brandão, A. A., Feitosa, A. D. M., et al. (2020). Brazilian guidelines of hypertension – 2020. *Arq. Bras. Cardiol.* 116, 516–658. doi: 10.36660/abc.20201238

Beaver, W. L., Wasserman, K., and Whipp, B. J. (1986). A new method for the detection of anaerobic threshold by gas exchange. *J. Appl. Physiol.* 60, 2020–2027. doi: 10.1152/jappl.1986.60.6.2020

Cepeda, F. X., Toschi-Dias, E., Maki-Nunes, C., Rondon, M. U., Alves, M. J., Braga, A. M., et al. (2015). Obstructive sleep apnea impairs post exercise sympathovagal balance in patients with metabolic syndrome. *Sleep* 38, 1059–1066. doi: 10.5665/sleep.4812

Chapleau, M. W., Li, Z., Meyrelles, S. S., Ma, X., and Abboud, F. M. (2001). Mechanisms determining sensitivity of baroreceptor afferents in health and disease. *Ann. N. Y. Acad. Sci.* 940, 1–19. doi: 10.1111/j.1749-6632.2001.tb03662.x

Drager, L. F., Queiroz, E. L., Lopes, H. F., Genta, P. R., Krieger, E. M., and Lorenzi-Filho, G. (2009). Obstructive sleep apnea is highly prevalent and correlates with impaired glycemic control in consecutive patients with the metabolic syndrome. *J. Cardiometab. Syndr.* 4, 89–95. doi: 10.1111/j.1559-4572.2008.00046.x

Fagius, J., and Wallin, B. G. (1993). Long-term variability and reproducibility of resting human muscle nerve sympathetic activity at rest, as reassessed after a decade. *Clin. Auton. Res.* 3, 201–205. doi: 10.1007/BF01826234

Farah, R., Shurtz-Swirski, R., and Nicola, M. (2009). High blood pressure response to stress ergometry could predict future hypertension. *Eur. J. Intern. Med.* 20, 366–368. doi: 10.1016/j.ejim.2008.09.016

Gami, A. S., Witt, B. J., Howard, D. E., Erwin, P. J., Gami, L. A., Somers, V. K., et al. (2007). Metabolic syndrome and risk of incident cardiovascular events and death: a systematic review and meta-analysis of longitudinal studies. *J. Am. Coll. Cardiol.* 49, 403–414. doi: 10.1016/j.jacc.2006.09.032

Grassi, G., Dell'Oro, R., Quarti-Trevano, F., Scopelliti, F., Seravalle, G., and Paleari, F. (2005). Neuroadrenergic and reflex abnormalities in patients with metabolic syndrome. *Diabetologia* 48, 1359–1365. doi: 10.1007/s00125-005-1798-z

Grassi, G., Seravalle, G., Trevano, F. Q., Dell'oro, R., Bolla, G., Cuspidi, C., et al. (2007). Neurogenic abnormalities in masked hypertension. *Hypertension* 50, 537–542. doi: 10.1161/HYPERTENSIONAHA.107.092528

Grundy, S. M., Cleeman, J. I., Daniels, S. R., Donato, K. A., Eckel, R. H., Franklin, B. A., et al. (2005). Diagnosis and management of the metabolic syndrome: an American Heart Association/National Heart, Lung, and Blood institute scientific statement. *Circulation* 112, 2735–2752. doi: 10.1161/CIRCULATIONAHA.105.169404

Hamer, M., and Steptoe, A. (2012). Vascular inflammation and blood pressure response to acute exercise. *Eur. J. Appl. Physiol.* 112, 2375–2379. doi: 10.1007/s00421-011-2210-y

Kader Abdel Wahab, M. A. (2016). Is an exaggerated blood pressure response to exercise in hypertensive patients a benign phenomenon or a dangerous alarm? *Eur. J. Prev. Cardiol.* 23, 572–576. doi: 10.1177/2047487315583136

Keller, K., Stelzer, K., Ostad, M. A., and Post, F. (2017). Impact of exaggerated blood pressure response in normotensive individuals on future hypertension and prognosis: systematic review according to PRISMA guideline. *Adv. Med. Sci.* 62, 317–329. doi: 10.1016/j.advms.2016.11.010

La Rovere, M. T., Pinna, G. D., and Raczak, G. (2008). Baroreflex sensitivity: measurement and clinical implications. *Ann. Noninvasive Electrocardiol.* 13, 191–207. doi: 10.1111/j.1542-474X.2008.00219.x

Lambert, E., Straznicky, N., Eikelis, N., Esler, M., Dawood, T., Masuo, K., et al. (2007). Gender differences in sympathetic nervous activity: influence of body mass and blood pressure. *J. Hypertens.* 25, 1411–1419. doi: 10.1097/HJH.0b013e3281053af4

Laterza, M. C., de Matos, L. D., Trombetta, I. C., Braga, A. M., Roveda, F., Alves, M. J., et al. (2007). Exercise training restores baroreflex sensitivity in never-treated hypertensive patients. *Hypertension* 49, 1298–1306. doi: 10.1161/HYPERTENSIONAHA.106.085548

Lew, J., Sanghavi, M., Ayers, C. R., McGuire, D. K., Omland, T., Atzler, D., et al. (2017). Sex-based differences in cardiometabolic biomarkers. *Circulation* 135, 544–555. doi: 10.1161/CIRCULATIONAHA.116.023005

Lopes-Vicente, W. R. P., Rodrigues, S., Cepeda, F. X., Jordão, C. P., Costa-Hong, V., Dutra-Marques, A. C. B., et al. (2017). Arterial stiffness and its association with clustering of metabolic syndrome risk factors. *Diabetol. Metab. Syndr.* 9:87. doi: 10.1186/s13098-017-0286-1

Maki-Nunes, C., Toschi-Dias, E., Cepeda, F. X., Rondon, M. U., Alves, M. J., Fraga, R. F., et al. (2015). Diet and exercise improve chemoreflex sensitivity in patients with metabolic syndrome and obstructive sleep apnea. *Obesity* 23, 1582–1590. doi: 10.1002/oby.21126

Mancia, G., Fagard, R., Narkiewicz, K., Redón, J., Zanchetti, A., Böhm, M., et al. (2013). 2013 ESH/ESC Guidelines for the management of arterial hypertension: the Task Force for the management of arterial hypertension of the European Society of Hypertension (ESH) and of the European Society of Cardiology (ESC). *J. Hypertens* 31, 1281–1357. doi: 10.1097/01.hjh.0000431740.32696.cc

Miyai, N., Arita, M., Morioka, I., Miyashita, K., Nishio, I., and Takeda, S. (2000). Exercise BP response in subjects with high-normal BP: exaggerated blood pressure response to exercise and risk of future hypertension in subjects with high-normal blood pressure. *J. Am. Coll. Cardiol.* 36, 1626–1631. doi: 10.1016/s0735-1097(00)00903-7

O'Brien, E., Parati, G., Stergiou, G., Asmar, R., Beilin, L., Bilo, G., et al. (2013). European Society of Hypertension position paper on ambulatory blood pressure monitoring. *J. Hypertens.* 31, 1731–1768. doi: 10.1097/HJH.0b013e328363e964

Parati, G., Castiglioni, P., Faini, A., Di Rienzo, M., Mancia, G., Barbieri, R., et al. (2019). Closed-Loop cardiovascular interactions and the baroreflex cardiac arm: modulations over the 24 h and the effect of hypertension. *Front. Physiol.* 10:477. doi: 10.3389/fphys.2019.00477

Parati, G., Di Rienzo, M., and Mancia, G. (2000). How to measure baroreflex sensitivity: from the cardiovascular laboratory to daily life. *J. Hypertens.* 18, 7–19.

Rodrigues, S., Cepeda, F. X., Toschi-Dias, E., Dutra-Marques, A. C. B., Carvalho, J. C., Costa-Hong, V., et al. (2017). The role of increased glucose on neurovascular dysfunction in patients with the metabolic syndrome. *J. Clin. Hypertens.* 19, 840–847. doi: 10.1111/jch.13060

Romero-Corral, A., Sert-Kuniyoshi, F. H., Sierra-Johnson, J., Orban, M., Gami, A., Davison, D., et al. (2010). Modest visceral fat gain causes endothelial dysfunction in healthy humans. *J. Am. Coll. Cardiol.* 56, 662–666. doi: 10.1016/j.jacc.2010.03.063

Schultz, M. G., Otahal, P., Cleland, V. J., Blizzard, L., Marwick, T. H., and Sharman, J. E. (2013). Exercise-induced hypertension, cardiovascular events, and mortality in patients undergoing exercise stress testing: a systematic review and meta-analysis. *Am. J. Hypertens.* 26, 357–366. doi: 10.1093/ajh/hps053

Schultz, M. G., Otahal, P., Picone, D. S., and Sharman, J. E. (2015). Clinical relevance of exaggerated exercise blood pressure. *J. Am. Coll. Cardiol.* 66, 1843–1845. doi: 10.1016/j.jacc.2015.08.015

Seravalle, G., Lonati, L., Buzzi, S., Cairo, M., Quarti Trevano, F., Dell'Oro, R., et al. (2015). Sympathetic nerve traffic and baroreflex function in optimal, normal, and high-normal blood pressure states. *J. Hypertens.* 33, 1411–1417. doi: 10.1097/HJH.0000000000000567

Sharman, J. E., Boutouyrie, P., Perier, M. C., Thomas, F., Guibout, C., Khettab, H., et al. (2018). Impaired baroreflex sensitivity, carotid stiffness, and exaggerated exercise blood pressure: a community-based analysis from the Paris Prospective Study III. *Eur. Heart J.* 39, 599–606. doi: 10.1093/eurheartj/ehx714

Shimabukuro, M., Higa, N., Masuzaki, H., Sata, M., and Ueda, S. (2016). Impact of individual metabolic risk components or its clustering on endothelial and smooth muscle cell function in men. *Cardiovasc. Diabetol.* 15:77. doi: 10.1186/s12933-016-0394-5

Silva, L. E. V., Dias, D. P. M., da Silva, C. A. A., Salgado, H. C., and Fazan, R. Jr. (2019). Revisiting the sequence method for baroreflex analysis. *Front. Neurosci.* 13:17. doi: 10.3389/fnins.2019.00017

Thanassoulis, G., Lyass, A., Benjamin, E. J., Larson, M. G., Vita, J. A., Levy, D., et al. (2012). Relations of exercise blood pressure response to cardiovascular risk factors and vascular function in the Framingham Heart Study. *Circulation* 125, 2836–2843. doi: 10.1161/CIRCULATIONAHA.111.063933

Toschi-Dias, E., Trombetta, I. C., Dias da Silva, V. J., Maki-Nunes, C., Cepeda, F. X., Alves, M. J., et al. (2013). Time delay of baroreflex control and oscillatory pattern of sympathetic activity in patients with metabolic syndrome and obstructive sleep apnea. *Am. J. Physiol. Heart Circ. Physiol.* 304, H1038–H1044.

Triggiani, A. I., Valenzano, A., Trimigno, V., Di Palma, A., Moscatelli, F., Cibelli, G., et al. (2019). Heart rate variability reduction is related to a high amount of visceral adiposity in healthy young women. *PLoS One* 14:e0223058. doi: 10.1371/journal.pone.0223058

Trombetta, I. C., Maki-Nunes, C., Toschi-Dias, E., Alves, M. J., Rondon, M. U., Cepeda, F. X., et al. (2013). Obstructive sleep apnea is associated with increased chemoreflex sensitivity in patients with metabolic syndrome. *Sleep* 36, 41–49. doi: 10.5665/sleep.2298

Trombetta, I. C., Somers, V. K., Maki-Nunes, C., Drager, L. F., Toschi-Dias, E., Alves, M. J., et al. (2010). Consequences of comorbid sleep apnea in the metabolic syndrome: implications for cardiovascular risk. *Sleep* 33, 1193–1199. doi: 10.1093/sleep/33.9.1193

Tsioufis, C., Chatzis, D., Tsiachris, D., Katsi, V., Toutouzas, K., Tousoulis, D., et al. (2008). Exaggerated exercise blood pressure response is related to tissue Doppler imaging estimated diastolic dysfunction in the early stages of hypertension. *J. Am. Soc. Hypertens.* 2, 158–164. doi: 10.1016/j.jash.2007.11.002

Tsioufis, C., Kasiakogias, A., Tsiachris, D., Kordalis, A., Thomopoulos, C., Giakoumis, M., et al. (2012). Metabolic syndrome and exaggerated blood pressure response to exercise in newly diagnosed hypertensive patients. *Eur. J. Prev. Cardiol.* 19, 467–473. doi: 10.1177/1741826711410819

Tzemos, N., Lim, P. O., Mackenzie, I. S., and MacDonald, T. M. (2015). Exaggerated exercise blood pressure response and future cardiovascular disease. *J. Clin. Hypertens. (Greenwich)* 17, 837–844. doi: 10.1111/jch.12629

Williams, B., Mancia, G., Spiering, W., Agabiti Rosei, E., Azizi, M., Burnier, M., et al. (2019). 2018 ESC/ESH Guidelines for the management of arterial hypertension. *Eur. Heart J.* 39, 3021–3104. doi: 10.1093/eurheartj/ehy339

Wustmann, K., Kucera, J. P., Scheffers, I., Mohaupt, M., Kroon, A. A., de Leeuw, P. W., et al. (2009). Effects of chronic baroreceptor stimulation on the autonomic cardiovascular regulation in patients with drug-resistant arterial hypertension. *Hypertension* 54, 530–536. doi: 10.1161/HYPERTENSIONAHA.109.134023

Conflict of Interest: The authors declare that the research was conducted in the absence of any commercial or financial relationships that could be construed as a potential conflict of interest.

frontiers in Neuroscience

ORIGINAL RESEARCH
published: 16 July 2021
doi: 10.3389/fnins.2021.707345

Analytic and Integrative Framework for Understanding Human Sympathetic Arterial Baroreflex Function: Equilibrium Diagram of Arterial Pressure and Plasma Norepinephrine Level

Fumiyasu Yamasaki[1]†, Takayuki Sato[2†], Kyoko Sato[1‡] and André Diedrich[3]*

[1] Department of Clinical Laboratory, Kochi Medical School, Nankoku, Japan, [2] Department of Cardiovascular Control, Kochi Medical School, Nankoku, Japan, [3] Department of Biomedical Engineering, Autonomic Dysfunction Center, Vanderbilt University Medical Center, Vanderbilt University, Nashville, TN, United States

OPEN ACCESS

Edited by:
Flavia Ravelli,
University of Trento, Italy

Reviewed by:
Vlasta Bari,
IRCCS Policlinico San Donato, Italy
Michele Orini,
University College London, United Kingdom

***Correspondence:**
Fumiyasu Yamasaki
yamasaki-f@kochi-u.ac.jp

† These authors have contributed equally to this work

‡Present address:
Kyoko Sato,
Department of Medicine, Tokyo Women's Medical University Medical Center East, Tokyo, Japan

Specialty section:
This article was submitted to Autonomic Neuroscience, a section of the journal Frontiers in Neuroscience

Received: *09 May 2021*
Accepted: *24 June 2021*
Published: *16 July 2021*

Citation:
Yamasaki F, Sato T, Sato K and Diedrich A (2021) Analytic and Integrative Framework for Understanding Human Sympathetic Arterial Baroreflex Function: Equilibrium Diagram of Arterial Pressure and Plasma Norepinephrine Level. Front. Neurosci. 15:707345. doi: 10.3389/fnins.2021.707345

Background: The sympathetic arterial baroreflex is a closed-loop feedback system for stabilizing arterial pressure (AP). Identification of unique functions of the closed system in humans is a challenge. Here we propose an analytic and integrative framework for identifying a static operating point and open-loop gain to characterize sympathetic arterial baroreflex in humans.

Methods and Results: An equilibrium diagram with two crossing functions of mechanoneural (MN) and neuromechanical (NM) arcs was analyzed during graded tilt maneuvers in seven healthy subjects. AP and plasma norepinephrine level (PNE), as a surrogate for sympathetic nerve activity, and were recorded after vagal modulation of heart function was blocked by atropine. The MN-arc curve was described as a locus of operating points during –7, 0, 15, and 60° head-up tilting (HUT) on a PNE-AP plane. The NM-arc curve was drawn as a line between operating points before and after ganglionic blockade (trimethaphan, 0.1 $mg{\cdot}ml^{-1}{\cdot}kg^{-1}$) during 0° or 15° HUT. Gain values were estimated from the slopes of these functional curves. Finally, an open-loop gain, which is a most important index for performance of arterial baroreflex, was given by a product of the gain values of MN (G_{MN}) and NM arcs (G_{NM}). Gain values of MN was 8.92 ± 3.07 $pg{\cdot}ml^{-1}{\cdot}mmHg^{-1}$; and G_{NM} at 0° and 15° HUT were 0.61 ± 0.08 and 0.36 ± 0.05 $mmHg{\cdot}ml{\cdot}pg^{-1}$, respectively. A postural change from supine to 15° HUT significantly reduced the open-loop gain from 5.62 ± 0.98 to 3.75 ± 0.62. The effects of HUT on the NM arc and open-loop gain seemed to be similar to those of blood loss observed in our previous animal studies.

Conclusion: An equilibrium-diagram analysis contributes to a quantitative and integrative understanding of function of human sympathetic arterial baroreflex.

Keywords: baroreflex, blood pressure, equilibrium diagram, feedback system, mechanoneural arc, neuromechanical arc, norepinephrine, open-loop gain

INTRODUCTION

Arterial baroreflex through sympathetic efferents is the most important negative feedback control system to attenuate the effects of rapid daily perturbations in arterial pressure (AP) (Guyton et al., 1972; Sato et al., 1999b). For example, the fall in AP during a postural change from lying to standing is instantaneously sensed by arterial baroreceptors which initiate an immediate compensatory vasoconstriction and increase in heart rate through activation of efferent sympathetic pathways. Without such compensatory baroreflex response, the simple standing maneuver would cause a fall in AP with the consequence of reduction of brain perfusing and possible loss of consciousness (Ketch et al., 2002; Parikh et al., 2002; Ondrusova et al., 2017).

Guyton et al. (1972) have developed an open-loop analytical approach for characterizing a physiological system with a feedback loop based on new concepts such as the Guyton's equilibrium diagram for right atrial pressure, venous return, and cardiac output. This diagram enables us to quantitatively and analytically understand how the unique value of the cardiac output is determined by the cardiovascular system. A similar analytical approach for identifying a static operating point of sympathetic arterial baroreflex is needed to understand the mechanism by which AP and sympathetic nerve activity are determined under the closed-loop conditions.

Our previous animal studies with vascular isolation of baroreceptors revealed that the decomposition of the baroreflex loop into mechanoneural (MN) and neuromechanical (NM) arcs allows us to analytically determine the static operating point by equilibrating respective functional curves of the two arcs (Sato et al., 1999b). However, the baroreceptor isolation approach is not applicable to humans. The purpose of the present investigation was to develop a new method and integrative framework for analyzing sympathetic baroreflex control of AP in humans.

MATERIALS AND METHODS

Theoretical Considerations: Coupling of Mechanoneural and Neuromechanical Arcs

A simplified diagram representing characteristics of the sympathetic arterial baroreflex system is shown in **Figure 1A**. The vasomotor center modulates sympathetic vasomotor nerve activity (SNA) in response to the changes in AP produced by external disturbance to the cardiovascular system. The changes in AP are immediately sensed by arterial baroreceptors. Changes of efferent SNA with chronotropic and inotropic effects on the heart and vasoconstrictor effects on smooth muscles in peripheral vessels (Hainsworth and Karim, 1976; Robertson et al., 2012; Ichikawa et al., 2019) exert direct influence over AP counteracting the disturbance. As a result, the effect of external disturbance on AP is attenuated by arterial baroreflex. We denote a controlling element of the simplified baroreflex model as a MN arc and a controlled element as a NM arc. In the MN arc, the input is AP, and the output is SNA. In the NM arc, the input is SNA, and the output is AP. Because the variables characterizing the functions of the two arcs are common, we can superimpose the two functional curves and analytically identify the operating point, i.e., the point defined by AP and SNA under the closed-loop conditions of the feedback system, and as an intersection between them on an equilibrium diagram (**Figure 1B**). The validity of such an equilibrium-diagram analysis for arterial baroreflex has been verified by the previous animal study through a baroreceptor-isolation approach (Sato et al., 1999b).

First, under the closed-loop conditions of the arterial baroreflex system, we draw the functional curve of the MN arc by loading an external disturbance, postural tilting, and on the NM arc. In a supine position, the arterial baroreflex system should operate at an intersection point (*Point 0*) of the two curves on an equilibrium diagram (**Figure 1B**). During head-up tilt (HUT) the functional curve of the NM arc is shifted downward, and the operating point should move downward and rightward toward higher SNA (*Point 1*).

Trimethaphan is a rapidly acting ganglionic blocking agent and can be used to abolish postganglionic neural activity and to nullify the responsiveness of SNA to AP change (Jordan et al., 1998; Shannon et al., 1998). Therefore, during trimethaphan the operating point should move leftward (SNA reduction) and downward (AP fall) (*Point 2*). Assuming that the PNE can be substituted for SNA, we can redraw the functional curves of the two arcs in the AP-PNE relationship. Therefore, the functional characteristics of the MN and NM arcs are expressed as the PNE response to AP and the AP response to PNE, respectively. Finally, we can identify the functional curve of the MN arc as the line passing through *Points 0* and *1*, and that of the NM arc as the line passing through *Points 0* and *2*. We can also estimate the gain of the MN arc (G_{MN}) from the slope of the functional curve of the MN arc against the AP axis, and the gain of the NM arc (G_{NM}) from the slope of the NM arc against the PNE axis. Finally, an open-loop gain, G_L, is given by a product of G_{MN} and G_{NM}. G_L is a most important index for performance of arterial baroreflex, because the effect of external disturbance should be attenuated to $1/[1 + G_L]$ by the closed-loop feedback system (Riggs, 1963; Milhorn, 1966; Kent et al., 1972; Sato et al., 1999b).

Protocol

To test this concept, a following protocol with tilt and ganglionic blockade was conducted in human volunteers. The research protocol was approved by the ethical review board of Kochi Medical School (Reference number: 2021-4) and followed the Declaration of Helsinki and the ethical standards of the responsible committee on human experimentation.

Subjects

Seven normal male volunteers aged between 19 and 37 years participated in this study, which was held between November 21, 2001 and November 30, 2001. Their heights and weights were between 1.67 and 1.82 m, and between 57 and 86 kg, respectively.

Measurement

Each subject was placed on a tilting bed in a quiet and temperature-controlled room (20°C) about 2–3 h after lunch.

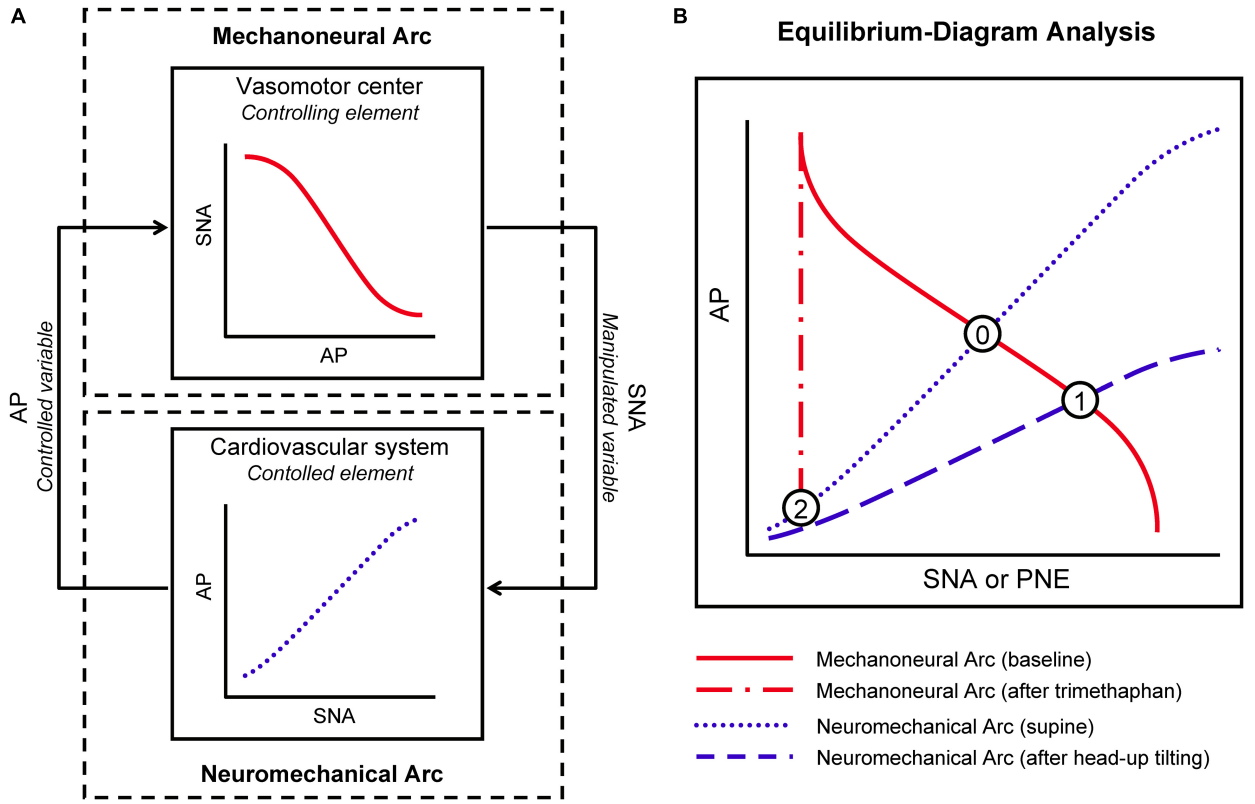

FIGURE 1 | Conceptual scheme for integrative analysis of human sympathetic arterial baroreflex. Sympathetic arterial baroreflex is a feedback control system, which is divided into mechanoneural (MN) and neuromechanical (NM) arcs **(A)**. In the MN arc, its input is a controlled variable, arterial pressure (AP), and its output is a manipulated variable, sympathetic nerve activity (SNA); in the NM arc, its input and output are SNA and AP, respectively. The functional curves of the two arcs can be superimposed on an equilibrium diagram **(B)**. Under closed-loop conditions of the feedback system, its operating point should be a point of intersection between the two curves. PNE, plasma norepinephrine level. See text for detailed explanation of *Points 0, 1,* and *2*.

Surface electrodes were attached to the chest for monitoring of electrocardiogram (ECG). AP was tonometrically measured with a continuous non-invasive blood pressure-monitoring instrument (JENTOW, Colin Electronics, Komaki, Japan) (Sato et al., 1993). The tonometric sensor was attached to the left radial artery. The left upper limb was fixed in shoulder abduction position at 90° of rotation with the use of an arm support. We kept the position of the sensor at the level of the clavicle to monitor the approximate pressure of the subclavian and carotid AP, because arterial baroreceptors sense AP at such regions. An indwelling needle was placed in a forearm vein. Blood was sampled and analyzed for measurement of PNE with an assay. Atropine (0.4 $mg{\cdot}kg^{-1}$) was infused via the forearm venous line to block vagal effects during the protocol (Halmagyi et al., 1969).

Estimation of Mechanoneural Arc

After a 20 min stabilization period in resting supine position, the posture of the subject was changed to a head-down position of 7°, supine position, HUT position of 15°, and HUT position of 60° every 5 min. The electrical signals of AP, ECG, and angle of the tilting bed were digitized at a rate of 500 Hz by means of analog-to-digital converter (AD12-8(PM); Contec, Tokyo, Japan) and stored. At the end of each 5-min period, blood was sampled for PNE assay.

Estimation of Neuromechanical Arc

While trimethaphan (Arfonad, Roche) was infused at a rate of 0.1 $\mu g{\cdot}kg^{-1}{\cdot}min^{-1}$, AP and ECG were recorded in a supine position for 5 min. After blood sampling, the posture of the subject was kept in a HUT position of 15° for 5 min under careful monitoring of AP and ECG. At the end of a study protocol, the last blood sampling was made.

Data Analysis

In each period, AP and heart rate were computed from the data for the last 30 s. AP was calculated by averaging of digitized values. PNE was measured by a high performance liquid chromatography (HLC-8030, Toso, Tokyo, Japan). The relationship between AP and PNE was analyzed for each subject. To characterize the functional curve of the MN arc, we plotted PNE values against AP values measured in four different body positions before trimethaphan infusion. A regression line was fitted to these four points by a least square method, and its slope and AP-axis intercept ($AP_{MN,\ 0}$) was computed. The slope with respect to AP axis was considered as G_{MN}. To identify

the functional curve of the NM arc in supine position, we plotted supine AP values against PNE values before and after trimethaphan infusion. The line passing through the two points was calculated. The slope with respect to PNE axis, $G_{NM}(0)$, was considered as the gain of the NM arc in supine position. The AP-axis intercept of the line, $AP_{NM,\ 0}(0)$, was considered as the AP that is generated by the cardiovascular system at null PNE in supine position. To identify the functional curve of the NM arc in 15-degree HUT position, we plotted the AP values in 15-degree HUT position against PNE values before and after trimethaphan infusion, and calculated $G_{NM}(15)$ and $AP_{NM,\ 0}(15)$. The open-loop gains, $G_L(0)$ and $G_L(15)$, at the operating points in supine and 15-degree HUT positions were estimated from the product of G_{MN} and $G_{NM}(0)$, and that of G_{MN} and $G_{NM}(15)$, respectively.

Paired measurements were analyzed by a Wilcoxon signed-rank test or a Steel multiple-comparison test. Differences were considered significant at $P < 0.05$. Values are expressed as means ± SD.

RESULTS

Postural Tilting Tests

Effects of postural tilting on AP, heart rate, and PNE are shown in **Figure 2** and **Table 1**. Under the baseline condition after atropine injection, head-down tilting increased AP and decreased PNE, and conversely HUT decreased AP and increased PNE. In response to AP changes, PNE exhibited opposite changes.

Trimethaphan significantly lowered both AP and PNE in supine and HUT positions. HUT significantly decreased AP, while it did not increase PNE during trimethaphan infusion. The compensatory responses of PNE to AP changes observed under the baseline condition vanished completely after trimethaphan infusion.

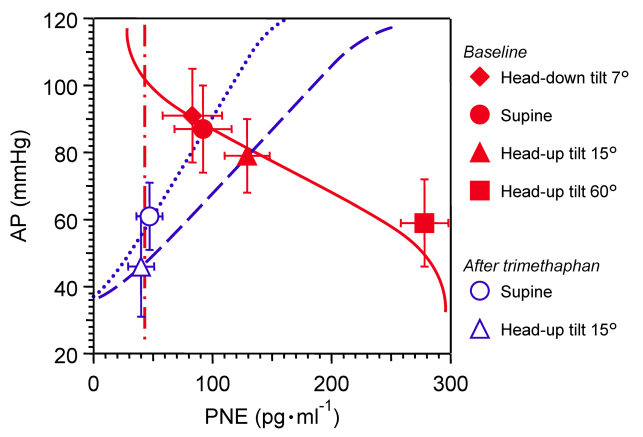

FIGURE 2 | Graph showing effects of postural tilting on arterial pressure (AP), and plasma norepinephrine level (PNE) during baseline and after trimethaphan infusion. Note that a reference level for AP measurement was not the heart but the clavicle; because the controlled or feedback variable of arterial baroreflex should be AP sensed by arterial baroreceptors localized in the wall of the aortic arch and carotid sinus. Values are means ± SD. See text and **Table 1** for detailed explanation.

TABLE 1 | Effects of postural tilting on arterial pressure (AP), heart rate, and plasma norepinephrine level.

Angle of bed, degrees	–7	0	+15	+60
Baseline				
Arterial pressure, mmHg	91 ± 14*	87 ± 13	79 ± 11*	59 ± 13*
Heart rate, beats.min^{-1}	96 ± 9	98 ± 13	100 ± 15	118 ± 15*
Norepinephrine, pg.ml^{-1}	83 ± 25*	92 ± 24	129 ± 19*	278 ± 42*
After trimethaphan				
Arterial pressure, mmHg		61 ± 10†	46 ± 15*†	
Heart rate, beats.min^{-1}		89 ± 16†	86 ± 17†	
Norepinephrine, pg.ml^{-1}		47 ± 11†	40 ± 11†	

*Note that a reference level for measurement of AP was not the heart but the clavicle; because the controlled or feedback variable of arterial baroreflex should be AP sensed by arterial baroreceptors localized in the wall of the aortic arch and carotid sinus. Values are means ± SD. *P < 0.05 from supine position. †P < 0.05 from baseline. See text and* ***Figure 2*** *for detailed explanation.*

TABLE 2 | Estimation of arterial pressure offset (AP), gain (G) of mechanoneural (MN) and neuromechanical (NM) arcs, and open-loop gain (G_L).

Parameter	Estimated value
MN arc	
G_{MN}, pg·ml^{-1}·mmHg^{-1}	8.92 ± 3.07
$AP_{MN,\ 0}$, mmHg	103.0 ± 9.5
Correlation coefficient	–0.96 ± 0.05
NM arc	
Supine position	
$G_{NM}(0)$, mmHg·ml·pg^{-1}	0.61 ± 0.08
$AP_{NM,\ 0}(0)$, mmHg	34.1 ± 4.9
Head-up position of 15 degrees	
$G_{NM}(15)$, mmHg·ml·pg^{-1}	0.36 ± 0.05*
$AP_{NM,\ 0}(15)$, mmHg	33.4 ± 8.6
Open-loop gain	
$G_L(0)$	5.62 ± 0.98
$G_L(15)$	3.75 ± 0.62*

*Note that values for open-loop gain have no unit. AP is the estimated pressure at zero neural activity. Values are means ± SD. *P < 0.05 from supine position. See section "Materials and Methods" for detailed explanation of definition of parameters.*

Estimation of Parameters of Two Arc Curves and Total Loop

Shown in **Table 2** are the estimated values for parameters of two arc curves and open loop. G_{NM} and G_L were significantly reduced by HUT.

DISCUSSION

Here we proposed a model and mechanism for determination of the static operating point of sympathetic arterial baroreflex, showing an integrative framework is applicable to humans. The present results also revealed an important functional index for

the regulatory system, open-loop gain, in humans. The open-loop gain, which is referred to as *homeostatic index* (Riggs, 1963; Milhorn, 1966), and is a measure of the ability of the regulatory system to buffer an impact of external disturbance.

Measurement of Controlled or Feedback Variable

During AP measurement in clinical settings, the arm should be horizontal at the level of the heart as denoted by the midsternal level. The reason for the arm position is that a hydrostatic difference in AP between the brachial artery and the heart should be nullified (Beevers et al., 2001). However, such knowledge should be reconsidered only when we measure AP to evaluate arterial-baroreflex function against orthostatic stress. A standing person with a height of 1.8 m who has AP of 100 mmHg at the level of his heart must have AP of 80–85 mmHg in his baroreceptor areas of aortic-depressor and carotid-sinus nerves because of a difference of 200–250 mmH_2O in a hydrostatic level (Netea et al., 1998). It should be considered that the controlled or feedback variable of the arterial-baroreflex system should be the AP which is sensed by not the heart but arterial baroreceptors at the aortic arch, brachiocephalic trunk, and carotid sinus (Sato et al., 2002). According to these fundamentals of feedback control theory, we fixed an AP sensor at the level of the clavicle so that we could monitor the approximate value of baroreceptor AP during postural tilting (Yamasaki et al., 2003; Ichikawa et al., 2019).

Equilibrium-Diagram Analysis With Baroreceptor Isolation Approach

Our previous animal study (Sato et al., 1999b) made a first report on a new analytic framework for understanding sympathetic arterial baroreflex, i.e., equilibrium-diagram analysis of MN, and NM arcs. Using baroreceptor-isolation approach, we could impose any level or waveform of pressure on baroreceptors with a sophisticated servo pump. Under the open-loop conditions, relationship between baroreceptor pressure and SNA and that between SNA and AP were quantitatively measured, and then the operating point of the closed-loop conditions was predicted by equilibrium-diagram analysis. While in real time imposing instantaneous AP on vascularly isolated baroreceptors, we observed the operating point of the closed-loop conditions. Agreement between analytically predicted and actually observed operating points of the closed-loop conditions validated equilibrium-diagram analysis for sympathetic arterial baroreflex.

Our previous study with modeling and simulation revealed the effect of an external disturbance, loss of blood, on MN and NM arcs. The loss of blood volume in the range of 0.5-2% of body weight reduced G_{NM} and $AP_{NM,\ 0}$ dependently on its severity, while it did not affect any parameter of the MN arc. A graphical analysis with equilibrium diagram of MN and NM arcs helps us to understand a mechanism for a shift of the operating point after external disturbance to the circulatory system under the closed-loop or open-loop conditions of arterial baroreflex.

Equilibrium-Diagram Analysis in Humans

Although many earlier studies of arterial baroreflex elucidated its particular features, such as baroreceptor transduction properties (Sato et al., 1998), central mechanisms (Harada et al., 1993), and effector organ contributions in animals (Shoukas and Sagawa, 1973; Hainsworth and Karim, 1976) and humans (Jordan et al., 1998; Shannon et al., 1998), and few efforts have been made to elucidate an overall behavior of human arterial baroreflex. Accumulation of detailed knowledge of fragmentary components did not allow us to integratively understand how the arterial baroreflex is capable of attenuating the effect of external perturbation on human AP.

Shown in **Figure 3A** is a representative equilibrium diagram of human MN and NM arcs for understanding of the operating point of sympathetic baroreflex control of AP. Each arc curve is reproduced with its average parameters summarized in **Table 2**. The effects on the NM arc of HUT in humans seem to be very similar to those of blood loss in animals (Sato et al., 1999b). This similarity would result from a similarity in hemodynamic effects between the two types of external disturbances (Guyton et al., 1972; Yamasaki et al., 2006). Therefore, we suppose that HUT reduces cardiac preload and cardiac output (Critchley et al., 1997) and subsequently decreases G_{NM}, and $AP_{NM,\ 0}$ dependently on its angle. In terms of systems physiology, a block diagram of human sympathetic baroreflex control of AP against postural tilting can be drawn as shown in **Figure 3B**. Taken together, an imposition of the external disturbance, postural tilting, on the circulatory system is considered to alter G_{NM} and $AP_{NM,\ 0}$, and thus these parameters are regarded as functions of tilt angle φ. Therefore, the functional curve of the NM arc is expressed as follows: $AP = G_{NM}(\varphi)\ PNE + AP_{NM,\ 0}(\varphi)$.

Using the equilibrium diagram, we can graphically explain how sympathetic arterial baroreflex attenuates the effect of external disturbance on the circulatory system in humans. As illustrated in **Figure 3A**, the operating point moves from *Point 1* to *Point 2* along the functional curve of the MN arc in response to changes in tilt angle. The difference in AP before and after HUT with angle of 15° is estimated to be 6 mmHg during baseline condition. However, if the MN arc does not respond to AP change at all, the operating point should move down vertically from *Point 1* to *Point 3*, and thus the AP difference before and after tilting is assumed to reach 24 mmHg. Consequently, the effect of 15-degree HUT on AP is considered to be attenuated to 1/4 by sympathetic arterial baroreflex. If this attenuation ratio is used for estimation of G_L, it should be equal to three according to the following formula: G_L = 1/(attenuation ratio)–1 (Kent et al., 1972; Sato et al., 1999b). However, the estimated value for G_L is not consistent with $G_L(0)$. The reason for this inconsistency is that HUT affects G_{NM} as well as $AP_{NM,\ 0}$. If G_{NM} were independent of tilt angle (**Figure 3C**), the NM-arc curve in 15-degree HUT position would become parallel to that in supine position, and then the AP difference between *Point 1* and *Point 2* before and after tilting is assumed to be less than 4 mmHg during baseline condition. Therefore, the G_L estimated from the attenuation ratio should exactly coincide with the $G_L(0)$. Even though a block diagram similar to **Figure 3D** is well

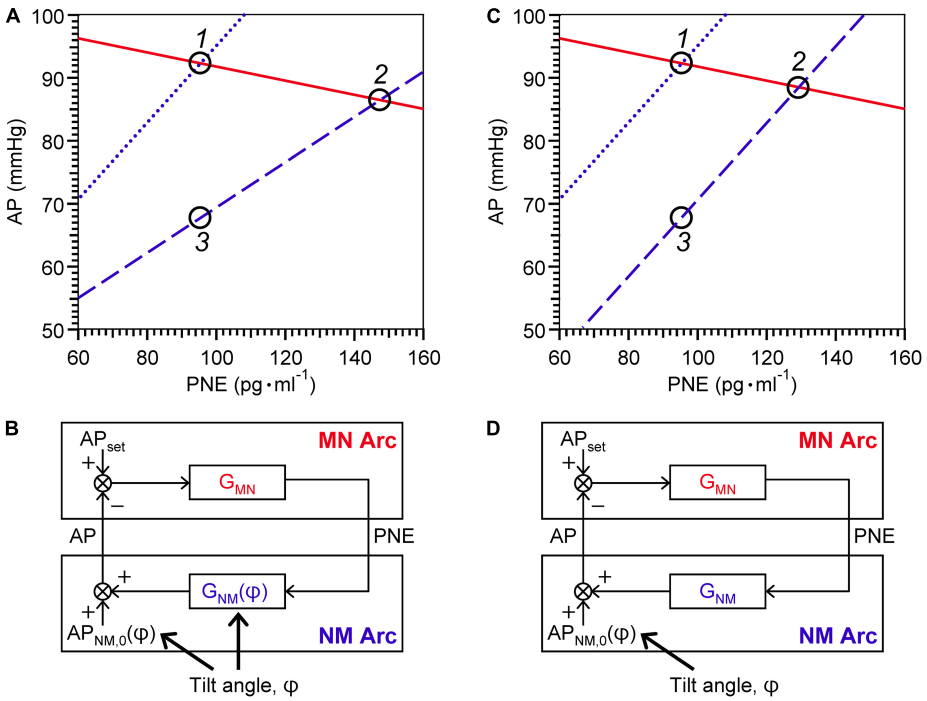

FIGURE 3 | Graphical representation of physiological meanings of gain factors of MN and NM arcs and a loop **(A,C)** against 15° head-up tilting (HUT), and block diagrams of sympathetic arterial baroreflex with **(B)** and without **(D)** a tilt-induced effect on the NM-arc gain. **(A)** The MN- (solid line), supine NM- (dotted line), and HUT NM- (dashed line) are reproduced with its average parameters summarized in **Table 2**. For a line of the MN arc, AP = – 1/G_{MN} PNE + $AP_{MN,0}$; for a line of the NM arc in supine position, AP = $G_{NM}(0)$ PNE + $AP_{NM,0}(0)$; and for a line of the NM arc in 15° HUT, AP = $G_{NM}(15)$ PNE + $AP_{NM,0}(15)$. **(C)** The MN- and supine NM-arc curves are identical with **(A)** while the HUT NM-arc curve is assumed to move down in parallel with the supine NM-arc curve. Using equilibrium diagrams **(A,C)**, we can graphically explain how sympathetic arterial baroreflex attenuates the effect of external disturbance on the circulatory system in humans. During baseline condition, the operating point moves from *Point 1* to *Point 2* along the functional curve of the MN arc in response to changes in tilt angle **(A)**. The difference in AP before and after 15° HUT is estimated to be 6 mmHg. However, if the MN arc does not respond to AP change at all, the operating point should move down vertically from *Point 1* to *Point 3*, and thus the AP difference before and after tilting is assumed to reach 24 mmHg. Consequently, the effect of 15° HUT on AP is considered to be attenuated to 1/4 by sympathetic arterial baroreflex. If this attenuation ratio is used for estimation of G_L, it is calculated to be 3 according to the following formula: G_L = 1/(attenuation ratio) – 1. However, the estimated value for G_L is not consistent with $G_L(0)$. The reason for this inconsistency is that HUT affects G_{NM} as well as $AP_{NM,\ 0}$. If G_{NM} were independent of tilt angle, the NM-arc curve in 15° HUT position would become parallel to that in supine position **(C)**, and then the AP difference between *Point 1* and *Point 2* before and after tilting is assumed to be less than 4 mmHg during baseline condition. Therefore, the G_L estimated from the attenuation ratio should exactly coincide with the $G_L(0)$. AP, arterial pressure; PNE, plasma norepinephrine level; AP_{set}, set-point value for AP; $AP_{NM,0}$, AP that is generated by the cardiovascular system at null PNE; G_{MN}, gain for MN arc; G_{NM}, gain for NM arc; φ, tilt angle. See text for detailed explanation.

known as an explanation for function of arterial baroreflex with postural tilt-induced perturbation (Milhorn, 1966; Kamiya et al., 2014), it should be repeatedly emphasized that postural tilting should affect not only $AP_{NM,\ 0}$ but also G_{NM} as an external disturbance to the cardiovascular system (**Figure 3B**). The present results obtained by the equilibrium-diagram analysis would contribute to an integrative understanding of physiology of human sympathetic arterial baroreflex and pathophysiology of supine hypertension with orthostatic hypotension (Ketch et al., 2002; Parikh et al., 2002).

As proposed by our previous study with animals (Sato et al., 1999b), $AP_{MN,\ 0}$ is assumed to be an approximation to a set-point value for a controlled variable of the feedback control system. When AP becomes higher than the set-point value, there is no response of PNE to AP. An integrative and analytic framework with the equilibrium diagram enables us to graphically understand the function of each component and variable of arterial baroreflex.

Open-Loop Gain

Many investigators have estimated the open-loop gain of sympathetic baroreflex control of AP by perfusing vascularly isolated areas such as one carotid sinus, both carotid sinuses, or the aortic arch at various pressures while measuring AP changes in animals. The ratio of AP change to baroreceptor pressure change, i.e., open-loop gain, was reported to be between 1.0 and 3.5 (Kent et al., 1972; Shoukas and Sagawa, 1973; McRitchie et al., 1976; Burattini et al., 1994; Sato et al., 1999a; Sunagawa et al., 2001). However, such an invasive approach is not applicable to humans, and thus open-loop gain of human baroreflex control of AP has been not yet clarified. Although baroreflex sensitivity or cardiac baroreflex gain is usually used as an index for human baroreflex function (Cooper and Hainsworth, 2001; Ogoh et al., 2006; Fisher et al., 2007; Horsman et al., 2013; Lund et al., 2018; Shahzad et al., 2018), such an index is not an effective surrogate for *homeostatic index* of arterial baroreflex (Riggs, 1963; Milhorn, 1966). To our best knowledge, this is the first study to present

an equilibrium-diagram analysis of human sympathetic arterial baroreflex. Using this framework, we can outline the MN and NM arcs and estimate the open-loop gain.

Limitations

Our previous study with animals revealed an entire picture of the MN and NM arcs with sigmoidal shape by altering a sufficiently wide range of baroreceptor pressure (Sato et al., 1999b). The present human study, on the other hand, could not draw overall characteristics of the two arcs because it is quite difficult to make such a wide range of change in AP. As shown previously, however, the functional curves of the two arcs appeared to be linear in a limited range near baseline operating points of sympathetic arterial baroreflex.

Although PNE was used as an index of sympathetic nerve activity in the present study, PNE is considered to be determined by a difference between the norepinephrine spillover rate from postganglionic sympathetic nerve endings to plasma and the norepinephrine clearance (Esler et al., 1982). Therefore, the interpretation of PNE data, e.g., interindividual comparison of the gain of the MN or NM arc alone, should be made carefully; while, on the contrary, the estimated value for open-loop gain, which has no unit of measurement, has a physiological meaning even when being compared among individuals.

In this study, data were obtained from a small number of healthy and young volunteers. Therefore, we could not conclude that the parameters of the MN and NM arcs shown here are representative of a normal population. Further studies with a large number of healthy or diseased people at different ages are needed for an overall understanding of baroreflex function or dysfunction (Jordan et al., 1998; Shannon et al., 1998).

CONCLUSION

In the present study, an equilibrium-diagram analysis for functional curves of MN and NM arcs of human sympathetic baroreflex revealed the mechanism by which AP is stably controlled against postural tilting. Such an analytical framework would help a quantitative and integrative understanding of pathophysiology of arterial baroreflex dysfunction and failure.

DATA AVAILABILITY STATEMENT

The datasets generated for this study are available on request to the corresponding author FY, yamasaki-f@kochi-u.ac.jp.

ETHICS STATEMENT

The studies involving human participants were reviewed and approved by the Ethical Review Board of Kochi Medical School. Written informed consent for participation was not required for this study in accordance with the national legislation and the institutional requirements.

AUTHOR CONTRIBUTIONS

TS conceived research. FY and TS designed the experiment. FY, KS, and TS performed data acquisition. FY and KS preprocessed data. FY, TS, and AD analyzed the data, performed statistical analysis, and created figures and tables. FY, TS, and AD interpreted results and drafted the manuscript. All authors read, edited, and approved the manuscript for submission.

FUNDING

AD was supported by the National Heart, Lung, and Blood Institute of the National Health (Award Number NIH 1R01HL142583).

REFERENCES

Beevers, G., Lip, G. Y., and O'Brien, E. (2001). ABC of hypertension. Blood pressure measurement. Part I-sphygmomanometry: factors common to all techniques. *BMJ.* 322, 981–985. doi: 10.1136/bmj.322.7292.981

Burattini, R., Socionovo, G., and Bellocchi, F. (1994). On the approximation of static open-loop characteristics of baroreceptor reflex. *Am. J. Physiol.* 267, H267–H275. doi: 10.1152/ajpheart.1994.267.1.H267

Cooper, V. L., and Hainsworth, R. (2001). Carotid baroreceptor reflexes in humans during orthostatic stress. *Exp. Physiol.* 86, 677–681. doi: 10.1113/eph8602213

Critchley, L. A. H., Conway, F., Anderson, P. J., Tomlinson, B., and Critchley, J. A. J. H. (1997). Non-invasive continuous arterial pressure, heart rate and stroke volume measurements during graded head-up tilt in normal man. *Clin. Auton. Res.* 7, 97–101. doi: 10.1007/bf02267754

Esler, M., Leonard, P., O'Dea, K., Jackman, G., Jennings, G., and Korner, P. (1982). Biochemical quantification of sympathetic nervous activity in humans using radiotracer methodology: fallibility of plasma noradrenaline measurements. *J. Cardiovasc. Pharmacol.* 4 (Suppl.I), S152–S157. doi: 10.1097/00005344-198200041-00030

Fisher, J. P., Ogoh, S., Ahmed, A., Aro, M. R., Gute, D., and Fadel, P. J. (2007). Influence of age on cardiac baroreflex function during dynamic exercise in humans. *Am. J. Physiol. Heart Circ. Physiol.* 293, H777–H783. doi: 10.1152/ajpheart.00199.2007

Guyton, A. C., Coleman, T. G., and Granger, H. J. (1972). Circulation: overall regulation. *Annu. Rev. Physiol.* 34, 13–46. doi: 10.1146/annurev.ph.34.030172.000305

Hainsworth, R., and Karim, F. (1976). Responses of abdominal vascular capacitance in the anaesthetized dog to changes in carotid sinus pressure. *J. Physiol.* 262, 659–677. doi: 10.1113/jphysiol.1976.sp011614

Halmagyi, D. F., Neering, I. R., Varga, D., and Pullin, J. (1969). Sustained complete autonomic blockade. *Br. J. Pharmacol.* 35, 271–282. doi: 10.1111/j.1476-5381.1969.tb07986.x

Harada, S., Tokunaga, S., Momohara, M., Masaki, H., Tagawa, T., Imaizumi, T., et al. (1993). Inhibition of nitric oxide formation in the nucleus tractus solitarius increases renal sympathetic nerve activity in rabbits. *Circ. Res.* 72, 511–516. doi: 10.1161/01.res.72.3.511

Horsman, H. M., Peebles, K. C., Galletly, D. C., and Tzeng, Y. C. (2013). Cardiac baroreflex gain is frequency dependent: insights from repeated sit-to-stand maneuvers and the modified Oxford method. *Appl. Physiol. Nutr. Metab.* 38, 753–759. doi: 10.1139/apnm-2012-0444

Ichikawa, A., Yamasaki, F., Ueda, M., Todaka, H., Miyao, E., Yoshinaga, Y., et al. (2019). Relationship between the fall in blood pressure in the standing position

and diaphragmatic muscle thickness: proof of concept study. *Blood Press. Monit.* 24, 284–288. doi: 10.1097/MBP.0000000000000403

Jordan, J., Shannon, J. R., Black, B. K., Lance, R. H., Squillante, M. D., Costa, F., et al. (1998). NN-nicotinic blockade as an acute human model of autonomic failure. *Hypertension* 31, 1178–1184. doi: 10.1161/01.hyp.31.5.1178

Kamiya, A., Kawada, T., and Sugimachi, M. (2014). Systems physiology of the baroreflex during orthostatic stress: from animals to humans. *Front. Physiol.* 5:256. doi: 10.3389/fphys.2014.00256

Kent, B. B., Drane, J. W., Blumenstein, B., and Manning, J. W. (1972). A mathematical model to assess changes in the baroreceptor reflex. *Cardiology* 57, 295–310. doi: 10.1159/000169528

Ketch, T., Biaggioni, I., Robertson, R., and Robertson, D. (2002). Four faces of baroreflex failure: hypertensive crisis, volatile hypertension, orthostatic tachycardia, and malignant vagotonia. *Circulation* 105, 2518–2523. doi: 10.1161/01.cir.0000017186.52382.f4

Lund, M. T., Salomonsson, M., Jonassen, T. E. N., and Holstein-Rathlou, N. H. (2018). A method for assessment of the dynamic response of the arterial baroreflex. *Acta Physiol. Oxf.* 222, e12962. doi: 10.1111/apha.12962

McRitchie, R. J., Vatner, S. F., Heyndrickx, G. R., and Braunwald, E. (1976). The role of arterial baroreceptors in the regulation of arterial pressure in conscious dogs. *Circ. Res.* 39, 666–670. doi: 10.1161/01.res.39.5.666

Milhorn, H. T. Jr. (1966). *Application of Control Theory to Physiological Systems*. Philadelphia, PA: W. B. Saunders.

Netea, R. T., Bijlstra, P. J., Lenders, J. W., Smits, P., and Thien, T. (1998). Influence of the arm position on intra-arterial blood pressure measurement. *J. Hum. Hypertens.* 12, 157–160. doi: 10.1038/sj.jhh.1000479

Ogoh, S., Yoshiga, C. C., Secher, N. H., and Raven, P. B. (2006). Carotid-cardiac baroreflex function does not influence blood pressure regulation during head-up tilt in humans. *J. Physiol. Sci.* 56, 227–233. doi: 10.2170/physiolsci.RP001306

Ondrusova, K., Svacinova, J., Javorka, M., Novak, J., Novakova, M., and Novakova, Z. (2017). Impaired baroreflex function during orthostatic challenge in patients after spinal cord injury. *J. Neurotrauma* 34, 3381–3387. doi: 10.1089/neu.2017.4989

Parikh, S. M., Diedrich, A., Biaggioni, I., and Robertson, D. (2002). The nature of the autonomic dysfunction in multiple system atrophy. *J. Neurol. Sci.* 200, 1–10. doi: 10.1016/s0022-510x(02)00126-0

Riggs, D. S. (1963). *Mathematical Approach to Physiological Problems*. Baltimore, MD: Williams and Wilkins.

Robertson, D., Diedrich, A., and Chapleau, M. W. (2012). Editorial on arterial baroreflex issue. *Auton. Neurosci.* 172, 1–3. doi: 10.1016/j.autneu.2012.10.010

Sato, T., Kawada, T., Inagaki, M., Shishido, T., Takaki, H., Sugimachi, M., et al. (1999b). New analytic framework for understanding sympathetic baroreflex control of arterial pressure. *Am. J. Physiol.* 276, H2251–H2261. doi: 10.1152/ajpheart.1999.276.6.H2251

Sato, T., Kawada, T., Miyano, H., Shishido, T., Inagaki, M., Yoshimura, R., et al. (1999a). New simple methods for isolating baroreceptor regions of carotid sinus and aortic depressor nerves in rats. *Am. J. Physiol.* 276, H326–H332. doi: 10.1152/ajpheart.1999.276.1.H326

Sato, T., Kawada, T., Shishido, T., Miyano, H., Inagaki, M., Miyashita, H., et al. (1998). Dynamic transduction properties of in situ baroreceptors of rabbit aortic depressor nerve. *Am. J. Physiol.* 274, H358–H365. doi: 10.1152/ajpheart.1998.274.1.H358

Sato, T., Kawada, T., Sugimachi, M., and Sunagawa, K. (2002). Bionic technology revitalizes native baroreflex function in rats with baroreflex failure. *Circulation* 106, 730–734. doi: 10.1161/01.cir.0000024101.77521.4d

Sato, T., Nishinaga, M., Kawamoto, A., Ozawa, T., and Takatsuji, H. (1993). Accuracy of a continuous blood pressure monitor based on arterial toometry. *Hypertension* 21, 866–874. doi: 10.1161/01.hyp.21.6.866

Shahzad, T., Saleem, S., Usman, S., Mirza, J., Islam, Q. U., Ouahada, K., et al. (2018). System dynamics of active and passive postural changes: Insights from principal dynamic modes analysis of baroreflex loop. *Comput. Biol. Med.* 100, 27–35. doi: 10.1016/j.compbiomed.2018.06.022

Shannon, J. R., Jordan, J., Black, B. K., Costa, F., and Robertson, D. (1998). Uncoupling of the baroreflex by NN-cholinergic blockade in dissecting the components of cardiovascular regulation. *Hypertension* 32, 101–107. doi: 10.1161/01.hyp.32.1.101

Shoukas, A. A., and Sagawa, K. (1973). Control of total systemic vascular capacity by the carotid sinus baroreceptor reflex. *Circ. Res.* 33, 22–33. doi: 10.1161/01.res.33.1.22

Sunagawa, K., Sato, T., and Kawada, T. (2001). Integrative sympathetic baroreflex regulation of arterial pressure. *Ann. N. Y. Acad. Sci.* 940, 314–323. doi: 10.1111/j.1749-6632.2001.tb03687.x

Yamasaki, F., Sato, K., Ando, M., and Sato, T. (2003). Analytic and integrative framework for understanding of human sympathetic baroreflex. *Circulation* 108 (Suppl IV):630.

Yamasaki, F., Ushida, T., Yokoyama, T., Ando, M., Yamashita, K., and Sato, T. (2006). Artificial baroreflex: clinical application of a bionic baroreflex system. *Circulation* 113, 634–639. doi: 10.1161/circulationaha.105.587915

Conflict of Interest: The authors declare that the research was conducted in the absence of any commercial or financial relationships that could be construed as a potential conflict of interest.

frontiers in Neuroscience

METHODS
published: 30 August 2021
doi: 10.3389/fnins.2021.694512

Closed-Loop Identification of Baroreflex Properties in the Frequency Domain

Toru Kawada[1], Keita Saku[1] and Tadayoshi Miyamoto[2]*

[1] Department of Cardiovascular Dynamics, National Cerebral and Cardiovascular Center, Osaka, Japan, [2] Department of Sport and Health Sciences, Faculty of Sport and Health Sciences, Osaka Sangyo University, Osaka, Japan

The arterial baroreflex system plays a key role in maintaining the homeostasis of arterial pressure (AP). Changes in AP affect autonomic nervous activities through the baroreflex neural arc, whereas changes in the autonomic nervous activities, in turn, alter AP through the baroreflex peripheral arc. This closed-loop negative feedback operation makes it difficult to identify open-loop dynamic characteristics of the neural and peripheral arcs. Regarding sympathetic AP controls, we examined the applicability of a nonparametric frequency-domain closed-loop identification method to the carotid sinus baroreflex system in anesthetized rabbits. This article compares the results of an open-loop analysis applied to open-loop data, an open-loop analysis erroneously applied to closed-loop data, and a closed-loop analysis applied to closed-loop data. To facilitate the understanding of the analytical method, sample data files and sample analytical codes were provided. In the closed-loop identification, properties of the unknown central noise that modulated the sympathetic nerve activity and the unknown peripheral noise that fluctuated AP affected the accuracy of the estimation results. A priori knowledge about the open-loop dynamic characteristics of the arterial baroreflex system may be used to advance the assessment of baroreflex function under closed-loop conditions in the future.

Keywords: baroreflex, white noise, sympathetic nerve activity, arterial pressure, transfer function

OPEN ACCESS

Edited by:
André Diedrich, Vanderbilt University, United States

Reviewed by:
Robert Brychta, National Institute of Diabetes and Digestive and Kidney Diseases, National Institutes of Health (NIH), United States
Rong Zhang, University of Texas Southwestern Medical Center, United States

****Correspondence:***
Toru Kawada
torukawa@ncvc.go.jp

Specialty section:
This article was submitted to Autonomic Neuroscience, a section of the journal Frontiers in Neuroscience

Received: *13 April 2021*
Accepted: *26 July 2021*
Published: *30 August 2021*

Citation:
Kawada T, Saku K and Miyamoto T (2021) Closed-Loop Identification of Baroreflex Properties in the Frequency Domain. Front. Neurosci. 15:694512. doi: 10.3389/fnins.2021.694512

INTRODUCTION

The arterial baroreflex system is one of the most important negative feedback systems that stabilize arterial pressure (AP). Identifying the dynamic characteristics of the arterial baroreflex system is essential to understand the homeostasis of AP in daily activities. When we focus on sympathetic AP controls, the arterial baroreflex system can be divided into two principal subsystems (Ikeda et al., 1996). One is the neural arc subsystem, which defines the relationship between a baroreceptor pressure input and efferent sympathetic nerve activity (SNA). The other is the peripheral arc subsystem, which defines the relationship between SNA and AP. The neural and peripheral arcs can be regarded as the controller and the plant of the arterial baroreflex system, respectively. Under normal physiological conditions, the arterial baroreflex system operates as a closed-loop negative feedback system. Changes in AP affect SNA, whereas changes in SNA, in turn, affect AP. This closed-loop operation hampers the application of a nonparametric frequency-domain

system identification method based on a conventional transfer function analysis because the Fourier transformation is mathematically noncausal.

Although we reported a nonparametric frequency-domain closed-loop identification method in previous studies (Kawada et al., 1997; Kawada and Sugimachi, 2016, 2019), the method was described as a set of equations. A certain gap exists between a set of equations and its implementation to programming. This paper, therefore, provides sample codes for the analytical method with sample data files. Although the codes were written in good faith, they could contain unexpected errors. The use may be limited because the codes were developed for analyzing specific datasets. The programs are explained using open-source software GNU Octave and Scilab so that most readers can test the codes on their own (see Appendix). However, the programs were originally developed in commercial software Matlab (MathWorks). The readers are asked to understand those limitations and use the programs on their responsibility. Most figures were drawn on the basis of screenshots so that the readers can easily follow the results of the sample codes.

A dilemma faced frequently in the medical engineering field is that the accuracy of system identification is not parallel with the usefulness of the identification result. Even if the system identification is not perfect, the result may remain useful for diagnosis, risk stratification, prediction of prognosis, and so on. In this article, however, accuracy was sought as a goal of the closed-loop identification. Before explaining the method of closed-loop identification, we will review open-loop dynamic characteristics of the arterial baroreflex system including those in animal models of cardiovascular diseases. The open-loop dynamic characteristics of a system are regarded as the answer to the closed-loop identification. If the closed-loop identification is successful, the identification result will conform to the open-loop dynamic characteristics. After reviewing the methods and results of an open-loop analysis applied to open-loop data, we will discuss a closed-loop analysis. In the section of the closed-loop analysis, we will discuss an open-loop analysis erroneously applied to closed-loop data, followed by a closed-loop analysis applied to closed-loop data.

MATERIALS AND EQUIPMENT

The sample data were obtained from past studies (Kawada et al., 1997, 2001). All animal experiments were performed following strict accordance with the Guiding Principles for the Care and Use of Animals in the field of Physiological Sciences, as approved by the Physiological Society of Japan. The experimental protocols were reviewed and approved by the Animal Subject Committee at the National Cerebral and Cardiovascular Center.

The detailed experimental setup was described previously (Kawada et al., 1997, 2001). For the open-loop analysis, the AP was recorded via a catheter-tip, high-fidelity pressure transducer inserted from the femoral artery in anesthetized rabbits. The heart rate (HR) was derived from the AP signal through a cardiotachometer. The carotid sinus baroreceptor regions were isolated from the systemic circulation so that the baroreceptor input pressure was controlled externally with a servo-pump system. The vagal and aortic depressor nerves were sectioned bilaterally at the neck to minimize confounding reflex effects from the aortic arch and cardiopulmonary regions. Efferent SNA was recorded from a branch of the cardiac sympathetic nerve. The nerve signal was amplified and bandpass filtered between 150 to 1,000 Hz. The signal was then full-wave rectified and low-pass filtered with a cut-off frequency of 30 Hz using an analog circuit. Although SNA was expressed in μV, the absolute magnitude of SNA varied depending on the recording conditions, such as the contact between the electrodes and nerve. After the completion of the preparation, the carotid sinus pressure (CSP) was adjusted to AP to obtain the closed-loop operating point of the carotid sinus baroreflex. After that, the CSP was perturbed according to a binary white noise signal around the operating point pressure.

For the closed-loop analysis, the isolated carotid sinuses were connected to the left common carotid artery. Hence, the carotid sinus baroreflex operated as a closed-loop system despite the isolation of the carotid sinus regions. A catheter for blood withdrawal and infusion was inserted from the other femoral artery and placed at the abdominal aorta.

OPEN-LOOP ANALYSIS

Time-Series Data

See the Appendix to set up GNU Octave. **Figure 1** shows the first 10 s (2,000 points) of the sample data file "rabbit1-open.dat," which can be drawn by the following codes:

```
A = recread('c:/SampleData\rabbit1-open.dat', 4);
figure, recplot(A(:, 1:2000), 200);
```

The user-defined function **recread** reads the data file into a matrix variable A. The first argument specifies the data file name. The folder name needs to be changed according to the location of the sample data file. The second argument specifies the number of channels in the data file as 4. The user-defined function **recplot** plots the time series data. The sampling rate (200 Hz) is specified as a numeric argument. Alternatively, the time-axis data can be provided as the first input argument of **recplot** as follows:

```
A = recread('c:/SampleData\rabbit1-open.dat', 4);
t = (0:2000 − 1) / 200;
figure, recplot(t, A(:, 1:2000));
```

When neither the sampling rate nor the time-axis data are specified, the abscissa indicates the number of data points. The first channel of **Figure 1** indicates CSP, which was changed every 500 ms according to a binary white noise signal. Small ripples were present at high and low values of CSP owing to a limited performance tuning of the servo-pump system. In the second channel, SNA was suppressed during the high CSP level. A closer look indicates a certain delay between the increment of CSP and the suppression of the burst activities of SNA. The third and fourth channels represent the AP and HR signals, respectively. Since the data file is a bare binary file, the number of recorded

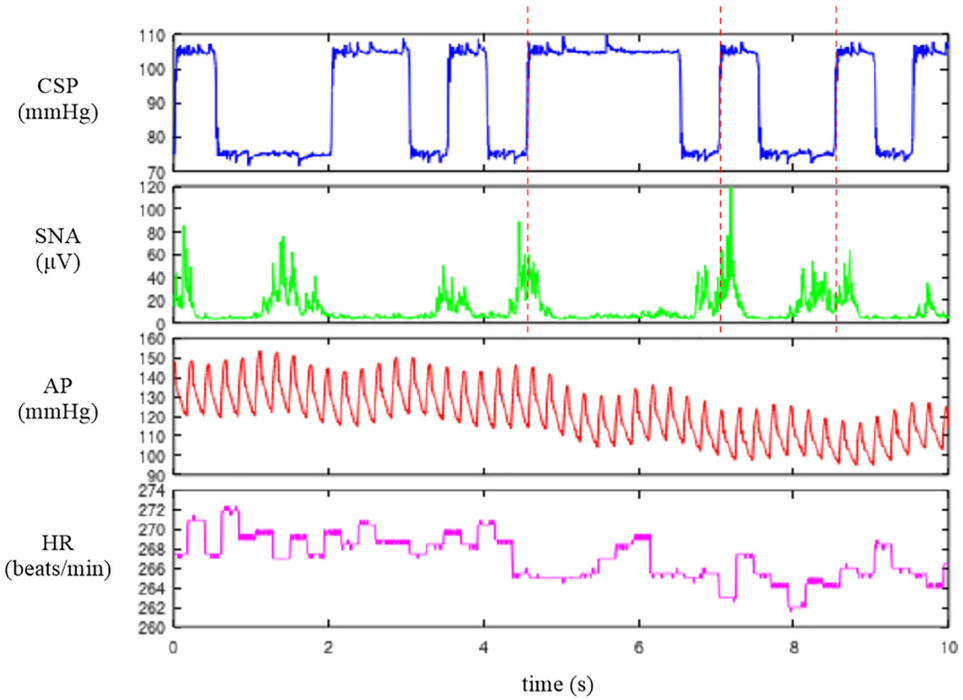

FIGURE 1 | Time series of carotid sinus pressure (CSP), sympathetic nerve activity (SNA), arterial pressure (AP), and heart rate (HR) obtained in one rabbit. CSP was perturbed according to a binary white noise signal. A slight delay was observed between an increment in CSP (vertical dotted lines) and the suppression of the burst activity of SNA.

channels and the format of the stored value need to be known separately. It is advisable to check the waveform of each signal before processing the data. If the data are not decoded correctly (for instance, if the number of recorded channels is wrong), the signals are corrupted.

Depending on the system under study, the original sampling rate may be unnecessary to capture the overall system dynamic characteristics. Typically, we down-sampled the signals from 200 to 10 Hz. **Figure 2** illustrates the whole data of "rabbit1-open.dat" after 10-Hz resampling, which can be obtained from the following codes:

```
B = recresample(A, 20);
figure, recplot(B, 10)
```

The user-defined function **recresample** down-samples the data by simply taking an average of each signal every 20 points. After the resampling, the information on the systolic and diastolic pressures of AP is lost. If one wants to analyze the systolic and diastolic pressures, those values need to be obtained before the resampling procedure.

Conventional Linear Transfer Function Analysis

The neural arc transfer function from CSP to SNA, the peripheral arc transfer function from SNA to AP, and the transfer function of the total reflex arc from CSP to AP were estimated. Although the data before initiating the CSP perturbation were not recorded on the file, a transition from no perturbation to binary perturbation occasionally caused transient changes in the SNA and AP responses. To analyze the stationary portion of the data, we typically discarded the data for the first 120 s (1,200 points) after the initiation of the CSP perturbation. The 10-Hz resampled data were then divided into eight half-overlapping segments of 1,024 points each (**Figure 2**). The segment length was 102.4 s, which corresponded to the fundamental frequency (f_1) of 0.0098 Hz of the Fourier transformation. Depending on the system under study, the segment length would need to be adjusted. As a rule of thumb, the phase value of the estimated transfer function at the lowest frequency approaches zero radians for a system with a positive response and $-\pi$ radians for a system with a negative response when the segment length is sufficiently long to capture the system dynamic characteristics. The segment length may need to be prolonged when the phase value at the lowest frequency is not close to either zero or $-\pi$ radians. An increase in the number of (non-overlapped) segments contributes to reducing the random errors in the transfer function estimation (Bendat and Piersol, 2010). However, too long an observation period would violate the assumption that the system under study can be regarded as time-invariant.

In each segment, a linear trend was removed, and a Hanning window was applied. Next, the frequency spectra of the input signal, $X(f)$, and the output signal, $Y(f)$, were obtained through the fast Fourier transformation. Ensemble averages of the input power, $XX(f)$, output power, $YY(f)$, and cross spectra between the input and output signals, $YX(f)$, were calculated over the eight

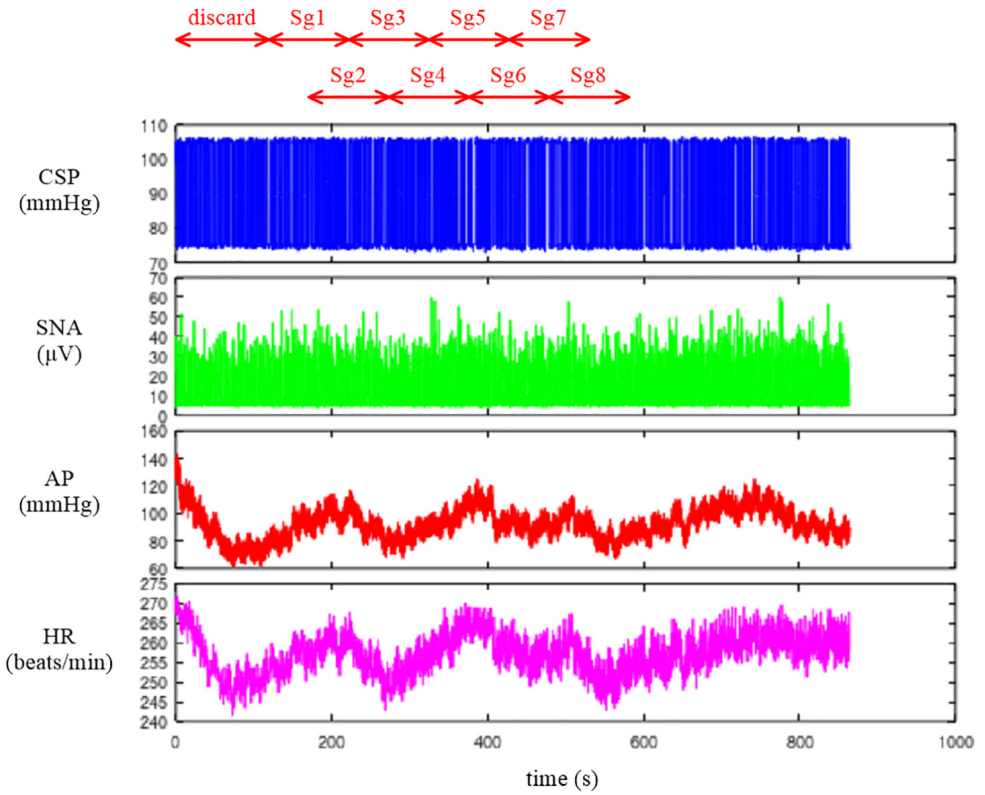

FIGURE 2 | Time series of carotid sinus pressure (CSP), sympathetic nerve activity (SNA), arterial pressure (AP), and heart rate (HR) after 10-Hz resampling. Typically, the data from the first 120 s were discarded to analyze the stationary portion of the data. Sg1 through Sg8 denote the half-overlapping segments for the open-loop transfer function analysis.

segments. The linear transfer function is then obtained using the following equation (Bendat and Piersol, 2010):

$$H(f) = \frac{YX(f)}{XX(f)} \tag{3.2.1}$$

The magnitude-squared coherence function can also be obtained using the following equation (Bendat and Piersol, 2010):

$$Coh(f) = \frac{|YX(f)|^2}{XX(f)YY(f)} \tag{3.2.2}$$

The coherence function indicates the linear dependence of the output signal on the input signal in the frequency domain. The zero coherence indicates that the output signal is linearly uncorrelated with the input signal. The unity coherence indicates that the output signal is completely explained by the linear dynamics with the input signal.

Plotting the Transfer Functions

Since the transfer function is complex-valued, it can be described by the modulus (absolute value) and phase angle as follows:

$$\begin{aligned} Gain(f) &= abs(H(f)) \\ Phase(f) &= angle(H(f)) \end{aligned} \tag{3.3.1}$$

The modulus of the transfer function is referred to as gain because it describes the amplitude ratio of the output signal to the input signal at each frequency. The phase of the transfer function describes the difference in the phase between the input and output signals at each frequency.

A caveat in plotting the estimated transfer function is that f in the above equations needs to be interpreted as an index of the frequency relative to the fundamental frequency. In addition, the lower bound of the array subscript (the integer number pointing to the element in the array) is 1, not 0, in programming languages that use a matrix as an elementary variable including GNU Octave and Matlab. Hence, the first element of the transfer function, $H(1)$, corresponds to the direct current component of the Fourier transformation, which is not used in the transfer function analysis. The second element, $H(2)$, represents the transfer function at the fundamental frequency ($f_1 = 0.0098$ Hz). The $(1 + k)$th element, $H(1 + k)$, represents the k-th harmonic component observed at $(k \times f_1)$ Hz.

When we use a programming language allowing 0 for the lower bound of the array subscript (such as Microsoft Visual Basic) and implement the Fourier transformation accordingly, the situation is different. The first element becomes $H(0)$, and the relation with the frequency index becomes more straightforward; i.e., $H(k)$ represents the k-th harmonic component at $(k \times f_1)$ Hz.

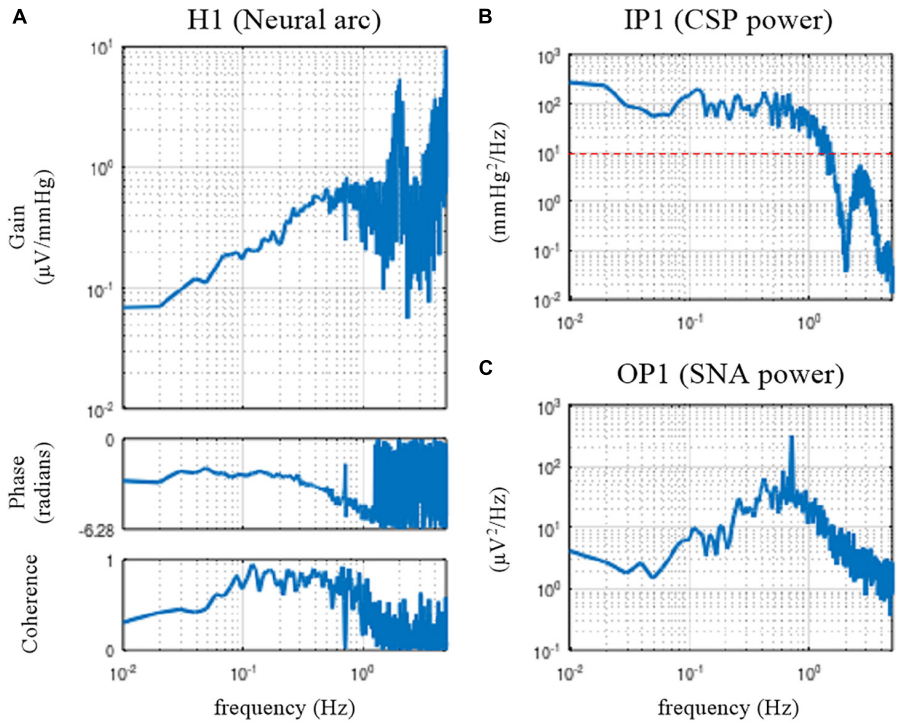

FIGURE 3 | Open-loop transfer function of the baroreflex neural arc, H1 **(A)**, the input power of the carotid sinus pressure (CSP), IP1 **(B)**, and the output power of the sympathetic nerve activity (SNA), OP1 **(C)**. The neural arc revealed high-pass or derivative characteristics, which means that dynamic gain increased as the frequency increased from 0.01 to 0.5 Hz.

Open-Loop Dynamic Characteristics of the Neural and Peripheral Arcs

Neural Arc

Figure 3 illustrates the open-loop dynamic characteristics of the baroreflex neural arc obtained from the following codes:

```
[H1 C1 IP1 OP1] = calctf(B, [1 2]);
IP1 = IP1 / 10 / 0.3746; OP1 = OP1 / 10 / 0.3746;
figure, subplot(1, 2, 1), tfplot(H1, C1, 'r');
subplot(2, 2, 2), psplot(IP1), subplot(2, 2, 4), psplot(OP1);
```

The user-defined function **calctf** calculates the transfer function from channel 1 (row 1, CSP) to channel 2 (row 2, SNA) of the matrix variable B and returns the neural arc transfer function, H1, coherence function, C1, input power spectra, IP1, and output power spectra, OP1. Since the power spectra were calculated on the basis of the unit sampling rate of 1 Hz, they need to be divided by 10 to adjust the values for the 10-Hz resampling data. Further, the power spectra were not corrected for process loss caused by the window function. In the case of the Hanning window, the correction factor of 1/0.3746 may be applied. The denominator of the correction factor for the segment length of 1,024 can be obtained from the following calculation:

```
c = sum(hanning(1024).^ 2) / 1024
```

where "^2" denotes the element-wise application of the power of 2.

The user-defined function **tfplot** plots the transfer function and the coherence function. The common logarithm (the logarithm with base 10) of the gain value and the phase value are plotted against the common logarithm of the frequency (a Bode plot). The third input argument of **tfplot** dictates that the phase is plotted in the range from -2π to 0 radians rather than the default range from $-\pi$ to π radians. The user-defined function **psplot** plots the power spectra. The upper frequency bound of the abscissa displayed by **tfplot** and **psplot** was 5 Hz, which is half of the sampling frequency of 10 Hz. When the sampling rate of the analyzed data is different from 10 Hz, the sampling rate needs to be specified as a numeric argument for **tfplot** and **psplot**. The lower frequency bound of the abscissa displayed by **tfplot** and **psplot** was determined from the length of H1, which equals the segment length of 1,024. By default, the lower frequency bound is the same as the fundamental frequency (10/1,024 = 0.0098 Hz).

The dynamic gain of the neural arc transfer function increased as the frequency increased from 0.01 to 0.5 Hz (**Figure 3A**). These characteristics are referred to as the high-pass or derivative characteristics of the neural arc (Ikeda et al., 1996). The input power spectra showed that CSP power was fairly constant up to 1 Hz and dropped sharply, making a nadir at 2 Hz (**Figure 3B**). The nadir occurs at the frequency corresponding to the switching interval of the CSP input signal (500 ms). Since the input power is the denominator to calculate the transfer function (Eq. 3.2.1), the input power at a given frequency needs to be sufficiently large for a stable estimation of the transfer function. A white

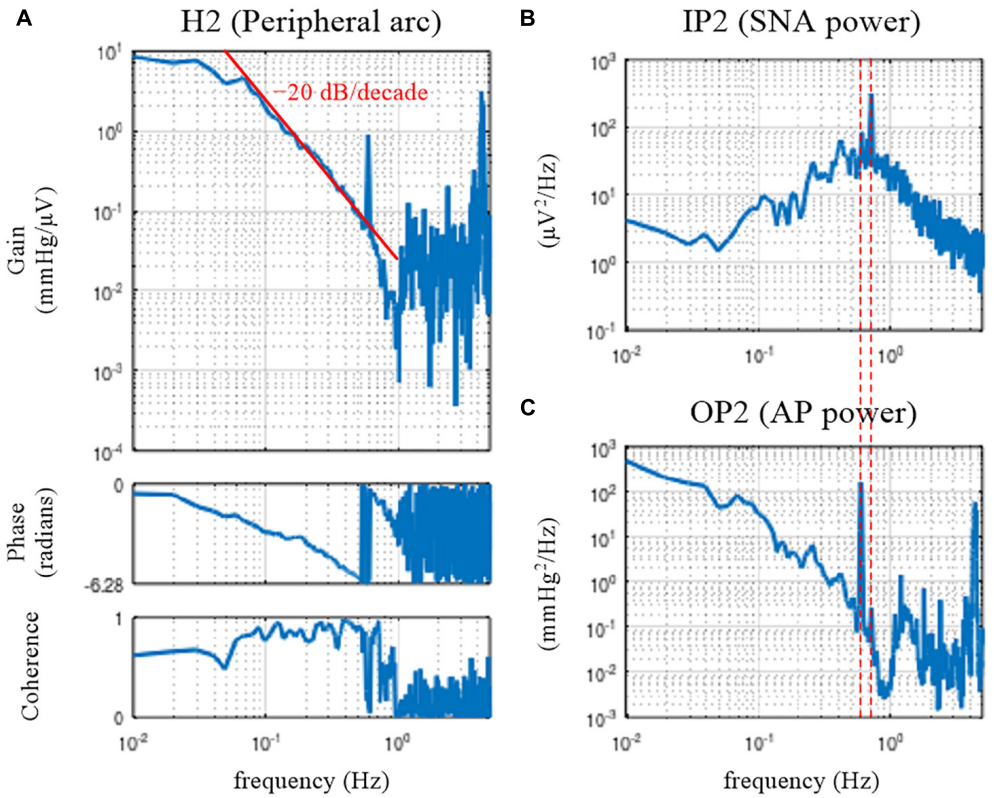

FIGURE 4 | Open-loop transfer function of the baroreflex peripheral arc, H2 **(A)**, the input power of the sympathetic nerve activity (SNA), IP2 **(B)**, and the output power of the arterial pressure (AP), OP2 **(C)**. The peripheral arc revealed low-pass characteristics, with the slope of decreasing gain between 0.1 and 0.5 Hz close to the –20 decibel/decade (the oblique red line). The vertical dotted lines indicate that the frequency of the peak in the SNA power (endogenous respiratory frequency) is not the same as the frequency of the peak in the AP power (artificial ventilation frequency).

noise signal, which is rich in frequency components, is an ideal input signal to rigorously test a system within a short observation period (Marmarelis and Marmarelis, 1978). Since a theoretical white noise is unrealizable, a band-limited white noise signal is used in actual applications. In this example, the input power decreased to 10 $mmHg^2/Hz$ (the red horizontal dotted line) at approximately 1.5 Hz, and hence, the transfer function may be reliable up to 1.5 Hz at the most. The peak in the gain plot at 2 Hz was the artifact due to the division by small numbers at the nadir of the input power. The coherence function reduced to near zero in the frequency range above approximately 1.2 Hz in these data.

The phase of the neural arc transfer function was close to $-\pi$ radians at the lowest frequency, indicating that the signal inversion for the negative feedback occurred in the neural arc. The inhibitory neurons projecting from the caudal ventrolateral medulla to the rostral ventrolateral medulla are responsible for signal inversions (Masuda et al., 1992). The phase plot is slightly convex-upward relative to $-\pi$ radians. The phase was delayed as the frequency increased from 0.2 to 1 Hz. A discontinuous phase deflection was observed at approximately 0.7 Hz, which was accompanied by a discontinuous drop in the coherence at the same frequency. The gain plot also shows a small deflection at 0.7 Hz. The SNA power had a sharp peak at 0.7 Hz (**Figure 3C**). This peak is considered a physiological noise of SNA associated with endogenous respiratory activity, which was linearly uncorrelated with the CSP input signal.

Peripheral Arc

Figure 4 illustrates the open-loop dynamic characteristics of the baroreflex peripheral arc obtained from the following codes:

```
[H2 C2 IP2 OP2] = calctf(B, [2 3]);
IP2 = IP2 / 10 / 0.3746; OP2 = OP2 / 10 / 0.3746;
figure, subplot(1, 2, 1), tfplot(H2, C2, 'r');
subplot(2, 2, 2), psplot(IP2), subplot(2, 2, 4), psplot(OP2);
```

The peripheral arc transfer function was calculated between channel 2 (row 2, SNA) and channel 3 (row 3, AP) of the matrix variable B. The dynamic gain of the peripheral arc transfer function decreased as the frequency increased from 0.05 to 1 Hz, indicating the low-pass characteristics of the cardiovascular response to SNA (**Figure 4A**). A sharp peak was observed at 0.58 Hz in the gain plot. This peak was due to the AP fluctuations at the frequency of artificial ventilation (35 cycles/min). The frequency of the peak in the AP power (0.58 Hz) was different from the frequency of the peak in the SNA power (approximately 0.7 Hz) (**Figures 4B,C**). The mechanical inflation and deflation of the lungs affected AP independently of SNA. Hence, the

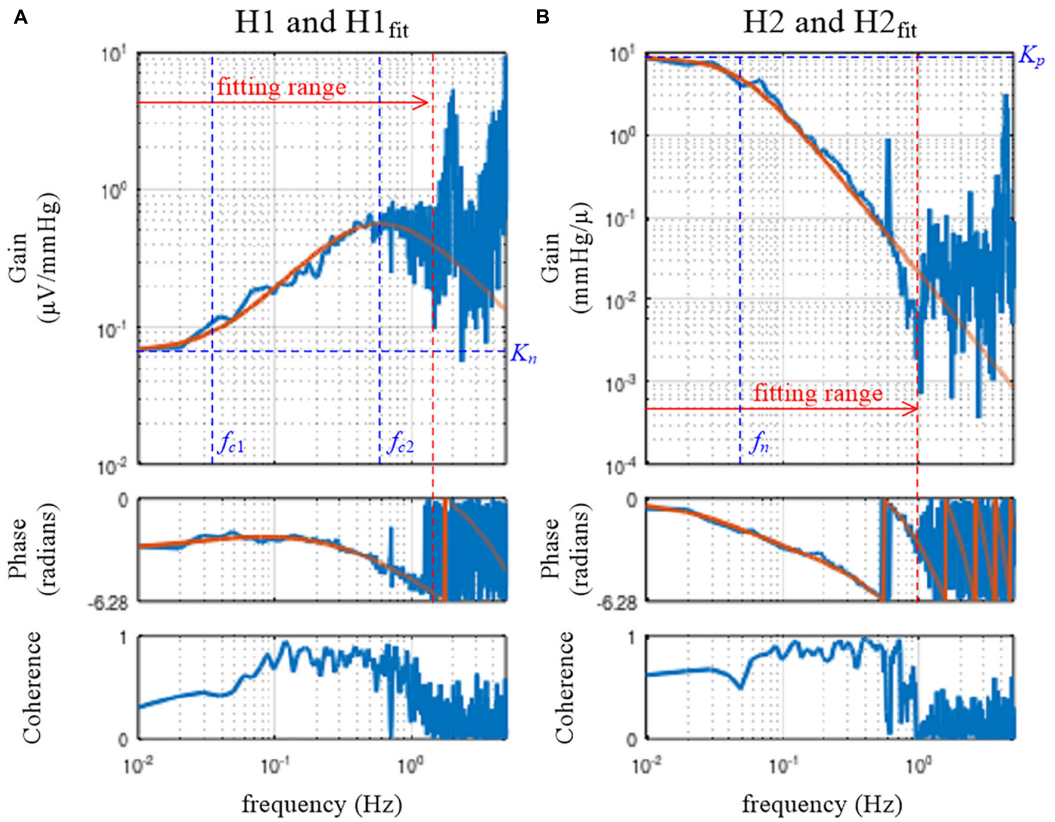

FIGURE 5 | Fitting results of the mathematical models to the estimated transfer functions for the neural arc, H1 **(A)**, and for the peripheral arc, H2 **(B)**. The smooth orange lines represent the transfer functions of the mathematical models, $H1_{fit}$ (Eq. 3.5.1) and $H2_{fit}$ (Eq. 3.5.2). K_n, the steady-state gain of $H1_{fit}$; f_{c1}, the corner frequency describing the derivative characteristics of $H1_{fit}$; f_{c2}, the corner frequency describing the high-cut characteristics of $H1_{fit}$; K_p, the steady-state gain of $H2_{fit}$; f_n: the natural frequency of $H2_{fit}$.

peak in the gain plot at 0.58 Hz, which was accompanied by a discontinuous drop of the coherence, does not represent the true characteristics of the AP response to SNA. The decreasing slope of dynamic gain between 0.1 and 0.5 Hz was close to the line of the −20 dB/decade (the oblique red line), which means that the dynamic gain decreased to 1/100 with a 10-fold increase in the frequency.

The phase approached 0 radians at the lowest frequency, suggesting that the steady-state AP response to a step input in SNA was positive. The phase was delayed as the frequency increased and reached -2π radians at approximately 0.6 Hz. Although the phase was wrapped between -2π and 0 radians in this plot, we may unwrap the phase by assuming a continuous phase change along the frequency axis.

Mathematical Models of Transfer Functions

Model Description

Enumerating all gain and phase values on the Bode plot is one way to describe the estimated transfer function. However, by fitting a mathematical model to the estimated transfer function, we can describe the transfer function with only a few parameter values. The neural arc transfer function may be described using the following mathematical model (Kawada et al., 2002):

$$H1_{model}(f) = -K_n \frac{1 + \frac{f}{f_{c1}}j}{\left(1 + \frac{f}{f_{c2}}j\right)^2} e^{-2\pi f L_n j} \qquad (3.5.1)$$

where j denotes the unit imaginary number ($j = \sqrt{-1}$). K_n, f_{c1}, f_{c2}, and L_n denote the steady-state gain (in μV/mmHg), the corner frequency relating to the derivative characteristics (in Hz), the corner frequency relating to the high-cut characteristics (in Hz), and the pure delay (in s), respectively. The negative sign in front of K_n indicates that the signal is inverted through the neural arc. The dynamic gain of $H1_{model}$ asymptotically approaches K_n as the frequency tends to 0.

The peripheral arc transfer function may be described using a second-order low-pass filter with pure delay as follows (Kawada et al., 2002):

$$H2_{model}(f) = \frac{K_p}{1 + 2\zeta \frac{f}{f_n}j + \left(\frac{f}{f_n}j\right)^2} e^{-2\pi f L_p j} \qquad (3.5.2)$$

where K_p, f_n, ζ, and L_p denote the steady-state gain (in mmHg/μV), the natural frequency (in Hz), the damping ratio (dimensionless), and the pure delay (in s), respectively. Depending on the value of ζ, the system behaves as underdamped ($0 \leq \zeta < 1$), critically damped ($\zeta = 1$), or overdamped ($1 < \zeta$). The dynamic gain of $H2_{model}$ asymptotically approaches K_p as the frequency tends to 0.

The structure of the mathematical model is not uniquely determined for a given transfer function. As an example, the denominator of $H1_{model}$ could have the same form as that of $H2_{model}$, in which case the total number of parameters in $H1_{model}$ increases from 4 to 5 (Petiot et al., 2001). Although an increase in the number of parameters of the mathematical model can improve the fitting ability of a model to the estimated transfer function, the meaning of each parameter may become more complicated. Further, possible interdependence between parameters makes the parameter estimation more unstable.

Parameter Estimation

The fitting of the mathematical model to the estimated transfer function requires nonlinear least-squares fitting. Although there are many ways to perform such a task, we provided the user-defined function **simplex** based on a method described by Nelder and Mead (1965). Although the convergence of this method is slow, it has a merit in that it does not require a derivative form of the target function. A risk of the convergence to a local minimum needs to be noted, though the risk is not specific to this method.

The error function for the least-squares fitting is difficult to assign because the transfer function is complex-valued. Empirically, we use the following error function, which gives a reasonable fitting result on the Bode plot:

$$err = \sum_{k=1}^{N} \frac{\left|\log_{10}\left[H_{est}(f)\right] - \log_{10}\left[H_{model}(f)\right]\right|^2}{k} \qquad (3.5.3)$$
$$\mathrm{f} = \mathrm{f}_1 \times \mathrm{k}$$

where H_{est} and H_{model} denote the estimated and model transfer functions, respectively. N represents the number of data points from the lowest frequency used for the fitting. During the implementation to the programming, the fact that H_{est} is discrete and $H_{est}(1)$ corresponds to the direct current component needs to be considered.

Figure 5A depicts the fitting result of $H1_{model}$ to the neural arc transfer function, which was obtained from the following codes:

```
x = (0:512)'/(1024/10);
H1model = @(x, p) − p(1) * (1+x/p(2) * 1j)./
          (1 + x/p(3) * 1j).^2. * exp(−2 * pi * x * p(4) * 1j);
pout1 = simplex(x(2:151), H1(2:151), [abs(H1(2)) 0.1 1 0.5],
        H1model);
H1fit = [H1model(x, pout1); zeros(511,1)];
figure, subplot(1, 2, 1), tfplot([H1 H1fit], C1, 'r');
```

The first line defines the variable x as the array of frequency values, including 0 for the direct current component. For instance, x(1) is 0, x(2) is the fundamental frequency, x(3) is the second harmonic frequency, and so on. The upper bound of x corresponds to half of the sampling rate; i.e., x(513) = 5.

The second line defines the target function, $H1_{model}$, based on Eq 3.5.1. The variable p is the array of parameters, such that p(1), p(2), p(3), and p(4) correspond to K_n, f_{c1}, f_{c2}, and L_n, respectively. In the above definition, $H1_{model}$ takes the variables x and p as the input arguments and returns the transfer function values corresponding to x.

The user-defined function **simplex** performs nonlinear least-squares fitting. The first and second arguments of **simplex** are the frequency and the corresponding transfer function values, respectively. Only the first 150 points from the fundamental frequency were used. Note that the subscript range should be "(2:151)", not "(1:150)", to skip the direct current component. The third argument of **simplex** gives initial parameter values for K_n, f_{c1}, f_{c2}, and L_n. The initial value for K_n was given as the absolute value of H1(2) rather than a hard number because the dynamic gain of the neural arc varied significantly depending on the absolute amplitude of SNA (e.g., the quality of the SNA recording, position of the electrode relative to the nerve, etc.). Alternatively, we may use arbitrary units for presenting SNA after normalizing SNA values by the average dynamic gain value of H1 in the frequency range, for instance, below 0.03 Hz (Kawada et al., 2001). When the SNA is normalized, the initial value for K_n can be unity. The last argument of **simplex** specifies $H1_{model}$ as a target function.

The variable pout1 receives the array of parameter values for K_n, f_{c1}, f_{c2}, and L_n that attained the minimum value of the error function. In this example, the parameter values of pout1(1) = 0.066, pout1(2) = 0.035, pout1(3) = 0.598, and pout1(4) = 0.198 were obtained.

$H1_{fit}$ is the fitting result calculated based on x and pout1. Since the user-defined function **tfplot** determines the frequency axis based on the length of the transfer function data, the length of $H1_{fit}$ needs to be adjusted to 1,024 points for its proper presentation on the Bode plot. For this purpose, an array of zeros was added, but this has nothing to do with a zero-padding procedure to increase the frequency resolution. If $H1_{fit}$ does not fit to H1 well by visual inspection of the Bode plot, the initial parameter values need to be changed according to the profile of H1. For instance, the initial value for f_{c2} may be selected near the frequency of the maximum gain within the fitting range (**Figure 5A**).

Figure 5B depicts the fitting result of $H2_{model}$ to the peripheral arc transfer function, which was obtained from the following codes:

```
H2model = @(x, p) p(1)./(1+2 * p(3) * x/p(2) * 1j
  +(x/p(2) * 1j).^2). * exp(−2 * pi * x * p(4) * 1j);
pout2 = simplex(x(2:101), H2(2:101), [abs(H2(2)) 0.1 1.5 1],
H2model);
H2fit = [H2model(x, pout2); zeros(511,1)];
subplot(1, 2, 2), tfplot([H2 H2fit], C2, 'r');
```

The target function, $H2_{model}$, is defined based on Eq. 3.5.2. For the peripheral arc, only the first 100 points from the fundamental frequency were used to determine the parameters of $H2_{model}$. The initial parameter values for K_p, f_n, ζ, and L_p were given as the

third argument of **simplex**. The initial value for ζ was arbitrarily assigned to 1.5, but a different value could be tested. After the fitting was performed, parameter values of pout2(1) = 8.812, pout2(2) = 0.049, pout2(3) = 0.925, and pout2(4) = 0.962 were obtained in this example. Using the variables x and pout2, the fitting result was calculated as $H2_{fit}$ and compared with H2 using **tfplot**.

In the user-defined function **simplex**, the fitting weight of the error between the model and estimated transfer functions is reduced by a factor of $1/k$ according to Eq. 3.5.3 because the data points become denser as the frequency increased on the Bode plot. The error function can be modified if needed as an optional input argment to **simplex**:

```
w = 1./(1:100)'. * C2(2:101);
pout2 = simplex(x(2:101), H2(2:101),
[abs(H2(2)) 0.1 1.5 1], H2model, w);
H2fit = [H2model(x, pout2); zeros(511,1)];
subplot(1, 2, 2), tfplot([H2 H2fit], C2, 'r');
```

In the above codes, the array for the fitting weight is provided, taking the coherence, C2, into consideration. When the coherence value at a given frequency is low, the fitting weight of the error is reduced. The resulting $H2_{fit}$, however, was not changed much in this example.

Simulation of Baroreflex Dynamic Characteristics

Design of a Block Diagram

Once the parameters of the model transfer functions are determined, a closed-loop baroreflex response can be simulated by using software such as Xcos (Scilab) and Simulink (Matlab). In the following examples, Xcos was used. Before constructing a block diagram in Xcos, the following variables need to be defined on the Scilab console:

```
fc1 = 0.035; fc2 = 0.6; Ln = 0.2;
fn = 0.049; zeta = 0.92; Lp = 0.96;
```

Figure 6A illustrates the block diagram simulating the baroreflex response to a step pressure perturbation ("dynamic_step.zcos"). The neural and peripheral arc transfer functions can be implemented using a function block named CLR. The frequency response of a system described in the ***s***-domain can be obtained by replacing ***s*** with $j\omega$, where $\omega = 2\pi f$. For instance, the first-order low-pass filter with a corner frequency of f_c can be converted from the frequency domain to the ***s***-domain as follows:

$$H(f) = \frac{1}{1 + \frac{f}{f_c}j} = \frac{1}{1 + \frac{2\pi fj}{2\pi f_c}} \leftrightarrow H(s) = \frac{1}{1 + \frac{1}{2\pi f_c}s} \tag{3.6.1}$$

Hence, the CLR block describing the neural arc, excluding the parameters of dynamic gain and pure delay, can be designed as

$$H1_{model}(s) = \frac{1 + \frac{1}{2\pi f_{c1}}s}{\left(1 + \frac{1}{2\pi f_{c2}}s\right)^2} \tag{3.6.2}$$

Likewise, the CLR block describing the peripheral arc, excluding the parameters of dynamic gain and pure delay, can be designed as

$$H2_{model}(s) = \frac{1}{1 + 2\zeta\frac{1}{2\pi f_n}s + \left(\frac{1}{2\pi f_n}\right)^2 s^2} \tag{3.6.3}$$

As a tip of programming, the constant π (3.14159...) is given by "pi" in GNU Octave and Matlab, whereas it is given by "%pi" in Scilab. The pure delay can be implemented using a TIME_DELAY block. For convenience, the delay was defined by a variable L_n or L_p rather than by a hard number. The buffer size of the TIME_DELAY block was increased to 4,096 to avoid an error relating to the short of the buffer size. The gain of the total reflex arc can be assigned using a GAINBLK block. The gain value was set to −1 to reflect the negative feedback nature of the total reflex arc.

The step input can be implemented using a STEP_FUNCTION block. The step time was set at 10, and the final value was set at −30, which means that a pressure disturbance of −30 mmHg was imposed at 10 s. The output from the STEP_FUNCTION block was then combined with the output from the peripheral arc using a SUMMATION block. The number of inputs to the SUMMATION block was set to 2. The output from the SUMMATION block was displayed on a CSCOPE block. The refresh period parameter of the CSCOPE block was set to 60. The CSCOPE block requires a clock input, which was generated by a CLOCK_c block. The interval of the CLOCK_c block was set at 0.005 s (200 Hz), which is the rate at which the visualization is refreshed. The output from the SUMMATION block can also be stored on a workspace variable A using a TOWS_c block. The buffer size of the workspace variable was set to the time resolution (200 Hz) multiplied by the total simulation time (60 s).

Role of the Neural Arc

The contribution of the neural arc to the baroreflex-mediated dynamic AP response can be examined by removing the CLR block of the neural arc from the simulation (**Figure 6B**, "dynamic_step_no_neural.zcos"). The simulation result is then stored on another workspace variable B. **Figure 7** compares the simulation results with and without the neural arc, which was obtained by the following code on the Scilab console:

```
t = (0:length(A.values) − 1)' / 200;
figure, plot(t, [A.values B.values]);
```

When the first recovery point that exceeded the steady-state response was used to compare the response speed, the removal of the neural arc delayed the recovery of AP by a few seconds in this example. Although the actual baroreflex system is nonlinear and the presence of the pulsatility affects the AP response (Chapleau et al., 1989; Kawada et al., 1992, 2002), the simulation results suggest that the neural arc accelerates the baroreflex-mediated AP response (Ikeda et al., 1996).

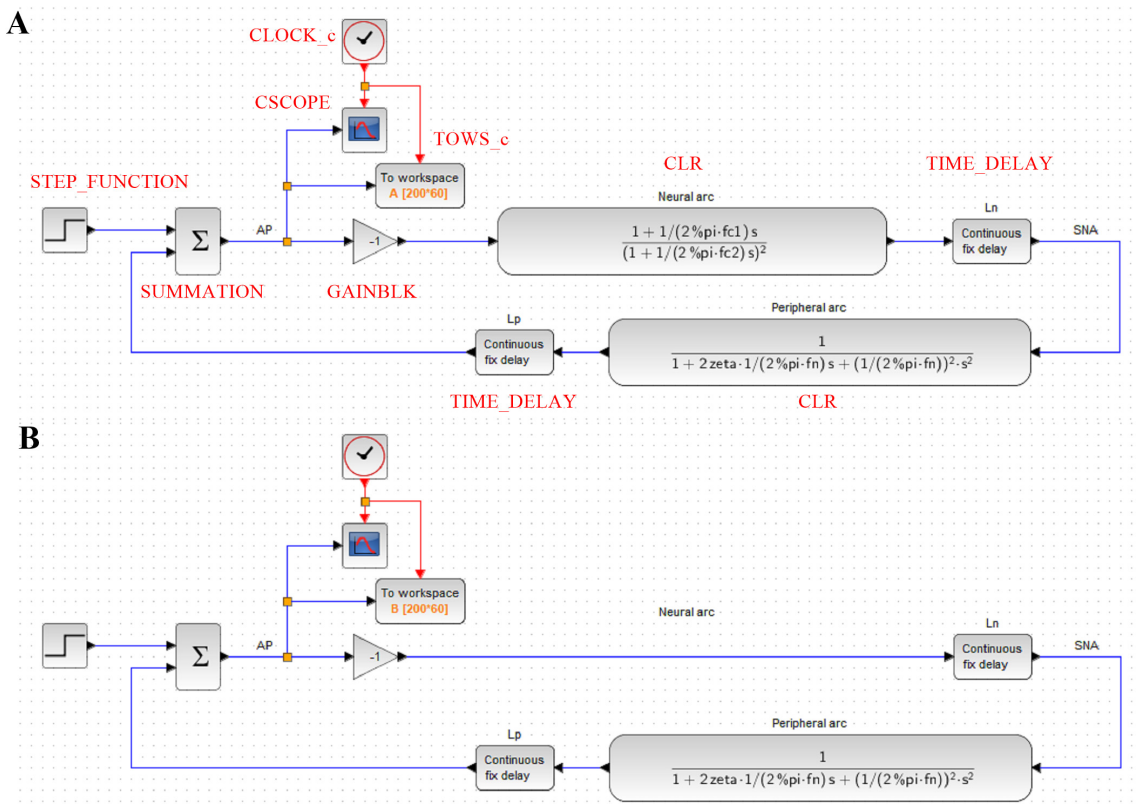

FIGURE 6 | (A) A block diagram of the arterial baroreflex system for simulating the closed-loop arterial pressure (AP) change in response to a step pressure perturbation. The red capital letters denote the types of function blocks of Xcos (Scilab). SNA, sympathetic nerve activity; Ln, the pure delay relating to the neural arc; Lp, the pure delay relating to the peripheral arc. **(B)** A block diagram that lacks the dynamic characteristics of the neural arc.

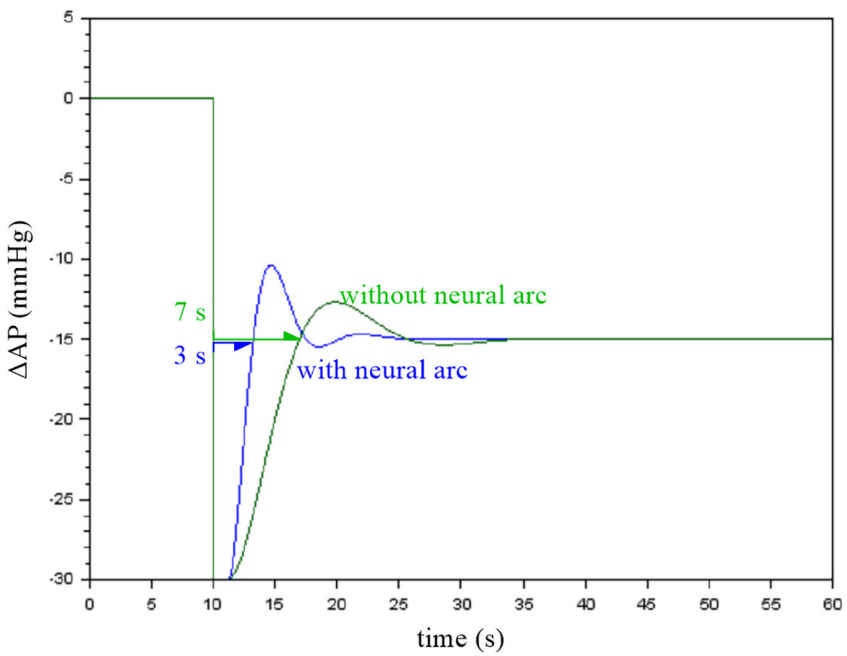

FIGURE 7 | Simulation results showing the effect of the neural arc on the closed-loop arterial pressure (AP) response to a step pressure perturbation. The neural arc shortened the recovery time as assessed by the first point that reached the steady-state response.

Static Nonlinearity of the Baroreflex

Although we do not treat the nonlinearity of the baroreflex in this article, the open-loop static characteristics of the neural arc approximated an inverse sigmoidal function. By contrast, the static characteristics of the peripheral arc approximated a straight line within the physiological response range of the baroreflex (Kawada and Sugimachi, 2016). These static characteristics may be implemented in the simulation, which helps interpret certain aspects of the baroreflex characteristics, such as the dependence of the baroreflex gain on the pulsatility of AP (Kawada et al., 1992, 2002) and on AP waveforms (Kawada et al., 2017).

Open-Loop Dynamic Characteristics of the Total Reflex Arc

Total Reflex Arc

The neural and peripheral arc subsystems are serially connected to constitute the total reflex arc. When the two transfer functions, H1 and H2, are serially connected, the overall transfer function, H3, is obtained from the product of H1 and H2 in the frequency domain. In theory, the gain of H3 is a product of gain values of H1 and H2. The phase of H3 is a sum of phase values of H1 and H2. This result can easily be understood using a polar form of the transfer function as follows:

$$\begin{aligned} H1(f) &= G1(f)e^{j\theta 1(f)} \\ H2(f) &= G2(f)e^{j\theta 2(f)} \\ H3(f) = H1(f)H2(f) &= G1(f)G2(f)e^{j[\theta 1(f)+\theta 2(f)]} \end{aligned} \tag{3.7.1}$$

where G1 and θ1 are the gain and phase values of H1, respectively, and G2 and θ2 are the gain and phase values of H2, respectively.

The open-loop dynamic characteristics of the total reflex arc can be directly estimated as a transfer function from CSP to AP using the following codes:

```
[H3 C3] = calctf(B, [1 3]);
figure, subplot(1, 2, 1), tfplot(H3, C3);
```

The dynamic gain of the total reflex arc decreased as the frequency increased, indicating the low-pass characteristics (**Figure 8A**). The peak at 0.58 Hz is an artifact relating to the artificial ventilation frequency. The decreasing slope of dynamic gain between 0.1 and 0.5 Hz was less steep than the line of the −20 dB/decade (the oblique red line) observed for the peripheral arc (**Figure 4**, left) and close to the line of the −10 dB/decade (the oblique green line). The increasing slope of dynamic gain in the neural arc (**Figure 3**, left) contributes to increasing dynamic gain values of the total reflex arc between 0.1 and 0.5 Hz. This is the reason why the closed-loop AP response to an exogenous pressure perturbation becomes faster with the neural arc than without (**Figure 7**; Ikeda et al., 1996).

The phase at the lowest frequency approached π radians, but this result needs to be interpreted as −π radians because of the causality between CSP and AP under baroreflex open-loop conditions. The causality came from the isolated baroreceptor preparation where CSP was controlled independently of AP. The phase delayed as the frequency increased and reached −π radians (or should be interpreted as −3π radians) at approximately 0.5 Hz.

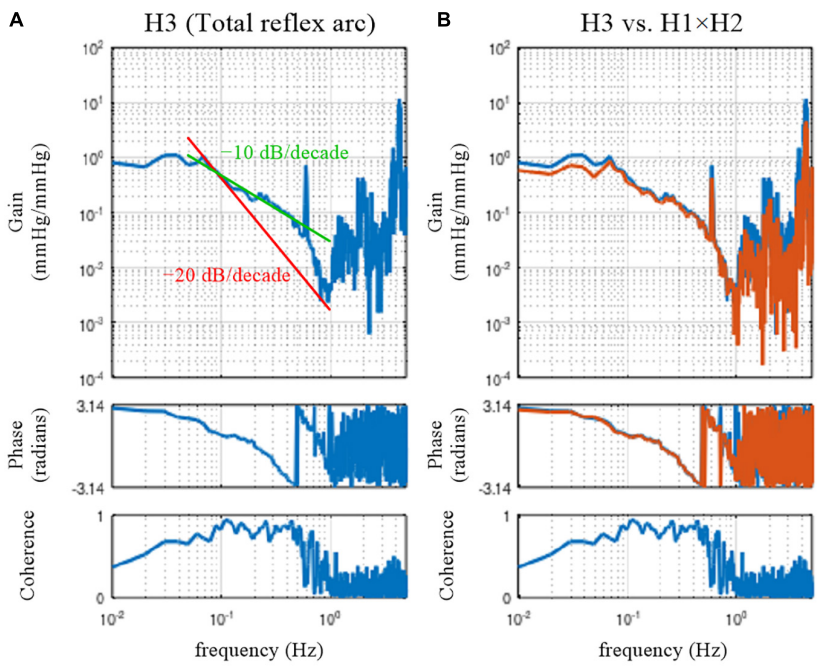

FIGURE 8 | (A) Open-loop transfer function of the baroreflex total loop, H3. The slope of decreasing gain between 0.1 and 0.5 Hz was less steep than that of the –20 decibel/decade (the oblique red line) and was close to that of the –10 decibel/decade (the oblique green line). **(B)** Comparison of H3 (the blue lines) and the product of the neural and peripheral arc transfer functions (H1 × H2, the orange lines).

Comparison With a Product of Neural and Peripheral Arc Transfer Functions

In actual datases, the total reflex arc transfer function, H3, does not exactly equal the product of H1 and H2 because of the nonlinearity of the system and the presence of noise in the system. The following codes are used to compare H3 and the product of H1 and H2:

```
[H1 C1] = calctf(B, [1 2]); [H2 C2] = calctf(B, [2 3]); [H3 C3]
        = calctf(B, [1 3]);
subplot(1, 2, 2), tfplot([H3 H1. * H2], C3);
```

where "H1. * H2" indicates the element-wise multiplication of H1 and H2. As can be seen in **Figure 8B**, there was a deviation of H3 (the blue lines) from the product of H1 and H2 (the orange lines) mainly in the lower frequency range. When the calculations of the cross and power spectra are written down, the three transfer functions are estimated as

$$H1(f) = \frac{E\left[SNA(f)CSP^*(f)\right]}{E\left[CSP(f)CSP^*(f)\right]}$$
$$H2(f) = \frac{E\left[AP(f)SNA^*(f)\right]}{E\left[SNA(f)SNA^*(f)\right]} \quad (3.7.2)$$
$$H3(f) = \frac{E\left[AP(f)CSP^*(f)\right]}{E\left[CSP(f)CSP^*(f)\right]}$$

where $\boldsymbol{E}[]$ represents the ensemble averaging operation over multiple segments. X* denotes the complex conjugate of X; i.e., $X^* = a - bj$ when $X = a + bj$. Dividing H3 by H1 yields

$$\frac{H3(f)}{H1(f)} = \frac{E\left[AP(f)CSP^*(f)\right]}{E\left[SNA(f)CSP^*(f)\right]} \quad (3.7.3)$$

The right-hand side of Eq. 3.7.3 is not the same as the equation for calculating H2 in Eq. 3.7.2. **Figure 9A** illustrates a block diagram of a baroreflex open-loop experiment. CSP is controlled independently of AP. N_c represents the unknown central noise that fluctuates SNA, such as that derived from a central command. N_p represents the unknown peripheral noise that fluctuates AP, such as that associated with artificial ventilation. If N_p is absent, and the peripheral arc subsystem is purely linear, the relationship between SNA and AP can be described as

$$AP(f) = H2(f)SNA(f) \quad (3.7.4)$$

Substituting AP in Eq. 3.7.3 with Eq 3.7.4 yields

$$\frac{H3(f)}{H1(f)} = \frac{H2(f)E\left[SNA(f)CSP^*(f)\right]}{E\left[SNA(f)CSP^*(f)\right]} = H2(f) \quad (3.7.5)$$

The above transformation assumes that H2 is time-invariant during the observation period and can be treated as a constant with respect to the ensemble averaging operation. Hence, when N_p is absent and the peripheral arc subsystem is purely linear, H3/H1 mathematically equals H2; i.e., the product of H1 and H2 equals H3.

Next, let us suppose that N_c is absent and the neural arc subsystem is purely linear. In this case, the relationship between CSP and SNA can be described as

$$SNA(f) = H1(f)CSP(f) \quad (3.7.6)$$

Substituting SNA in the calculation of H2 in Eq. 3.7.2 with Eq. 3.7.6 yields

$$H2(f) = \frac{E\left[AP(f)\left(H1(f)CSP(f)\right)^*\right]}{E\left[SNA(f)\left(H1(f)CSP(f)\right)^*\right]} = \frac{E\left[AP(f)CSP^*(f)\right]H1^*(f)}{E\left[SNA(f)CSP^*(f)\right]H1^*(f)} = \frac{H3(f)}{H1(f)} \quad (3.7.7)$$

Hence, when N_c is absent and the neural arc subsystem is purely linear, the product of H1 and H2 again equals H3. The fact that H3 was not the same as the product of H1 and H2 in the actual datasets (**Figure 8B**) suggests that both N_c and N_p were present during the experiment. It may be of note that the nonlinear system responses in the neural and peripheral arcs are treated as N_c and N_p, respectively, from the viewpoint of the linear systems analysis. The nonlinearity of the total reflex arc was estimated in different papers (Moslehpour et al., 2015, 2016a,b).

On a different note, $\boldsymbol{E}[]$ can be replaced with a summation, $\Sigma[]$, when $\boldsymbol{E}[]$ appears in both the numerator and denominator of the calculation as follows:

$$XX(f) = E\left[X(f)X(f)^*\right] = \frac{\sum\left[X(f)X(f)^*\right]}{M}$$
$$YX(f) = E\left[Y(f)X(f)^*\right] = \frac{\sum\left[Y(f)X(f)^*\right]}{M} \quad (3.7.8)$$
$$H(f) = \frac{YX(f)}{XX(f)} = \frac{E\left[Y(f)X(f)^*\right]}{E\left[X(f)X(f)^*\right]} = \frac{\sum\left[Y(f)X(f)^*\right]}{\sum\left[X(f)X(f)^*\right]}$$

where $X(f)$ and $Y(f)$ denote the Fourier transforms of the input and output of the system, respectively, and M denotes the number of segments for the ensemble averaging operation.

Species Differences

The derivative characteristics of the neural arc and the low-pass characteristics of the peripheral arc are commonly observed for rabbits and rats (Kawada and Sugimachi, 2016). **Figures 10A–C** represent the neural arc, peripheral arc, and total reflex arc transfer functions, respectively, pooled from 12 Japanese white rabbits. In these plots, the SNA values were normalized by the averaged dynamic gain value of the neural arc below 0.03 Hz and expressed in arbitrary units (au). The parameter values of the models (smooth orange lines) fit to the averaged transfer functions were $f_{c1} = 0.058$ Hz, $f_{c2} = 0.482$ Hz, $L_n = 0.181$ s, $f_n = 0.058$ Hz, $\zeta = 1.208$, and $L_p = 0.782$ s. **Figures 10D–F** represent the neural arc, peripheral arc, and total reflex arc transfer functions, respectively, pooled from 12 Wistar-Kyoto

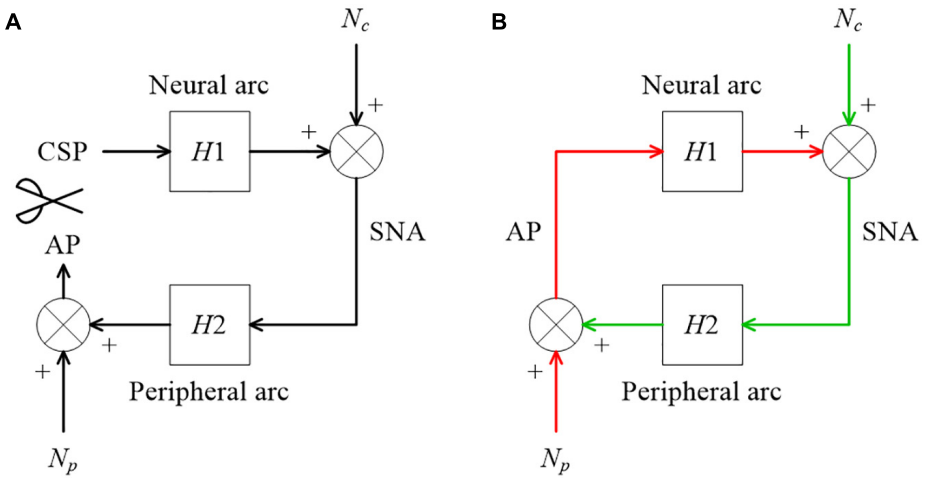

FIGURE 9 | (A) A conceptual block diagram describing the open-loop analysis of the carotid sinus baroreflex. Carotid sinus pressure (CSP) was controlled independently of arterial pressure (AP) by using a baroreceptor isolation procedure. H1 and H2 represent the linear transfer function of the neural and peripheral arcs, respectively. SNA, sympathetic nerve activity; N_c, unknown central noise; N_p, unknown peripheral noise. In the open-loop conditions, N_c does not affect CSP during the estimation of H1, and N_p does not affect SNA during the estimation of H2. **(B)** A conceptual block diagram describing the closed-loop operation of the carotid sinus baroreflex. A distinct difference from the open-loop experiment (9A) is that N_c inevitably affects AP through H2 (the green arrows) during the estimation of H1, and N_p inevitably affects SNA through H1 (the red arrows) during the estimation of H2. These closed-loop signal transductions hamper the application of the conventional open-loop analysis to the closed-loop data.

rats. The parameter values were $f_{c1} = 0.161$ Hz, $f_{c2} = 1.023$ Hz, $L_n = 0.118$ s, $f_n = 0.074$ Hz, $\zeta = 1.115$, and $L_p = 0.474$ s. The total reflex arc transfer function may be roughly described with a first-order low-pass filter with pure delay. The corner frequency and the pure delay were 0.038 Hz and 1.410 s, respectively, in rabbits. They were 0.029 Hz and 0.871 s, respectively, in rats. The data derived from Sprague-Dawley rats can be found in a previous article (Kawada and Sugimachi, 2016).

As for the total reflex arc transfer function, dogs also show low-pass characteristics with the natural frequency near 0.02 Hz (Kawada et al., 1992). Changes in vascular properties rather than ventricular properties contribute to the dynamic AP response to CSP (Sakamoto et al., 2015). In humans, the gain of the transfer function from AP to SNA and that from SNA to AP were calculated using closed-loop data (Ando et al., 1997). While the results indicate the derivative characteristics of the neural arc and the low-pass characteristics of the peripheral arc, further research is required regarding the accuracy of those gain estimations, as discussed in section Closed-Loop Analysis.

Animal Models of Cardiovascular Diseases

Open-loop dynamic characteristics of the carotid sinus baroreflex in animal models of cardiovascular diseases are briefly reviewed. In a rat model of chronic heart failure following myocardial infarction, the baroreflex-mediated dynamic AP regulation was depressed in both the magnitude and response speed, mainly due to the attenuation of the dynamic gain in the peripheral arc (Kawada et al., 2010). The depressed dynamic AP regulation may partly explain why non-compliance with salt and water restriction easily leads to acute decompensation even in stable cardiac patients (Lepage, 2008). Spontaneously hypertensive rats showed well-preserved dynamic characteristics of AP regulation compared with normotensive rats despite having significantly higher baseline AP (Kawada et al., 2011). Hence, changes in the baroreflex dynamic characteristics are not generally predictable from changes in static characteristics of the AP regulation, such as that determined from an inverse sigmoidal relationship between input and output pressures (Sata et al., 2015). In a streptozotocin-induced rat model of type 1 diabetes, f_{c2} (the corner frequency for the high-cut characteristics in the neural arc) was lower and ζ (the damping ratio in the peripheral arc) was larger compared with normal rats (Kawada et al., 2018), which suggests derangements in both the neural and peripheral arcs. Depending on types of diseases, functions of the neural and peripheral arcs are differently affected, though we do not have corresponding human data. An assessment of the baroreflex dynamic characteristics in humans will enable the creation of human baroreflex models in health and diseases. The human baroreflex models would add a component of autonomic control to a so-called "digital twin" of a patient, on which we will be able to tailor treatment strategies (Corral-Acero et al., 2020).

CLOSED-LOOP ANALYSIS

Although the open-loop analysis of the arterial baroreflex is straightforward, it requires baroreceptor isolation preparation and cannot be used in human studies. A closed-loop analysis of the baroreflex dynamic characteristics is a necessary study direction. We examined whether the system dynamic characteristics obtained from closed-loop analysis conformed to those obtained by open-loop analysis.

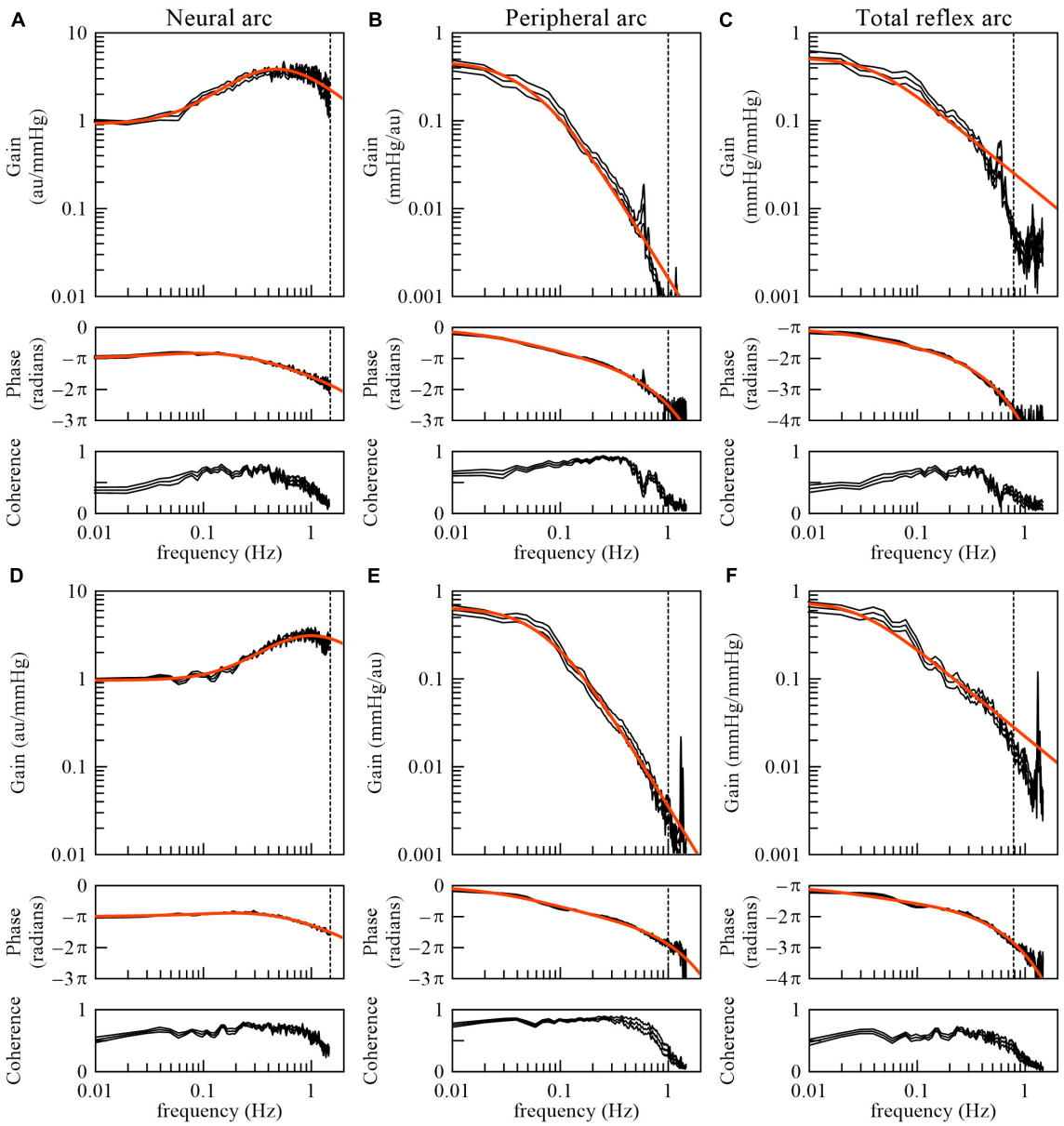

FIGURE 10 | The neural arc **(A)**, peripheral arc **(B)**, and total reflex arc **(C)** transfer functions pooled from 12 Japanese white rabbits. In panels **(B)** and **(C)**, the transfer gain shows a peak at artificial ventilation frequency (35 cycles/min = 0.58 Hz). The neural arc **(D)**, peripheral arc **(E)**, and total reflex arc **(F)** transfer functions pooled from 12 Wistar-Kyoto rats. In panels **(E)** and **(F)**, the transfer gain shows a peak at artificial ventilation frequency (80 cycles/min = 1.33 Hz). The black lines represent mean ± SE values. The smooth orange lines indicate mathematical models fit to the averaged transfer functions. The vertical dotted lines indicate the upper limit of the frequency range used for fitting. The total reflex arc transfer function was modeled with a first-order low-pass filter with pure delay. au, arbitrary units.

Why Does Open-Loop Transfer Function Analysis Not Work Correctly on Closed-Loop Data?

Numerical Consideration on Open-Loop Analysis Applied to Closed-Loop Data When Endogenous Noises Exist in Both the Neural and Peripheral Arcs

Figure 9B illustrates a block diagram of the arterial baroreflex under closed-loop conditions. N_c and N_p represent the unknown central and peripheral noise, respectively. The relationship between AP and SNA through the neural arc is described in the frequency domain as

$$SNA(f) = H1(f)AP(f) + N_c(f) \tag{4.1.1}$$

The relationship between SNA and AP through the peripheral arc is described as

$$AP(f) = H2(f)SNA(f) + N_p(f) \tag{4.1.2}$$

Why does conventional open-loop transfer function analysis not work correctly on these data? Let us treat AP and SNA as the input and output signals, respectively, to estimate the neural arc transfer function. The ensemble average of the cross spectra between terms of Eq. 4.1.1 and AP yields

$$E\left[SNA \cdot AP^*\right] = H1E\left[AP \cdot AP^*\right] + E\left[N_c \cdot AP^*\right] \quad (4.1.3)$$

The description of the frequency is omitted for the sake of brevity. The center dot denotes the multiplication of two complex values (at each frequency) in this article. Since H1 represents the system characteristics of the neural arc and is assumed to be time-invariant during the observation period, it is placed outside the ensemble averaging operation. Under baroreflex closed-loop conditions, $\boldsymbol{E}[N_c \cdot AP^*]$ does not diminish asymptotically because N_c affects AP through the peripheral arc (the green arrows in **Figure 9B**). Hence, the following equation, which ignores $\boldsymbol{E}[N_c \cdot AP^*]$, yields a biased estimation of H1:

$$H1_{biased} = \frac{E\left[SNA \cdot AP^*\right]}{E\left[AP \cdot AP^*\right]} \quad (4.1.4)$$

The same argument holds for estimating the peripheral arc transfer function under the baroreflex closed-loop conditions. When calculating ensemble averages of the cross spectra between terms of Eq. 4.1.2 and SNA, $\boldsymbol{E}[N_p \cdot SNA^*]$ does not disappear because N_p inevitably affects SNA through the neural arc (the red arrows in **Figure 9B**). Hence, the following equation, which ignores $\boldsymbol{E}[N_p \cdot SNA^*]$, also yields a biased estimation of H2:

$$H2_{biased} = \frac{E\left[AP \cdot SNA^*\right]}{E\left[SNA \cdot SNA^*\right]} \quad (4.1.5)$$

Numerical Consideration on Open-Loop Analysis Applied to Closed-Loop Data When Endogenous Noise Exists Only in the Neural or Peripheral Arc

When N_p is absent and N_c alone activates the baroreflex system, the input-output relationship through the peripheral arc becomes

$$AP(f) = H2(f)SNA(f) \quad (4.1.6)$$

Calculating ensemble averages of the cross spectra between terms of Eq. 4.1.6 and SNA yields

$$E\left[AP \cdot SNA^*\right] = H2E\left[SNA \cdot SNA^*\right] \quad (4.1.7)$$

Since $N_p = 0$, the estimation of H2 using the right-hand side of Eq. 4.1.5 is not biased in this case:

$$H2 = \frac{E\left[AP \cdot SNA^*\right]}{E\left[SNA \cdot SNA^*\right]} \quad (4.1.8)$$

Next, calculating ensemble averages of the cross spectra between terms of Eq. 4.1.6 and AP yields

$$E\left[AP \cdot AP^*\right] = H2E\left[SNA \cdot AP^*\right] \quad (4.1.9)$$

Comparing Eq. 4.1.9 with Eq. 4.1.4, we have

$$H1_{biased} = \frac{E\left[SNA \cdot AP^*\right]}{E\left[AP \cdot AP^*\right]} = \frac{1}{H2} \quad (4.1.10)$$

Hence, $H1_{biased}$ is an inverse of H2 and does not reflect H1 at all. To summarize, when only N_c exists, H2 can be estimated accurately, but $H1_{biased}$ simply returns an inverse of H2 regardless of the profile of H1. Conversely, when only N_p exists, H1 can be estimated accurately, but $H2_{biased}$ returns an inverse of H1. In the actual datasets, the relative accuracy of $H1_{biased}$ and $H2_{biased}$ depends on the relative magnitude of N_c and N_p (Kamiya et al., 2011).

Erroneous Application of Open-Loop Analysis to Closed-Loop Data

The sample data file "rabbit2-vx.dat" contains SNA and AP signals obtained from an anesthetized rabbit after vagotomy but before isolating the carotid sinus baroreceptor regions. Hence, the carotid sinus baroreflex operated as a closed-loop feedback system. **Figure 11** illustrates the results of an erroneous application of the conventional open-loop analysis to the closed-loop data, which was derived from the following codes:

```
A = recread('c:/SampleData/ rabbit2-vx.dat', 4);
B = recresample(A, 20);
[H1b C1b] = calctf(B, [3 2]); [H2b C2b] = calctf(B, [2 3]);
figure, subplot(1, 2, 1), tfplot(H1b, C1b, 'r'); subplot(1, 2, 2),
        tfplot(H2b, C2b, 'r');
```

In the gain plots, $H1_b$ and $H2_b$ roughly captured the derivative characteristics of the neural arc and the low-pass characteristics of the peripheral arc, respectively. However, the phase plot of $H1_b$ was convex downward rather than upward in the frequency range from 0.01 to 0.5 Hz. Numerically, the phase of the transfer function is derived from the cross spectra in the numerator of the transfer function calculation because the input power spectra in the denominator are real-valued. For the application of the conventional open-loop transfer function analysis to the closed-loop data, the phase of $H1_b$ was derived from $\boldsymbol{E}[SNA \cdot AP^*]$ (Eq. 4.1.4), whereas the phase of $H2_b$ was derived from $\boldsymbol{E}[AP \cdot SNA^*]$ (Eq. 4.1.5), which is $(\boldsymbol{E}[SNA \cdot AP^*])^*$. Because angle(X) = −angle(X*), there is a fixed relation of angle($H1_b$) = −angle($H2_b$). Hence, the phase plots in **Figure 11** cannot be simultaneously correct for $H1_b$ and $H2_b$ over the entire frequency range. This means that gain plots cannot be simultaneously correct for $H1_b$ and $H2_b$, either, because gain and phase are inseparable quantity of a transfer function. We cannot tell about the causality between SNA and AP from the results of the conventional open-loop analysis applied to the closed-loop data. As a numerical consequence (Eq. 3.2.2), $C1_b$ equals $C2_b$.

When the rabbit is under conscious conditions, the magnitudes of N_c and N_p and their balance may be different from those under anesthetized conditions. The sample data file "rabbit3-awake.dat" contains SNA and AP signals obtained from a conscious rabbit sitting in a small box. The SNA was recorded from a branch of the renal nerve via a pair of stainless-steel wire electrodes implanted using a sterile procedure a few days before. The AP was measured via a catheter inserted into the central ear artery under local anesthesia. The carotid sinus baroreceptor regions and the vagal and aortic depressor nerves were kept intact. The result of an erroneous application of the conventional open-loop analysis to the closed-loop data is

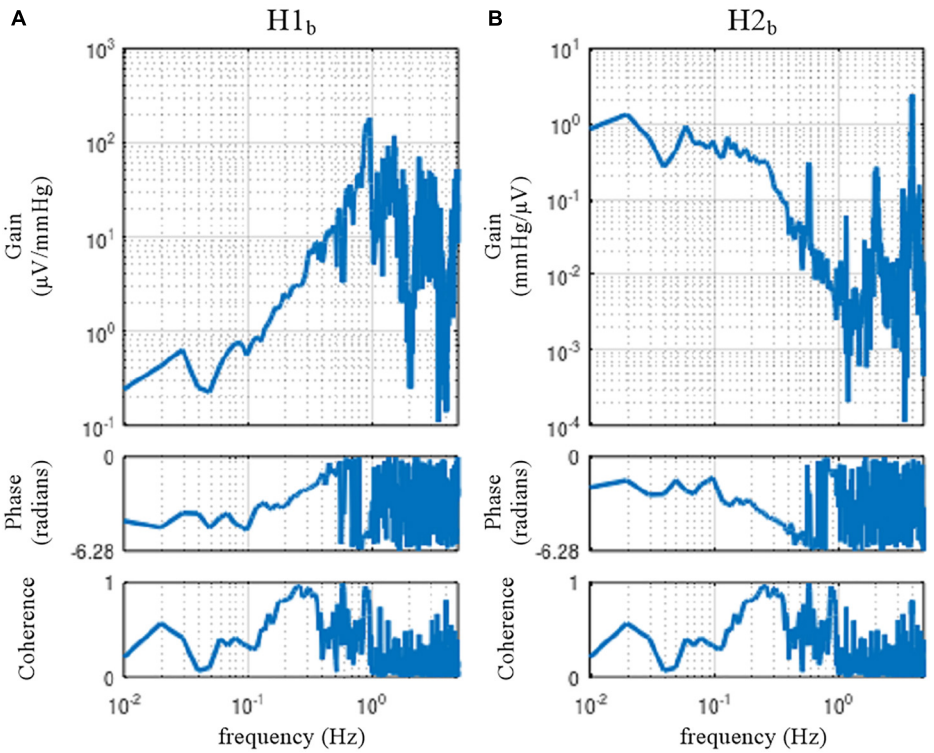

FIGURE 11 | The neural arc **(A)** and peripheral arc **(B)** transfer functions as estimated from an erroneous application of conventional open-loop analysis to the closed-loop data obtained from an anesthetized rabbit. $H1_b$ and $H2_b$ were derived from Eqs. 4.1.4 and 4.1.5, respectively. A fixed relation of angle($H1_b$) = –angle($H2_b$) was observed. $C1_b$ equals $C2_b$.

shown in **Figure 12**. Although we expected that the situations of the identifiability of the system dynamic characteristics would differ between conscious and anesthetized conditions, **Figure 12** seems qualitatively similar to **Figure 11**, despite the differences in the experimental preparations (intact vs. sectioned vagi, the recording of renal vs. cardiac sympathetic nerve).

Closed-Loop Identification With Exogenous Pressure Perturbation

Numerical Consideration

Figure 13 illustrates a block diagram of the arterial baroreflex under closed-loop conditions with an exogenous pressure perturbation. V and H_v denote the command of the exogenous pressure perturbation and the transfer function from V to AP, respectively. The relationship between SNA and AP through the peripheral arc is described in the frequency domain as

$$AP(f) = H2(f)SNA(f) + N_p(f) + H_v(f)V(f) \tag{4.2.1}$$

For the closed-loop identification, calculating ensemble averages of the cross spectra between terms of Eq. 4.1.1 and V yields

$$E\left[SNA \cdot V^*\right] = H1E\left[AP \cdot V^*\right] + E\left[N_c \cdot V^*\right] \tag{4.2.2}$$

When V is a white noise signal, N_c and V become statistically independent, and $\boldsymbol{E}[N_c \cdot V^*]$ asymptotically diminishes. Hence, the neural arc transfer function can be estimated from the following equation:

$$H1 = \frac{E\left[SNA \cdot V^*\right]}{E\left[AP \cdot V^*\right]} \tag{4.2.3}$$

Once H1 is estimated, N_c can be estimated from Eq. 4.1.1 as

$$N_c = SNA - H1 \cdot AP \tag{4.2.4}$$

Calculating ensemble averages of the cross spectra between terms of Eq. 4.2.1 and N_c yields

$$E\left[AP \cdot N_c^*\right] = H2E\left[SNA \cdot N_c^*\right] + E\left[N_p \cdot N_c^*\right] + H_vE\left[V \cdot N_c^*\right] \tag{4.2.5}$$

In the above equation, $\boldsymbol{E}[N_p \cdot N_c{}^*]$ asymptotically diminishes because all linear couplings between SNA and AP are expressed by H1 and H2 in the diagram shown in **Figure 13**, and N_p and N_c are linearly uncorrelated, by definition. The last term, $\boldsymbol{E}[V \cdot N_c{}^*]$, also asymptotically diminishes when V is a white noise signal. Accordingly, the peripheral arc transfer function can be estimated from the following equation:

$$H2 = \frac{E\left[AP \cdot N_c^*\right]}{E\left[SNA \cdot N_c^*\right]} \tag{4.2.6}$$

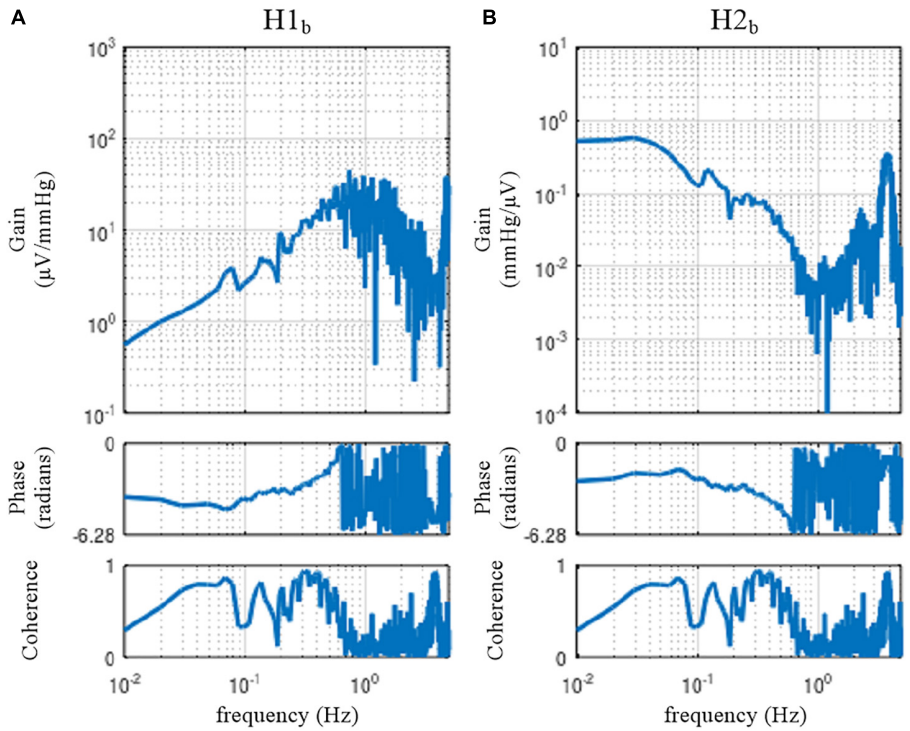

FIGURE 12 | The neural arc **(A)** and peripheral arc **(B)** transfer functions estimated by an erroneous application of conventional open-loop analysis to the closed-loop data obtained from a conscious rabbit. $H1_b$ and $H2_b$ were derived from Eqs. 4.1.4 and 4.1.5, respectively. There was a fixed relation of angle($H1_b$) = –angle($H2_b$). $C1_b$ equals $C2_b$.

It should be noted that the reliability of the H2 estimation depends on the properties of N_c. Inputs from higher brain centers generate N_c, as evidenced by the variation of SNA under a fixed CSP (Moslehpour et al., 2016b). However, if there is not enough power of N_c in a certain frequency range, the H2 estimation becomes unreliable because of divisions by small numbers. For calculating H2, a direct estimation of N_c is not necessary. Substituting N_c in Eq. 4.2.6 with Eq. 4.2.4 yields

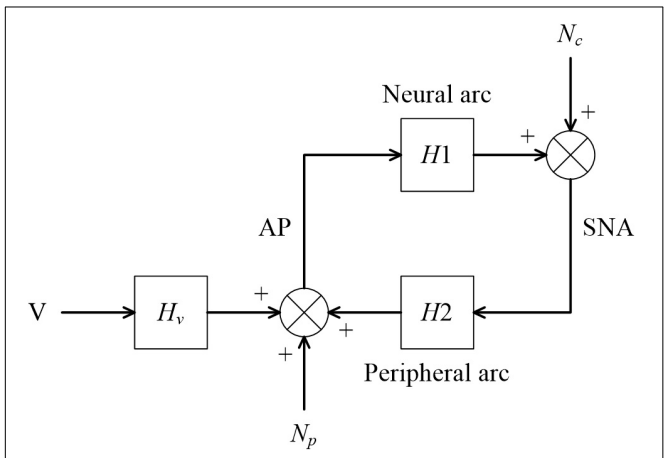

FIGURE 13 | A conceptual block diagram describing the closed-loop identification of the carotid sinus baroreflex using an exogenous pressure perturbation. H1 and H2 represent the linear transfer function of the neural and peripheral arcs, respectively. V and H_v represent the command for the exogenous pressure perturbation and the transfer function from the command signal to arterial pressure (AP), respectively. N_c, unknown central noise; N_p, unknown peripheral noise; SNA, sympathetic nerve activity.

$$H2 = \frac{E\left[AP \cdot (SNA - H1 \cdot AP)^*\right]}{E\left[SNA \cdot (SNA - H1 \cdot AP)^*\right]} = \frac{E\left[AP \cdot SNA^*\right] - H1^* E\left[AP \cdot AP^*\right]}{E\left[SNA \cdot SNA^*\right] - H1^* \left(E\left[AP \cdot SNA^*\right]\right)^*} \quad (4.2.7)$$

Application of Closed-Loop Identification

The sample data file "rabbit4-closed.dat" contains SNA and AP signals during an exogenous pressure perturbation induced by blood withdrawal and infusion obtained in an anesthetized and vagotomized rabbit. **Figure 14** depicts the 10-Hz resampled data of the whole recording. The first channel represents the command signal for blood infusion (a positive value) and withdrawal (a negative value). The command was changed according to a binary white noise signal with a switching interval of 1 s. The second and third channels represent SNA and AP signals, respectively. In the fourth channel, HR showed a decreasing trend in this example.

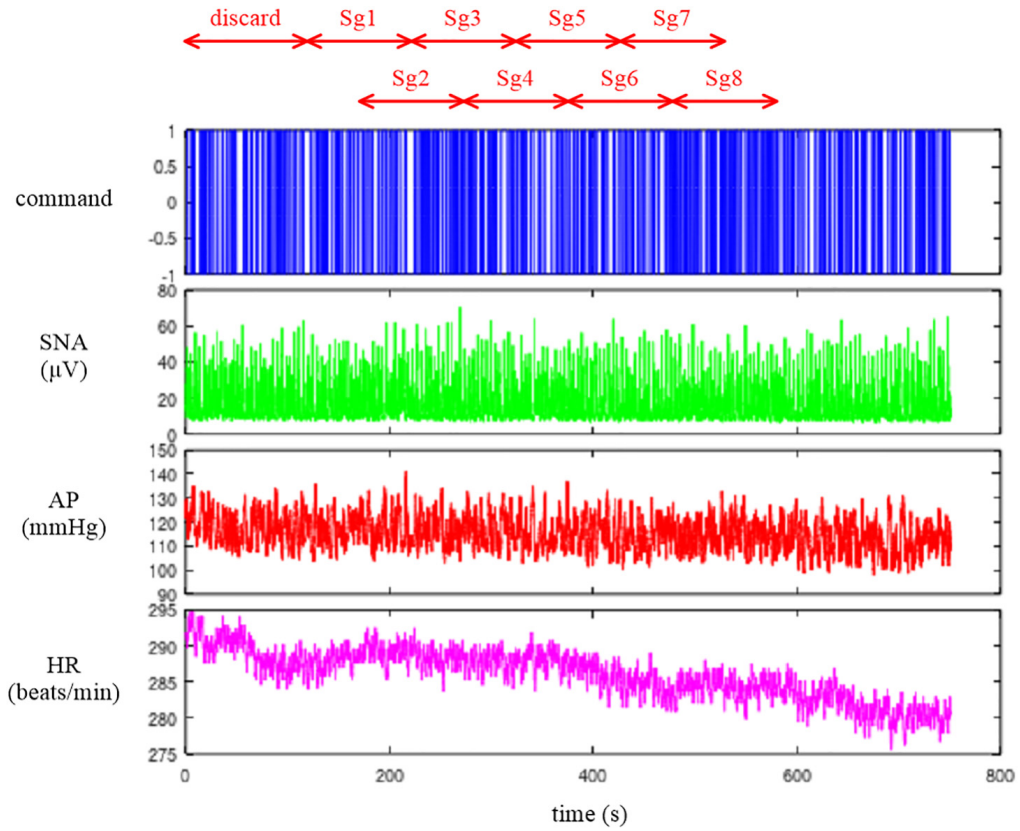

FIGURE 14 | Time series of a command signal for an exogenous pressure perturbation, sympathetic nerve activity (SNA), arterial pressure (AP), and heart rate (HR) after 10-Hz resampling. The data from the first 120 s were discarded to analyze the stationary portion of the data. Sg1 through Sg8 denote the half-overlapping segments for the closed-loop transfer function analysis.

Figure 15 illustrates the results of a closed-loop identification, obtained from the following codes:

```
A = recread('c:/SampleData\rabbit4-closed.dat', 4);
B = recresample(A, 20); figure, recplot(B, 10);
[H1c H2c] = opeclo(B, [1 3 2]);
figure, subplot(1, 2, 1), tfplot(H1c, 'r'); subplot(1, 2, 2),
        tfplot(H2c, 'r');
```

The user-defined function **opeclo** calculates the open-loop transfer functions from the closed-loop data with an exogenous pressure perturbation. The second argument of **opeclo** specifies the channels in the following order: the command signal, the AP signal that is directly affected by the exogenous perturbation, and the SNA signal. In **Figure 15**, the estimated $H1_c$ and $H2_c$ captured the derivative and low-pass characteristics, respectively. The phase plot of $H1_c$ revealed the out-of-phase relationship with a slightly convex-upward shape. The phase plot of $H2_c$ showed that the phase approached 0 radians at the lowest frequency and delayed with increasing frequency. In contrast to **Figures 11**, **12**, the phases of $H1_c$ and $H2_c$ did not show a fixed relation of angle($H1_c$) = −angle($H2_c$). However, the estimation of $H1_c$ in the frequency range above 0.5 Hz was more dispersed than that derived from the open-loop experiment (**Figure 3**). This is partly because the switching interval for the blood infusion and withdrawal was 1 s, and the input power of the exogenous pressure perturbation decreased in the frequency range above 0.5 Hz. The estimation of $H2_c$ in the lower frequency range was more dispersed than that derived from the open-loop experiment (**Figure 4**). This result is partly because the estimation of $H2_c$ relies on the unknown endogenous noise component of SNA. There were no statistically significant differences between the transfer function parameters estimated via the closed-loop method and those estimated via the open-loop method in the same animals, excepting f_{c2} in the neural arc (Kawada et al., 1997). The parameter f_{c2} was not compared because the lack of input power in the higher frequency range hampered a reliable estimation of f_{c2} in the closed-loop method.

LIMITATIONS

First, we did not treat the cardiac branch of the arterial baroreflex partly because most of the data were obtained from anesthetized animals with vagotomy. The vagal branch exerts a rapid HR response compared with the sympathetic branch (Kawada et al., 2019). For the analysis of clinical data,

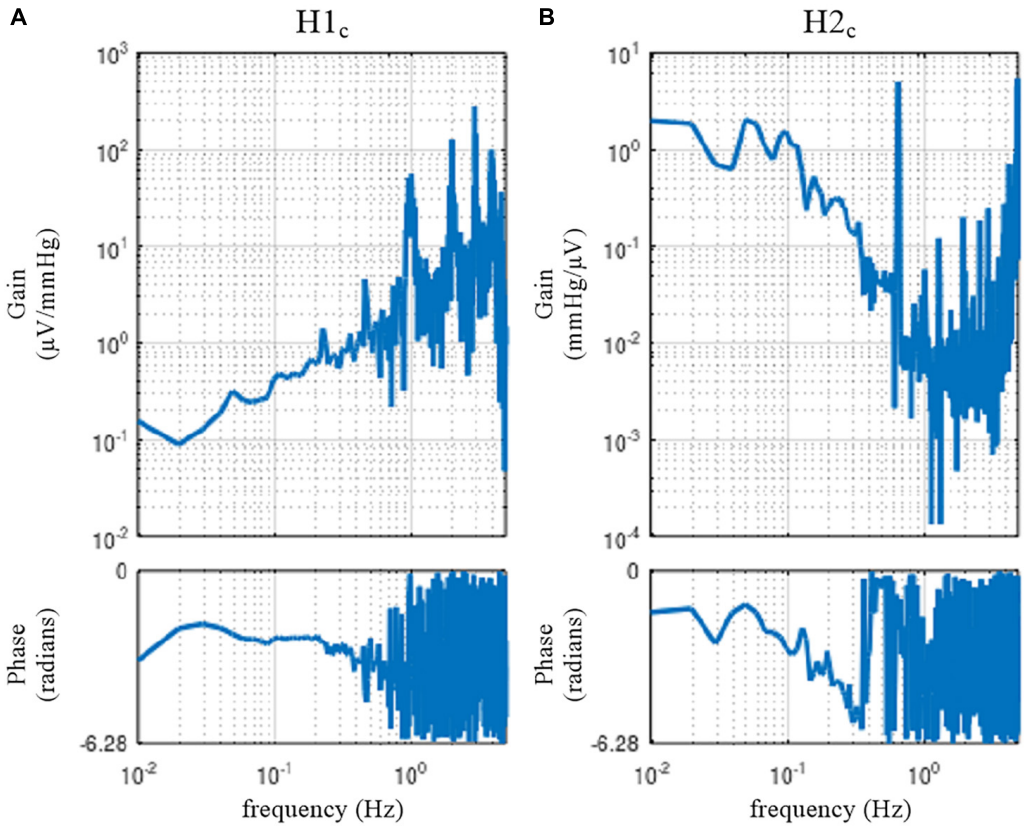

FIGURE 15 | The neural arc **(A)** and peripheral arc **(B)** transfer functions as estimated by a closed-loop identification method with an exogenous pressure perturbation by blood infusion and withdrawal. $H1_C$ and $H2_C$ were derived from Eqs. 4.2.3 and 4.2.6, respectively.

whether the dynamic properties of the cardiac branch can be estimated accurately under conditions with the intact vagi needs to be examined because cardiac vagal nerve activity predominantly regulates HR in humans under resting conditions (Hori and Okamoto, 2012).

Second, the AP regulation involves mechanisms other than the arterial baroreflex such as autoregulation and blood volume control. The autoregulation manifests in association with blood flow control. For instance, cerebral blood flow is autoregulated near constant over a wide pressure range, while it could be more pressure passive during low cardiac output conditions (Lie et al., 2021). The blood volume control by the kidneys is essential for long-term AP control. An open-loop analysis on the baroreflex-mediated AP changes and associated urine output function may provide a clue to connect the arterial baroreflex and the blood volume control (Kawada et al., 2020). Further studies are clearly required for an integrative understanding of the AP regulation.

CONCLUSION

Although there are many closed-loop identification studies, validation is made indirectly on the basis of the predictability of the output signal from the input signal. In this article, we compared the results of a closed-loop identification with the open-loop dynamic characteristics of the baroreflex system. Although the frequency-domain closed-loop identification employing an exogenous pressure perturbation was successful in separately assessing the transfer functions of the neural and peripheral arcs, there remains an issue of estimation accuracy in the higher frequency range of the neural arc and in the lower frequency range of the peripheral arc. Further efforts are required to identify open-loop dynamic characteristics of the arterial baroreflex system from closed-loop data. Alternatively, a priori knowledge about the open-loop dynamic characteristics of the arterial baroreflex system may be used to advance the assessment of baroreflex function under closed-loop conditions. In this regard, Mannoji et al. (2019) proposed that the ratio of power spectra of AP between two frequencies be used to derive an index of baroreflex gain. Clinical data demonstrated that aging steepens the slope of the AP power spectra, probably reflecting the deterioration of the arterial baroreflex in older subjects (Mano et al., 2021). The noninvasive nature of the AP power spectral analysis is an advantage of the method. On the other hand, information on the index of baroreflex gain alone is insufficient to construct a cardiovascular simulator that enables the prediction of dynamic AP changes in response to

interventions. Clinical application of closed-loop identification of baroreflex properties awaits further investigations.

DATA AVAILABILITY STATEMENT

The original contributions presented in the study are included in the article/supplementary material, further inquiries can be directed to the corresponding author/s.

ETHICS STATEMENT

The animal study was reviewed and approved by The Animal Subject Committee at the National Cerebral and Cardiovascular Center.

AUTHOR CONTRIBUTIONS

TK prepared the figures and drafted the manuscript. All authors discussed the contents of the manuscript, edited and revised the manuscript, and read and approved the final manuscript.

FUNDING

This study was partly supported by a Grant-in-Aid for Scientific Research (20K20622) and a grant from the Salt Science Research Foundation (No. 2125). Part of this work was carried out by the research grant from NTT Research. The authors confirm that the funders did not influence the study design, contents of the article, or selection of this journal.

REFERENCES

Ando, S., Dajani, H. R., and Floras, J. S. (1997). Frequency domain characteristics of muscle sympathetic nerve activity in heart failure and healthy humans. *Am. J. Physiol.* 273, R205–R212. doi: 10.1152/ajpregu.1997.273.1.R205

Bendat, J. S., and Piersol, A. G. (2010). *Random Data. Analysis and Measurement Procedures*. Hoboken, NJ: Wiley.

Chapleau, M. W., Hajduczok, G., and Abboud, F. M. (1989). Pulsatile activation of baroreceptors causes central facilitation of baroreflex. *Am. J. Physiol.* 256, H1735–H1741. doi: 10.1152/ajpheart.1989.256.6.H1735

Corral-Acero, J., Margara, F., Marciniak, M., Rodero, C., Loncaric, F., Feng, Y., et al. (2020). The 'Digital Twin' to enable the vision of precision cardiology. *Eur. Heart J.* 41, 4556–4564. doi: 10.1093/eurheartj/ehaa159

Hori, M., and Okamoto, H. (2012). Heart rate as a target of treatment of chronic heart failure. *J. Cardiol.* 60, 86–90. doi: 10.1016/j.jjcc.2012.06.013

Ikeda, Y., Kawada, T., Sugimachi, M., Kawaguchi, O., Shishido, T., Sato, T., et al. (1996). Neural arc of baroreflex optimizes dynamic pressure regulation in achieving both stability and quickness. *Am. J. Physiol.* 271, H882–H890. doi: 10.1152/ajpheart.1996.271.3.H882

Kamiya, A., Kawada, T., Shimizu, S., and Sugimachi, M. (2011). Closed-loop spontaneous baroreflex transfer function is inappropriate for system identification of neural arc but partly accurate for peripheral arc: predictability analysis. *J. Physiol.* 589, 1769–1790. doi: 10.1113/jphysiol.2011.203455

Kawada, T., Fujiki, N., and Hosomi, H. (1992). Systems analysis of the carotid sinus baroreflex system using a sum-of-sinusoidal input. *Jpn. J. Physiol.* 42, 15–34. doi: 10.2170/jjphysiol.42.15

Kawada, T., Hayama, Y., Nishikawa, T., Suehara, S., Sawada, S., Tanaka, T., et al. (2020). Open-loop analysis on sympathetically mediated arterial pressure and urine output responses in rats: effect of renal denervation. *J. Physiol. Sci.* 70, 32. doi: 10.1186/s12576-020-00759-w

Kawada, T., Li, M., Kamiya, A., Shimizu, S., Uemura, K., Yamamoto, H., et al. (2010). Open-loop dynamic and static characteristics of the carotid sinus baroreflex in rats with chronic heart failure after myocardial infarction. *J. Physiol. Sci.* 60, 283–298. doi: 10.1007/s12576-010-0096-9

Kawada, T., Shimizu, S., Hayama, Y., Yamamoto, H., Saku, K., Shishido, T., et al. (2018). Derangement of open-loop static and dynamic characteristics of the carotid sinus baroreflex in streptozotocin-induced type 1 diabetic rats. *Am. J. Physiol. Regul. Integr. Comp. Physiol.* 315, R553–R567. doi: 10.1152/ajpregu.00092.2018

Kawada, T., Shimizu, S., Kamiya, A., Sata, Y., Uemura, K., and Sugimachi, M. (2011). Dynamic characteristics of baroreflex neural and peripheral arcs are preserved in spontaneously hypertensive rats. *Am. J. Physiol. Regul. Integr. Comp. Physiol.* 300, R155–R165. doi: 10.1152/ajpregu.00540.2010

Kawada, T., Shimizu, S., Yamamoto, H., Miyamoto, T., Kamiya, A., Shishido, T., et al. (2017). Effects of different input pressure waveforms on the carotid sinus baroreflex-mediated sympathetic arterial pressure response in rats. *J. Appl. Physiol.* 123, 914–921. doi: 10.1152/japplphysiol.00354.2017

Kawada, T., Shishido, T., Inagaki, M., Tatewaki, T., Zheng, C., Yanagiya, Y., et al. (2001). Differential dynamic baroreflex regulation of cardiac and renal sympathetic nerve activities. *Am. J. Physiol. Heart Circ. Physiol.* 280, H1581–H1590. doi: 10.1152/ajpheart.2001.280.4.H1581

Kawada, T., and Sugimachi, M. (2016). Open-loop static and dynamic characteristics of the arterial baroreflex system in rabbits and rats. *J. Physiol. Sci.* 66, 15–41. doi: 10.1007/s12576-015-0412-5

Kawada, T., and Sugimachi, M. (2019). Linear and nonlinear analysis of the carotid sinus baroreflex dynamic characteristics. *Adv. Biomed. Eng.* 8, 110–123. doi: 10.14326/abe.8.110

Kawada, T., Sugimachi, M., Sato, T., Miyano, H., Shishido, T., Miyashita, H., et al. (1997). Closed-loop identification of carotid sinus baroreflex open-loop transfer characteristics in rabbits. *Am. J. Physiol.* 273, H1024–H1031. doi: 10.1152/ajpheart.1997.273.2.H1024

Kawada, T., Yamamoto, H., Hayama, Y., Nishikawa, T., Tanaka, K., and Sugimachi, M. (2019). Contrasting open-loop dynamic characetristics of sympathetic and vagal systems during baroreflex-mediated heart rate control in rats. *Am. J. Physiol.* 317, R879–R890. doi: 10.1152/ajpregu.00231.2019

Kawada, T., Zheng, C., Yanagiya, Y., Uemura, K., Miyamoto, T., Inagaki, M., et al. (2002). High-cut characteristics of the baroreflex neural arc preserve baroreflex gain against pulsatile pressure. *Am. J. Physiol. Heart Circ. Physiol.* 282, H1149–H1156. doi: 10.1152/ajpheart.00750.2001

Lepage, S. (2008). Acute decompensated heart failure. *Can. J. Cardiol* 24 (Suppl B):, 6B–8B. doi: 10.1016/s0828-282x(08)71022-5

Lie, S. L., Hisdal, J., and Høiseth, L. Ø (2021). Cerebral blood flow velocity during simultaneous changes in mean arterial pressure and cardiac output in healthy volunteers. *Eur. J. Appl. Physiol* 121, 2207–2217. doi: 10.1007/s00421-021-04693-6

Mannoji, H., Saku, K., Nishikawa, T., Tohyama, T., Kamada, K., Abe, K., et al. (2019). Estimation of the baroreflex total loop gain by the power spectral analysis of continuous arterial pressure recordings. *Am. J. Physiol. Heart Circ. Physiol.* 316, H828–H839. doi: 10.1152/ajpheart.00681.2018

Mano, J., Saku, K., Kinoshita, H., Mannoji, H., Kanaya, S., and Sunagawa, K. (2021). Aging steepens the slope of power spectrum density of 30-minute continuous blood pressure recording in healthy human subjects. *PLoS One* 16:e0248428. doi: 10.1371/journal.pone.0248428

Marmarelis, P. Z., and Marmarelis, V. Z. (1978). *Analysis of Physiological Systems: The White-Noise Approach*. New York, NY: Plenum.

Masuda, N., Ootsuka, Y., and Terui, N. (1992). Neurons in the caudal ventrolateral medulla mediate the somato-sympathetic inhibitory reflex response via GAVA receptors in the rostral ventrolateral medulla. *J. Auton. Nerv. Syst.* 40, 91–98. doi: 10.1016/0165-1838(92)90020-h

Moslehpour, M., Kawada, T., Sunagawa, K., Sugimachi, M., and Mukkamala, R. (2015). Nonlinear identification of the total baroreflex arc. *Am. J. Physiol. Regul. Integr. Comp. Physiol.* 309, R1479–R1489. doi: 10.1152/ajpregu.00278.2015

Moslehpour, M., Kawada, T., Sunagawa, K., Sugimachi, M., and Mukkamala, R. (2016a). Nonlinear identification of the total baroreflex arc: chronic

hypertension model. *Am. J. Physiol. Regul. Integr. Comp. Physiol.* 310, R819–R827. doi: 10.1152/ajpregu.00424.2015

Moslehpour, M., Kawada, T., Sunagawa, K., Sugimachi, M., and Mukkamala, R. (2016b). Nonlinear identification of the total baroreflex arc: higher-order nonlinearity. *Am. J. Physiol. Regul. Integr. Comp. Physiol.* 311, R994–R1003. doi: 10.1152/ajpregu.00101.2016

Nelder, J. A., and Mead, R. (1965). A simplex method for function minimization. *Comput. J.* 7, 308–313. doi: 10.1093/comjnl/7.4.308

Petiot, E., Barrès, C., Chapuis, B., and Julien, C. (2001). Frequency response of renal sympathetic nervous activity to aortic depressor nerve stimulation in the anaesthetized rat. *J. Physiol.* 537, 949–959. doi: 10.1111/j.1469-7793.2001.00949.x

Sakamoto, T., Kakino, T., Sakamoto, K., Tobushi, T., Tanaka, A., Saku, K., et al. (2015). Changes in vascular properties, not ventricular properties, predominantly contribute to baroreflex regulation of arterial pressure. *Am. J. Physiol. Heart Circ. Physiol.* 308, H49–H58. doi: 10.1152/ajpheart.00552.2014

Sata, Y., Kawada, T., Shimizu, S., Kamiya, A., Akiyama, T., and Sugimachi, M. (2015). Predominant role of neural arc in sympathetic baroreflex resetting of spontaneously hypertensive rats. *Circ. J.* 79, 592–599. doi: 10.1253/circj.CJ-14-1013

Conflict of Interest: The authors declare that the research was conducted in the absence of any commercial or financial relationships that could be construed as a potential conflict of interest.

Publisher's Note: All claims expressed in this article are solely those of the authors and do not necessarily represent those of their affiliated organizations, or those of the publisher, the editors and the reviewers. Any product that may be evaluated in this article, or claim that may be made by its manufacturer, is not guaranteed or endorsed by the publisher.

APPENDIX

Setup of GNU Octave

GNU Octave is available at https://www.gnu.org/software/octave/. The sample codes were tested using GNU Octave, version 6.2.0 (Local) (GUI). After installing the GNU Octave, the path for user function files (∗.m) needs to be added through the [SetPath] command in the [Edit] menu. Execute "demo_open" to generate **Figures 1–8**. Execute "demo_closed" to generate **Figures 11–15**.

Setup of Scilab

Scilab is available at https://www.scilab.org. The sample codes were tested using Scilab version 6.1.0 (64-bit) Desktop. Open "dynamic_step.zcos" in Xcos after initializing the parameters used in the block diagram (see section "Design of a Block Diagram").

frontiers in Neuroscience

METHODS
published: 27 September 2021
doi: 10.3389/fnins.2021.697582

Baroreflex Curve Fitting Using a WYSIWYG Boltzmann Sigmoidal Equation

Karsten Heusser[1], Ramona Heusser[2], Jens Jordan[1,3], Vasile Urechie[4], André Diedrich[4] and Jens Tank[1]*

[1] Institute of Aerospace Medicine, German Aerospace Center, Cologne, Germany, [2] Immanuel Kant High School, Wilthen, Germany, [3] University of Cologne, Cologne, Germany, [4] Division of Clinical Pharmacology, Department of Medicine, Autonomic Dysfunction Center, Vanderbilt University Medical Center, Nashville, TN, United States

Arterial baroreflex assessment using vasoactive substances enables investigators to collect data pairs over a wide range of blood pressures and reflex reactions. These data pairs relate intervals between heartbeats or sympathetic neural activity to blood pressure values. In an X-Y plot the data points scatter around a sigmoidal curve. After fitting the parameters of a sigmoidal function to the data, the graph's characteristics represent a rather comprehensive quantitative reflex description. Variants of the 4-parameter Boltzmann sigmoidal equation are widely used for curve fitting. Unfortunately, their 'slope parameters' do not correspond to the graph's actual slope which complicates the analysis and bears the risk of misreporting. We propose a modified Boltzmann sigmoidal function with preserved goodness of fit whose parameters are one-to-one equivalent to the sigmoidal curve's characteristics.

Keywords: baroreflex curve, baroreflex gain, baroreflex sensitivity, RR interval, muscle sympathetic nerve activity, sigmoidal curve fitting, Boltzmann sigmoidal equation

OPEN ACCESS

Edited by:
Alberto Porta,
University of Milan, Italy

Reviewed by:
Michal Javorka,
Comenius University, Slovakia
Vlasta Bari,
IRCCS Policlinico San Donato, Italy
Teodor Buchner,
Warsaw University of Technology, Poland

****Correspondence:***
Karsten Heusser
karsten.heusser@dlr.de
orcid.org/0000-0002-2571-5585

Specialty section:
This article was submitted to Autonomic Neuroscience, a section of the journal Frontiers in Neuroscience

Received: *19 April 2021*
Accepted: *31 August 2021*
Published: *27 September 2021*

Citation:
Heusser K, Heusser R, Jordan J, Urechie V, Diedrich A and Tank J (2021) Baroreflex Curve Fitting Using a WYSIWYG Boltzmann Sigmoidal Equation. Front. Neurosci. 15:697582. doi: 10.3389/fnins.2021.697582

INTRODUCTION

Baroreflexes play an important role in the regulation of the circulatory system. As negative feedback systems they stabilize arterial pressure around the so-called operating pressure. This feature is also known as blood pressure buffering to prevent large deviations from its setpoint. Often cardiovascular diseases are associated with impaired baroreflexes. Therefore, baroreflex quantification may be useful to assess the current state, progression, and therapeutic improvements of cardiovascular diseases. Moreover, precise baroreflex measurements can help unravel complex physiologic or pharmacologic mechanisms (Heusser et al., 2016).

Although there are numerous methods to evaluate baroreflex function they all share the same basic principle of relating the reflex response (output) to the stimulus intensity (input). Typically, systolic arterial pressure is taken as input and heartbeat interval (RR interval, RRI) as output. The quantitative relationship between these parameters is used to characterize the so-called cardiac or vagal or cardiovagal baroreflex. Baroreflex gain or sensitivity is the most reported index. Values range from virtually zero in patients with complete baroreflex failure (Heusser et al., 2005) up to 40 ms/mmHg in trained athletes (Baumert et al., 2006). In cardiovascular laboratories, investigators may be interested in baroreflex mechanisms over a wide range of blood pressures that does not only include the linear part of the stimulus–response relationship but also saturation and threshold

portions (Parati et al., 2000). Such data can be obtained by injection or infusion of the vasoactive substances sodium nitroprusside (vasodilator) and phenylephrine (vasoconstrictor). In an X-Y plot, data pairs relating RRI or sympathetic neural activity to blood pressure readings scatter around sigmoidal curves.

Logistic functions (Verhulst, 1838) are widely used for sigmoidal curve fitting, whose prototype was invented to describe population growth with saturation (**Figure 1**). This function has four characteristic values: Bottom = 0.0, Top = 1.0, and maximum Slope = 0.25 at Midrange = 0.0.

Most real data that follow a sigmoidal X-Y relationship have other characteristics than the prototypic logistic function. For example, as can be seen from the curve in **Figure 2**, RR intervals show asymptotic behavior against a lower and upper limit (Bottom and Top) of the baroreflex response which are different from 0.0 and 1.0 of Verhulst's logistic function. Likewise, the abscissa value of the central inflection point (Midrange) and the slope of the graph at that point (Slope) vary from Verhulst's values, 0.0 and 0.25, respectively. In 1972, Kent et al. proposed a generalized 4-parameter logistic function, often referred to as Boltzmann sigmoidal equation, to model the baroreflex relationship between systemic arterial and carotid sinus pressure (see Equation 1 in **Table 1**). Kent et al. used A1..A4 as parameter names. In the following, we will use the more informative terms [B]ottom, [T]op, [R]ange (= T–B), [S]lope, and [M]idrange (or V50). Numerous investigators have applied the equation in its original form or variants thereof for sigmoidal curve fitting to their two-dimensional data (**Table 2**). The usefulness of the method has been confirmed for decades. It should be particularly emphasized that all 4-parameter equation variants yield absolutely identical output after ideal fitting of the 4 parameters. In other words, after successful fitting of the equations' parameters to the same data their graphs would perfectly overlap. This statement applies to the traditional equations as well as our modified Equation 8 which will be presented in the Methods section.

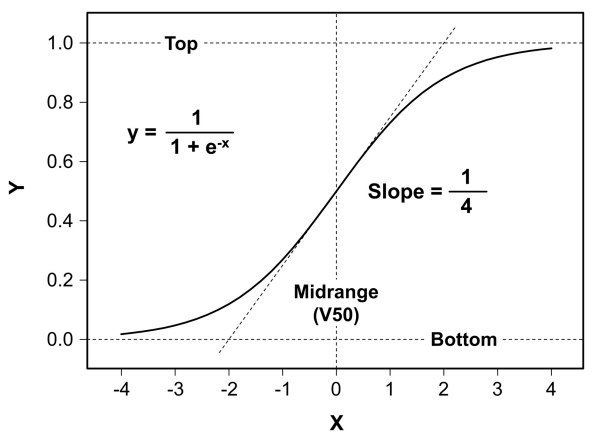

FIGURE 1 | Logistic function. The logistic function (without any parameters) represents the prototype of widely used functions for sigmoidal curve fitting to appropriate classes of two-dimensional experimental data. The graph has four characteristic values: Bottom = 0.0, Top = 1.0, maximum Slope = 0.25 at Midrange = 0.0, which is the abscissa of the curve's central inflection point.

Ishikawa et al. introduced a fifth parameter (Equation 6) to account for data asymmetry (Ishikawa et al., 1984). According to Ricketts and Head (Ricketts and Head, 1999) Sigmaplot (formerly SPSS now Systat Software Inc.) offers a very similar asymmetric sigmoidal curve fitting equation (Equation 7). The latter authors propose their own asymmetric function (not shown).

The upper part of **Figure 2** shows the nomenclature related to functions by taking the example of the Boltzmann sigmoidal function which has 4 parameters (2^{nd} column). The lower part of the figure shows example parameter values that have been obtained by parameter optimization (nonlinear curve fitting) to fit the example data as given in Results section "Curve fitting by means of the modified Boltzmann sigmoidal equation to experimental data." What all these 5 traditional equations have in common is that their Slope parameters (2^{nd} column) do *not* represent the slopes of the resultant graphs at their steepest portion at Midrange (see superposed curves in the 3^{rd} column) as naïve users might expect.

The misnomer has several drawbacks. First, there is the risk of using the fitting result 'as is' by users who are not aware of the mismatch. Second, users who know about the problem that the parameter represents a surrogate only, called, e.g., "gain coefficient" (do Carmo et al., 2007), "coefficient for the determination of gain" (Scrogin et al., 1994), "slope factor" (Shade et al., 1990), "slope coefficient" (Leitch et al., 1997; Kanbar et al., 2007), "slope parameter" (Devanne et al., 1997), "curvature parameter" (Schenberg et al., 1995), "curvature coefficient" (Cardoso et al., 2005), or "coefficient of curvature" (Leitch et al., 1997), have to determine the true value by further calculation. Third, curve fitting algorithms may need decent starting values or intervals for parameter optimization to successfully converge. Suitable presets for Bottom, Top or Range, and Midrange can be visually derived by the user from X-Y plots of the experimental data. Yet, the Slope parameter as visually estimated from the plots deviates from a useful preset. The latter needs further calculation which complicates the preparation step for curve fitting. Forth, scientific novices cannot readily understand why, after successful curve fitting, three of the four parameter values are equivalent to the graph's characteristics but Slope (baroreflex gain) is not.

Here we propose a modified Boltzmann sigmoidal equation that ensures one-to-one correspondence between the parameter names and the mathematical characteristics of the resultant graphs. The proposal will simplify sigmoidal curve fitting and, in particular, avoid misinterpretation and misreporting of baroreflex sensitivity.

METHODS

Equation 8 is our proposal for a modified Boltzmann sigmoidal equation:

Modified Boltzmann sigmoidal function

$$y = f(x) \quad B + \frac{T - B}{1 + e^{\frac{4S(M-x)}{T-B}}} \tag{8}$$

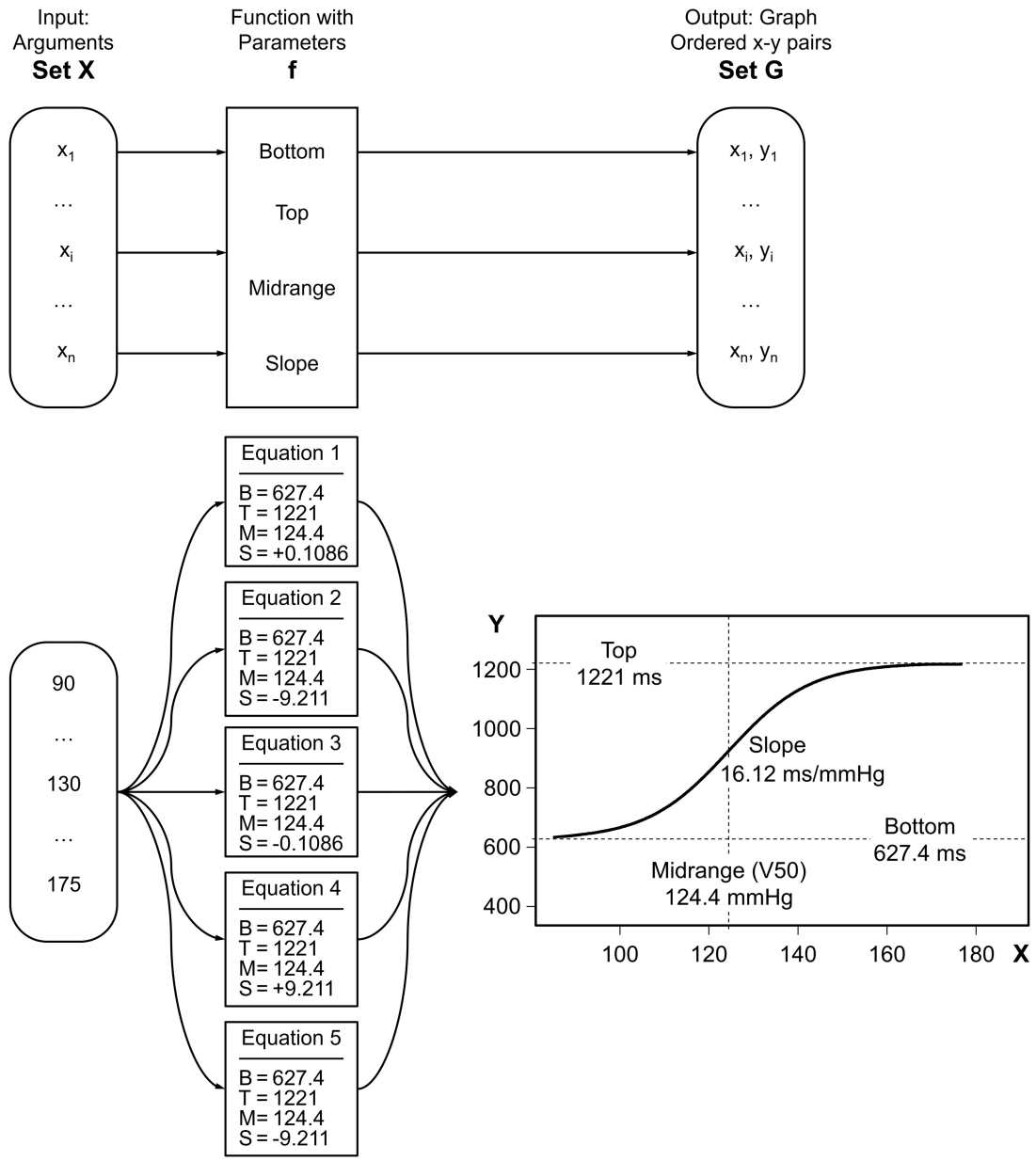

FIGURE 2 | Discrepancy between the equations' Slope parameters and their graphs' slopes. The five function boxes in the middle column of the figure implement the versions of the 4-parameter logistic equations in **Table 1**. The parameters [B]ottom, [T]op, and [M]idrange are identically set for all functions while [S]lope settings differ. However, the functions' *graphs* are identical. In other words, the curves representing them are exactly superposed (bottom right). Their identical Slopes at the inflection point at Midrange are 16.12. Hence, there is a discrepancy between [S]lope *parameter* settings in the functions (middle column) and the functions' *graphs* (on the right).

Linear form of the equation for usage in fitting tools

$$Y = B + (T - B)/\{1 + exp[4^*S^*(M - X)/(T - B)]\}$$

The range T–B can be replaced by R. Then, the four parameters would be B, R, M, and S. The formula is *not* meant to better fit the data; the goodness of fit is exactly the same as for the other 4-parameter variants of the formula (see superposed curves in **Figure 2** and report screenshots in **Figure 3**). Rather, our intention is to reconcile parameter naming and meaning. In the following, we are going to mathematically prove that the four parameters of the modified equation, namely [B]ottom, [T]op, [M]idrange, and [S]lope, exactly reflect the graph's characteristics. We will do so point by point with the implicit understanding that [S]lope $\neq 0$ and [R]ange = [T]op–[B]ottom > 0.0. Normally, the relationship between RR interval and blood pressure has a positive slope. In contrast, the relationships between heart rate or sympathetic nerve activity and blood pressure feature negative slopes.

TABLE 1 | Versions of 4- and 5-parameter Boltzmann sigmoidal equations.

Specifics	No explicit range parameter	Explicit range parameter
Equation 1: Exponent S(x–M)	$y = f(x) = B + \frac{T-B}{1+e^{S(x-M)}}$	$y = f(x) = B + \frac{R}{1+e^{S(x-M)}}$
Equation 2: Exponent (x–M)/S	$y = f(x) = B + \frac{T-B}{1+e^{\frac{(x-M)}{S}}}$	$y = f(x) = B + \frac{R}{1+e^{\frac{(x-M)}{S}}}$
Equation 3: Exponent S(M–x) = –S (x–M)	$y = f(x) = B + \frac{T-B}{1+e^{S(M-x)}}$	$y = f(x) = B + \frac{R}{1+e^{S(M-x)}}$
Equation 4: Exponent (M–x)/S	$y = f(x) = B + \frac{T-B}{1+e^{\frac{(M-x)}{S}}}$	$y = f(x) = B + \frac{R}{1+e^{\frac{(M-x)}{S}}}$
Equation 5: Absolute term T instead of B	$y = f(x) = T + \frac{B-T}{1+e^{\frac{(M-x)}{S}}}$	$y = f(x) = T + \frac{-R}{1+e^{\frac{(M-x)}{S}}}$
Equation 6: [A]symmetry parameter added		$y = f(x) = B + \frac{R}{\left(1+e^{S(x-M)}\right)^A}$
Equation 7: Sigmaplot's asymmetric function		$y = f(x) = B + \frac{R}{\left(1+e^{S(M-x)}\right)^A}$

TABLE 2 | Selected references referring to variants of the 4-parameter Boltzmann sigmoidal equation.

Equation 1	Kent et al., 1972; Dorward et al., 1985; Verberne et al., 1987; Rocchiccioli et al., 1989; Saad et al., 1989; Shade et al., 1990; Itoh and van den Buuse, 1991; Kawada et al., 1992; Martel et al., 1994; Veelken et al., 1994; Bartholomeusz and Widdop, 1995; Schenberg et al., 1995; Sagawa et al., 1997; He et al., 1999; Sampaio et al., 1999; Ma et al., 2002; Bealer, 2003; Miki et al., 2003; Cheng et al., 2004; Nagura et al., 2004; Sabharwal et al., 2004; McDowall and Dampney, 2006; do Carmo et al., 2007; Kanbar et al., 2007; Kawada et al., 2019
Equation 2	Mthombeni et al., 2012
Equation 3	Mthombeni et al., 2012
Equation 4	Leitch et al., 1997; B = 0: Devanne et al., 1997; Stewart et al., 2021
Equation 5	Cardoso et al., 2005

RESULTS

Sections "[B]ottom is the lower limit of the function" through "The [S]lope parameter's value really represents the slope of the modified Boltzmann sigmoidal curve at the inflection point" prove the correspondence between parameter naming and functional meaning. Captions comment the stepwise proof construction. Section "Threshold and saturation" derives calculation of threshold and saturation pressure. Section "Curve fitting by means of the modified Boltzmann sigmoidal equation to experimental data" exemplifies the usefulness of our proposed equation using real baroreflex data from healthy and diseased subjects, and in section "Practicing curve fitting by means of the modified Boltzmann sigmoidal curve" we invite the readers to test the method on simulated data.

[B]ottom Is the Lower Limit of the Function

With positive slopes the graphs asymptote to [B]ottom toward the left:

(1) $S > 0$, $T–B > 0$

a. $z = \frac{4S(M-x)}{T-B}, x \to -\infty \Longrightarrow z \to +\infty$

b. $\lim_{z\to+\infty} B + \frac{T-B}{1+e^z} = B + 0 = B$

c. $\lim_{x\to-\infty} B + \frac{T-B}{1+e^{\frac{4S(M-x)}{T-B}}} = B$

d. $\lim_{x\to-\infty} f(x) = B$

With negative slopes the graphs asymptote to [B]ottom toward the right:

(2) $S < 0$, $T–B > 0$

a. $z = \frac{4S(M-x)}{T-B}, x \to +\infty \Longrightarrow z \to +\infty$

b. $\lim_{z\to+\infty} B + \frac{T-B}{1+e^z} = B + 0 = B$

c. $\lim_{x\to+\infty} B + \frac{T-B}{1+e^{\frac{4S(M-x)}{T-B}}} = B$

d. $\lim_{x\to+\infty} f(x) = B$

[T]op Is the Upper Limit of the Function

With positive slopes the graphs asymptote to [T]op toward the right:

(3) $S > 0$, $T–B > 0$

a. $z = \frac{4S(M-x)}{T-B}, x \to +\infty \Longrightarrow z \to -\infty$

b. $\lim_{z\to-\infty} B + \frac{T-B}{1+e^z} = B + \frac{T-B}{1+0} = B + T - B = T$

c. $\lim_{x\to+\infty} B + \frac{T-B}{1+e^{\frac{4S(M-x)}{T-B}}} = T$

d. $\lim_{x\to+\infty} f(x) = T$

1	Boltzmann Eq. 1	
2	Best-fit values	
3	Bottom	627.4
4	Top	1221
5	V50	124.4
6	Slope	0.1086
7	Std. Error	
8	Bottom	60.97
9	Top	36.29
10	V50	1.895
11	Slope	0.02468
12	95% CI (profile likelihood)	
13	Bottom	457.4 to 707.9
14	Top	1164 to 1313
15	V50	119.6 to 127.8
16	Slope	0.06829 to 0.1552
17	Goodness of Fit	
18	Degrees of Freedom	504
19	R square	0.4684
20	Absolute Sum of Squares	12542489
21	Sy.x	157.8
22		
23	Number of points	
24	# of X values	508
25	# Y values analyzed	508

1	Boltzmann Eq. 4	
2	Best-fit values	
3	Bottom	627.4
4	Top	1221
5	V50	124.4
6	Slope	9.211
7	Std. Error	
8	Bottom	60.97
9	Top	36.29
10	V50	1.895
11	Slope	2.094
12	95% CI (profile likelihood)	
13	Bottom	457.4 to 707.9
14	Top	1164 to 1313
15	V50	119.6 to 127.8
16	Slope	6.444 to 14.64
17	Goodness of Fit	
18	Degrees of Freedom	504
19	R square	0.4684
20	Absolute Sum of Squares	12542489
21	Sy.x	157.8
22		
23	Number of points	
24	# of X values	508
25	# Y values analyzed	508

1	Boltzmann Eq. 8	
2	Best-fit values	
3	Bottom	627.4
4	Top	1221
5	V50	124.4
6	Slope	16.12
7	Std. Error	
8	Bottom	60.97
9	Top	36.29
10	V50	1.895
11	Slope	1.663
12	95% CI (profile likelihood)	
13	Bottom	457.4 to 707.9
14	Top	1164 to 1313
15	V50	119.6 to 127.8
16	Slope	13.44 to 19.52
17	Goodness of Fit	
18	Degrees of Freedom	504
19	R square	0.4684
20	Absolute Sum of Squares	12542489
21	Sy.x	157.8
22		
23	Number of points	
24	# of X values	508
25	# Y values analyzed	508

FIGURE 3 | Screenshots of GraphPad® Prism report tables after fitting different Boltzmann sigmoidal functions to real cardiac baroreflex data. We used the nonlinear curve fitting tool of GraphPad Prism (GraphPad, RRID:SCR_002798) to fit the four parameters of the Boltzmann sigmoidal functions related to Equation 1, Equation 4, and Equation 8 to experimentally obtained cardiac baroreflex data from a previous study (Heusser et al., 2016). The result tables report identical values for the optimized parameters Bottom, Top, and Midrange (V50). However, Slopes in line #6 are different. The only Slope that corresponds to the actual slope of the curve (see slope triangle in **Figure 4**: 16.12 ms/mmHg) is reported by our proposed WYSIWYG Equation 8 as can be expected according to Results section "The [S]lope parameter's value really represents the slope of the modified Boltzmann sigmoidal curve at the inflection point." Furthermore, the screenshots exemplify that, after parameter fitting, the resulting graphs are absolutely identical since the Goodness of Fit quantifiers are identical (lines #19–21) which is in agreement with the exactly overlapping curves in **Figure 4**. Sy.x is a variant of the standard deviation of the residuals that takes the degrees of freedom into account: Sy.x = sqrt [(sum of squared residuals) / (n – degrees of freedom)].

With negative slopes the graphs asymptote to [T]op toward the left:

(4) $S < 0,\ T\text{–}B > 0$

a. $z = \dfrac{4S(M-x)}{T-B}, x \to -\infty \Longrightarrow z \to -\infty$

b. $\lim\limits_{z\to-\infty} B + \dfrac{T-B}{1+e^{z}} = B + \dfrac{T-B}{1+0} = B + T - B = T$

c. $\lim\limits_{x\to-\infty} B + \dfrac{T-B}{1+e^{\frac{4S(M-x)}{T-B}}} = T$

d. $\lim\limits_{x\to-\infty} f(x) = T$

[M]idrange (V50) Is the Abscissa of an Inflection Point

Using the abbreviations

$$[R]\,ange = [T]\,op - [B]\,ottom \text{ and}$$

$$[G]\,radient = 4{*}\,[S]\,lope \to\ [S]\,lope = \frac{G}{4}$$

our proposed equation can be written as

$$f(x) = B + \frac{R}{1+e^{\frac{G(M-x)}{R}}} \tag{9}$$

To prove the assertion we need the first, second, and third derivatives. They are:

$$f'(x) = \frac{R(-1)\left(-\frac{G}{R}\right)e^{\frac{G(M-x)}{R}}}{\left(1+e^{\frac{G(M-x)}{R}}\right)^{2}} = \frac{G*\ e^{\frac{G(M-x)}{R}}}{\left(1+e^{\frac{G(M-x)}{R}}\right)^{2}} \tag{10}$$

$$f''(x) = \left(\frac{G^2}{R}\right)\left(\frac{e^{\frac{G(M-x)}{R}}\left[-1+e^{\frac{G(M-x)}{R}}\right]}{\left[1+e^{\frac{G(M-x)}{R}}\right]^{3}}\right) \tag{11}$$

$$f'''(x) = \left(\frac{-2G^3}{R^2}\right)\left(\frac{e^{\frac{G(M-x)}{R}}\left[1-e^{\frac{G(M-x)}{R}}+e^{\left(\frac{G(M-x)}{R}\right)^{2}}\right]}{\left[1+e^{\frac{G(M-x)}{R}}\right]^{4}}\right) \tag{12}$$

Below we outline that the necessary but not sufficient condition for [M]idrange to be the abscissa of an inflection point of the

modified Boltzmann sigmoidal equation, namely $f''(M) = 0$, is fulfilled. Note that [M]idrange is passed as x argument to Equation 11:

$$f''(M) = \left(\frac{G^2}{R}\right)\left(\frac{e^{\frac{G(M-M)}{R}}\left[-1+e^{\frac{G(M-M)}{R}}\right]}{\left[1+e^{\frac{G(M-M)}{R}}\right]^3}\right)$$

$$f''(M) = \left(\frac{G^2}{R}\right)\left(\frac{e^0\left[-1+e^0\right]}{\left[1+e^0\right]^3}\right) = \left(\frac{G^2}{R}\right)\left(\frac{1\ [-1+1\ ]}{[1+1\ ]^3}\right)$$
$$= \left(\frac{G^2}{R}\right)\left(\frac{0}{8}\right) = 0$$

Given that we disallow [G]radient, which is 4*[S]lope, to be zero, the sufficient condition for [M]idrange to be the abscissa of an inflection point, namely $f'''(M) \neq 0$, is fulfilled, too, as demonstrated below. Note that [M]idrange is passed as x argument to Equation 12:

$$f'''(M) = \left(\frac{-2G^3}{R^2}\right)\left(\frac{e^{\frac{G(M-M)}{R}}\left[1-e^{\frac{G(M-M)}{R}}+e^{\left(\frac{G(M-M)}{R}\right)^2}\right]}{\left[1+e^{\frac{G(M-M)}{R}}\right]^4}\right)$$

$$f'''(M) = \left(\frac{-2G^3}{R^2}\right)\left(\frac{e^0\left[1-e^0+e^{0^2}\right]}{\left[1+e^0\right]^4}\right)$$
$$= \left(\frac{-2G^3}{R^2}\right)\left(\frac{1\,[1-1+1]}{[1+1]^4}\right) = \left(\frac{-2G^3}{R^2}\right)\left(-\frac{1}{16}\right)$$

$$f'''(M) \neq 0$$

The Point at x = [M]idrange (V50) Is the Only Inflection Point of the Function

In order for our proposed function to have only one inflection point, $f''(x) = 0$ must be true for only one x value. To show that this is the case, we reuse Equation 11 while highlighting two crucial terms by enclosing them in curly brackets:

$$f''(x) = \left(\frac{G^2}{R}\right)\left(\frac{\left\{e^{\frac{G(M-x)}{R}}\right\}\left\{-1+e^{\frac{G(M-x)}{R}}\right\}}{\left[1+e^{\frac{G(M-x)}{R}}\right]^3}\right)$$

$f''(x)$ may become zero if at least one of the factors shown in curly brackets above becomes zero.

As e^z *for all* $z \in \mathbb{R}$ cannot be zero, we have to figure out how to zero the factor on the right:

$$-1+e^{\frac{G(M-x)}{R}} = 0 \Leftrightarrow e^{\frac{G(M-x)}{R}} = 1 \Rightarrow \frac{G(M-x)}{R} = 0$$
$$\Rightarrow \text{M–x} = 0$$
$$x = M$$

Calculating the function's value for x = [M]idrange using Equation 8

$$y = f(M) = B + \frac{T-B}{1+e^{\frac{4S(M-M)}{T-B}}} = B + \frac{T-B}{1+e^0}$$
$$= B + \frac{T-B}{2} = \frac{B+T}{2}$$

shows that it is halfway between the limits [B]ottom and [T]op in analogy to the logistic function prototype whose value is 0.5 at its inflection point (**Figure 1**).

The [S]lope Parameter's Value Really Represents the Slope of the Modified Boltzmann Sigmoidal Curve at the Inflection Point

Here we reuse the abbreviations and first derivative as outlined for Equation 9 in section "[M]idrange (V50) is the abscissa of an inflection point":

$$[R]\,ange = [T]\,op - [B]\,ottom \text{ and}$$
$$[G]\,radient = 4 * [S]\,lope \rightarrow [S]\,lope = \frac{G}{4}$$
$$f'(x) = \frac{G * e^{\frac{G(M-x)}{R}}}{\left(1+e^{\frac{G(M-x)}{R}}\right)^2}$$

and we pass [M]idrange as x argument to the first derivative:

$$f'(M) = \frac{G * e^{\frac{G(M-M)}{R}}}{\left(1+e^{\frac{G(M-M)}{R}}\right)^2} = \frac{G * e^0}{\left(1+e^0\right)^2} = \frac{G}{(1+1)^2} = \frac{G}{4}$$

$$f'(M) = S$$

Threshold and Saturation

Midrange is an abscissa-related curve characteristic. In our examples (**Figures 2**, **4**), it is the arterial pressure around which pressure disturbances are effectively buffered by the reflex response. Bottom and Top are distinct ordinate values that represent the upper and lower limits of the reflex response. Abscissa values corresponding to Bottom and Top could indicate the pressure range in which the reflex can operate. Unfortunately, such values do not exist for mathematical reasons, since sigmoidal functions show asymptotic behavior against Bottom and Top. The practical solution was to define Threshold and Saturation as the abscissas, where the sigmoidal curve crosses the 5 and 95% margins of the function's range (Range = Top – Bottom) (Sabharwal et al., 2004; McDowall and Dampney, 2006). Consequently, the ordinate interval related to Threshold and Saturation covers 90% of the reflex response range (**Figure 4**). The following derivation is guided by a corrective proposal (McDowall and Dampney, 2006).

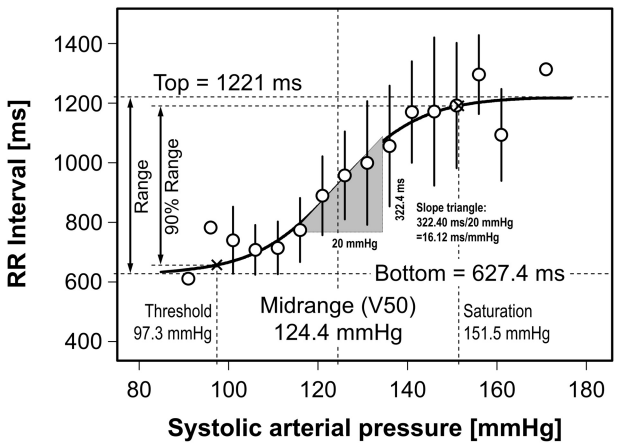

FIGURE 4 | Fitting different Boltzmann sigmoidal functions to real cardiac baroreflex data. Sigmoidal curve fitting to real data from a previous study (Heusser et al., 2016) and illustration of related terminology. After fitting the four parameters of three different equations to these data the resultant function curves overlap exactly. The slope triangle denotes the maximum slopes of the three sigmoidal curves at their inflection point. See Results "Curve fitting by means of the modified Boltzmann sigmoidal equation to experimental data" for more information.

To calculate Threshold and Saturation the first step is to rearrange our proposed Equation 8 to solve for x:

$$y = f(x) = B + \frac{T-B}{1+e^{\frac{4S(M-x)}{T-B}}} \Longrightarrow y - B = \frac{T-B}{1+e^{\frac{4S(M-x)}{T-B}}} \Longrightarrow$$

$$\frac{T-B}{y-B} = 1 + e^{\frac{4S(M-x)}{T-B}} \Longrightarrow \frac{T-B}{y-B} - 1 = e^{\frac{4S(M-x)}{T-B}} \Longrightarrow$$

$$\ln\left(\frac{T-B}{y-B} - 1\right) = \frac{4S(M-x)}{T-B} \Longrightarrow \frac{\ln\left(\frac{T-B}{y-B} - 1\right) * (T-B)}{4S} = M - x \Longrightarrow$$

$$x = M - \frac{\ln\left(\frac{T-B}{y-B} - 1\right) * (T-B)}{4S}$$

In the second step, we have to pass Bottom + 5% of Range as y argument:

$$x = M - \frac{\ln\left(\frac{T-B}{B+0.05(T-B)-B} - 1\right) * (T-B)}{4S}$$

$$x = M - \frac{\ln\left(\frac{T-B}{0.05(T-B)} - 1\right) * (T-B)}{4S}$$

$$x = M - \frac{\ln\left(\frac{1}{0.05} - 1\right) * (T-B)}{4S}$$

$$x = M - \frac{\ln(19) * (T-B)}{4S}$$

$$x = M - \frac{2.944 * (T-B)}{4S}$$

$$x = M - 0.7361 * \frac{T-B}{S}$$

In the third step, we have to pass Bottom + 95% of Range as y argument:

$$x = M - \frac{\ln\left(\frac{T-B}{B+0.95(T-B)-B} - 1\right) * (T-B)}{4S}$$

Intermediate steps as above.

$$x = M + 0.7361 * \frac{T-B}{S}$$

Result summary: Threshold and Saturation can be calculated using the formula

$$\boxed{x = Midrange \pm 0.7361 * Range/Slope}$$

Passing the data obtained by curve fitting (**Figure 4**)

$$x = 124.4\ mmHg \pm 0.7361 * 593.6\ ms/16.12\ ms/mmHg$$

$$x = 124.4\ mmHg \pm 0.7361 * 36.8\ mmHg$$

$$x = 124.4\ mmHg \pm 27.1\ mmHg$$

results in *Threshold pressure = 97.3 mmHg* and *Saturation pressure = 151.5 mmHg.*

Curve Fitting by Means of the Modified Boltzmann Sigmoidal Equation to Experimental Data

Cardiac baroreflex data have been experimentally obtained earlier in a double-blind, randomized, cross-over study in healthy subjects (Heusser et al., 2016). Stepwise infusions of the vasodilator sodium nitroprusside and the vasoconstrictor phenylephrine elicited blood pressures changes over a large range which is needed for baroreflex *curve* construction. Comparison of these curves after intake of placebo (see **Figure 4**) and ivabradine (not shown) challenged the so-called use-dependence of ivabradine and might explain its potential for untoward effects. Such an insight would not have been possible with spontaneous methods for baroreflex quantification.

The data points in **Figure 4** relate RR intervals and systolic pressures. They have been binned in 5-mmHg intervals. Bin means are represented as open circles and standard deviations as error bars. Circles related to bins with only one data point lack error bars. Curve fitting procedures were weighted according to the number of data points in each bin. As examples, three variants of the Boltzmann sigmoidal equation, namely Equations 1, 4 and 8 – the latter being our proposal – have been fitted to the data. All three resulting baroreflex curves exactly overlap. Consequently, the goodness of fit (see lines #19–21 in the screenshots in **Figure 3**) is identical for the three equations. The inserted slope triangle in **Figure 4**

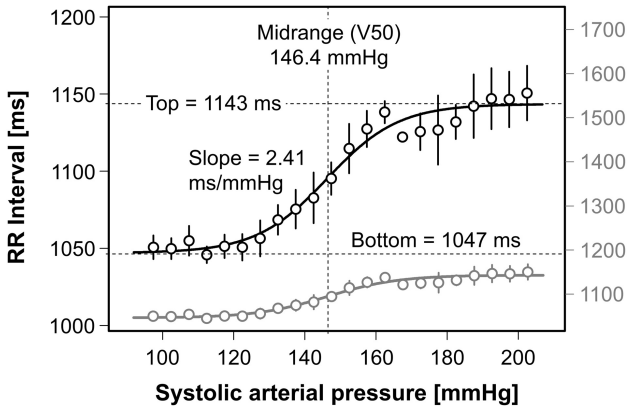

FIGURE 5 | Cardiac baroreflex curve in dysautonomia with marked reductions in response range and baroreflex sensitivity. Sigmoidal curve fitting using Equation 8 has been applied to real data from a patient with dysautonomia. The lower representation of the same data and fitting curve (gray) allows for visual comparison between healthy and diseased subjects because the resolution of the related ordinate on the right (gray) is similar to that in **Figure 4**. Note the marked reduction in response range (<100 ms) and baroreflex gain (2.41 ms/mmHg).

pertains to the maximum slope of the curves at their central inflection points. The lengths of the triangle's sides have been chosen for purely graphical reasons. Their ratio of 322.4 ms/20 mmHg = 16.12 ms/mmHg denotes the cardiovagal baroreflex sensitivity (baroreflex gain). In contrast, the Slope *parameters* reported after curve fitting using traditional versions of the Boltzmann equation (**Equation 1**: +0.1086 and **Equation 4**: +9.211) do *not* correspond to the curve's actual slope of +16.12 ms/mmHg (line #6 in the screenshots in **Figure 3**). In contrast, if the modified Boltzmann equation is used all 4 parameter values reflect the graph's characteristics properly. Hence, only the modified equation features 'what you see is what you get' (WYSIWYG).

The modified equation can also be used in patients with disorders of autonomic cardiovascular regulation. The data in **Figure 5** represent responses to low-dose injections of sodium nitroprusside (0.25 μg/kg) and phenylephrine (6.25 μg/74 kg) in such a patient. In healthy subjects, these test interventions would hardly change arterial pressure because of the buffering capacity of intact baroreflexes. Yet, in the patient, who also suffers from sympathetic vasoconstrictor incompetence (data not shown), the RR-interval response range is less than 100 ms despite a provoked change in systolic pressure of more than 100 mmHg. Moreover, the baroreflex gain (2.41 ms/mmHg) is much smaller than in healthy subjects. The gray data in **Figure 5** are scaled as in **Figure 4** for easy visual comparison.

Practicing Curve Fitting by Means of the Modified Boltzmann Sigmoidal Curve

Interested readers are referred to the Microsoft Excel spreadsheet in the **Supplementary Material**. The spreadsheet generates two-dimensional data (blood pressure + RR intervals) with adjustable noise. Equation 4 and Equation 8 have been chosen for sigmoidal curve fitting by means of the Excel Solver Add-in. We also suggest to imitate the solver's attempts to find a good fit by manual adjustments of the equation parameters. By doing so, the reader will realize that adjustments are more direct and easier to achieve when the *modified* Boltzmann equation is used.

DISCUSSION

Boltzmann sigmoidal equations are frequently used for nonlinear curve fitting to two-dimensional data. Their usefulness has been confirmed for decades. Commonly used forms of the equation have 4 parameters that represent the lower and upper limit or range of the data, the abscissa of the inflection point, and the slope at the latter. They are variants of the formula proposed by Kent et al. (Kent et al., 1972) to provide "a generalized mathematical model of the carotid sinus reflex which contains parameters with meaningful physiological interpretation." However, while three of the four parameters are directly related to the visible characteristics of the fitting curve, the slope parameter is not. Instead, the actual slope of the curve has to be determined separately. We proposed a modification of the Boltzmann sigmoidal function without this weakness to assist users expecting "what you see is what you get" (WYSIWYG). We mathematically proved that the function's parameters are one-to-one equivalent to the resultant curve's characteristics and successfully applied the method to real and artificial baroreflex data. The proposed equation looks slightly more complicated than conventional variants, but it offers some benefits. Once the user has entered the formula in his/her favorite fitting tool, the extra work is loaded onto the computer instead of the user. The traditional mismatch between the slope parameter and the graph's actual slope is resolved. After the fitting procedure has reached an acceptable result, the reported parameters can be taken as they are computed without any additional postprocessing. The goodness of fit is exactly the same as for the existing variants of the Boltzmann sigmoidal function.

Parameter identifiers like A1..A4 (Kent et al., 1972; Miki et al., 2003; McDowall and Dampney, 2006; do Carmo et al., 2007), P1..P4 (Saad et al., 1989; Itoh and van den Buuse, 1991; Kawada et al., 1992; Bartholomeusz and Widdop, 1995; Sampaio et al., 1999), m1..m4 (Bealer, 2003), a..d (Veelken et al., 1994; He et al., 1999), or a0..a3 (Stewart et al., 2021) are commonly used. More informative names are also assigned to some parameters (Verberne et al., 1987; Schenberg et al., 1995; Cardoso et al., 2005), e.g., BP50, HR_{min}, and HR_{max}. The slope parameter, however, continued to be a nomenclatural problem, e.g., "ß is the parameter that governs the slope of the barocurve, i.e., the gain of the baroreflex" (Schenberg et al., 1995) or "dx = a curvature coefficient that is independent of range" (Lee et al., 2002). We hope that our proposal will encourage researchers to embrace meaningful parameter names for sigmoidal curve fitting, including Slope without uncertainty. In our opinion, the more direct identifiers [B]ottom and [T]op as used in Equation 8 should be preferred over [B] and [R]ange, even if we used [R]ange in the Results Section for brevity. In so doing, parameter

presetting during the curve fitting preparation step, as often required by fitting tools, is simplified.

Our proposal has the same limitations as the conventional equations. For instance, data asymmetry is not considered (Ishikawa et al., 1984; Ricketts and Head, 1999), and the approach is not able to cope with baroreflex hysteresis (Studinger et al., 2007). The method can only be successfully applied if the blood pressure excursions are large enough to cover the nonlinear parts of the response. Moreover, there is an issue that may occur in vasoactor infusion protocols, namely that the operating pressure *after* stepwise increasing infusion of sodium nitroprusside may be lower than *before*. Thus, subsequent infusion of phenylephrine starts from lower pressures than with nitroprusside infusion. This 'fracture' in the baroreflex data needs to be handled before curve fitting to prevent slope overestimation. We used Microsoft Excel and the Excel Solver Add-in to illustrate the ideas behind this work using simulated data (see **Supplementary Material**) because this spreadsheet software is widely known (Microsoft Excel, RRID:SCR_016137). We do not claim particular suitability or superiority over other tools and did not compare curve fitting capabilities of different tools.

CONCLUSION

Using the proposed WYSIWYG variant of the 4-parameter Boltzmann sigmoidal function for nonlinear curve fitting yields exactly the same results as the traditional ones. In contrast, after successful curve fitting, the resultant value for the Slope parameter can be taken "as is" without any further calculation. Thus, usage of the WYSIWYG equation instead of traditional variants is less time-consuming, cumbersome, and error-prone. The equation has a sound mathematical background which promotes correct physiological interpretation of the results. We encourage the reader to benefit from these advantages.

DATA AVAILABILITY STATEMENT

The original contributions presented in the study are included in the article, further inquiries can be directed to the corresponding author.

ETHICS STATEMENT

The studies involving human participants were reviewed and approved by Ethics Committee of Hannover Medical School Study Code CCB-CRC-07-02, Vote #5223NM. The patients/participants provided their written informed consent to participate in this study.

AUTHOR CONTRIBUTIONS

KH contrived the method and wrote the manuscript draft. RH contrived the mathematical proofs. JJ and JT supplied physiological and clinical background. VU and AD checked maths. All authors contributed to the article and approved the submitted version.

SUPPLEMENTARY MATERIAL

The Supplementary Material for this article can be found online at: https://www.frontiersin.org/articles/10.3389/fnins.2021.697582/full#supplementary-material

REFERENCES

Bartholomeusz, B., and Widdop, R. (1995). Effect of acute and chronic treatment with the angiotensin II subtype 1 receptor antagonist EXP 3174 on baroreflex function in conscious spontaneously hypertensive rats. *J. Hypertens.* 13, 219–225. doi: 10.1097/00004872-199502000-00009

Baumert, M., Brechtel, L., Lock, J., Hermsdorf, M., Wolff, R., Baier, V., et al. (2006). Heart rate variability, blood pressure variability, and baroreflex sensitivity in overtrained athletes. *Clin. J. Sport Med.* 16, 412–417. doi: 10.1097/01.jsm.0000244610.34594.07

Bealer, S. L. (2003). Peripheral hyperosmolality reduces cardiac baroreflex sensitivity. *Auton. Neurosci.* 104, 25–31. doi: 10.1016/S1566-0702(02)00265-5

Cardoso, L. M., Pedrosa, M. L., Silva, M. E., Moraes, M. F. D., and Colombari, E. (2005). Baroreflex function in conscious rats submitted to iron overload. *Braz. J. Med. Biol. Res.* 38, 205–214. doi: 10.1590/S0100-879X2005000200008

Cheng, Y., Cohen, B., Oréa, V., Barrès, C., and Julien, C. (2004). Baroreflex control of renal sympathetic nerve activity and spontaneous rhythms at Mayer wave's frequency in rats. *Auton. Neurosci.* 111, 80–88. doi: 10.1016/j.autneu.2004.02.006

Devanne, H., Lavoie, B., and Capaday, C. (1997). Input-output properties and gain changes in the human corticospinal pathway. *Exp. Brain Res.* 114, 329–338. doi: 10.1007/PL00005641

do Carmo, J. M., Huber, D. A., Castania, J. A., Fazan, V. P., Fazan, R. Jr., and Salgado, H. C. (2007). Aortic depressor nerve function examined in diabetic rats by means of two different approaches. *J. Neurosci. Methods* 161, 17–22. doi: 10.1016/j.jneumeth.2006.10.002

Dorward, P. K., Riedel, W., Burke, S. L., Gipps, J., and Korner, P. (1985). The renal sympathetic baroreflex in the rabbit. Arterial and cardiac baroreceptor influences, resetting, and effect of anesthesia. *Circ. Res.* 57, 618–633. doi: 10.1161/01.RES.57.4.618

He, X.-R., Wang, W., Crofton, J. T., and Share, L. (1999). Effects of 17β-estradiol on the baroreflex control of sympathetic activity in conscious ovariectomized rats. *Am. J. Physiol. Regul. Integr. Comp. Physiol.* 277, R493–R498. doi: 10.1152/ajpregu.1999.277.2.R493

Heusser, K., Tank, J., Brinkmann, J., Schroeder, C., May, M., Grosshennig, A., et al. (2016). Preserved autonomic cardiovascular regulation with cardiac pacemaker inhibition: a crossover trial using high-fidelity cardiovascular phenotyping. *J. Am. Heart Assoc.* 5:e002674. doi: 10.1161/JAHA.115.002674

Heusser, K., Tank, J., Luft, F. C., and Jordan, J. (2005). Baroreflex failure. *Hypertension* 45, 834–839. doi: 10.1161/01.HYP.0000160355.93303.72

Ishikawa, N., Kallman, C. H., and Sagawa, K. (1984). Rabbit carotid sinus reflex under pentobarbital, urethan, and chloralose anesthesia. *Am. J. Physiol. Heart Circ. Physiol.* 246, H696–H701. doi: 10.1152/ajpheart.1984.246.5.H696

Itoh, S., and van den Buuse, M. (1991). Sensitization of baroreceptor reflex by central endothelin in conscious rats. *Am. J. Physiol. Heart Circ. Physiol.* 260, H1106–H1112. doi: 10.1152/ajpheart.1991.260.4.H1106

Kanbar, R., Oréa, V., Barres, C., and Julien, C. (2007). Baroreflex control of renal sympathetic nerve activity during air-jet stress in rats. *Am. J. Physiol. Regul. Integr. Comp. Physiol.* 292, R362–R367. doi: 10.1152/ajpregu.00413.2006

Kawada, T., Fujiki, N., and Hosomi, H. (1992). System analysis of the carotid sinus baroreflex system using a sum-of-sinusoidal input. *Jap. J. Physiol.* 42, 15–34. doi: 10.2170/jjphysiol.42.15

Kawada, T., Hayama, Y., Nishikawa, T., Yamamoto, H., Tanaka, K., and Sugimachi, M. (2019). Even weak vasoconstriction from rilmenidine can be unmasked in vivo by opening the baroreflex feedback loop. *Life Sci.* 219, 144–151. doi: 10.1016/j.lfs.2019.01.009

Kent, B. B., Drane, J. W., Blumenstein, B. B., and Manning, J. W. (1972). A mathematical model to assess changes in the baroreceptor reflex. *Cardiology* 57, 295–310. doi: 10.1159/000169528

Lee, J. S., Morrow, D., Andresen, M. C., and Chang, K. S. (2002). Isoflurane depresses baroreflex control of heart rate in decerebrate rats. *J. Am. Soc. Anesthesiol.* 96, 1214–1222. doi: 10.1097/00000542-200205000-00026

Leitch, J. W., Newling, R., Nyman, E., Cox, K., and Dear, K. (1997). Limited utility of the phenylephrine-nitroprusside sigmoid curve method of measuring baroreflex function after myocardial infarction. *Eur. J. Cardiovasc. Prev. Rehabil.* 4, 179–184. doi: 10.1177/174182679700400304

Ma, X., Abboud, F. M., and Chapleau, M. W. (2002). Analysis of afferent, central, and efferent components of the baroreceptor reflex in mice. *Am. J. Physiol. Regul. Integr. Comp. Physiol.* 283, R1033–R1040. doi: 10.1152/ajpregu.00768.2001

Martel, E., Lacolley, P., Champeroux, P., Brisac, A.-M., Laurent, S., Cuche, J.-L., et al. (1994). Early disturbance of baroreflex control of heart rate after tail suspension in conscious rats. *Am. J. Physiol. Heart Circ. Physiol.* 267, H2407–H2412. doi: 10.1152/ajpheart.1994.267.6.H2407

McDowall, L. M., and Dampney, R. A. (2006). Calculation of threshold and saturation points of sigmoidal baroreflex function curves. *Am. J. Physiol. Heart Circ. Physiol.* 291, H2003–H2007. doi: 10.1152/ajpheart.00219.2006

Miki, K., Yoshimoto, M., and Tanimizu, M. (2003). Acute shifts of baroreflex control of renal sympathetic nerve activity induced by treadmill exercise in rats. *J. Physiol.* 548, 313–322. doi: 10.1113/jphysiol.2002.033050

Mthombeni, N. H., Mpenyana-Monyatsi, L., Onyango, M. S., and Momba, M. N. (2012). Breakthrough analysis for water disinfection using silver nanoparticles coated resin beads in fixed-bed column. *J. Hazard. Mater.* 217, 133–140. doi: 10.1016/j.jhazmat.2012.03.004

Nagura, S., Sakagami, T., Kakiichi, A., Yoshimoto, M., and Miki, K. (2004). Acute shifts in baroreflex control of renal sympathetic nerve activity induced by REM sleep and grooming in rats. *J. Physiol.* 558, 975–983. doi: 10.1113/jphysiol.2004.064527

Parati, G., Di Rienzo, M., and Mancia, G. (2000). How to measure baroreflex sensitivity: from the cardiovascular laboratory to daily life. *J. Hypertens.* 18, 7–19. doi: 10.1097/00004872-200018010-00003

Ricketts, J. H., and Head, G. A. (1999). A five-parameter logistic equation for investigating asymmetry of curvature in baroreflex studies. *Am. J. Physiol. Integr. Comp. Physiol.* 277, R441–R454. doi: 10.1152/ajpregu.1999.277.2.R441

Rocchiccioli, C., Saad, M., and Elghozi, J.-L. (1989). Attenuation of the baroreceptor reflex by propofol anesthesia in the rat. *J. Cardiovasc. Pharmacol.* 14, 631–635. doi: 10.1097/00005344-198910000-00015

Saad, M. A., Huerta, F., Trancard, J., and Elghozi, J.-L. (1989). Effects of middle cerebral artery occlusion on baroreceptor reflex control of heart rate in the rat. *J. Auton. Nerv. Syst.* 27, 165–172. doi: 10.1016/0165-1838(89)90098-2

Sabharwal, R., Coote, J., Johns, E., and Egginton, S. (2004). Effect of hypothermia on baroreflex control of heart rate and renal sympathetic nerve activity in anaesthetized rats. *J. Physiol.* 557, 247–259. doi: 10.1113/jphysiol.2003.059444

Sagawa, S., Torii, R., Nagaya, K., Wada, F., Endo, Y., and Shiraki, K. (1997). Carotid baroreflex control of heart rate during acute exposure to simulated altitudes of 3,800 m and 4,300 m. *Am. J. Physiol. Integr. Comp. Physiol.* 273, R1219–R1223. doi: 10.1152/ajpregu.1997.273.4.R1219

Sampaio, K. N., Mauad, H., Biancardi, V. C., Barros, J. L., Amaral, F. T., Schenberg, L. C., et al. (1999). Cardiovascular changes following acute and chronic chemical lesions of the dorsal periaqueductal gray in conscious rats. *J. Auton. Nerv. Syst.* 76, 99–107. doi: 10.1016/S0165-1838(99)00015-6

Schenberg, L. C., Lucas Brandão, C. A., and Vasquez, E. C. (1995). Role of periaqueductal gray matter in hypertension in spontaneously hypertensive rats. *Hypertension* 26, 1125–1128. doi: 10.1161/01.HYP.26.6.1125

Scrogin, K. E., Veelken, R., and Luft, F. C. (1994). Sympathetic baroreceptor responses after chronic NG-nitro-L-arginine methyl ester treatment in conscious rats. *Hypertension* 23, 982–986. doi: 10.1161/01.HYP.23.6.982

Shade, R. E., Bishop, V. S., Haywood, J. R., and Hamm, C. K. (1990). Cardiovascular and neuroendocrine responses to baroreceptor denervation in baboons. *Am. J. Physiol. Regul. Integr. Comp. Physiol.* 258, R930–R938. doi: 10.1152/ajpregu.1990.258.4.R930

Stewart, J. M., Warsy, I. A., Visintainer, P., Terilli, C., and Medow, M. S. (2021). Supine parasympathetic withdrawal and upright sympathetic activation underly abnormalities of the baroreflex in postural tachycardia syndrome: effects of pyridostigmine and digoxin. *Hypertension* 77, 1234–1244. doi: 10.1161/HYPERTENSIONAHA.120.16113

Studinger, P., Goldstein, R., and Taylor, J. A. (2007). Mechanical and neural contributions to hysteresis in the cardiac vagal limb of the arterial baroreflex. *J. Physiol.* 583, 1041–1048. doi: 10.1113/jphysiol.2007.139204

Veelken, R., Hilgers, K. F., Ditting, T., Leonard, M., Mann, J., Geiger, H., et al. (1994). Impaired cardiovascular reflexes precede deoxycorticosterone acetate-salt hypertension. *Hypertension* 24, 564–570. doi: 10.1161/01.HYP.24.5.564

Verberne, A. J., Lewis, S. J., Worland, P. J., Beart, P. M., Jarrott, B., Christie, M. J., et al. (1987). Medial prefrontal cortical lesions modulate baroreflex sensitivity in the rat. *Brain Res.* 426, 243–249. doi: 10.1016/0006-8993(87)90878-X

Verhulst, P. F. (1838). Notice sur la loi que la population poursuit dans son accroissement. *Corresp. Mathématique Phys.* 10, 113–121.

Conflict of Interest: The authors declare that the research was conducted in the absence of any commercial or financial relationships that could be construed as a potential conflict of interest.

Publisher's Note: All claims expressed in this article are solely those of the authors and do not necessarily represent those of their affiliated organizations, or those of the publisher, the editors and the reviewers. Any product that may be evaluated in this article, or claim that may be made by its manufacturer, is not guaranteed or endorsed by the publisher.

frontiers in Neuroscience

ORIGINAL RESEARCH
published: 09 December 2021
doi: 10.3389/fnins.2021.720031

Cardiovagal Baroreflex Hysteresis Using Ellipses in Response to Postural Changes

Babak Dabiri, Joana Brito and Eugenijus Kaniusas*

Institute of Electrodynamics, Microwave and Circuit Engineering, Vienna University of Technology, Vienna, Austria

The cardiovagal branch of the baroreflex is of high clinical relevance when detecting disturbances of the autonomic nervous system. The hysteresis of the baroreflex is assessed using provoked and spontaneous changes in blood pressure. We propose a novel ellipse analysis to characterize hysteresis of the spontaneous respiration-related cardiovagal baroreflex for orthostatic test. Up and down sequences of pressure changes as well as the working point of baroreflex are considered. The EuroBaVar data set for supine and standing was employed to extract heartbeat intervals and blood pressure values. The latter values formed polygons into which a bivariate normal distribution was fitted with its properties determining proposed ellipses of baroreflex. More than 80% of ellipses are formed out of nonoverlapping and delayed up and down sequences highlighting baroreflex hysteresis. In the supine position, the ellipses are more elongated (by about 46%) and steeper (by about 4.3° as median) than standing, indicating larger heart interval variability (70.7 versus 47.9 ms) and smaller blood pressure variability (5.8 versus 8.9 mmHg) in supine. The ellipses show a higher baroreflex sensitivity for supine (15.7 ms/mmHg as median) than standing (7 ms/mmHg). The center of the ellipse moves from supine to standing, which describes the overall sigmoid shape of the baroreflex with the moving working point. In contrast to regression analysis, the proposed method considers gain and set-point changes during respiration, offers instructive insights into the resulting hysteresis of the spontaneous cardiovagal baroreflex with respiration as stimuli, and provides a new tool for its future analysis.

Keywords: cardiovagal baroreflex hysteresis, baroreflex sensitivity, ellipse, autonomic nervous system, orthostatic

OPEN ACCESS

Edited by:
Yue-Der Lin,
Feng Chia University, Taiwan

Reviewed by:
Ramon Gonzalez-Camarena,
Autonomous Metropolitan University, Mexico
Jens Tank,
German Aerospace Center, Helmholtz Association of German Research Centers (HZ), Germany

****Correspondence:***
Babak Dabiri
babak.dabiri.razlighi@tuwien.ac.at

Specialty section:
This article was submitted to Autonomic Neuroscience, a section of the journal Frontiers in Neuroscience

Received: *03 June 2021*
Accepted: *10 November 2021*
Published: *09 December 2021*

Citation:
Dabiri B, Brito J and Kaniusas E (2021) Cardiovagal Baroreflex Hysteresis Using Ellipses in Response to Postural Changes. Front. Neurosci. 15:720031. doi: 10.3389/fnins.2021.720031

INTRODUCTION

Blood pressure in humans is governed by the arterial and cardiopulmonary baroreflex, an essential part of the autonomic nervous system. Here, changes in pressure, e.g., spontaneous due to breathing or artificial due to vasoactive drug administration, act as stimuli on baroreceptors. The subsequent changes in heart rate, stroke volume, and total peripheral resistance following changes in the parasympathetic and sympathetic nervous systems compose the reflex response, which, in fact, aims to buffer changes in pressure (Kaniusas, 2012). In particular, sequences of pressure values and the associated heart rate values due to efferent vagal activity to the sinoatrial node form the cardiovagal

baroreflex hysteresis loop (deBoer et al., 1987; Bertinieri et al., 1988; Parati et al., 1988; Turjanmaa et al., 1990; Saul et al., 1991).

Chapleau et al. (1988) show, in animals, that a change in static pressure levels induces a dominant sigmoidal relationship between the pressure and baroreceptor activity (of the carotid sinus), whereas this relationship is almost linear for the pulsatile pressure (Chapleau and Abboud, 1987). A linear regression over the linear portion of the sigmoidal function between systolic pressure and heart rate values determines the cardiovagal baroreflex gain, known also as baroreflex sensitivity (BRS; deBoer et al., 1987; Parati et al., 1988; Turjanmaa et al., 1990). A reduced BRS value *BRS* is usually associated with cardiovascular failure (La Rovere et al., 2008), orthostatic intolerance (Cooper and Hainsworth, 2002), neurally mediated syncope (Benarroch, 2008), and amplified pain perception (Suarez-Roca et al., 2019).

For rising and falling systolic pressure values, an elliptical shape of the baroreflex hysteresis becomes dominant (Chapleau and Abboud, 1987; Eckberg and Sleight, 1992; Rudas et al., 1999). The baroreceptor activity seems to be stronger for downward pressure changes as compared with upward pressure changes (Chapleau and Abboud, 1987). However, comparisons of *BRS* for upward and downward pressure changes yield controversial results; e.g., upward changes yield higher *BRS* in Studinger et al. (2007), whereas no differences are observed in De Maria et al. (2019). A spontaneous cardiovagal baroreflex cycle (CBC) results in a course of spontaneous and periodic breathing, which is composed of rise-to-fall and/or fall-to-rise pressure sequences with the associated heart rate values. The presence of hysteresis and varying baroreceptor activity highlight the necessity to consider directional changes of both pressure and heart rate values in terms of the fitted CBC.

To investigate large parts of nonlinear and asymmetrical hysteresis, a wide range of (spontaneous or induced) pressure changes is needed as usually can be used only in animal studies (Chapleau and Abboud, 1987) and also in humans with vasoactive substances (Rudas et al., 1999; Studinger et al., 2007). Small changes of pressure would mainly disclose only the linear parts of the hysteresis near the working point. To investigate the baroreflex, common autonomic provocations include orthostatic tests, head up tilt tests, neck chamber testing, handgrip tests, and the Valsalva maneuver (Hainsworth, 1998; Convertino, 2001; La Rovere et al., 2008; Hart et al., 2011; Ichinose and Nishiyasu, 2012; De Maria et al., 2019; Incognito et al., 2019) as well as pharmacologic interventions (La Rovere et al., 1998; Ler et al., 2010; Hart et al., 2011; Taylor et al., 2013; Incognito et al., 2020). Here, the provoked pressure changes provide a possibility to extract the sympathetic outflow of the autonomic nervous system (e.g., by recording sympathetic nerve activity to the blood vessels) and the corresponding parasympathetic vagal outflow (e.g., by recording heart periods) in terms of baroreflex regulation (Saul et al., 1991; Hart et al., 2011; Taylor et al., 2013).

For instance, the orthostatic stress as a simple, noninvasive test, reduces the spontaneous *BRS* from supine to standing (from 17.5 to 7.65 ms/mmHg; Steptoe and Vögele, 1990) by elevating the vascular sympathetic outflow in response to gravitationally relocated blood volume as assessed by studies without considering the directional change in pressure and, thus, without considering hysteresis. Vasoactive substances (to increase and/or decrease blood pressure) were used to investigate the mechanical arm of the baroreflex over a wide range of pressure changes, reflecting the relationship between the systolic blood pressure and the carotid artery diameter, known as the modified Oxford method (Hunt et al., 2001; Studinger et al., 2007; Ler et al., 2010; De Maria et al., 2019). Here, the coinvestigated neural arm reflects the associated changes in heart rate and carotid artery diameter (Smyth et al., 1969).

From a processing perspective, the morphology of the (spontaneous and nonspontaneous) CBC hysteresis is characterized using quantitative and qualitative parameters. Variability of up and down baroreflex sequences were investigated for orthostatic test and different age (Rudas et al., 1999; Taylor et al., 2013; De Maria et al., 2019). Studinger et al. (2007) show how the baroreflex resets the next heart period solely by the neural arm with the vasoactive substance administration process. Mechanical and neural baroreflex arms were investigated for continuous blood pressure changes (Studinger et al., 2007; Taylor et al., 2013, 2014). Whereas *BRS* for rising and falling blood pressure (e.g., 12 ms/mmHg during supine versus 7.5 ms/mmHg during treadmill activity; De Maria et al., 2019) using vasoactive substances is usually considered in quantitative terms, an alteration in the working point on the hysteresis is usually subjected to qualitative analysis only (Studinger et al., 2007). Independent up and down sequences were assessed without considering their succession in time and, thus, neglecting the neuronal arm accounting for respiration-related directional pressure changes from one sequence to another (Bertinieri et al., 1985; Steptoe and Vögele, 1990; De Maria et al., 2018, 2019). A bivariate phase-rectified signal averaging technique was used to quantify upward and downward sequences (De Maria et al., 2018). A 3-D planar ellipse method was introduced to describe both arms of the baroreflex using vasoactive substances (Ler et al., 2010).

In this work, we propose a novel approach using sophisticated ellipse analysis to characterize cardiovagal baroreflex hysteresis on two levels: (i) cardiovagal hysteresis due to the respiration-related spontaneous pressure change (i.e., not pharmacologically induced), and (ii) cardiovagal hysteresis due to the static pressure change in the course of the orthostatic test. In contrast to the state of the art, we separately consider the up and down sequences of spontaneous pressure changes (for expiration and inspiration, respectively), which show individual values of *BRS* and then compose a full ellipse (for a whole respiratory cycle) with its own *BRS*. This BRS accounts for all three: mechanical arm, neural arm acting within single sequences, and neuronal arm accounting for directional pressure changes (set-point changes). Spontaneous and intrinsic regulatory processes are considered only without any artificial pressure perturbation and without the associated cofactors/interferences affecting barosensory vessel mechanics. In addition, we analyze quantitatively the working point changes of the baroreflex during the orthostatic test using our ellipse-based analysis. Here, we employ the maneuver of the change in posture to vary the static blood pressure in a binary way and, thus, to characterize the position and change of the working point and the sigmoidal behavior of the CBC.

MATERIALS AND METHODS

This study was performed on the EuroBaVar data set[1], provided by the Working Group on Blood Pressure and Heart Rate Variability of the European Society of Hypertension. The electrocardiogram data consists of 42 recordings of 21 subjects (17 females, median age = 38.4 years, median height = 1.65 m, median weight = 64.1 kg, and median body mass index = 23.3 kg/m^2), including both series of recordings, series A (n = 8) and series B (n = 13), and both positions, supine and upright, each position lasting for 10–12 min. Informed consent was obtained, and the study was approved by the Paris–Necker committee for the protection of human subjects in biomedical research. Study subjects were composed of 12 normotensive, 4 healthy, 3 hypertensive (1 treated with medication and 2 nonmedicated), one diabetic, and one heart transplantation patients. The detailed data can be found in Laude et al. (2004) and Choi et al. (2006). Noninvasive monitoring devices were used such as a three-lead electrocardiogram (Cardiocap II; Datex Engstrom, Helsinki, Finland) and a continuous beat-to-beat blood pressure monitor (Finometer MIDI; Finapres Inc., Enschede, Netherlands) with all signals recorded at a 500-Hz sampling rate.

The respiratory signal was not recorded. However, we assume that up and down sequences in each CBC are due to the respiratory sinus arrhythmia and correspond to expiration and inspiration phases, respectively (Silva et al., 2019). This is because other nonrespiratory periodic modulating mechanisms in the frequency region of the respiration were not present during recordings.

In the recorded data, *RR*-intervals of the duration *RR*, the systolic pressure P_S, and the diastolic pressure P_D were identified and verified visually. Up and down baroreflex sequences with three or more beats, i.e., in which P_S and *RR* values progressively increased or decreased, were extracted in all recordings. Only those P_S and *RR* sequences were considered that had a mutual correlation coefficient >0.85, i.e., the sequences that were assumed to reflect predominantly the cardiovagal *BRS* (Hughson et al., 1993). There was no minimum P_S change required for the sequence to be valid. If an up sequence was immediately followed by a down sequence or vice versa, both sequences were considered as CBC. Consequently, for n consecutive up and down sequences (with $n > 2$), we end up with $(n-1)$ CBCs.

As illustrated in **Figure 1C**, the resulting CBC as a function of P_S (x-axis) and *RR* (y-axis) shows a polygon shape. Here, the filled points represent the up sequence, and the empty points represent the down sequence.

Ellipse Analyses for Nonintersecting Sequences

To approximate CBC—composed of nonintersecting sequences only—with ellipses, we identified them in the 2-D area (encompassed by x- and y-axes) in a way that ellipses enclose the whole polygon while exhibiting the minimum area. For this, an iterative procedure of the convex minimization problem, known as the Khachiyan algorithm (Kumar and Yildirim, 2005), was employed.

For the ellipses to show the same area as the original polygons, we linearly downscaled these resulting ellipses with respect to their centers but without changing their orientation angle with respect to the x- and y-axes. Here, the center of the ellipse, its minor and major axes, as well as the orientation angle comprise the representative parameters of CBC.

Ellipse Analysis for all Sequences

In the case that up and down sequences have one or more intersection points as it is often the case (see **Supplementary Material**), multiple closed polygons necessarily appear (**Supplementary Figure 1**). Because the aforementioned method considers only nonintersecting sequences, we estimate the best fitted ellipse for both nonintersecting and intersecting sequences using a proposed image-based procedure.

First, we cropped the 2-D area of the prospective CBC with the pixel resolution of 0.1 mmHg × 0.1 ms from the minimum values of P_S (=75 mmHg) and *RR* (=500 ms) of all recordings to the respective maximum values (175 mmHg and 1,500 ms) of all recordings. Thus, the resulting image had a total resolution of 1,000 × 10,000 px^2. The image was binarized with black color outside of the polygon and white color inside of it (**Supplementary Figure 1**).

Then, a bivariate normal distribution is fitted into each closed polygon within the generated binary image. The covariance matrix of the distribution determines the shape of the distribution. The contour lines of each distribution form an ellipse. In particular, the direction and length of the major and minor axes of the ellipse for each closed polygon are given by eigenvectors and eigenvalues of the covariance matrix. The orientation angle of the respective closed polygon is given by the first eigenvector and represents the respective angle between the major axis and the x-axis. The intersection of the major and minor axes determines the weighted center of the ellipse shape (for each closed polygon).

Consequently, we end up with as many ellipses as closed polygons. The area A_O of the overall ellipse for CBC is defined as the sum of respective individual areas A_I of the closed polygons, whereas the center coordinates (x_O, y_O) of the overall ellipse and its orientation angle θ_O resulted out of a weighting procedure considering individual ellipses with their center coordinates (x_I, y_I) and individual orientation angles θ_I for each closed polygon to give

$$x_O = \frac{\sum x_I \cdot A_I}{\sum A_I},\ y_O = \frac{\sum y_I \cdot A_I}{\sum A_I},\ \theta_O = \frac{\sum \theta_I \cdot A_I}{\sum A_I},$$
$$\text{and } A_O = \sum A_I. \quad (1)$$

Because the individual closed polygons show comparable values of θ_I in the range of ±1%, the total length l_{O_MAJOR} of the major axis of the overall ellipse is simply estimated as the sum of respective lengths l_{I_MAJOR} of major axes of all individual closed polygons. The total length l_{O_MINOR} of the minor axis for CBC

[1]http://www.eurobavar.altervista.org

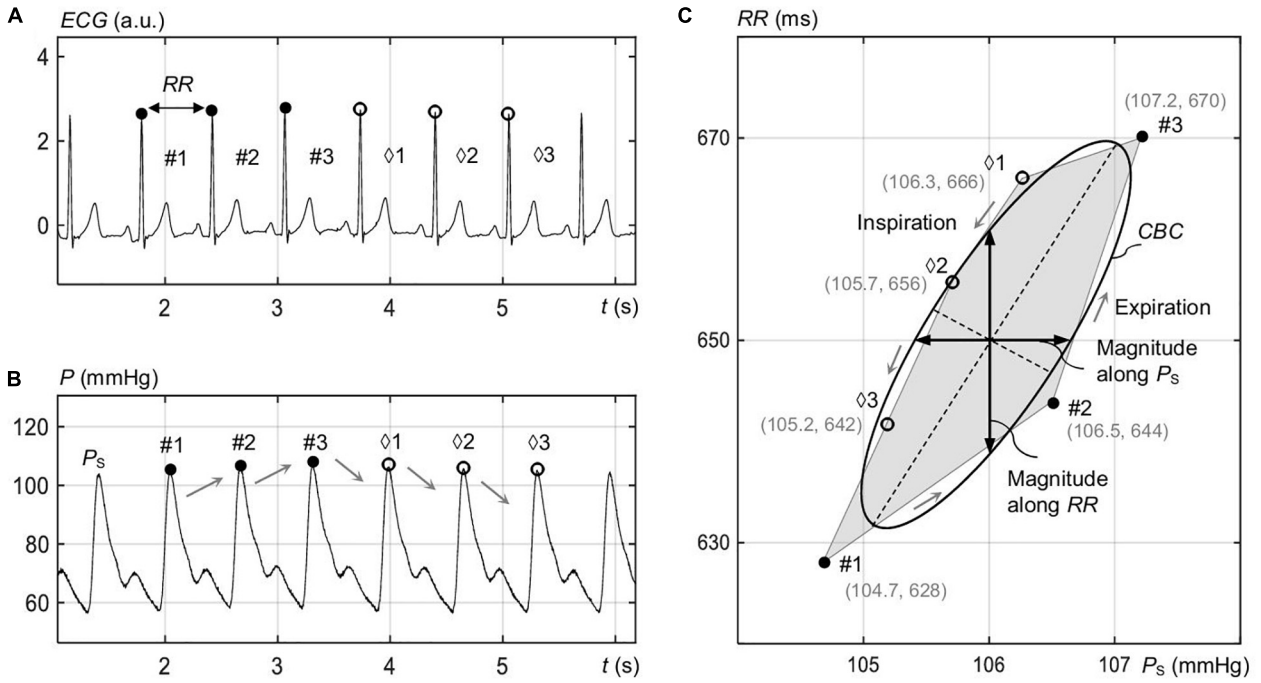

FIGURE 1 | Identification of the spontaneous CBC in the course of respiration for elliptic processing. **(A)** Electrocardiogram signal ECG with rising *RR* values for the marked intervals #1 to #3 (expiration) and falling *RR* for the intervals ◇1 to ◇3 (inspiration). **(B)** The blood pressure *P* with the associated rising and falling systolic pressure P_S values. **(C)** Vertices with filled dots correspond to rising P_S and *RR*, and empty dots correspond to falling P_S and *RR*. The shown ellipse represents the overall ellipse of the image-based procedure.

resulted out of a weighting procedure of individual l_{I_MINOR}—in analogy with Eq. 1—to give

$$l_{\mathrm{O\_MINOR}} = \frac{\sum l_{\mathrm{I\_MINOR}} \cdot A_{\mathrm{I}}}{\sum A_{\mathrm{I}}} \text{ and } l_{\mathrm{O\_MAJOR}} = \sum l_{\mathrm{I\_MAJOR}}. \quad (2)$$

All formed individual and overall ellipses are visually controlled to encompass closed polygons. The value of *BRS* for CBC is estimated out of θ_{O} based on

$$BRS = \tan^{-1}\theta_{\mathrm{O}}. \quad (3)$$

To quantitatively assess the share of intersecting and nonintersecting up and down sequences forming hysteresis of CBC, each sequence is fitted individually with a subellipse (as illustrated within the inset of **Figure 8** by dashed subellipses). A ratio $a/(b/2)$ is built of the minor axis ($=a$) of each subellipse to the half of the minor axis ($=b/2$) of the overall CBC ellipse. Nonoverlapping sequences show $a/(b/2) \leq 1$, whereas those with an overlap show $a/(b/2) > 1$.

Regression Method

Linear regression analysis was applied to the selected sequences of P_S and *RR*. Ascending and descending trends were separately assessed. For the linear regression analysis, the sequences of P_S and *RR* were used without any delay in between (**Figure 1C**; Steptoe and Vögele, 1990).

Statistics

A paired *t*-test was used to compare the mean *BRS* and the mean magnitudes of the hysteresis (defined as the maximum change in *RR* for a constant P_S) as well as to compare P_S, P_D, and *RR* between supine and standing positions. A Wilcoxon signed rank test was used to compare the median *BRS* values between supine and standing positions. The differences were considered statistically significant when the error probability $p < 0.05$. Data are presented as median and/or interquartile range (IQR), supplemented by mean ± standard deviation. All data were processed and analyzed in MATLAB R2020b (The MathWorks Inc., Natick, MA, United States).

RESULTS

Beat-to-Beat Analysis for Respiration

Figure 1 illustrates consecutive up and down sequences of *RR* (**Figure 1A**) and P_S (**Figure 1B**) in the course of respiration for a single recording, forming a spontaneous CBC (**Figure 1C**). In fact, the up sequence reflects expiration, whereas the down sequence reflects inspiration, in line with the process of respiratory sinus arrythmia. An ellipse is shown in **Figure 1C** that approximates a closed polygon, composed of P intervals and P_S values for the points #1 to #3 (up sequence) and ◇1 to ◇3 (down sequence) as estimated by the image-based procedure. The median respiration rate for standing was 12.6 (12.7 ± 2) 1/min, whereas that for supine was 11.1 (11.3 ± 1.9) 1/min.

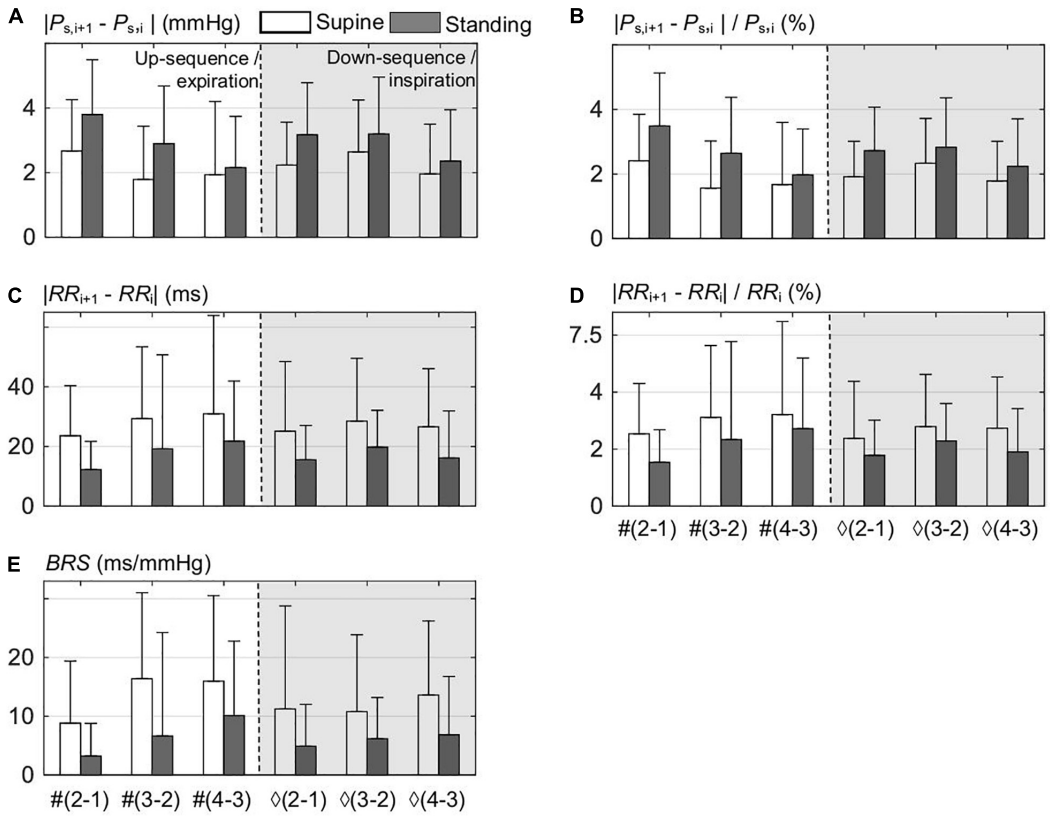

FIGURE 2 | Beat-to-beat analysis of up sequences composed out of *i*th points, i.e., from #1 to #3, and down sequences out of ◇1 to ◇3 points; both sequences compose the spontaneous CBC for supine and standing. **(A)** The differences between the consecutive (*i*+1) and *i* values within the sequence of the systolic blood pressure P_S. **(B)** Normalized differences of **(A)**. **(C)** The differences between the consecutive (*i*+1) and *i* values within the sequence of *RR* values. **(D)** Normalized differences of **(C)**. **(E)** The associated values of the baroreflex sensitivity *BRS* for all differences.

Beat-to-Beat Analysis for Postural Changes

A detailed beat-to-beat analysis of up and down sequences composing the spontaneous CBC is shown in **Figure 2** for supine and standing. In particular, the beat-to-beat deflections of P_S (**Figure 2A**) and *RR* (**Figure 2C**) illustrate that the maximum P_S deflection occurs at the onset of expiration in both supine and standing. The standing position has a higher deflection in P_S and a lower one in *RR* than the supine position, which already indicates a higher baroreflex efficiency in supine with stronger smoothed changes in P_S. In particular, the mean deflection in P_S in standing amounts to about ±2.4% and in supine to ±1.8% (**Figure 2B**) considering single beat-to-beat deflections, whereas the mean deflection in *RR* follows a reverse trend, i.e., in standing, it amounts to about ±2.5%, whereas in supine to ±3% (**Figure 2D**).

Figure 2E shows that the mean value of *BRS* for standing is only about half of that in supine (=53%), which again highlights the higher baroreflex efficiency in supine. It is instructive to observe that the magnitude of deflections in P_S is inversely related to the values of *BRS* and is proportional to those in *RR*, which confirms the buffering activity of baroreflex—proportional to *BRS*—with respect to P_S at the cost of *RR* variability (**Figures 2B,D**). Please note that the lowest value of *BRS* results at the first two beats of up sequences, i.e., at the start of expiration.

Ellipse Analysis for Postural Changes

Figure 3A compares ellipses for supine and standing for all recordings, including median and IQR ellipses of all estimated (overall) ellipses based on an image-based procedure. The distributions of *RR* and P_S are illustrated in **Figures 3B,C** for supine and standing. In fact, the median values of these distributions determine the center coordinates of median ellipses (**Figure 3A**). For visual simplicity, IQR ellipses in **Figure 3A** are relocated in a way that their centers overlap with the center of the associated median ellipses. As expected, the angle θ_O increases from the 25th to the 75th quantile as also confirmed by quantitative data in **Table 1**.

In the supine position, the ellipses are more elongated and steeper than in standing (**Figure 3A**). Quantitative data in **Table 1** confirms that l_{O_MAJOR} and θ_O are statistically larger, whereas l_{O_MINOR} is statistically smaller for supine than standing. For supine and standing positions, the median of l_{O_MAJOR} is 70.8 (IQR 61.4) and 48.4 (IQR 29.4), whereas the median of l_{O_MINOR} is 3.6 (IQR 3.4) and 5.8 (IQR 4.2), respectively. In particular, the median of θ_O amounts to 85.8° for supine, which implies that the

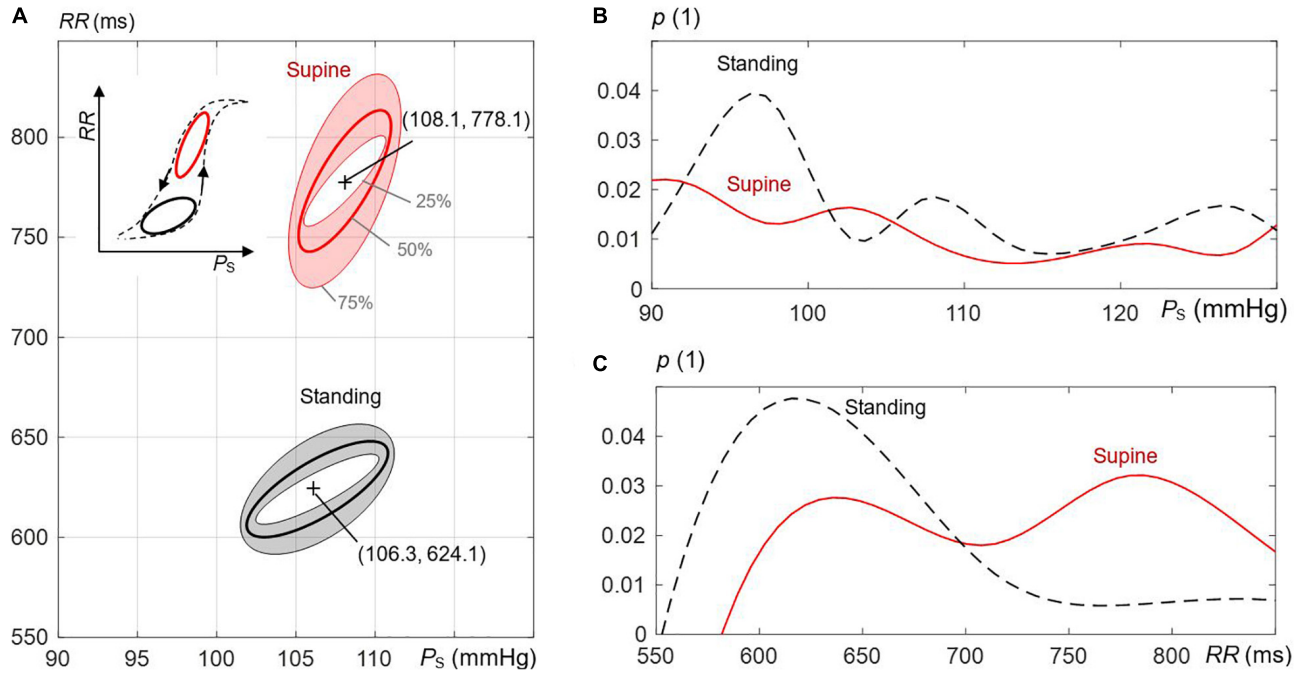

FIGURE 3 | The effect of postural changes on the estimated ellipses of the spontaneous CBC in the course of respiration. **(A)** Supine versus standing is illustrated; the shaded regions mark interquartile ranges, and bold lines mark median values. Inner and outer ellipses represent, respectively, the 25th to 75th interquartile, and the middle ellipse is the median ellipse. The supine position displays more elongated and steeper hysteresis (with respect to the axis of the systolic pressure P_S) than the standing position. The inset to the left shows the schematic behavior of the whole hysteresis, including both postural positions. The frequency distributions of **(B)** P_S and **(C)** RR-values *RR* for supine and standing with *p* as the probability.

TABLE 1 | Characteristic parameters of the overall ellipses of spontaneous cardiovagal baroreflex cycles for supine and standing (**Figure 3**).

	Major axis length c_{O_MAJOR}*		Minor axis length c_{O_MINOR}*		Orientation angle θ_O (°)	
	Supine	**Standing**	**Supine**	**Standing**	**Supine**	**Standing**
25th quantile (inner ellipse)	45.6	35.8	2.4	3.8	83.9	79.0
Median (middle ellipse)	70.8	48.4	3.6	5.8	85.8	81.5
75th quantile (outer ellipse)	107	65.2	5.8	8.0	87.4	84.6

All differences between supine and standing are statistically significant ($p < 0.05$).
**$(mmHg^2 + ms^2)^{1/2}$.*

median ellipse is steeper by 4.3° than for standing. The resulting center of concentric ellipses (median and IQR ellipses) for supine is located at (108.1 mmHg, 778.1 ms), i.e., at higher values than for standing with its coordinates (106.3 mmHg, 624.1 ms).

Figure 4 shows decomposed median and IQR ellipses from **Figure 3A** in that closed-loop courses of P_S and *RR* are derived over the respiratory period with the normalized duration of 2π. In both cases, for supine (**Figure 4A**) and standing (**Figure 4B**), a delayed course of *RR* with respect to P_S is visible, an intrinsic property of the baroreflex with P_S acting as stimulus and *RR* representing a delayed response. The delay is significantly smaller for supine than standing (39.4° versus 41.3° for median courses) as confirmed by numerical data in **Table 2**, indicating again a more effective baroreflex in supine. The delay increases from the 25th to the 75th interquartile (**Table 2**).

The peak-to-peak deflection of the median P_S over 2π is smaller for supine (5.8 mmHg with IQR 1.9 mmHg) than for standing (8.9 mmHg with IQR 2 mmHg), whereas the peak-to-peak deflection of the median *RR* is larger for supine (70.7 ms with IQR 61.5 ms) than for standing (47.9 ms with IQR 30 ms). This clearly indicates a higher *BRS* and, thus, an increased baroreflex efficiency for supine than standing and is in line with data from **Figures 2A–D**.

Ellipse Parameters for Postural Changes

Figure 5 shows the distributions of A_O (**Figure 5A**) and the ratio l_{O_MINOR}/l_{O_MAJOR} (**Figure 5B**) of the estimated overall ellipses for supine and standing. The median A_O for supine was 209 mmHg . ms (339 ± 516) and for standing 224 mmHg . ms (346 ± 527) with no statistical difference in between. However, for the ratio, there was a statistical difference ($p < 0.005$) with 0.11 (0.12 ± 0.8) for standing and 0.05 (0.07 ± 0.06) for supine, i.e., the ellipses for supine are significantly slimmer than for standing, which confirms the qualitative observation in **Figure 3A**.

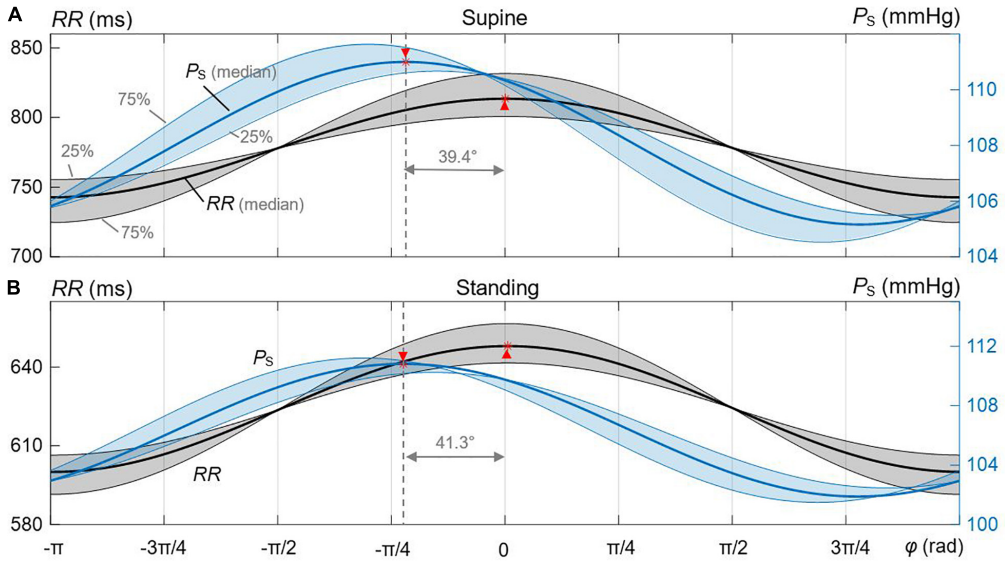

FIGURE 4 | Derived courses of P_S and *RR* out of the estimated median and IQR ellipses for the spontaneous CBC. The shaded regions represent the 25th and 75th interquartile ranges. **(A)** Supine. **(B)** Standing. The respective maxima and delays are marked between median-related courses of P_S and *RR*.

TABLE 2 | Characteristic parameters of the derived courses of P_S and *RR* out of the estimated median and IQR ellipses of spontaneous cardiovagal baroreflex cycles for supine and standing (**Figure 4**).

	Phase shift (°)		Deflection of *RR* (ms)		Deflection of P_S (mmHg)	
	Supine	**Standing**	**Supine**	**Standing**	**Supine**	**Standing**
25th quantile	27.3	29.8	45.4	35.1	5.2	7.7
Median	39.4	41.3	70.7	47.9	5.8	8.9
75th quantile	54.3	56.7	106.9	65.1	7.1	9.7

All differences between supine and standing are statistically significant ($p < 0.05$).

The radar plot in **Figure 6** summarizes P_S, P_D, *RR*, A_O, *BRS* (for both up and down sequences), and the ratio l_{O_MINOR}/l_{O_MAJOR} of the spontaneous CBCs for supine and standing using an image-based procedure. Each box length represents the 25th to 75th IQR with an indicated median value (see denoted axis for *RR* in **Figure 6**). The supine position shows significantly elevated *RR* and *BRS* and significantly depressed P_D, l_{O_MINOR}/l_{O_MAJOR} for supine in comparison with standing, whereas there is no significant difference found in A_O and P_S. In particular, the supine position with the median of 15.7 ms/mmHg shows a significantly higher *BRS* than standing with only 7 ms/mmHg. Likewise, the supine position has a larger *RR* as compared with standing (778 versus 624 ms).

Figure 7 illustrates that the baroreflex-related variability ΔP_S of P_S as a function of *RR* (**Figure 7A**) is reduced, whereas ΔRR of *RR* as a function of P_S (**Figure 7B**) is elevated for supine as compared with standing as a consequence of steeper ellipses in supine than standing (**Figure 3A**). The median magnitude of the formed hysteresis is about 50 ms and 3.7 mmHg for supine and about 32 ms and 5.8 mmHg for standing, in agreement with **Figure 2C**. For supine, this highlights a stronger baroreflex responses (in ms) at a given value of P_S and a stronger smoothing of blood pressure (in mmHg) at a given value of *RR*.

Figure 8 shows that the majority of CBC ellipses for supine and standing, respectively, are composed of nonoverlapping sequences. Namely, 83.4 and 81.8% of ellipses for supine and standing, respectively, show the ratio $a/(b/2) \leq 1$.

DISCUSSION

The present work introduces a novel ellipse-based method to characterize hysteretic behavior of the spontaneous CBC as governed through spontaneous respiration and, thus, spontaneous pressure changes. The applicability and rationale of the method are shown for orthostatic tests when comparing supine and standing.

Beat-to-Beat Analysis

The beat-to-beat analysis of **Figures 1**, **2** considers separately up and down sequences of spontaneous CBC (for expiration and inspiration, respectively) with individual *BRS* values, forming a base for ellipses (for the whole respiratory cycle) with its own *BRS*. An inverse relationship between beat-to-beat deflections in P_S and *RR* is clearly evident (**Figure 2**), and it highlights the rationale of the baroreflex to buffer changes in blood pressure

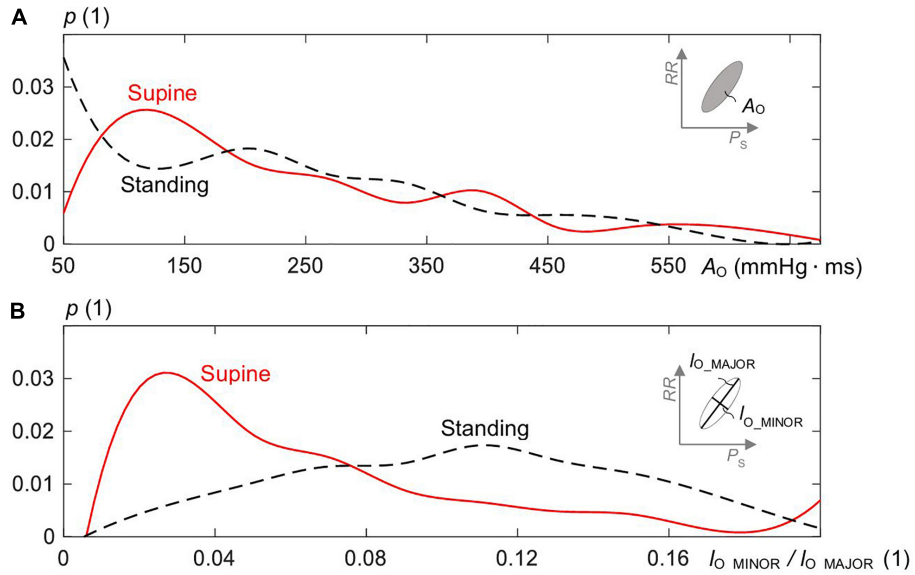

FIGURE 5 | Distribution of **(A)** the area A_O of the estimated ellipses of the spontaneous CBC and **(B)** the ratio of minor to major axis length ($=I_{O\_MINOR}/I_{O\_MAJOR}$) for supine and standing with p as the probability of the distribution.

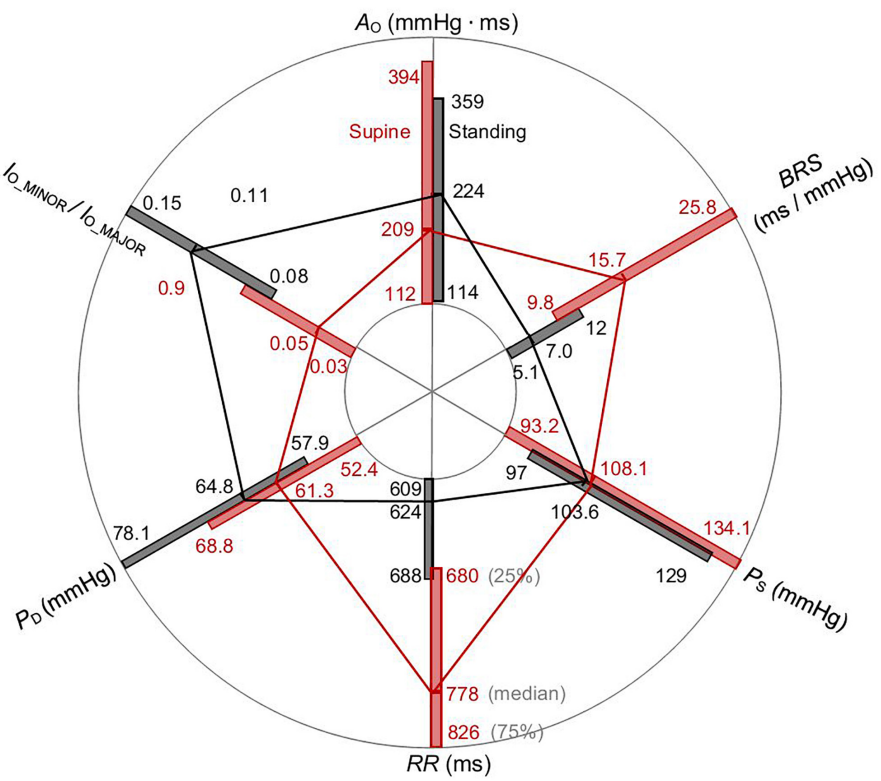

FIGURE 6 | Radar plot of P_S, P_D, RR, A_O, BRS, and the ratio I_{O_MINOR}/I_{O_MAJOR} of the spontaneous CBC for supine and standing. Whereas medians of RR and BRS are elevated, P_D and the ratio I_{O_MINOR}/I_{O_MAJOR} are declined for supine than standing. The values A_O and P_S do not significantly change for postural change.

at the cost of the heart-rate variability. The maximum deflection in P_S from one beat to the next can be seen at the onset of expiration (**Figure 2A**), where arterial vessels are maximally unloaded in the course of the respiration cycle (**Figure 1C**). In fact, barosensory vessels are more distensible for falling pressure than rising given relatively large changes in the pressure

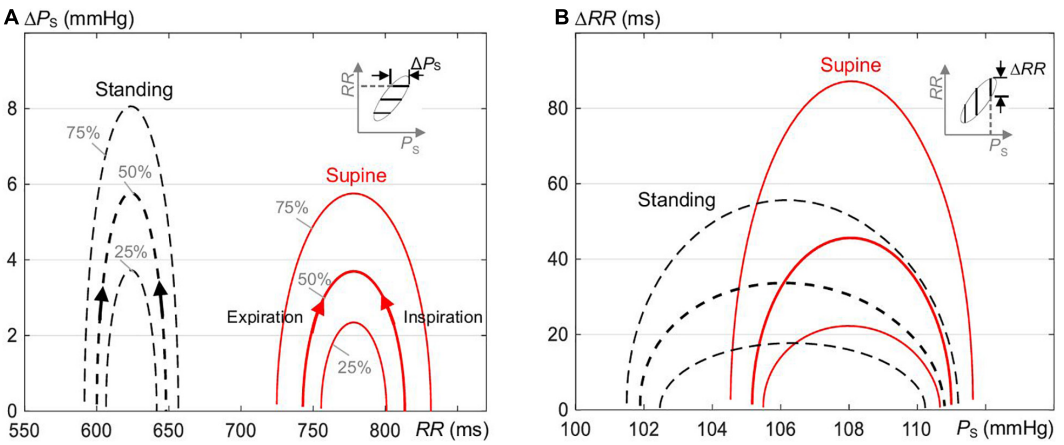

FIGURE 7 | The magnitude of hysteresis loop (**Figure 1C**) in terms of changes **(A)** ΔP_S of P_S as a function of *RR* and **(B)** ΔRR of *RR* as a function of P_S of the estimated ellipses of the spontaneous CBC for supine and standing (**Figure 3A**). The magnitude along P_S is increased and along *RR* is reduced for standing as compared with supine.

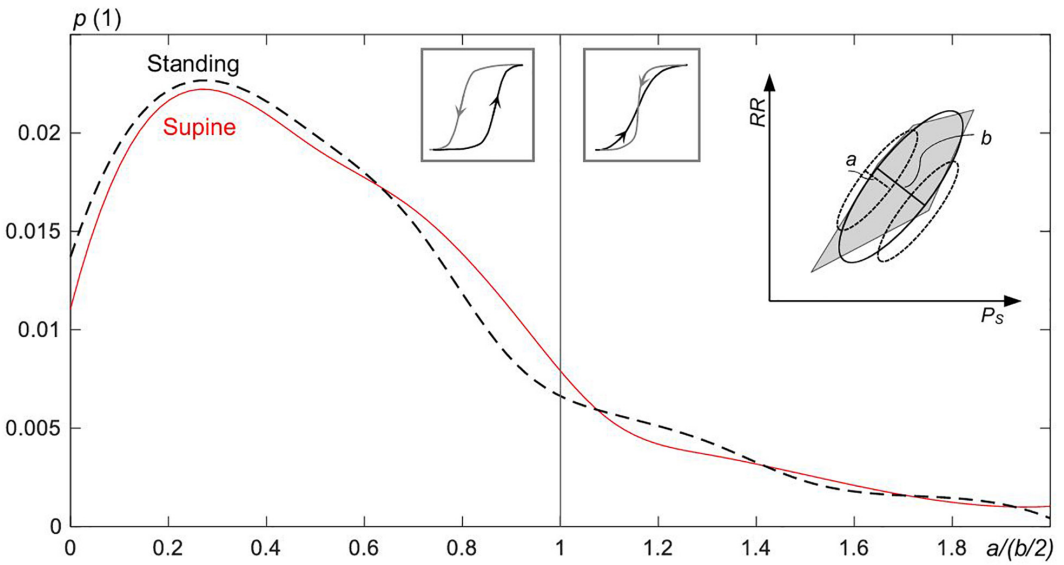

FIGURE 8 | The probability *p* for the overlap of up and down sequences within the hysteresis of the estimated ellipses of the spontaneous CBC for supine and standing. The ratio $a/(b/2)$—for the definition, see the inset figure to the right—goes to zero the broader the width of the hysteresis (=*b*) and the more linear is the down sequence or, in analogy, the up sequence (linearity is inversely proportional to *a*). For $a/(b/2) \leq 1$, the up and down sequences do not overlap; otherwise, sequences overlap with their strong fluctuations. Intersected sequences forming the hysteresis are less frequent (17.4% of all cases) than nonintersected sequences.

(Lénárd et al., 2000). Higher individual *BRS* result for supine than for standing (**Figure 2E**).

Baroreflex Hysteresis – General Perspective

For expiration, both P_S and *RR* increase, whereas the baroreflex resets at the end of expiration and then lowers P_S and *RR* for inspiration. In particular, the last beat of each sequence forms an initial condition for the subsequent sequence (for baroreflex activity), namely, for its first beat. Consequently, the formed (median) ellipse of the spontaneous CBC with up and down sequences shows a particular hysteretic width and shape. Because more than 80% of the spontaneous CBC ellipses are composed of nonoverlapping sequences (**Figure 8**), it underscores even more a hysteresis behavior of CBC. Hystereses characteristics seem to be characteristic for supine and standing (**Figure 3A**), i.e., for the change in the working point of the baroreflex following changes in the static blood pressure in the course of an orthostatic test.

The hysteresis behavior of CBCs—or the width of the fitted ellipse of the cardiovagal CBC—is due to heterogenicity in nature, speed, and population of afferent baroreceptors (Seagard et al., 1990) in addition to nonlinear mechanics of barosensory vessels and neuronal mechanisms (Studinger et al., 2007). The

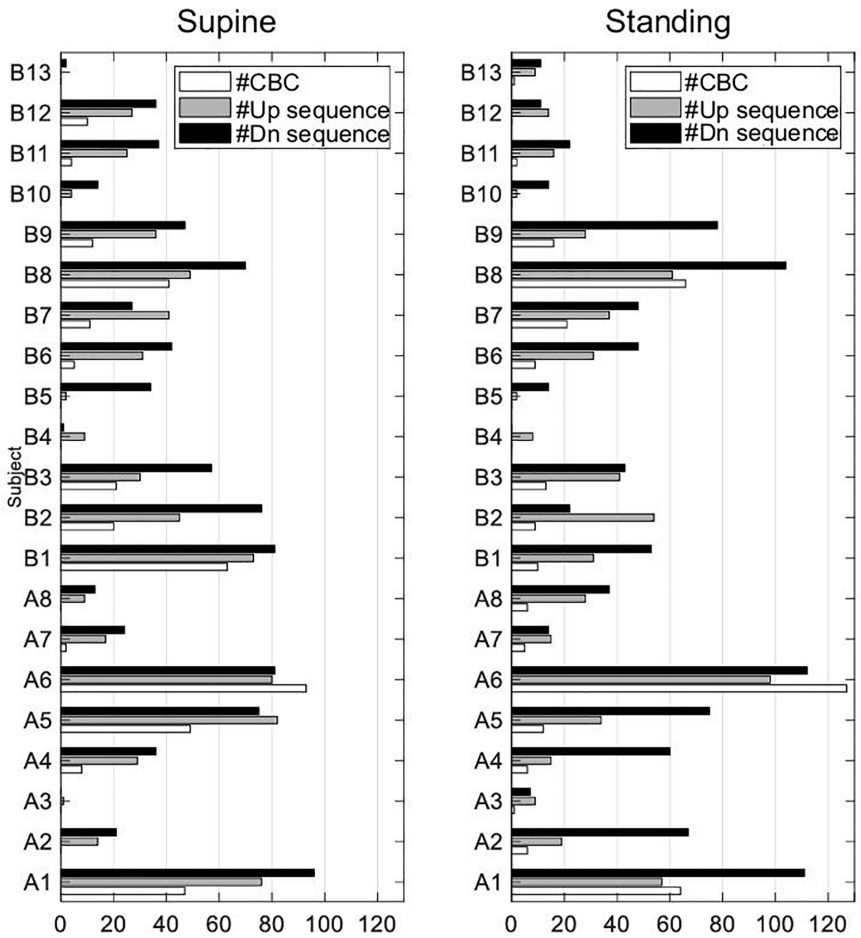

FIGURE 9 | Absolute number of used up and down sequences and sequences forming CBCs in all subjects of EuroBaVar data set.

fast myelinated A_β and A_δ fibers from baroreceptors are more sensitive to the pulsatile pressure change (Seagard et al., 1990; Rogers et al., 1993, 1996), whereas slow C fibers (and small A fibers) sense the absolute blood pressure changes. In addition, a relatively slow mechanical response of baro-sensory vessels (Bonyhay et al., 1997) and sympathovagal balance (Levy and Zieske, 1969) contributes to the hysteresis behavior of CBCs. The hystereses is also clearly favored by the observed delay between the *RR* and P_S courses (of about 40°; see **Figure 4**).

Baroreflex Hysteresis – Supine Versus Standing

In supine, the median ellipse is steeper and more elongated (**Figure 5B**), indicating a higher baroreflex efficiency here. Namely, the proposed elliptic method shows that the median ellipse is elongated in the *RR* direction in supine with the significantly larger median θ_O of 85.8°, the significantly larger median deflection in *RR* of 70.7 ms (baroreflex output) for the significantly smaller median deflection in P_S of 5.8 mmHg (baroreflex input) as compared with standing with the respective values 81.5°, 47.9 ms, and 8.9 mmHg (**Tables 1**, **2**). The resulting median values of *BRS* of the spontaneous CBC are significantly higher for supine with 15.7 ms/mmHg than standing with 7 ms/mmHg. The hysteresis area A_O shows no statistical differences between supine and standing; however, the ratio of minor to major axes l_{O_MINOR}/l_{O_MAJOR} indicates a significantly slimmer ellipses for supine than standing. Therefore, the elliptic method uncovers that the hysteresis elongation of the spontaneous CBC is larger, whereas the associated hysteresis width is smaller for supine than standing. Likewise, the hysteresis magnitude along *RR* with the median of 50 ms for supine is larger than 32 ms for standing, whereas the reverse is true for P_S, indicating a stronger smoothing action for supine (**Figure 7**).

The integrated *BRS* is reduced for standing due to a hypothesized reduction in the neural component of the baroreflex (Taylor et al., 2013). Namely, the gravitational pooling of blood within peripheral veins reduces the cardiac filling pressure, which, in turn, reduces the arterial blood pressure (Rowell, 1986; Nixon, 1988). The barosensory vessels become less inflated, whereas the afferent (vagal) activity of baroreceptors declines (Steinback et al., 2005; Taylor et al., 2013) and reduces the *BRS* of the spontaneous CBC in standing (**Figure 3A**) with damped respiratory sinus arrythmia (Faes et al., 2011).

In addition, the autonomic nervous system increases the total periphery resistance in standing while accelerating the sympathetic outflow (Incognito et al., 2019); e.g., higher angles of the tilt table elevate the muscle sympathetic nerve activity (Cooke et al., 1999). This outflow seems to add more nonlinearity through the efferent sympathetic pathway (Wang et al., 1993; Ursino, 1998) to the hysteresis of the spontaneous CBC than for supine, resulting in a wider hysteresis for standing.

The center of the estimated ellipse moves for positional changes, which shape the overall sigmoid shape of the baroreflex with the moving working point from supine to standing (**Figure 3A**). The right wing of the overall hysteresis marks the rising blood pressure, whereas the left wing marks the falling blood pressure, in line with stronger baroreceptor activity for increasing blood pressure than decreasing at a given blood pressure value (Chapleau and Abboud, 1987; Chapleau et al., 1988; Rudas et al., 1999). The local hystereses of CBCs lose their steepness and widen for standing in comparison to supine with the aforementioned changes in the local inclination angle θ_O and the local *BRS*. In terms of quantitative analysis, the working point of the baroreflex decreases significantly from 778 ms for supine to 624 ms for standing, whereas there is no significant change in P_S (**Figure 6**). Although individual spontaneous CBCs illustrate cardiopulmonary baroreflex regulation with respiration as stimulus, the overall baroreflex shape illustrates baroreflex regulation with static blood pressure changes (stemming from positional changes) as stimulus for both arterial and cardiopulmonary baroreflex (Fadel and Raven, 2012). Likewise, whereas the spontaneous CBC corresponds rather to the linear portion of the overall hysteresis and is controlled predominantly by the parasympathetic system, the overall hysteresis shows a sigmoidal shape and is determined by the interplay of both parasympathetic (vagal) and sympathetic outflows (Chapleau and Abboud, 1987; Chapleau et al., 1988; Ursino, 1998).

Detailed analysis of up and down sequences forming CBCs (**Supplementary Table 1** and **Figure 2A**) shows that up sequences tend to be steeper than down sequences for supine, whereas the reverse is true for standing. In fact, this difference in steepness tends to widen the formed hysteresis in the course of respiration. The larger width of hysteresis, such as in standing as compared with supine, underscores the reduced neural component of the baroreflex for standing than supine (Taylor et al., 2013), whereas the gain control is under the influence of both neural and mechanical components of baroreflex (Studinger et al., 2007).

The basic applicability of the elliptic method of CBC can be illustrated by considering spontaneous deflections of P_S. This deflection for up sequences is about 4.3 and 7.3 mmHg for supine and standing (as medians), respectively, and for down sequences about 5.2 and 7.3 mmHg for supine and standing, respectively. Compared with this, the elliptic method confirms these differences with 5.8 and 8.9 mmHg for supine and standing, respectively (**Table 2**). The elliptic method offers also insights into the time domain (**Figure 4**) in that it discloses a delayed *RR* course with respect to the P_S course over the spontaneous breathing cycle. Namely, the courses of P_S and *RR* follow the same trend in rising and falling as governed by the *BRS*, and once the pressure direction changes, the course of *RR* still follows its trend with a median delay of about 40° for spontaneous breathing. The delay is qualitatively comparable with that during paced breathing at 0.1 and 0.25 Hz, showing the respective delays of 60° down to 0° (Cooke et al., 1999; Karemaker and De Boer, 2017). The observed delay by 39.4° for supine is less than 41.3° for standing (**Table 2**) for spontaneous breathing, indicating a seemingly increased baroreflex efficiency in supine and a reduced contribution of the slow sympathetic baroreflex arm (Cooke et al., 1999). However, it should be noted that not only baroreflex, but also respiratory sinus arrythmia itself affects the observed *RR* values, whereas the latter effect depends on the respiration rate and even reaches its maximum at 0.1 Hz (Angelone and Coulter, 1964). Thus, the perceived change in the baroreflex efficiency from standing to supine should be considered with caution.

For paced breathing at the median respiratory frequency of 0.2 Hz, the delay changed from 53° for 80° tilt down to −12° for supine (Cooke et al., 1999; Karemaker and De Boer, 2017), whereas our data for spontaneous breathing with the median respiratory frequency of 0.18 Hz (0.19 ± 0.03) and 0.21 Hz (0.21 ± 0.03) for respective supine and standing show a delay of about 40°. Thus, paced breathing in supine seems to show lower and even reversed delays (i.e., a noncausal relationship between blood pressure and heart rate) as compared with spontaneous breathing. The type of respiration and the respiration rate clearly affect the amount of *RR* changes, the relationship between P_S and *RR*, and a resulting change of θ_O (related to the delay amount). The delay is a result of the different *BRS* values for up and down sequences and the set-point changes of the baroreflex when going from up to down sequences (and vice versa) as well as different latencies of neural and mechanical arms (Bonyhay et al., 1997; Studinger et al., 2007) and the sympathovagal interplay (Masuda et al., 1984). In fact, **Figure 4** shows how the mechanical and neural arms work in concert. Please note that only the neural arm is responsible for this set-point change during pressure direction changes (Studinger et al., 2007).

Methodological Issues

In our study, spontaneous respiration served as a modulatory input to the arterial pressure to characterize the hysteretic behavior of the spontaneous CBC. Derived parameters of the resulting ellipses, each for a single respiratory cycle, are suggested to characterize the spontaneous variability of hysteresis and, thus, to characterize the spontaneous CBCs. The spontaneous CBC has an advantage of considering only respiration-related baroreflex function, minimizing influence of other cofactors impacting baroreflex function. Here, the duration of the recording is not limited by the duration of any artificial perturbating stimulus and, thus, allows long-term investigations of the cardiovascular system in (chronic) conditions other than (temporary) clinical settings.

We considered sequences of P_S and *RR* without any delay in between regardless of the actual level of heart rate to keep the number of valid respiratory-related cycles of CBCs as high as possible. However, authors in Pickering and Davies (1973) show that mutually undelayed sequences of P_S and *RR* correlate best for heart rate below 75 1/min, whereas for higher heart rates, the value of P_S corelates best with the next *RR* value.

Baroreflex sequences were already analyzed without differentiating them into up and down sequences and without any vasoactive pressure induction (Bertinieri et al., 1985; Steptoe and Vögele, 1990; Hughson et al., 1993; Choi et al., 2006), analyzed with their differentiation for postural changes including head-up tilt (De Maria et al., 2018, 2019), or for vasoactive pharmacological substances inducing pressure changes in a relatively wide range (such as the modified Oxford method; Studinger et al., 2007; Taylor et al., 2013). In contrast, the proposed closed-loop ellipse method not only differentiates up and down sequences, but also explicitly considers their natural succession over the course of the spontaneous respiration cycle without using any artificial stimulus. In particular, the analyzed respiration-related CBC reflects a natural baroreflex during natural posture changes in contrast to head-up tilt or other artificial stimuli. The proposed method and its derived parameters, such as inclination angle θ_O, covers the neural and mechanical arms of the baroreflex without measuring the barosensory vessel diameters. In contrast to the state of the art, the considered closed-loop CBC has an advantage in considering pressure direction changes from expiration to inspiration and vice versa, thus considering the associated resetting of the baroreflex from one sequence to another (set-point changes). This yields a more robust estimation of the spontaneous cardiovagal hysteresis wings (**Figure 1C**).

Whereas, in the classical Oxford method, P_S is perturbated via pharmacological substances by >10% of the baseline P_S (usually by >15 mmHg; Taylor et al., 2013) to characterize the cardiovagal baroreflex, we use the spontaneous respiration-related perturbation of P_S in a smaller range of about 5.1 ± 3% (mean ± STD) of the baseline P_S for supine (5.6 ± 3.7 mmHg) and of about 7.1 ± 4% for standing (7.9 ± 4 mmHg); compare with **Table 2**. Thus, the proposed ellipse method characterizes the spontaneous CBCs without any pharmacological perturbations in the rather linear portion of baroreflex hysteresis with deflections of P_S in the approximate range of 7.9 ± 4 mmHg (**Figure 3A**).

Supplementary Table 1 compares *BRS* values for up and down sequences as estimated with the classical linear regression method and our proposed ellipse method, the latter being applied to individual up and down sequences as well as sequences composing CBC, see **Supplementary Figure 2**. There are no significant differences between both methods when considering up and down sequences, which is in line with De Maria et al. (2019) but contrasts with Eckberg and Sleight (1992) and Studinger et al. (2007). However, it can be observed in **Supplementary Table 1** and **Supplementary Figure 2** that sequences contributing to CBC (**Supplementary Figure 2B**) tend to show higher *BRS* than all sequences (**Supplementary Figure 2A**). In addition, the ellipse method on CBCs (Eq. 3) shows significantly higher median *BRS* for both supine and standing when compared with *BRS* for all sequences calculated with either the regression or ellipse method (**Supplementary Table 1** and **Supplementary Figure 2**). This is because most of the up and down sequences (>80%; see **Figure 8**) do not overlap, their individual gains are usually different (with this difference even depending on the posture; see **Supplementary Figure 2C**), and the set-points of the baroreflex "jump" from up to down sequences (and vice versa) when the direction of the pressure changes, all of them affecting *BRS* of the whole CBC (**Figure 1A**). In particular, the first beat of expiration has the maximum deflection in P_S (**Figure 2A**) and a little change in *RR* (**Figure 2C**), which pushes more weight to the lower part of the CBC and, thus, aligns the resulting ellipse toward larger θ_O and, thus, larger *BRS* of the whole CBC.

The larger *BRS* of the whole CBC as well as larger *BRS* of sequences contributing to CBC (**Supplementary Table 1**) in comparison with *BRS* of individual up and down sequences may highlight the additional effects of the neural arm involved in the set-point change. This is because the individual sequences account for only both the mechanical and the neural arms acting within the single sequence.

In addition, it can be observed in **Supplementary Table 1** that mean and median values strongly differ in some instances. This is due to frequent outliers that account for about 10% of all data points and, thus, affect the mean *BRS* but not the median *BRS*. The attained *BRS* using the proposed ellipse method were highly correlated by about 0.99 ($p < 0.005$) with *BRS* from the regression method in both supine and standing.

Because our analysis shows that about 17.4% of all up and down sequences forming CBC intersect with each other (**Figure 8**), whereas the Khachiyan algorithm (Kumar and Yildirim, 2005) cannot deal with intersected sequences, we focus on the image-based procedure. As an advantage, this procedure can consider both intersecting and nonintersecting sequences of CBCs.

Limitations

The data extraction from the EuroBaVar data set shows that only 3 out of 21 subjects (A1, A6, B8) contributed most of the up and down sequences, fulfilling the criteria to form a CBC in supine and standing; for absolute numbers, see **Figure 9**. Subject A5 mostly contributed to CBCs in supine. Sequences forming CBCs did not exist or were fewer than five in cases such as A3, B4, B5, B10, and B13. Although the analyzed subject pool is heterogenous, healthy subjects A1, A5, A6, and B8 seem to determine our results. This is because the observed results with healthy subjects yielded no statistical differences from those of all subjects. In addition, the relative number of outliers in the calculated *BRS* was quite high with about 10% and, thus, may have influenced the results, especially the observed differences between supine and standing. Because the proposed method uses consecutive up and down sequences with three or more beats to form CBC, i.e., in the course of the whole respiratory cycle, there must be six or more beats, high respiratory and slow cardiac rates might not meet these preconditions to form a proper CBC. In addition, weak dominance of the respiratory sinus arrhythmia, i.e., a weak modulation of the heart rate by respiration, may have influenced the detection of up and down sequences related to the respiration cycle. Because the respiration cycle was indirectly assessed from the respiratory sinus arrythmia and not directly measured, it may also influence our results. Here, paced breathing would have improved the formation and reliability of the formed CBC. The paced breathing

could serve as a basis to differentiate respiration contribution (high-frequency components) from nonrespiratory components (low-frequency components) in terms of the frequency analysis to investigate the respiratory-related latencies during postural changes (Cooke et al., 1999; Karemaker and De Boer, 2017). Because the respiration rate affects *BRS* (Lehrer et al., 2003), the varying respiration rate may have also influenced our results. Moreover, our study characterizes the cardiovagal hysteresis for supine and standing only and not for extreme changes in blood pressure as would be necessary for the assessment of the complete baroreflex hysteresis.

There are also indications that tidal volume may affect cardiovagal *BRS* (Tzeng et al., 2009). However, as the tidal volume was not measured during the study, we can only assume that it had no influence on *BRS*, which is supported by the observation in Graf and Riedel (2017) that postural changes had no significant effects on the median tidal volume.

CONCLUSION

A novel ellipse method is proposed to model and analyze spontaneous baroreflex sequences forming hysteresis during respiration and for changing posture from supine to standing. Gain and changes in set-points of sequences as well as the working point of baroreflex are considered with the method accounting for integrated mechanical and neural arms of the cardiovagal baroreflex. Observed differences between supine and standing offer instructive insights and provide a basis for future application of the proposed method in analyzing the arterial baroreflex under different conditions and stimuli.

DATA AVAILABILITY STATEMENT

The original contributions presented in the study are included in the article/**Supplementary Material**, further inquiries can be directed to the corresponding author/s.

ETHICS STATEMENT

The studies involving human participants were reviewed and approved by Paris-Necker Committee. The patients/participants provided their written informed consent to participate in this study.

AUTHOR CONTRIBUTIONS

BD and EK conceived and designed the research, interpreted the results, and drafted and revised manuscript. BD and JB performed the data analysis, prepared the figures and tables. The authors agreed to be accountable for all aspects of the work in ensuring that questions related to the accuracy or integrity of any part of the work are appropriately investigated and resolved. All authors contributed to the article and approved the submitted version.

ACKNOWLEDGMENTS

The authors would like to acknowledge the Working Group on Blood Pressure and Heart Rate Variability of the European Society of Hypertension for sharing the used data set in this work. The authors also acknowledge the TU Wien Bibliothek for financial support through its Open Access Funding Program.

SUPPLEMENTARY MATERIAL

The Supplementary Material for this article can be found online at: https://www.frontiersin.org/articles/10.3389/fnins.2021.720031/full#supplementary-material

Supplementary Figure 1 | The spontaneous CBC with overlapping up and down sequences. **(A)** The up sequence (#1 to #4) intersects with the down sequence (◇1 to ◇3). **(B)** The generated binary image of the intersected sequences with the two separated regions and the respective subellipses (red) for each region. **(C)** The generated overall ellipse (bold black) out of subellipses (gray) as based on Eqs 1–3.

Supplementary Figure 2 | The baroreflex sensitivity *BRS* assessed by the linear regression (LR) and the proposed ellipse (E) method for individual up and down sequences, CBC, and for supine and standing. **(A)** *BRS* of up sequences using LR and E methods, down sequences using LR and E methods (from the left to the right). **(B)** *BRS* of sequences forming CBC, up and down sequences using LR, up and down sequences using E. **(C)** *BRS* of up and down sequences using LR and E, *BRS* of CBC (Eq. 3). **(D)** *BRS* of up and down sequences forming CBC, LR versus E method.

Supplementary Table 1 | Comparison of baroreflex sensitivity BRS values [median (mean ± standard deviation)] assessed by the linear regression and the proposed ellipse method for individual up and down sequences and for supine and standing. For comparison, *BRS* from the cardiovagal baroreflex cycles (CBC; Eq. 3) is provided, compare with **Figure 6**.

REFERENCES

Angelone, A., and Coulter, N. A. Jr. (1964). Respiratory sinus arrhythemia: a frequency dependent phenomenon. *J. Appl. Physiol.* 19, 479–482. doi: 10.1152/jappl.1964.19.3.479

Benarroch, E. E. (2008). The arterial baroreflex: functional organization and involvement in neurologic disease. *Neurology* 71, 1733–1738. doi: 10.1212/01.wnl.0000335246.93495.92

Bertinieri, G., Di Rienzo, M., Cavallazzi, A., Ferrari, A. U., Pedotti, A., and Mancia, G. (1985). A new approach to analysis of the arterial baroreflex. *J. Hypertens. Suppl.* 3, S79–S81.

Bertinieri, G., Di Rienzo, M., Cavallazzi, A., Ferrari, A. U., Pedotti, A., and Mancia, G. (1988). Evaluation of baroreceptor reflex by blood pressure monitoring in unanesthetized cats. *Am. J. Physiol.* 254, H377–H383. doi: 10.1152/ajpheart.1988.254.2.H377

Bonyhay, I., Jokkel, G., Karlocai, K., Reneman, R., and Kollai, M. (1997). Effect of vasoactive drugs on carotid diameter in humans. *Am. J. Physiol.* 273, H1629–H1636.

Chapleau, M. W., and Abboud, F. M. (1987). Contrasting effects of static and pulsatile pressure on carotid baroreceptor activity in dogs. *Circ. Res.* 61, 648–658. doi: 10.1161/01.res.61.5.648

Chapleau, M. W., Hajduczok, G., and Abboud, F. M. (1988). New insights into the influence of pulsatile pressure on the arterial baroreceptor reflex. *Clin. Exp. Hypertens. A* 10(Suppl. 1), 179–191. doi: 10.3109/10641968809075971

Choi, Y., Ko, S., and Sun, Y. (2006). "Effect of postural changes on baroreflex sensitivity: a study on the eurobavar data set," in *Proceedings of the 2006*

Canadian Conference on Electrical and Computer Engineering, Ottawa: IEEE CCECE/CCGEI, 110–114.

Convertino, V. A. (2001). Lower body negative pressure as a tool for research in aerospace physiology and military medicine. *J. Gravit. Physiol.* 8, 1–14.

Cooke, W. H., Hoag, J. B., Crossman, A. A., Kuusela, T. A., Tahvanainen, K. U., and Eckberg, D. L. (1999). Human responses to upright tilt: a window on central autonomic integration. *J. Physiol.* 517(Pt 2), 617–628. doi: 10.1111/j.1469-7793.1999.0617t.x

Cooper, V. L., and Hainsworth, R. (2002). Effects of head-up tilting on baroreceptor control in subjects with different tolerances to orthostatic stress. *Clin. Sci. (Lond.)* 103, 221–226. doi: 10.1042/cs1030221

De Maria, B., Bari, V., Cairo, B., Vaini, E., Martins De Abreu, R., Perseguini, N. M., et al. (2019). Cardiac baroreflex hysteresis is one of the determinants of the heart period variability asymmetry. *Am. J. Physiol. Regul. Integr. Comp. Physiol.* 317, R539–R551. doi: 10.1152/ajpregu.00112.2019

De Maria, B., Bari, V., Ranucci, M., Pistuddi, V., Ranuzzi, G., Takahashi, A. C. M., et al. (2018). Separating arterial pressure increases and decreases in assessing cardiac baroreflex sensitivity via sequence and bivariate phase-rectified signal averaging techniques. *Med. Biol. Eng. Comput.* 56, 1241–1252. doi: 10.1007/s11517-017-1765-0

deBoer, R. W., Karemaker, J. M., and Strackee, J. (1987). Hemodynamic fluctuations and baroreflex sensitivity in humans: a beat-to-beat model. *Am. J. Physiol.* 253, H680–H689.

Eckberg, D. L., and Sleight, P. (1992). *Human Baroreflexes in Health and Disease*. Oxford: Clarendon Press.

Fadel, P. J., and Raven, P. B. (2012). Human investigations into the arterial and cardiopulmonary baroreflexes during exercise. *Exp. Physiol.* 97, 39–50. doi: 10.1113/expphysiol.2011.057554

Faes, L., Nollo, G., and Porta, A. (2011). Information domain approach to the investigation of cardio-vascular, cardio-pulmonary, and vasculo-pulmonary causal couplings. *Front. Physiol.* 2:80. doi: 10.3389/fphys.2011.00080

Graf, M., and Riedel, T. (2017). Electrical impedance tomography: amplitudes of cardiac related impedance changes in the lung are highly position dependent. *PLoS One* 12:e0188313. doi: 10.1371/journal.pone.0188313

Hainsworth, R. (1998). "Physiology of the cardiac autonomic system," in *Clinical Guide to Cardiac Autonomic Tests*, ed. M. Malik (Dordrecht: Springer Netherlands), 3–28. doi: 10.1007/978-94-017-1057-2_1

Hart, E. C., Wallin, B. G., Curry, T. B., Joyner, M. J., Karlsson, T., and Charkoudian, N. (2011). Hysteresis in the sympathetic baroreflex: role of baseline nerve activity. *J. Physiol.* 589, 3395–3404. doi: 10.1113/jphysiol.2011.208538

Hughson, R. L., Quintin, L., Annat, G., Yamamoto, Y., and Gharib, C. (1993). Spontaneous baroreflex by sequence and power spectral methods in humans. *Clin. Physiol.* 13, 663–676. doi: 10.1111/j.1475-097x.1993.tb00481.x

Hunt, B. E., Fahy, L., Farquhar, W. B., and Taylor, J. A. (2001). Quantification of mechanical and neural components of vagal baroreflex in humans. *Hypertension* 37, 1362–1368. doi: 10.1161/01.hyp.37.6.1362

Ichinose, M., and Nishiyasu, T. (2012). Arterial baroreflex control of muscle sympathetic nerve activity under orthostatic stress in humans. *Front. Physiol.* 3:314. doi: 10.3389/fphys.2012.00314

Incognito, A. V., Duplea, S. G., Lee, J. B., Sussman, J., Shepherd, A. D., Doherty, C. J., et al. (2019). Arterial baroreflex regulation of muscle sympathetic nerve activity at rest and during stress. *J. Physiol.* 597, 4729–4741.

Incognito, A. V., Samora, M., Shepherd, A. D., Cartafina, R. A., Guimarães, G. M. N., Daher, M., et al. (2020). Sympathetic arterial baroreflex hysteresis in humans: different patterns during low- and high-pressure levels. *Am. J. Physiol. Heart Circ. Physiol.* 319, H787–H792. doi: 10.1152/ajpheart.00505.2020

Kaniusas, E. (2012). *Biomedical Signals and Sensors, Linking Physiological Phenomena and Biosignals*. Berlin: Springer.

Karemaker, J., and De Boer, R. (2017). Vagal baroreflex latency in circulatory control: letters. *J. Physiol.* 595, 2197–2198. doi: 10.1113/JP273766

Kumar, P., and Yildirim, E. A. (2005). Minimum-volume enclosing ellipsoids and core sets. *J. Optim. Theory Appl.* 126, 1–21. doi: 10.1007/s10957-005-2653-6

La Rovere, M. T., Bigger, J. T. Jr., Marcus, F. I., Mortara, A., and Schwartz, P. J. (1998). Baroreflex sensitivity and heart-rate variability in prediction of total cardiac mortality after myocardial infarction. ATRAMI (Autonomic Tone and Reflexes After Myocardial Infarction) investigators. *Lancet* 351, 478–484. doi: 10.1016/s0140-6736(97)11144-8

La Rovere, M. T., Pinna, G. D., and Raczak, G. (2008). Baroreflex sensitivity: measurement and clinical implications. *Ann. Noninvasive Electrocardiol.* 13, 191–207. doi: 10.1111/j.1542-474x.2008.00219.x

Laude, D., Elghozi, J. L., Girard, A., Bellard, E., Bouhaddi, M., Castiglioni, P., et al. (2004). Comparison of various techniques used to estimate spontaneous baroreflex sensitivity (the EuroBaVar study). *Am. J. Physiol. Regul. Integr. Comp. Physiol.* 286, R226–R231. doi: 10.1152/ajpregu.00709.2002

Lehrer, P. M., Vaschillo, E., Vaschillo, B., Lu, S. E., Eckberg, D. L., Edelberg, R., et al. (2003). Heart rate variability biofeedback increases baroreflex gain and peak expiratory flow. *Psychosom. Med.* 65, 796–805.

Lénárd, Z., Fülöp, D., Visontai, Z., Jokkel, G., Reneman, R., and Kollai, M. (2000). Static versus dynamic distensibility of the carotid artery in humans. *J. Vasc. Res.* 37, 103–111. doi: 10.1159/000025721

Ler, A. S., Cohen, M. A., and Taylor, J. A. (2010). A planar elliptical model of cardio-vagal hysteresis. *Physiol. Meas.* 31, 857–873. doi: 10.1088/0967-3334/31/6/009

Levy, M. N., and Zieske, H. (1969). Autonomic control of cardiac pacemaker activity and atrioventricular transmission. *J. Appl. Physiol.* 27, 465–470. doi: 10.1152/jappl.1969.27.4.465

Masuda, Y., Pace, D. G., and Levy, M. N. (1984). The rate of arterial blood pressure change as a factor in the hysteresis of the baroreceptor reflex. *J. Hypertens.* 2, 189–194.

Nixon, P. G. F. (1988). *Human Circulation Regulation During Physical Stress*. London: Oxford University Press

Parati, G., Di Rienzo, M., Bertinieri, G., Pomidossi, G., Casadei, R., Groppelli, A., et al. (1988). Evaluation of the baroreceptor-heart rate reflex by 24-hour intra-arterial blood pressure monitoring in humans. *Hypertension* 12, 214–222. doi: 10.1161/01.hyp.12.2.214

Pickering, T. G., and Davies, J. (1973). Estimation of the conduction time of the baroreceptor-cardiac reflex in man. *Cardiovasc. Res.* 7, 213–219. doi: 10.1093/cvr/7.2.213

Rogers, R. F., Paton, J. F., and Schwaber, J. S. (1993). NTS neuronal responses to arterial pressure and pressure changes in the rat. *Am. J. Physiol.* 265, R1355–R1368.

Rogers, R. F., Rose, W. C., and Schwaber, J. S. (1996). Simultaneous encoding of carotid sinus pressure and dP/dt by NTS target neurons of myelinated baroreceptors. *J. Neurophysiol.* 76, 2644–2660. doi: 10.1152/jn.1996.76.4.2644

Rowell, L. B. (1986). *Human Circulation*. New York, NY: Oxford University Press.

Rudas, L., Crossman, A. A., Morillo, C. A., Halliwill, J. R., Tahvanainen, K. U., Kuusela, T. A., et al. (1999). Human sympathetic and vagal baroreflex responses to sequential nitroprusside and phenylephrine. *Am. J. Physiol.* 276, H1691–H1698.

Saul, J. P., Berger, R. D., Albrecht, P., Stein, S. P., Chen, M. H., and Cohen, R. J. (1991). Transfer function analysis of the circulation: unique insights into cardiovascular regulation. *Am. J. Physiol.* 261, H1231–H1245. doi: 10.1152/ajpheart.1991.261.4.H1231

Seagard, J. L., Brederode, J. F. V., Dean, C., Hopp, F. A., Gallenberg, L. A., and Kampine, J. P. (1990). Firing characteristics of single-fiber carotid sinus baroreceptors. *Circ. Res.* 66, 1499–1509. doi: 10.1161/01.res.66.6.1499

Silva, L. E. V., Dias, D. P. M., Da Silva, C. A. A., Salgado, H. C., and Fazan, R. (2019). Revisiting the sequence method for baroreflex analysis. *Front. Neurosci.* 13:17. doi: 10.3389/fnins.2019.00017

Smyth, H. S., Sleight, P., and Pickering, G. W. (1969). Reflex regulation of arterial pressure during sleep in man. A quantitative method of assessing baroreflex sensitivity. *Circ. Res.* 24, 109–121. doi: 10.1161/01.res.24.1.109

Steinback, C. D., O'leary, D. D., Bakker, J., Cechetto, A. D., Ladak, H. M., and Shoemaker, J. K. (2005). Carotid distensibility, baroreflex sensitivity, and orthostatic stress. *J. Appl. Physiol.* 99, 64–70. doi: 10.1152/japplphysiol.01248.2004

Steptoe, A., and Vögele, C. (1990). Cardiac baroreflex function during postural change assessed using non-invasive spontaneous sequence analysis in young men. *Cardiovasc. Res.* 24, 627–632. doi: 10.1093/cvr/24.8.627

Studinger, P., Goldstein, R., and Taylor, J. A. (2007). Mechanical and neural contributions to hysteresis in the cardiac vagal limb of the arterial baroreflex. *J. Physiol.* 583, 1041–1048. doi: 10.1113/jphysiol.2007.139204

Suarez-Roca, H., Klinger, R. Y., Podgoreanu, M. V., Ji, R. R., Sigurdsson, M. I., Waldron, N., et al. (2019). Contribution of baroreceptor function to pain

perception and perioperative outcomes. *Anesthesiology* 130, 634–650. doi: 10.1097/ALN.0000000000002510

Taylor, C. E., Willie, C. K., Ainslie, P. N., and Tzeng, Y. C. (2014). Assessment of human baroreflex function using carotid ultrasonography: what have we learnt? *Acta Physiol.* 211, 297–313. doi: 10.1111/apha.12302

Taylor, C. E., Willie, C. K., Atkinson, G., Jones, H., and Tzeng, Y. C. (2013). Postural influences on the mechanical and neural components of the cardiovagal baroreflex. *Acta Physiol.* 208, 66–73. doi: 10.1111/apha.12087

Turjanmaa, V., Kalli, S., Sydänmaa, M., and Uusitalo, A. (1990). Short-term variability of systolic blood pressure and heart rate in normotensive subjects. *Clin. Physiol.* 10, 389–401. doi: 10.1111/j.1475-097x.1990.tb00799.x

Tzeng, Y. C., Sin, P. Y., Lucas, S. J., and Ainslie, P. N. (2009). Respiratory modulation of cardiovagal baroreflex sensitivity. *J. Appl. Physiol.* 107, 718–724. doi: 10.1152/japplphysiol.00548.2009

Ursino, M. (1998). Interaction between carotid baroregulation and the pulsating heart: a mathematical model. *Am. J. Physiol.* 275, H1733–H1747. doi: 10.1152/ajpheart.1998.275.5.H1733

Wang, W., Brändle, M., and Zucker, I. H. (1993). Influence of vagotomy on the baroreflex sensitivity in anesthetized dogs with experimental heart failure. *Am. J. Physiol.* 265, H1310–H1317. doi: 10.1152/ajpheart.1993.265.4.H1310

Conflict of Interest: The authors declare that the research was conducted in the absence of any commercial or financial relationships that could be construed as a potential conflict of interest.

Publisher's Note: All claims expressed in this article are solely those of the authors and do not necessarily represent those of their affiliated organizations, or those of the publisher, the editors and the reviewers. Any product that may be evaluated in this article, or claim that may be made by its manufacturer, is not guaranteed or endorsed by the publisher.

frontiers in Neuroscience

ORIGINAL RESEARCH
published: 12 January 2022
doi: 10.3389/fnins.2021.791510

Synchronization of the Processes of Autonomic Control of Blood Circulation in Humans Is Different in the Awake State and in Sleep Stages

Anatoly S. Karavaev[1,2,3], Viktoriia V. Skazkina[2,4], Ekaterina I. Borovkova[1,2,3], Mikhail D. Prokhorov[2,3], Aleksey N. Hramkov[2], Vladimir I. Ponomarenko[3], Anastasiya E. Runnova[1,2], Vladimir I. Gridnev[1], Anton R. Kiselev[1,2,5], Nikolay V. Kuznetsov[4,6,7], Leonid S. Chechurin[4,6] and Thomas Penzel[2,8]*

[1] Department of Basic Research in Neurocardiology, Institute of Cardiological Research, Saratov State Medical University, Saratov, Russia, [2] Smart Sleep Laboratory, Saratov State University, Saratov, Russia, [3] Laboratory of Nonlinear Dynamics Modeling, Saratov Branch of the Institute of Radio Engineering and Electronics of Russian Academy of Sciences, Saratov, Russia, [4] LUT School of Engineering Science, LUT University, Lappeenranta, Finland, [5] Coordinating Center for Fundamental Research, National Medical Research Center for Therapy and Preventive Medicine, Moscow, Russia, [6] Faculty of Mathematics and Mechanics, St. Petersburg State University, St. Petersburg, Russia, [7] Institute for Problems in Mechanical Engineering RAS, St. Petersburg, Russia, [8] Interdisciplinary Sleep Medicine Center, Charité - Universitätsmedizin Berlin, Berlin, Germany

OPEN ACCESS

Edited by:
Yue-Der Lin,
Feng Chia University, Taiwan

Reviewed by:
Yina Wei,
Zhejiang Lab, China
Vlasta Bari,
IRCCS San Donato Polyclinic, Italy

***Correspondence:**
Anatoly S. Karavaev
karavaevas@gmail.com

Specialty section:
This article was submitted to Autonomic Neuroscience, a section of the journal Frontiers in Neuroscience

Received: *08 October 2021*
Accepted: *09 December 2021*
Published: *12 January 2022*

Citation:
Karavaev AS, Skazkina VV, Borovkova EI, Prokhorov MD, Hramkov AN, Ponomarenko VI, Runnova AE, Gridnev VI, Kiselev AR, Kuznetsov NV, Chechurin LS and Penzel T (2022) Synchronization of the Processes of Autonomic Control of Blood Circulation in Humans Is Different in the Awake State and in Sleep Stages. Front. Neurosci. 15:791510. doi: 10.3389/fnins.2021.791510

The influence of higher nervous activity on the processes of autonomic control of the cardiovascular system and baroreflex regulation is of considerable interest, both for understanding the fundamental laws of the functioning of the human body and for developing methods for diagnostics and treatment of pathologies. The complexity of the analyzed systems limits the possibilities of research in this area and requires the development of new tools. Earlier we propose a method for studying the collective dynamics of the processes of autonomic control of blood circulation in the awake state and in different stages of sleep. The method is based on estimating a quantitative measure representing the total percentage of phase synchronization between the low-frequency oscillations in heart rate and blood pressure. Analysis of electrocardiogram and invasive blood pressure signals in apnea patients in the awake state and in different sleep stages showed a high sensitivity of the proposed measure. It is shown that in slow-wave sleep the degree of synchronization of the studied rhythms is higher than in the awake state and lower than in sleep with rapid eye movement. The results reflect the modulation of the processes of autonomic control of blood circulation by higher nervous activity and can be used for the quantitative assessment of this modulation.

Keywords: autonomic control, cardiovascular system, sleep studies, synchronization, apnea, interbeat intervals, blood pressure

INTRODUCTION

Arterial baroreflex plays an important role in the functioning of the autonomic nervous system (Subramanian et al., 2019). It is involved in the regulation of blood pressure (BP) (Osborn et al., 2005; Albaghdadi, 2007), heart rate (HR) (Lanfranchi and Somers, 2002), and respiration (Guyenet, 2014). According to a number of studies, the baroreflex and the processes of autonomic control

determine the complex dynamics of blood circulation, in particular, the non-linear dynamics of heart rhythm (Tan, 2013; Ernst, 2017; Karavaev et al., 2019). It is known that autonomic control loops are sensitive to changes in the physiological state of healthy subjects (Ivanov et al., 1999; Valente et al., 2018; Ishbulatov et al., 2020). There is a significant change in baroreflex functions with aging (Sharma and Goodwin, 2006; Schumann et al., 2010; Shiogai et al., 2010; Elliott et al., 2016; Parashar et al., 2016; Natarajan et al., 2020; Pietri and Stefanadis, 2021). Impaired baroreflex regulation and impaired heart rate variability often accompany cardiovascular diseases (Kiselev et al., 2012a,b; Ponomarenko et al., 2013; Swenne, 2013; Karavaev et al., 2016). Therefore, the baroreflex sensitivity and the activity of autonomic control processes are often used to assess the physiological state of subjects and act as the markers of the development of pathologies of various systems of the body (Lázaro et al., 2019; Hadaya and Ardell, 2020; Wessel et al., 2020).

The regulation of the cardiovascular system and respiration is influenced by cortical structures that influence the baroreflex regulation under normal conditions (Furness, 2006; Duschek et al., 2013; Jerath and Beveridge, 2020) and during the development of pathologies (Lewis et al., 2006; Molkov et al., 2014). Considerable attention of researchers is paid to the peculiarities of baroreflex regulation and autonomic control of cardiovascular system during sleep (Brandenberger et al., 2003). The analysis of experimental signals in such studies involves the use of different methods for the assessment of baroreflex function and autonomic control (Shaffer and Ginsberg, 2017). Historically, the first are methods of statistical, correlation, and spectral analysis of RR-intervals (Task Force of the European Society of Cardiology [TFESC], 1996), which reflect the processes of frequency modulation of the HR by the autonomic control loops (Prokhorov et al., 2021). The analysis of RR-intervals traditionally includes the study of the so-called Low-Frequency (LF) band (0.04–0.14 Hz), which is mainly associated with the processes of sympathetic control of heart rate (Wagner and Persson, 1998), and the High-Frequency (HF) band (0.14–0.40 Hz), which is associated with the processes of parasympathetic control (Task Force of the European Society of Cardiology [TFESC], 1996; Lewis et al., 2006). Information about sympathetic regulation of blood pressure can be obtained by analyzing blood pressure signals in the LF-band (O'Leary and Woodbury, 1996; Elstad et al., 2011; Orini et al., 2012). At the same time, the frequency components of the blood pressure signal in the HF-band are mainly associated with the mechanical conduct of the respiration process into the vessels (Bernardi et al., 1996; Dash et al., 2010; Javed et al., 2010).

Despite considerable interest in the problem, the existing number of works describing the activity of autonomic control loops in the awake state and in different sleep stages: rapid eye movement (REM) and non-REM (NREM) demonstrates some contradictory results. In particular, in a seminal study (Somers et al., 1993) it is noted that the activity of the sympathetic branch of the autonomic control system increases in the REM sleep and decreases in the stages of NREM sleep relative to the awake state. Other studies show a decrease (Berlad et al., 1993; Parmeggiani, 1994), increase (Hornyak et al., 1991; Somers et al., 1993; Van de Borne et al., 1994) or the absence of changes (Vanoli et al., 1995) in the activity of sympathetic regulation of blood circulation in REM sleep compared with NREM sleep (Elsenbruch et al., 1999) showed a statistical difference between spectral assessments of the signals of systolic blood pressure (SBP), diastolic blood pressure and RR-intervals in the awake state, NREM and REM sleep; and (Legramante et al., 2003) shows their significant fluctuation depending on the sequence of the REM and NREM stages during the night.

The study (Zemaityte et al., 1984) revealed increases in the activity of the parasympathetic branch of the autonomic nervous system during REM sleep and decreases in NREM sleep state relative to the waking state. Such observations are explained by the modulation of the activity of the centers of autonomic control by the processes of higher nervous activity (Van Roon et al., 2004; Cheng et al., 2010).

In addition to the use of typical spectral assessments, baroreflex sensitivity assessments are often used (Laude et al., 2004; La Rovere et al., 2008; Maestri et al., 2009). However, the effectiveness of its use for the diagnosis of different sleep stages remains an open question. Thus, an increase in the sensitivity of the arterial baroreflex in sleep was noted in Smyth et al. (1969), Conway et al. (1983), Pagani et al. (1988), Parati et al. (1988), and Van de Borne et al. (1994). Moreover, special experiments have shown that an increase in baroreflex sensitivity is not a simple consequence of decreasing in mean arterial pressure during sleep (Smyth et al., 1969).The authors of Bristow et al. (1969) and Nakazato et al. (1998) show no significant changes in different sleep stages.

Furthermore, it is worth noting, that although several methods have been developed to study baroreflex sensitivity in humans, most of these techniques are of limited value for daily practice and require specialized pharmacological or mechanical manipulations (Smyth et al., 1969; Eckberg et al., 1975; Palmero et al., 1981; Airaksinen et al., 1993; Bernardi et al., 1995; Mortara et al., 1997; Pinna et al., 2000).

Nevertheless, the study of baroreflex function and autonomic control during sleep is of great importance in patients and healthy subjects, and research interest in this issue does not decrease (Guilleminault et al., 1981; Lombardi et al., 2019).

Thus, although the analysis of heart rate variability properties seems to correlate with the psychophysical state of the patient and the baroreflex function is associated with sleep stages, the sensitivity of linear analysis methods is limited (Billman, 2013).

Therefore, more sensitive non-linear methods of analysis are used in recent years. Such methods aim at assessing different measures of complexity in RR-intervals and blood pressure signals (Pichot et al., 2016; Ishaque et al., 2021). Earlier in the work (Karavaev et al., 2009) we proposed a quantitative measure representing the total percentage S of phase synchronization between the LF oscillations in RR-intervals and BP (Karavaev et al., 2021). In the works (Kiselev et al., 2012a,b, 2016b), we showed that the previously proposed method (Karavaev et al., 2009) is promising for solving problems of medical diagnostics. This measure allows us to predict the development of complications of myocardial infarction (Kiselev et al., 2012a), to select the drug therapy for arterial hypertension

(Kiselev et al., 2012b), and to obtain important information about the structure of interactions between the elements of autonomic control of the cardiovascular system (Kiselev et al., 2020). In work (Ponomarenko et al., 2021), we showed a change in the coherence of respiration processes and parasympathetic regulation of the heart rate in the HF-band in the awake state and different stages of sleep. However, studies of the synchronization of the processes of autonomic control of blood circulation in the LF-band with changes in the physiological state of the subjects during sleep and awake state remain unknown.

Therefore, the purpose of this work is to identify changes in the synchronization of processes of autonomic control of the HR and BP when analyzing the LF-components of RR-intervals and blood pressure signals in the awake state, REM and NREM stages of sleep, as well as to study the possibility of classifying such states during the analysis of synchronization and other assessments characterizing the properties of heart rate variability (Task Force of the European Society of Cardiology [TFESC], 1996) and baroreflex sensitivity (Pagani et al., 1988).

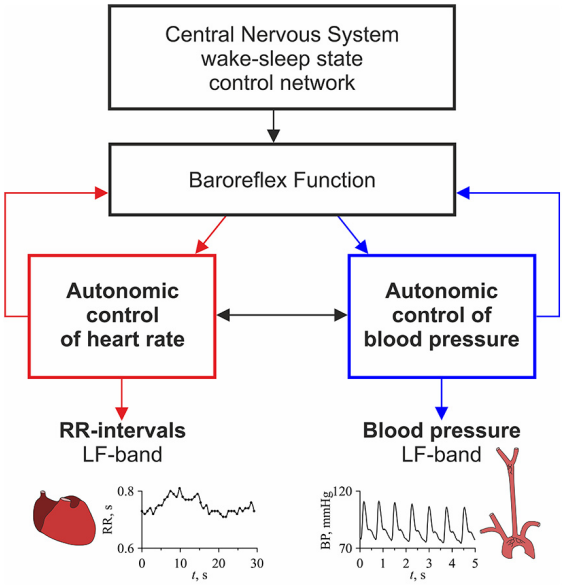

FIGURE 1 | A simplified schematic illustration of the study.

MATERIALS AND METHODS

Object of Study

Figure 1 shows a simplified schematic illustration of the object of study. The autonomic nervous system is actively involved in the control of HR and BP, using baroreflex functions (Task Force of the European Society of Cardiology [TFESC], 1996; Ringwood and Malpas, 2001). The work (Kiselev et al., 2020) shows, this control is provided by relatively independent processes that interact with each other. Information about the processes of autonomic control of HR and BP can be extracted from the LF-components of RR-intervals and BP signals (Task Force of the European Society of Cardiology [TFESC], 1996; Ringwood and Malpas, 2001; Prokhorov et al., 2003). It shows that these LF-components can be synchronized, and the degree of their synchronization correlates with the state of the cardiovascular system (Karavaev et al., 2009). It is known that the wake-sleep state control network of the central nervous system modulates the activity of the elements of the autonomic nervous system, and this influence changes during the transition from the awake state to sleep stages (Van Roon et al., 2004; Cheng et al., 2010). Thus, the degree of synchronization between the processes of autonomic control of HR and BP should reflect the effect of the wake-sleep state control network of the central nervous system on the autonomic nervous system.

Experimental Data

We analyzed the electrocardiogram (ECG), BP, and respiration signals of 22 male patients (mean age 52 $\pm$ 10 years, body mass index 32.4 $\pm$ 6.0 kg/m^2) obtained in a clinical study (Peter et al., 1989; Grote et al., 1995). All patients were hospitalized due to obstructive breathing disorders during sleep (mean respiratory disturbance index 47.2 $\pm$ 27.3 n/h), and arterial hypertension was also revealed in the patients. Recordings were made before the therapy.

The ECG signal was recorded in standard lead I according (Kligfield et al., 2007). The BP signal (time dependence of blood pressure during invasive arterial pressure monitoring) was recorded with an invasive monitoring system from the radial is artery. The respiration signal was recorded with a flowing oronasal airflow. All signals were filtered with the bandpass of 0.03–45 Hz and sampled at 100 Hz. For each subject, we extracted three 20-min fragments from the night record, one corresponding to the awake state, one to the stage S3 of NREM sleep, and one to REM sleep. The awake state and sleep stages were scored in accordance with the recommendations of Rechtschaffen and Kales (1968) by means of electro-oculogram, electroencephalogram, and electromyogram. The analyzed fragments did not contain artifacts or long periods of apnea.

Total Percentage of Phase Synchronization

To analyze the degree of synchronization between the LF oscillations in HR and BP, we use a quantitative measure representing the total percentage S of phase synchronization of the studied processes. The method is based on the approach for detecting synchronization of complex systems from the analysis of their non-stationary time series (Karavaev et al., 2009; Kiselev et al., 2016a). Comparison of the proposed method with other known methods for detecting synchronization showed its higher sensitivity (Borovkova et al., 2020, 2021).

Figure 2 illustrates the main stages of the method. From the experimental ECG signal we extract a sequence of RR-intervals, i.e., a series of time intervals between the two successive R peaks. To obtain equidistant time series from not equidistant sequence of RR-intervals, we approximate it with cubic b-splines

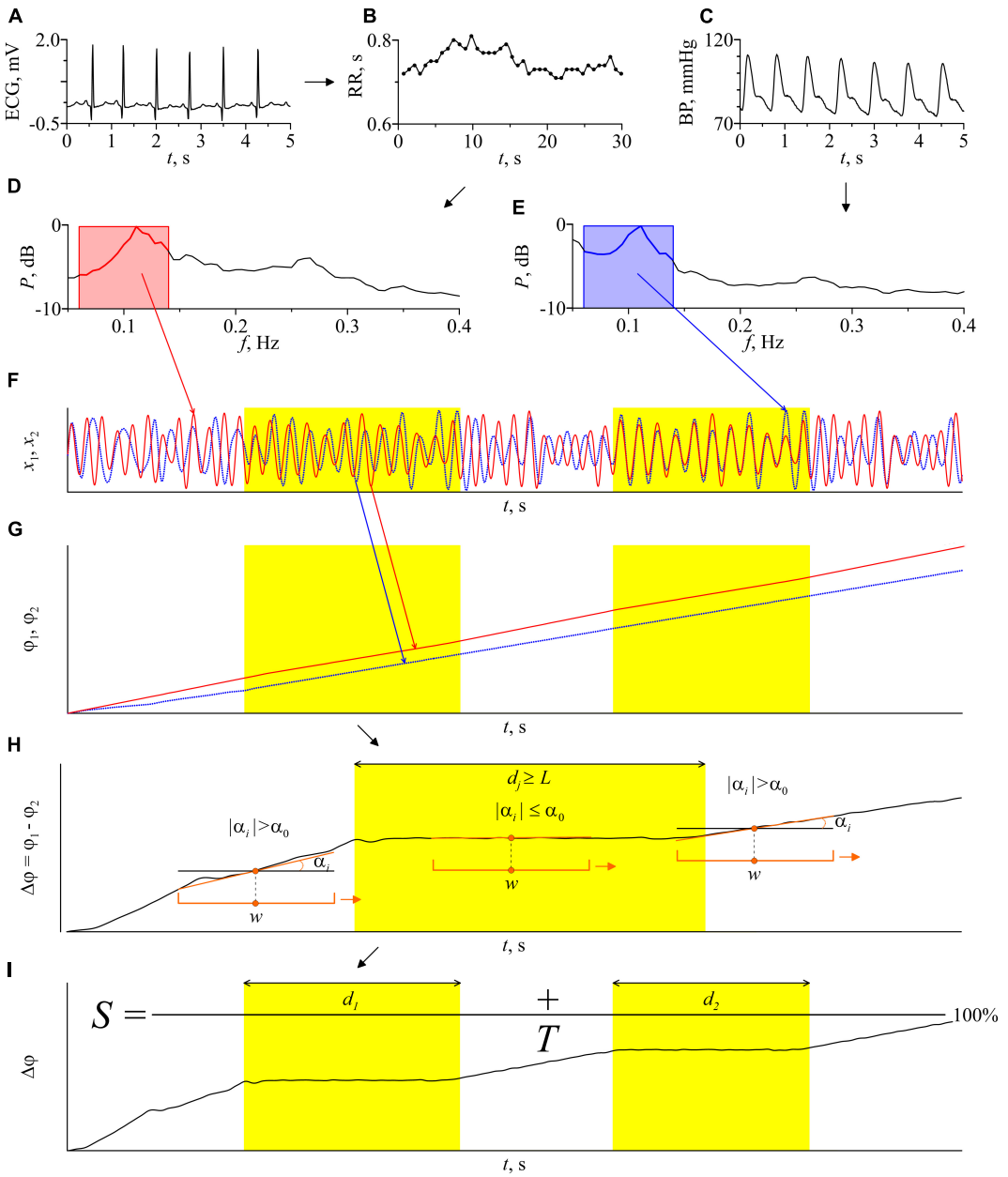

FIGURE 2 | Schematic illustration of the method for estimating the total percentage *S* of phase synchronization. **(A)** ECG signal; **(B)** RR-intervals. Dots show experimental values of RR-intervals, interpolation by cubic β-splines is shown by a line; **(C)** the BP signal; **(D)** the power spectrum of the RR-interval signal; **(E)** power spectrum of the blood pressure signal. The bandwidth of the bandpass filters is marked in pink and blue on the power spectra graphs; **(F)** signals of RR-intervals and blood pressure filtered in the LF-band and normalized to unity amplitude; **(G)** instantaneous phases of the filtered signals of RR-intervals and blood pressure; **(H)** the instantaneous phases difference of the signals and an illustration of the automatic procedure for finding the epochs of synchronization. Orange bracket marks a window sliding along the time series $\Delta\phi(t)$ with a shift of 1 discrete sample. *w* is the sliding window width. The orange line is a linear approximation of the time series $\Delta\phi(t)$ in every sliding window. α_i is the slope of the approximating line in *i*th sliding window. α_0 is the method parameter, maximum slope angle, d_j is the length of *j*th epoch of synchronization. Parameter *L* has the meaning of the minimum length of the synchronization epoch; **(I)** illustration of the procedure for calculating the index of the total percentage of phase synchronization *S*. *T* is the time series length, d_1 and d_2 are the length of the identified epochs of synchronization. The epochs of synchronization are shown in yellow.

and resampled with a frequency of 5 Hz. Then, we filter the sequence of RR-intervals and the signal of BP using a filter with the bandpass of 0.06–0.14 Hz. After that, we resample the filtered BP signal with a sampling frequency of 5 Hz. The filtered signals are normalized so that their maximum amplitude is equal to unity.

Next, we define the instantaneous phases $\phi_1(t)$ and $\phi_2(t)$ of the filtered RR-intervals and BP signal, respectively, as the angle

of rotation of the radius vector on the plane $(x(t), \tilde{x}(t))$, where $x(t)$ is the analyzed signal and $\tilde{x}(t)$ is the Hilbert transform of $x(t)$,

$$\tilde{x}(t) = \frac{1}{\pi}\text{P.V.}\int_{-\infty}^{+\infty}\frac{x(\tau)}{t-\tau}d\tau, \quad (1)$$

where P.V. means that the integral is taken in the sense of the Cauchy principal value on a time series (Rosenblum and Kurths, 1998). Then, we calculate the difference of instantaneous phases $\phi_1(t)$ and $\phi_2(t)$:

$$\Delta\phi(t) = \phi_2(t) - \phi_1(t). \quad (2)$$

The presence of 1:1 phase synchronization of two processes is defined by the condition:

$$|\phi_2(t) - \phi_1(t)| < C, \quad (3)$$

where C is a constant (Pikovsky et al., 2001). Thus, in the epochs of synchronization, $\Delta\phi(t)$ demonstrates horizontal plateaus, the oscillations on which are determined only by the measurement noise.

For automatic detection of phase synchronization epochs, we use the following algorithm. A window with a width w moves along the time series of $\Delta\phi(t)$ with a shift of one sample (0.2 s). Using the method of least squares, we linearly approximate $\Delta\phi(t)$ in each ith moving window by calculating a slope α_i. The presence of synchronization is defined by the condition $|\alpha_i| \leq \alpha_0$, where α_0 is the method parameter. To reduce the influence of random fluctuations of instantaneous phases, we use an additional condition $d_j \geq L$ for the detection of phase synchronization, where d_j is the length of the jth epoch of synchronization and L is the method parameter. Specialized statistical tests carried out in the study (Borovkova et al., 2020, 2021) allow us to choose the following parameters of the method: w = 22 s, α_0 0.004 rad, L = 10 s. These values are used throughout the paper.

A sufficiently wide w window (more than 2 characteristic periods of oscillations) allows one to reduce the influence of phase noise. The method's algorithm assumes that the epoch is identified as an epoch of synchronization if the slope of the approximating straight line remains below the threshold value for a continuous-time interval with a length of at least L (about 1 characteristic period). In this case, the window w is shifted each time by one sample of discrete-time. Such conditions make it possible to increase the accuracy of diagnostics of the boundaries of the epoch of synchronization when moving the window w between synchronous and asynchronous epochs. Then we calculate the total length of the identified epochs of phase synchronization and express it as a percentage relative to the time series length of the entire record. The total percentage of phase synchronization is calculated as follows:

$$S = \frac{\sum_{j=1}^{N} d_j}{T} \times 100\%, \quad (4)$$

where T is the time series length of the entire record and N is the number of epochs of synchronization. The calculation of the phase synchronization index S uses the LF-filtered time series of RR-intervals and BP as a whole: 20-min time series (6000 samples at a sampling rate of 5 Hz).

The method for calculating measure S is implemented using the Python programming language. The program is available for free use at[1].

Statistical Significance of the Index *S*

Signals of complex systems of biological nature are usually nonlinear, non-stationary, and susceptible to noise and artifacts of different nature. Therefore, each values of index S obtained from experimental data was accompanied by the estimate the statistical significance. For each 20-min pair of ECG and BP signals, we generate a statistical ensemble of 100 pairs of surrogate time series by randomizing the phases of the Fourier-harmonics of analyzed signals in accordance with the method proposed in Theiler et al. (1992) and Schreiber and Schmitz (1996). This method for surrogate data preparation preserves periodogram of the experimental signals, but destroys couplings between them. Then, we calculate a total percentage of phase synchronization S_k, $k = 1, \ldots, 100$ for each kth pair of surrogates and sorted S_k values in ascending order. The measure S calculated from the experimental signals is considered statistically significant ($p < 0.05$) if it is greater than the 95th S_k value calculated from surrogate data.

Heart Rate Variability Indices

Some well-known works (Smyth et al., 1969; Pagani et al., 1988; Vanoli et al., 1995; Nakazato et al., 1998; Elsenbruch et al., 1999; Legramante et al., 2003) show a change in the baroreflex function and, as a consequence, the values of common assessments characterizing the properties of heart rate and blood pressure change during the transition from the awake state to different stages of sleep. Linear methods of spectral and statistical analysis of signals are often used for these investigations (Task Force of the European Society of Cardiology [TFESC], 1996). The following assessments are widely used to separate the awake state and different stages of sleep: X_{mean} (ms) - mean length of RR-intervals, *SDNN* - the standard deviation of length of the RR-intervals, HF_{RR} (ms^2) - the power of the spectrum of the HF components of the RR-intervals and BP, LF_{RR} (ms^2) - the power of the spectrum of the LF components of the RR-intervals. We calculate these assessments in this work. We used the first 5 min of the RR-interval signal. The calculation of the assessments of heart rate variability was carried out by the well-known methodological recommendations (Task Force of the European Society of Cardiology [TFESC], 1996).

Baroreflex Sensitivity Index

Baroreflex sensitivity (BRS) is also a recognized tool for assessing the autonomic control of the cardiovascular system.

In this work, the assessment of the baroreflex sensitivity was carried out based on spectral analysis of the signal of RR-intervals and systolic blood pressure and was used along with other typical tools for diagnosing the stages of sleep and the awake state (Smyth et al., 1969; Pagani et al., 1988;

[1]http://nonlinmod.sgu.ru/comprog_en.htm

Legramante et al., 2003). BRS assessments are often based on calculating the power spectral density of the RR-intervals and SBP signals in the LF and/or HF frequency bands (Pagani et al., 1988; Legramante et al., 2003; Dietrich et al., 2010). In Dietrich et al. (2010), results showed similar values of BRS assessments carried out by different methods. Therefore in this paper, BRS was assessed by calculating the alpha index in accordance with the recommendations (Pagani et al., 1988).

In this work the BRS was assessed based on the signals of the RR-intervals and the signal of SBP. To calculate the assessment of BRS, we isolated a non-equidistant sequence of peaks from invasive BP signal (one peak per cardiocycle - at the moment of systole). Subsequently, this non-equidistant series of the SBP signal and the RR-intervals signal was interpolated with a cubic β-spline up to a sampling frequency of 5 Hz. The power spectra were calculated from them, and the integrated power in the LF-band (0.04–0.15 Hz) was estimated.

$$BRS = \sqrt{\int_{f_1}^{f_2} S(f_{LF_{RR}})df \Big/ \int_{f_1}^{f_2} S(f_{LF_{SBP}})df}, \quad (5)$$

where f_1 0.04 Hz, f_2 0.15 Hz, is $\int_{f_1}^{f_2} S(f_{LF_{RR}})df$ the integrated power of the spectrum of the LF-component of the RR-intervals, $\int_{f_1}^{f_2} S(f_{LF_{SBP}})df$ is the integrated power of the spectrum of the LF-component of the SBP.

This assessment of *BRS* estimate is based on the assumption of a high degree of linear correlation between RR-intervals and SBP variability in the LF-band. This method is simple enough to quickly estimate BRS based on standard spectral characteristics.

Statistical Analysis

We used receiver operating characteristic (ROC) to assess the quality of the binary classification of calculated indices for different pairs of states (REM vs awake, REM vs. NREM, and NREM vs. awake).

Let us illustrate the procedure for constructing ROC-curves by analyzing the *S* index as an example. To construct the ROC curve for each pair, we went through the threshold value of the parameter of total percentage of phase synchronization S_0 from 0 to 100% with step 1%. Each threshold value S_0 we compared with grades S_i, i = 1,..,22 for all subjects in the first (in each matched pair) state and S_j, j = 1,..,22 – in the second state. To estimate TPR, we calculated the split of results $S_i > S_0$. To estimate FPR we calculated the split of results $S_j > S_0$. Each point on the ROC curve shows the relationship between TPR and FPR for each threshold value S_0. Comparison of the ROC curves was carried out in the course of calculating the characteristic - Area Under the Curve (AUC).

Similarly, we constructed ROC curves for the other comparable assessments. At the same time, for the X_{mean} and HF_{RR} indices, for classifying states in accordance with the results *a priori* known from Oh et al. (2019), it was assumed that during the transition from the awake and REM sleep to the deep sleep, the assessments should increase, and for other cases-decrease.

For each ROC-curve, we found the threshold value of the index corresponding to the put off point (the point closest to the point TPR = 1.0, FPR = 0.0). For put off points, we calculated the odds ratio and *p*-value.

To check the reliability of differences in the estimates of the mean values of assessments for different stages, we used the Kruskal-Wallis test (Kruskal, 1952), which takes into account multiple testing, and the Mann-Whitney *U*-test (Mann and Whitney, 1947), which does not take into account the correction for multiple testing but allowing for pairwise comparison.

RESULTS

Figure 3 shows the experimental signals and the results of their analysis for one of the subjects in the awake state, NREM sleep, and REM sleep. **Figures 3A–C** present the ECG signals in the awake state, NREM sleep, and REM sleep, respectively.

RR-intervals show low variability, that typical in subjects at rest (**Figures 3D–F**). BP signals in the awake state, NREM sleep, and REM sleep are presented in **Figures 3G–I**, respectively. The values of BP correspond to those observed in healthy subjects (Young et al., 2020). The power spectra of the RR-intervals are shown in **Figures 3J–L**, while the power spectra of the BP signals are shown in **Figures 3M–O**. These power spectra are normalized to the maximum value in the three considered states, which takes place for NREM sleep. The characteristic peaks in the LF-band of power spectra are associated with the processes of autonomic control and baroreflex activity, while the peaks in the HF-band are associated with the respiration.

In the spectra of RR-intervals, the power in the LF-band in the awake state is higher than in NREM sleep and lower than in REM sleep. This is consistent with the known results (Somers et al., 1993; Kantelhardt et al., 2002). On the contrary, the power in the HF-band in the awake state is lower than in NREM sleep and higher than in REM sleep. This result agrees well with other studies (Zemaityte et al., 1984; Bartsch et al., 2012).

In the power spectra of BP signals, the HF-component is most pronounced in NREM sleep. Oscillatory activity in the HF-band of BP signal is usually related to the respiratory driven BP oscillations through changes in the intra-thoracic pressure if the respiratory frequency remains within the normal limits (Dornhorst et al., 1954; De Boer et al., 1987; Sleight et al., 1995; Conci et al., 2001). The study of such effects was beyond the scope of this paper.

Figures 3P–R depict the dependences $\Delta\phi(t)$ for the awake state, NREM sleep, and REM sleep, respectively. The length of phase synchronization epochs in REM sleep is noticeably greater than in other two states. In the awake state, $\Delta\phi(t)$ slowly fluctuates around 0. In NREM sleep, a slow positive trend of $\Delta\phi(t)$ is observed, which indicates that the instantaneous phase of LF-component in RR-intervals grows faster than the phase of LF-component in BP signal. In REM sleep, a negative trend of $\Delta\phi(t)$ takes place that indicates the faster increase of the phase of BP signal LF-component with respect to the phase of LF-component in RR-intervals. However, the sign of trend in $\Delta\phi(t)$ differs in different subjects. In **Figure 3**, the total percentage

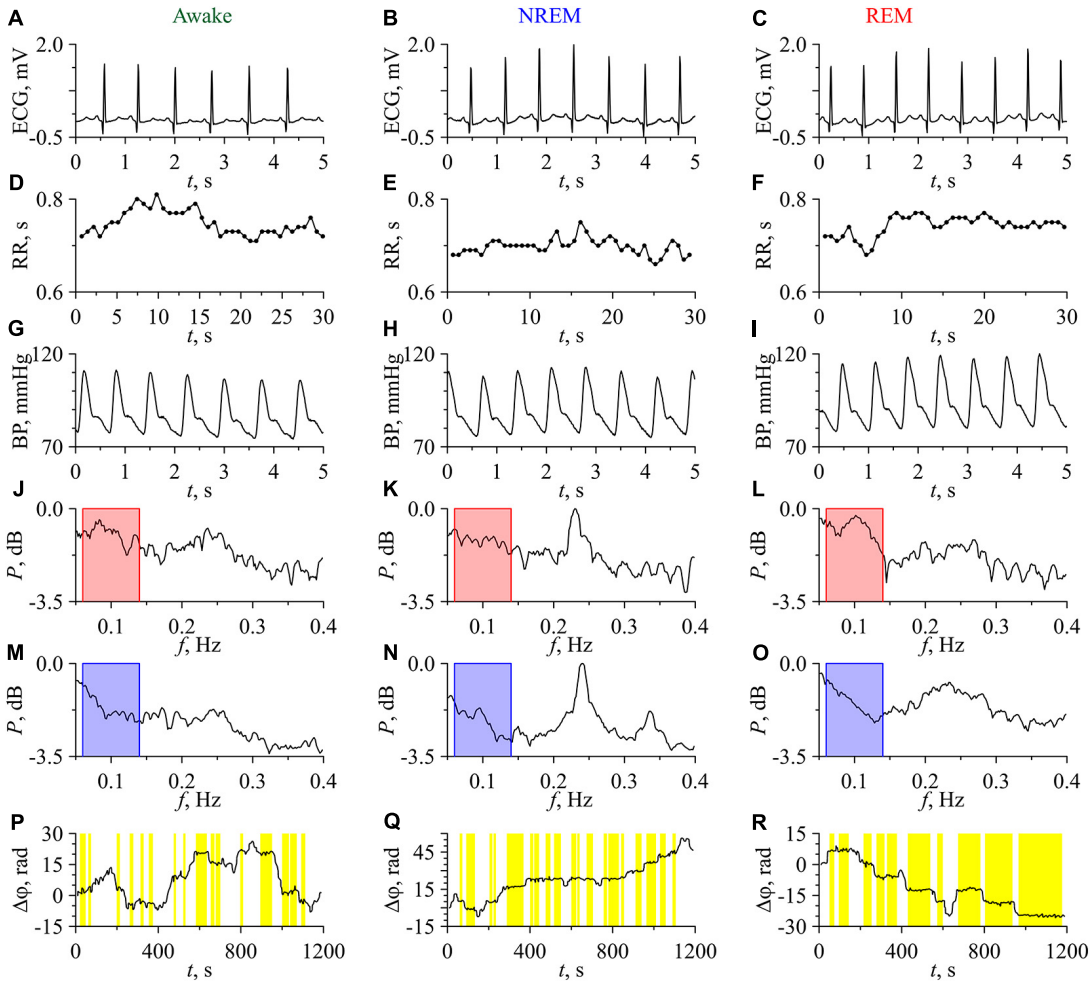

FIGURE 3 | Experimental signals, their Fourier power spectra and the difference of instantaneous phases for the subject No. 1 (No. C04Z1N2) in the awake state (first column), NREM sleep (second column), and REM sleep (third column). **(A–C)** ECG signals; **(D–F)** RR-intervals. Experimental values are shown with dots and interpolation by cubic β-splines is shown with line; **(G–I)** BP signals; **(J–L)** Fourier power spectra of RR-intervals; **(M–O)** Fourier power spectra of BP signals. The bandpass of filtering is shown in the power spectra plots in pink and blue; **(P–R)** Phase differences. Epochs of phase synchronization are shown in yellow.

S of phase synchronization is 29.6% in the awake state, 43.3% in NREM sleep, and 65.8% in REM sleep. All these values are statistically significant.

Figure 4 presents the results of the analysis of synchronization between the studied processes of autonomic control of blood circulation. In **Figure 4A**, the *S* values in the awake state, NREM sleep, and REM sleep are shown for each of 22 subjects. In all subjects, the *S* values in REM sleep are higher than in the awake state. In 18 subjects, the *S* values in REM sleep are higher than in NREM sleep. The difference between the *S* values in the awake state and in NREM sleep is less pronounced. From all *S* values in **Figure 4A**, only five values (two values in the awake state and three values in NREM sleep) are not significant. **Figure 4B** shows the distribution function *F* calculated for significant *S* values. In **Figure 4C**, box-and-whisker diagrams for *S* values are presented. From these figures it follows that, on average, *S* takes the highest values in REM sleep and the lowest values in the awake state. The most pronounced difference is observed between *S* values in the awake state and in REM sleep stage. In NREM sleep, the *S* values have high variance and are on average higher than in the awake state and lower than in REM sleep, **Figure 4C**.

The quantitative results of comparing the changes in the total percentage of phase synchronization *S* with known assessments in the awake state and different stages of sleep are presented in **Table 1**.

Table 1 shows that the index *S* demonstrates the best divergence of the distributions of values between awake state and REM sleep compared to other indices.

Table 2 gives the results of a pairwise test of the statistical significance of intergroup differences using the Mann-Whitney *U*-test and the Kruskal-Wallis test, which takes into account multiple testing.

Tables 1, **2** show that pairwise testing with the Mann–Whitney *U*-test shows that the index *S* separates REM sleep and awake state, as well as REM sleep and NREM sleep. *SDNN* and LF_{RR} separate groups REM sleep and NREM sleep, as well as NREM

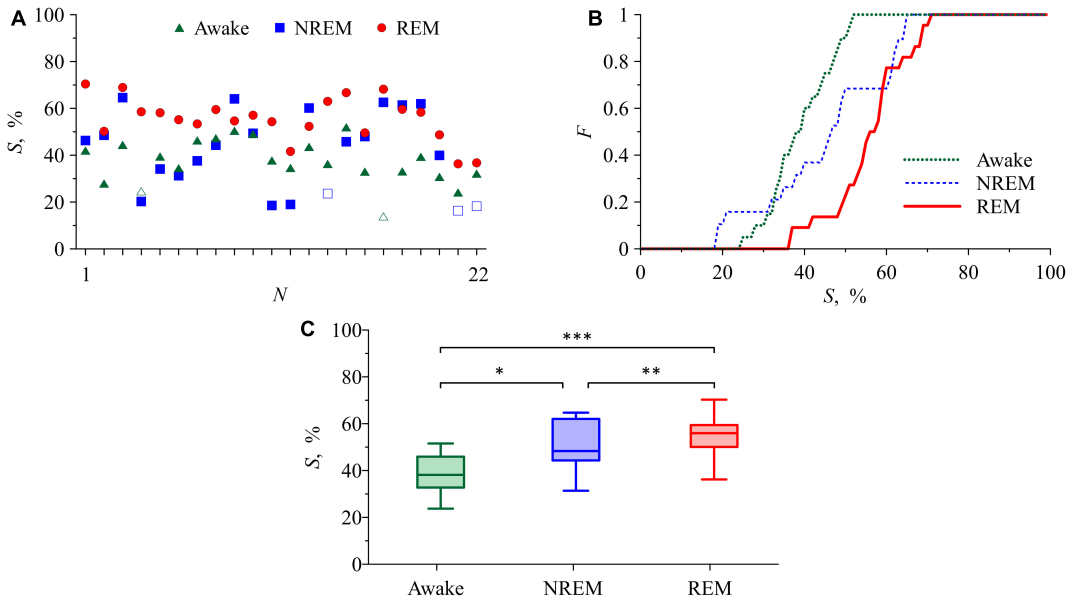

FIGURE 4 | (A) *S* values in the awake state, NREM sleep, and REM sleep for each of the subjects. Statistically insignificant *S* values are shown with white squares and white triangles. **(B)** Distribution function for *S*. **(C)** Box-and-whisker diagrams for *S* values in the awake state, NREM sleep, and REM sleep. The box boundaries are the first and third quartiles, the horizontal line is the median, the whiskers are the minimum and maximum values. Figures **(B,C)** include only statistically significant *S* values ($p < 0.05$). The asterisks in panel **(C)** correspond to the *p*-level of intergroup differences, assessed using the Mann-Whitney *U*-test: $p = 0.01$ for "*" and "***" and $p < 0.01$ for "***".

TABLE 1 | The values of the calculated assessments in the awake state and in sleep stages.

Subject's state	Awake	NREM	REM
S, %	38.46 (32.99; 45.31)	48.24 (42.08; 61.69)	56.1 (50.23; 59.58)
X_{mean}, ms	901.83 (800.13; 1051.96)	982.15 (877.66; 1075.63)	932.72 (797.13; 1093.44)
SDNN, ms	62.02 (38.02; 90.46)	35.93 (26.87; 49.84)	60.26 (40.13; 93.33)
HF_{RR}, ms^2	83.84 (42.05; 150.47)	209.37 (97.07; 539.01)	75.23 (38.61; 305.85)
LF_{RR}, ms^2	397.57 (248.53; 722.90)	199.18 (98.20; 373.10)	365.06 (206.91; 1192.66)
BRS	15.14 (13.32; 17.93)	13.27 (11.35; 21.56)	15.98 (10.19; 19.80)

Values are presented in the format: median (first quartile; third quartile).

TABLE 2 | Statistical significance of intergroup differences in the awake state and in sleep stages using different assessments.

Indexes	*p*-values Mann–Whitney *U*-test			Kruskal-Wallis test
	REM vs. awake	REM vs. NREM	NREM vs. awake	
S, %	**<0.01**	**0.01**	**0.01**	**<0.01**
X_{mean}, ms	0.49	0.65	0.18	0.42
SDNN, ms	0.63	**<0.01**	**0.01**	**<0.01**
HF_{RR}, ms^2	0.97	0.05	**0.01**	**0.03**
LF_{RR}, ms^2	0.99	**0.04**	**0.03**	0.05
BRS	0.95	0.70	0.82	0.96

Pairwise comparisons were made using the Mann-Whitney U-test, multiple testing using the Kruskal-Wallis test. Statistically significant ($p < 0.05$) values are highlighted in bold.

sleep and the awake state. HF_{RR} separates group NREM sleep and the awake state. This is confirmed by the results of multiple testing using the Kruskal-Wallis test (**Table 2**), which confirms significant group differences for all of the listed indices, except for the LF_{RR}.

Thus, only 4 out of 6 assessments demonstrated significant intergroup differences between the compared states for the experimental sample used. At the same time, only the *S* index made it possible to separate the REM sleep and the awake state groups significantly.

ROC analysis was carried out to assess the capabilities of the compared assessments when solving the problem of classifying of the awake state and sleep stages.

Figure 5 shows the ROC-curves for the *S* index. The ROC analysis results for the index *S* are consistent with the results of the analysis of intergroup differences. *S* demonstrates a noticeably better ability among the compared indices to classify REM sleep and the awake state (red line in **Figure 5A**), slightly worse results for REM and NREM sleep (red line in **Figure 5B**), worst of all these assessments allows classifying NREM sleep and awake states (**Figure 5C**). Among other assessments, the *SDNN* and HF_{RR}, LF_{RR} indexes can be noted, for classifying the REM sleep and NREM sleep (black, orange and purple lines, respectively, in **Figure 5B**) and NREM sleep and awake states (black, orange and purple lines, respectively, in **Figure 5C**). The *BRS* assessment shows the ability to classify NREM sleep and awake state (green line in **Figure 5C**).

The quantitative results of comparing the possibilities of classifying states using these assessments are shown in **Table 3**.

Thus, **Table 3** shows that the degree of synchronization of the processes of autonomic control of blood circulation with the calculation of the *S* index, in contrast to other assessments, makes it possible to classifying the state of REM sleep and the awake state. In **Figure 5**, the ROC-curve for this pair of states is higher than the other two ROC-curves. It gives good results TPR = 0.86 and specificity FPR = 0.14 for put off point (**Table 3**). The *S* and *SDNN* indexes differentiate between REM sleep and NREM sleep. The *SDNN* and HF_{RR} indices differentiate between REM sleep and NREM sleep. The LF_{RR} indice differentiate between NREM sleep and the awake state. Significant results ($p < 0.05$) are highlighted in bold.

DISCUSSION

The baroreflex function ensures the operation of the loops of autonomic control of blood circulation, which sensitively react to changes in the physiological state of the body. The studies (Mrowka et al., 2000, 2003; Shiogai et al., 2010; Bartsch et al., 2012) shows a statistically significant change in the cardiorespiratory synchronization and direction of coupling with aging. It is shown that the degree of cardiorespiratory synchronization in healthy subjects, on average, correlates well with the depth of sleep, being minimal in REM sleep and higher in deep sleep than in the awake state (Bartsch et al., 2012). Thus, the study of synchronization between the rhythms of the cardiovascular system gives important information about the state of the subjects and reflects physiological changes in the dynamics of the loops of baroreflex regulation in different stages of sleep.

In this paper, in different sleep stages, we study the phase synchronization of oscillations in the autonomic control loops of HR and BP, the activity of which is manifested mainly in the LF-band. The signals of these loops demonstrate complex chaotic non-stationary dynamics (Karavaev et al., 2019). To detect and quantify the synchronization between these signals, we used the previously proposed the method of synchronization analysis (Karavaev et al., 2009) and applied it to experimental signals of BP and RR-intervals. The method is implemented as freely distributed software.

The analysis of subjects in the awake state and different sleep stages allows us to reveal a number of interesting features. Despite the well-known effect of a decrease in the power of LF-oscillations in RR-intervals in NREM sleep (Somers et al., 1993), synchronization of the processes of autonomic control of blood circulation in NREM sleep increases with respect to the awake state (**Figure 4**). At the same time, we reveals the maximal synchronization during REM sleep, for which (Bartsch et al., 2012) reported the minimal values of cardiorespiratory synchronization. Our results confirm the conclusions obtained with the use of mathematical models in Van Roon et al. (2004) and Cheng et al. (2010) that the baroreflex function modulation by cortical structures has a complex independent nature. The change in the synchronization of the studied processes at different sleep stages can be explained by the change of the degree of effective interaction of these processes caused by such modulation. Presumably, the mechanisms of these interactions are realized through the brain stem structures (nucleus tract us solitarius, dorsal motor nucleus, nucleus ambiguous, and others), which interact with each other and with the structures of the cerebral cortex (Van Roon et al., 2004; Guyenet, 2014).

The potential of using the analysis of autonomic processes instead of the analysis of electroencephalograms is noted in Mayer et al. (2020) in the study of cardiorespiratory interaction. Currently, the classification of stages 1–3 of deep NREM sleep is successfully carried out by analyzing the instantaneous powers of various frequency components in electroencephalograms (Hassan and Subasi, 2017; Nakamura et al., 2017; Gupta and Pachori, 2021). At the same time, respiration, cardiac activity, and muscle tone also change significantly with the onset of NREM sleep (Flores et al., 2007; Noble and Hochman, 2019; Vanneau et al., 2021). However, the state of REM sleep is still reliably diagnosed only by assessing the eye dynamics and accompanying muscle activity (Liu et al., 2020). Some studies demonstrate certain changes in muscle activity and electrical activity of the brain, but these changes are not specific and very individual. In practice, the classification of REM sleep by automatic systems is very difficult (Cesari et al., 2018; Tripathy and Acharya, 2018). Nevertheless, it seems that this state may be described by analyzing the dynamics of various physiological signals, and not just based on the assessment of the appearance of eye movements.

The importance of this problem is emphasized by the fact that changes in the quality and quantity of REM sleep stages correlate with statistical assessments of mortality and the development of pathological conditions (Galbiati et al., 2019; Leary et al., 2020). At the same time, the known approaches based on estimates of linear spectral and statistical characteristics demonstrate a low sensitivity of the classification of REM sleep. The measure S used in our paper is based on the assessment of non-linear interactions of autonomic control loops of blood circulation and is promising for developing sensitive algorithms for the automatic classification of the REM sleep stage and the awake state. However, our analysis fails to discriminate between NREM and awake states, although such task is also

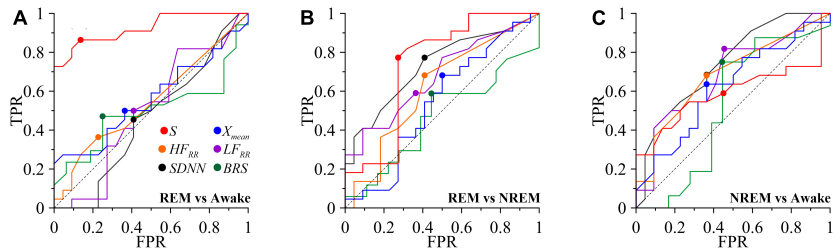

FIGURE 5 | ROC curves for classifying the awake state and sleep stages. TPR is true positive rate and FPR is false positive rate. **(A)** REM and awake state. **(B)** REM and NREM. **(C)** NREM and awake state. The diagonal line is shown with black dashed line. Put off point is marked with colored dots.

TABLE 3 | Results of the ROC analysis for classifying the awake state and sleep stages for the compared assessments, as well as the *p*-value and odds ratio for the put off points of the ROC curves.

Indexes	Subject's state	Point of ROC curve intersection with the diagonal					
		AUC	TPR	FPR	put off point	*p*-value	Odds ratio
S, %	REM vs awake	0.92	0.86	0.14	49	**<0.01**	40.1 (5.8–368.6)
	REM vs NREM	0.73	0.77	0.27	53	**<0.01**	9.1 (1.9–46.6)
	NREM vs awake	0.59	0.59	0.45	40	0.55	1.7 (0.4–6.8)
Xmean, ms	REM vs awake	0.56	0.50	0.36	904	0.54	1.8 (0.4–7)
	REM vs NREM	0.54	0.68	0.50	969	0.36	2.1 (0.5–8.8)
	NREM vs awake	0.62	0.64	0.36	929	0.13	3.1 (0.8–12.7)
SDNN, ms	REM vs awake	0.54	0.45	0.41	61	1.00	1.2 (0.3–4.7)
	REM vs NREM	0.74	0.77	0.41	663	**0.03**	4.9 (1.1–22.9)
	NREM vs awake	0.74	0.68	0.36	663	0.07	3.8 (0.9–16.1)
HF_{RR}, ms^2	REM vs awake	0.55	0.36	0.23	9903	0.51	1.9 (0.4–9)
	REM vs NREM	0.62	0.68	0.41	203	0.13	3 (0.8–13)
	NREM vs awake	0.69	0.68	0.36	103	0.07	3.8 (0.9–16.1)
LF_{RR}, ms^2	REM vs awake	0.50	0.50	0.41	353	0.77	1.4 (0.4–5.7)
	REM vs NREM	0.68	0.59	0.36	263	0.23	2.5 (0.6–10.3)
	NREM vs awake	0.69	0.82	0.45	293	**0.03**	5.4 (1.2–27.2)
BRS	REM vs awake	0.50	0.47	0.25	15.88	0.34	2.7 (0.5–15.4)
	REM vs NREM	0.47	0.59	0.44	14.36	0.61	1.8 (0.4–8.5)
	NREM vs awake	0.53	0.75	0.44	14.74	0.09	4.5 (0.8–26.7)

Statistically significant ($p < 0.05$) values are highlighted in bold.

important for the clinical and research practice. The indices *BRS* and *S* compared in our study showed different properties in distinguishing between the awake state and different stages of sleep. This is due to the different nature of these measures. Baroreflex sensitivity characterizes the changes in the response of baroreceptors caused by the changes in blood pressure. The result can be manifested in a change in the intensity of oscillations of the BP signal and RR-intervals in the LF-band. The index *S* characterizes a fundamentally non-linear effect of the phase coupling of oscillations in the loops of autonomic control of blood circulation. When calculating *S*, information on the dynamics of amplitudes of oscillations is not taken into account. For example, phase synchronization (and, accordingly, the index *S*) can increase with a decrease in the LF_{RR} oscillation power (and, accordingly, *BRS*), which can be seen from **Table 1**. Thus, the index *S* is not as a pure index of baroreflex sensitivity, but it provides important additional information on a non-linear interaction of the autonomic control loops. Therefore, in the studies of the dynamics of the autonomic control of blood circulation, the *S* and *BRS* indices do not replace, but complement each other, characterizing the features of the phase and amplitude dynamics, respectively, of analyzed systems. In the future, it looks promising to combine the advantages of the index *S* for detecting REM sleep with the capabilities of known approaches for classifying stages of NREM sleep, for example, using machine learning methods.

In this study, we analyze BP signals recorded by arterial catheterization in apnea patients. It is known that this pathology affects the processes of autonomic control (Guilleminault et al., 2005). Unfortunately, we are not able to compare the results of the analysis of patients and healthy subjects, since we do not have invasive BP records of healthy subjects. We expect that healthy subjects may have quantitative differences in *S* values compared to patients with apnea, but we assume that the conclusion about the differences in *S* values in different sleep stages and in awake state will remain valid. This assumption is based on

the fact that we excluded from the analysis the signal epochs with apnea attacks. To clarify this important issue, we plan to compare the synchronization between the LF-components of RR-intervals and photoplethysmogram signals in apnea patients and in healthy subjects.

CONCLUSION

The first methods for the assessment of human baroreflex function are based on statistical and spectral analysis of HR. However, such simple linear methods often lack the sensitivity to identify important features of this function in different physiological states. In these states, various systems of the body often change their properties simultaneously, demonstrating coherent and synchronous behavior. When studying such complex collective dynamics, non-linear methods of analysis have certain advantages. An example of such a non-linear method is the method based on the assessment of the degree of synchronization between the processes of autonomic control of HR rate and BP. This method exploits such a sensitive characteristic of the signal as its instantaneous phase. This approach allows us to identify the changes in the degree of coordinated behavior of the studied processes upon modulation of the baroreflex function by the processes of higher nervous activity.

We have found that in NREM sleep, the degree of synchronization of the LF-components of RR-intervals and BP signals is higher than in the awake state and lower than in REM sleep. The measure S may be promising for the development of algorithms for the automatic classification of sleep stages, especially for detecting REM sleep. The results of our study confirm the influence of the processes of higher nervous activity on the baroreflex function. Such influence can be considered in terms of modulation of the effective strength of coupling between the investigated loops of autonomic control.

DATA AVAILABILITY STATEMENT

The data analyzed in this study are subject to the following licenses/restrictions: These are data that belong to medical faculties and are not publicly available. Requests to access these datasets should be directed to TP, thomas.penzel@charite.de. The software that implements the method for diagnostics of synchronization developed by the authors is available at http://nonlinmod.sgu.ru/comprog_en.htm. It can be freely used in scientific research with reference to this work.

ETHICS STATEMENT

The studies involving human participants were reviewed and approved by the Ethics Committee of Klinikum der Philipps-Universität Marburg, Germany. The patients/participants provided their written informed consent to participate in this study.

AUTHOR CONTRIBUTIONS

All authors contributed to writing and discussion of the manuscript.

FUNDING

This work was supported by the Russian Science Foundation, Grant No. 19-12-00201 (data analysis using the method of phase synchronization detection) and the Project of RF Government, Grant No. 075-15-2019-1885 (sleep studies and physiological interpretation of the results).

REFERENCES

Airaksinen, K. E., Hartikainen, J. E., Niemelä, M. J., Huikuri, H. V., Mussalo, H. M., and Tahvanainen, K. U. (1993). Valsalva manoeuvre in the assessment of baroreflex sensitivity in patients with coronary artery disease. *Eur. Heart. J.* 14, 1519–1523. doi: 10.1093/eurheartj/14.11.1519

Albaghdadi, M. (2007). Baroreflex control of long-term arterial pressure. *Rev. Bras. Hipertens.* 14, 212–225.

Bartsch, R. P., Schumann, A. Y., Kantelhardt, J. W., Penzel, T., and Ivanov, P. C. (2012). Phase transitions in physiologic coupling. *Proc. Natl. Acad. Sci. U. S. A.* 109, 10181–10186. doi: 10.1073/pnas.1204568109

Berlad, I., Shlitner, S., Ben-Haim, S., and Lavie, P. (1993). Power spectrum analysis and heart rate variability in stage 4 and REM sleep: evidence for state-specific changes in autonomic dominance. *J. Sleep Res.* 2, 88–90. doi: 10.1111/j.1365-2869.1993.tb00067.x

Bernardi, L., Bianchini, B., Spadacini, G., Leuzzi, S., Valle, F., Marchesi, E., et al. (1995). Demonstrable cardiac reinnervation after human heart transplantation by carotid baroreflex modulation of RR interval. *Circulation* 92, 2895–2903. doi: 10.1161/01.CIR.92.10.2895

Bernardi, L., Radaell, A., Solda, P. L., Coats, A. J. S., Reeder, M., Calciati, A., et al. (1996). Autonomic control of skin microvessels: assessment by power spectrum of photoplethysmographic waves. *Clin. Sci.* 90, 345–355. doi: 10.1042/cs0900345

Billman, G. E. (2013). The LF/HF ratio does not accurately measure cardiac sympatho-vagal balance. *Front. Physiol.* 4:26. doi: 10.3389/fphys.2013.00026

Borovkova, E. I., Ishbulatov, Y. M., Hramkov, A. H., and Karavaev, A. S. (2021). Using a mathematical model of cardiovascular system for preparing surrogate data for testing methods of phase synchronization analysis. *Izvestiya Vysshikh Uchebnykh Zavedeniy. Prikladnaya Nelineynaya Dinamika* 29, 356–364. doi: 10.18500/0869-6632-2021-29-3-356-364

Borovkova, E. I., Karavaev, A. S., Kiselev, A. R., Gridnev, V. I., Hramkov, A. N., Chernets, E. P., et al. (2020). "Comparison of methods of quantitative analysis of phase synchronization according to test data modeling non-stationary signals of biological nature," in *IEEE 2020 4th Scientific School on Dynamics of Complex Networks and Their Application in Intellectual Robotics (DCNAIR)*, Piscataway: IEEE, 59–61. doi: 10.1109/DCNAIR50402.2020.9216742

Brandenberger, G., Viola, A. U., Ehrhart, J., Charloux, A., Geny, B., Piquard, F., et al. (2003). Age-related changes in cardiac autonomic control during sleep. *J. Sleep Res.* 12, 173–180. doi: 10.1046/j.1365-2869.2003.00353.x

Bristow, J. D., Honour, A. J., Pickering, T. G., and Sleight, P. (1969). Cardiovascular and respiratory changes during sleep in normal and hypertensive subjects. *Cardiovasc. Res.* 3, 476–485. doi: 10.1093/cvr/3.4.476

Cesari, M., Christensen, J. A. E., Kempfner, L., Olesen, A. N., Mayer, G., Kesper, K., et al. (2018). Comparison of computerized methods for rapid eye movement sleep without atonia detection. *Sleep* 41:zsy133. doi: 10.1093/sleep/zsy133

Cheng, L., Ivanova, O., Fan, H. H., and Khoo, M. C. (2010). An integrative model of respiratory and cardiovascular control in sleep-disordered breathing. *Respir. Physiol. Neurobiol.* 174, 4–28. doi: 10.1016/j.resp.2010.06.001

Conci, F., Di Rienzo, M., and Castiglioni, P. (2001). Blood pressure and heart rate variability and baroreflex sensitivity before and after brain death. *J. Neurol. Neurosurg. Psychiatry*. 71, 621–631. doi: 10.1136/jnnp.71.5.621

Conway, J., Boon, N., Jones, J. V., and Sleight, P. (1983). Involvement of the baroreceptor reflexes in the changes in blood pressure with sleep and mental arousal. *Hypertension* 5, 746–748. doi: 10.1161/01.hyp.5.5.746

Dash, S., Shelley, K. H., Silverman, D. G., and Chon, K. H. (2010). Estimation of respiratory rate from ECG, photoplethysmogram, and piezoelectric pulse transducer signals: a comparative study of time frequency methods. *IEEE Trans. Biomed. Eng.* 57, 1099–1107. doi: 10.1109/TBME.2009.2038226

De Boer, R. W., Karemaker, J. M., and Strackee, J. (1987). Hemodynamic fluctuations and baroreflex sensitivity in humans: a beat-to-beat model. *Am. J. Physiol.* 253, H680–H689. doi: 10.1152/ajpheart.1987.253.3.H680

Dietrich, A., Rosmalen, J. G. M., Althaus, M., van Roon, A. M., Mulder, L. J. M., Minderaa, R. B., et al. (2010). Reproducibility of heart rate variability and baroreflex sensitivity measurements in children. *Biol. Psychol.* 85, 71–78. doi: 10.1016/j.biopsycho.2010.05.0

Dornhorst, A. C., Howard, P., and Leathard, G. L. (1954). Respiratory variations in blood pressure. *Circulation.* 6, 553–558. doi: 10.1161/01.cir.6.4.553

Duschek, S., Werner, N. S., and Reyes Del Paso, G. A. (2013). The behavioral impact of baroreflex function: a review. *Psychophysiology* 50, 1183–1193. doi: 10.1111/psyp.12136

Eckberg, D. L., Cavanaugh, M. S., Mark, A. L., and Abboud, F. M. (1975). A simplified neck suction device for activation of carotid baroreceptors. *J. Lab. Clin. Med.* 85, 167–173. doi: 10.5555/uri:pii:0022214375904631

Elliott, J. E., Mantilla, C. B., Pabelick, C. M., Roden, A. C., and Sieck, G. C. (2016). Aging-related changes in respiratory system mechanics and morphometry in mice. *Am. J. Physiol. Lung. Cell. Mol. Physiol.* 311, L167–L176. doi: 10.1152/ajplung.00232.2016

Elsenbruch, S., Harnish, M. J., and Orr, W. C. (1999). Heart rate variability during waking and sleep in healthy males and females. *Sleep* 22, 1067–1071. doi: 10.1093/sleep/22.8.1067

Elstad, M., Walløe, L., Chon, K. H., and Toska, K. (2011). Low-frequency fluctuations in heart rate, cardiac output and mean arterial pressure in humans: what are the physiological relationships? *J. Hypertens.* 29, 1327–1336. doi: 10.1097/HJH.0b013e328347a17a

Ernst, G. (2017). Heart-rate variability-more than heart beats? *Front. Public. Health.* 5:240. doi: 10.3389/fpubh.2017.00240

Flores, A. E., Flores, J. E., Deshpande, H., Picazo, J. A., Xie, X. S., Franken, P., et al. (2007). Pattern recognition of sleep in rodents using piezoelectric signals generated by gross body movements. *IEEE Trans. Biomed. Eng.* 54, 225–233. doi: 10.1109/TBME.2006.886938

Furness, J. B. (2006). The organisation of the autonomic nervous system: peripheral connections. *Auton. Neurosci.* 130, 1–5. doi: 10.1016/j.autneu.2006.05.003

Galbiati, A., Verga, L., Giora, E., Zucconi, M., and Ferini-Strambi, L. (2019). The risk of neurodegeneration in REM sleep behavior disorder: a systematic review and meta-analysis of longitudinal studies. *Sleep Med. Rev.* 43, 37–46. doi: 10.1016/j.smrv.2018.09.008

Grote, L., Heitmann, J., Penzel, T., Cassel, W., Ploch, T., Hermann, J. P., et al. (1995). Arterial hypertension and sleep apnoea: effect of the angiotensin-converting enzyme (ACE) inhibitor cilazapril on continuously measured blood pressure during sleep and wakefulness. *J. Sleep Res.* 4, 112–116.

Guilleminault, C., Briskin, J. G., Greenfield, M. S., and Silvestri, R. (1981). The impact of autonomic nervous system dysfunction on breathing during sleep. *Sleep* 4, 263–278. doi: 10.1093/sleep/4.3.263

Guilleminault, C., Poyares, D., Rosa, A., and Huang, Y. S. (2005). Heart rate variability, sympathetic and vagal balance and EEG arousals in upper airway resistance and mild obstructive sleep apnea syndromes. *Sleep Med.* 6, 451–457. doi: 10.1016/j.sleep.2005.03.014

Gupta, V., and Pachori, R. B. (2021). FBDM based time-frequency representation for sleep stages classification using EEG signals. *Biomed. Signal Process. Control.* 64:102265. doi: 10.1016/j.bspc.2020.102265

Guyenet, P. G. (2014). Regulation of breathing and autonomic outflows by chemoreceptors. *Compr. Physiol.* 4, 1511–1562. doi: 10.1002/cphy.c140004

Hadaya, J., and Ardell, J. L. (2020). Autonomic modulation for cardiovascular disease. *Front. Physiol.* 11:617459. doi: 10.3389/fphys.2020.617459

Hassan, A., and Subasi, A. (2017). A decision support system for automated identification of sleep stages from single-channel EEG signals. *Knowl. Based Syst.* 128, 115–124. doi: 10.1016/j.knosys.2017.05.005

Hornyak, M., Cejnar, M., Elam, M., Matousek, M., and Wallin, B. G. (1991). Sympathetic muscle nerve activity during sleep in man. *Brain* 114, 1281–1295. doi: 10.1093/brain/114.3.1281

Ishaque, S., Khan, N., and Krishnan, S. (2021). Trends in heart-rate variability signal analysis. *Front. Digit. Health* 3:13. doi: 10.3389/fdgth.2021.639444

Ishbulatov, Y. M., Karavaev, A. S., Kiselev, A. R., Simonyan, M. A., Prokhorov, M. D., Ponomarenko, V. I, et al. (2020). Mathematical modeling of the cardiovascular autonomic control in healthy subjects during a passive head-up tilt test. *Sci. Rep.* 10:16525. doi: 10.1038/s41598-020-71532-7

Ivanov, P. C., Bunde, A., Amaral, L. A. N., Havlin, S., Fritsch-Yelle, J., Baevsky, R. M., et al. (1999). Sleep-wake differences in scaling behavior of the human heartbeat: analysis of terrestrial and long-term space flight data. *Europhys. Lett.* 48, 594–600. doi: 10.1209/epl/i1999-00525-0

Javed, F., Middleton, P. M., Malouf, P., Chan, G. S. H., Savkin, A. V., Lovell, N. H., et al. (2010). Frequency spectrum analysis of finger photoplethysmographic waveform variability during haemodialysis. *Physiol. Meas.* 31, 1203–1216. doi: 10.1088/0967-3334/31/9/010

Jerath, R., and Beveridge, C. (2020). Respiratory rhythm, autonomic modulation, and the spectrum of emotions: the future of emotion recognition and modulation. *Front. Psychol.* 11:1980. doi: 10.3389/fpsyg.2020.01980

Kantelhardt, J. W., Ashkenazy, Y., Ivanov, P. C., Bunde, A., Havlin, S., Penzel, T., et al. (2002). Characterization of sleep stages by correlations in the magnitude and sign of heartbeat increments. *Phys. Rev. E. Stat. Nonlin. Soft. Matter. Phys.* 65:051908. doi: 10.1103/PhysRevE.65.051908

Karavaev, A. S., Borovik, A. S., Borovkova, E. I., Orlova, E. A., Simonyan, M. A., Ponomarenko, V. I., et al. (2021). Low-frequency component of photoplethysmogram reflects the autonomic control of blood pressure. *Biophysics* 120, 2657–2664. doi: 10.1016/j.bpj.2021.05.020

Karavaev, A. S., Ishbulatov, Y. M., Ponomarenko, V. I, Bezruchko, B. P., Kiselev, A. R., and Prokhorov, M. D. (2019). Autonomic control is a source of dynamical chaos in the cardiovascular system. *Chaos* 29:121101. doi: 10.1063/1.5134833

Karavaev, A. S., Ishbulatov, Y. M., Ponomarenko, V. I., Prokhorov, M. D., Gridnev, V. I., Bezruchko, B. P., et al. (2016). Model of human cardiovascular system with a loop of autonomic regulation of the mean arterial pressure. *J. Am. Soc. Hypertens.* 10, 235–243. doi: 10.1016/j.jash.2015.12.014

Karavaev, A. S., Prokhorov, M. D., Ponomarenko, V. I., Kiselev, A. R., Gridnev, V. I., Ruban, E. I., et al. (2009). Synchronization of low-frequency oscillations in the human cardiovascular system. *Chaos* 19:033112. doi: 10.1063/1.3187794

Kiselev, A. R., Borovkova, E. I., Shvartz, V. A., Skazkina, V. V., Karavaev, A. S., Prokhorov, M. D., et al. (2020). Low-frequency variability in photoplethysmographic waveform and heart rate during on-pump cardiac surgery with or without cardioplegia. *Sci. Rep.* 10:2118. doi: 10.1038/s41598-020-58196-z

Kiselev, A. R., Gridnev, V. I., Prokhorov, M. D., Karavaev, A. S., Posnenkova, O. M., Ponomarenko, V. I., et al. (2012a). Evaluation of 5-year risk of cardiovascular events in patients after acute myocardial infarction using synchronization of 0.1-Hz rhythms in cardiovascular system. *Ann. Noninvasive. Electrocardiol.* 17, 204–213. doi: 10.1111/j.1542-474X.2012.00514.x

Kiselev, A. R., Gridnev, V. I., Prokhorov, M. D., Karavaev, A. S., Posnenkova, O. M., Ponomarenko, V. I., et al. (2012b). Selection of optimal dose of β-blocker treatment in myocardial infarction patients basing on changes in synchronization between 0.1 Hz oscillations in heart rate and peripheral microcirculation. *J. Cardiovasc. Med.* 13, 491–498. doi: 10.2459/JCM.0b013e3283512199

Kiselev, A. R., Mironov, S. A., Karavaev, A. S., Kulminskiy, D. D., Skazkina, V. V., Borovkova, E. I., et al. (2016b). A comprehensive assessment of cardiovascular autonomic control using photoplethysmograms recorded from the earlobe and fingers. *Physiol. Meas.* 37, 580–595. doi: 10.1088/0967-3334/37/4/580

Kiselev, A. R., Karavaev, A. S., Gridnev, V. I., Prokhorov, M. D., Ponomarenko, V. I., Borovkova, E. I., et al. (2016a). Method of estimation of synchronization strength between low-frequency oscillations in heart rate variability and

photoplethysmographic waveform variability. *Russ. Open Med. J.* 5:e0101. doi: 10.15275/rusomj.2016.0101

Kligfield, P., Gettes, L. S., Bailey, J. J., Childers, R., Deal, B. J., Hancock, E. W., et al. (2007). Recommendations for the Standardization and Interpretation of the Electrocardiogram. *J. Am. Coll. Cardiol.* 49, 1109–1127. doi: 10.1016/j.jacc.2007.01.024

Kruskal, W. H. (1952). A nonparametric test for the several sample problem. *Ann. Math. Stat.* 23, 525–540. doi: 10.1214/AOMS/1177729332

La Rovere, M. T., Pinna, G. D., and Raczak, G. (2008). Baroreflex sensitivity: measurement and clinical implications. *Ann. Noninvas. Electrocardiol.* 13, 191–207. doi: 10.1111/j.1542-474X.2008.00219.x

Lanfranchi, P. A., and Somers, V. K. (2002). Arterial baroreflex function and cardiovascular variability: interactions and implications. *Am. J. Physiol. Regul. Integr. Comp. Physiol.* 283, R815–R826. doi: 10.1152/ajpregu.00051.2002

Laude, D., Elghozi, J. L., Girard, A., Bellard, E., Bouhaddi, M., Castiglioni, P., et al. (2004). Comparison of various techniques used to estimate spontaneous baroreflex sensitivity (the EuroBaVar study). *Am. J. Physiol. Regul. Integr. Comp. Physiol.* 286, R226–R231. doi: 10.1152/ajpregu.00709.2002

Lázaro, J., Gil, E., Orini, M., Laguna, P., and Bailón, R. (2019). Baroreflex sensitivity measured by pulse photoplethysmography. *Front. Neurosci.* 13:339. doi: 10.3389/fnins.2019.00339

Leary, E. B., Watson, K. T., Ancoli-Israel, S., Redline, S., Yaffe, K., Ravelo, L. A., et al. (2020). Association of rapid eye movement sleep with mortality in middle-aged and older adults. *JAMA Neurol.* 77, 1241–1251. doi: 10.1001/jamaneurol.2020.2108

Legramante, J. M., Marciani, M. G., Placidi, F., Aquilani, S., Romigi, A., Tombini, M., et al. (2003). Sleep-related changes in baroreflex sensitivity and cardiovascular autonomic modulation. *J. Hypertens.* 21, 1555–1561. doi: 10.1097/01.hjh.0000084700.87421.fb

Lewis, M. J., Short, A. L., and Lewis, K. E. (2006). Autonomic nervous system control of the cardiovascular and respiratory systems in asthma. *Respir. Med.* 100, 1688–1705. doi: 10.1016/j.rmed.2006.01.019

Liu, G. R., Lustenberger, C., Lo, Y. L., Liu, W. T., Sheu, Y. C., and Wu, H. T. (2020). Save muscle information-unfiltered EEG signal helps distinguish sleep stages. *Sensors* 20:2024. doi: 10.3390/s20072024

Lombardi, C., Pengo, M. F., and Parati, G. (2019). Obstructive sleep apnea syndrome and autonomic dysfunction. *Autonom. Neurosci.* 221:102563. doi: 10.1016/j.autneu.2019.102563

Maestri, R., Raczak, G., Torunski, A., Sukiennik, A., Kozlowski, D., La Rovere, M. T., et al. (2009). Day-by-day variability of spontaneous baroreflex sensitivity measurements: implications for their reliability in clinical and research applications. *J. Hypertens.* 27, 806–812. doi: 10.1097/HJH.0b013e328322fe4b

Mann, H. B., and Whitney, D. R. (1947). On a test of whether one of two random variables is stochastically larger than the other. *Ann. Math. Stat.* 18, 50–60. doi: 10.1214/aoms/1177730491

Mayer, P., Herrero Babiloni, A., Beetz, G., Marshansky, S., Kaddaha, Z., Rompré, P. H., et al. (2020). The evaluation of autonomic arousals in scoring sleep respiratory disturbances with polysomnography and portable monitor devices: a proof of concept study. *Nat. Sci. Sleep* 12, 443–451. doi: 10.2147/NSS.S258276

Molkov, Y. I., Zoccal, D. B., Baekey, D. M., Abdala, A. P., Machado, B. H., Dick, T. E., et al. (2014). Physiological and pathophysiological interactions between the respiratory central pattern generator and the sympathetic nervous system. *Prog. Brain. Res.* 212, 1–23. doi: 10.1016/B978-0-444-63488-7.00001-X

Mortara, A., La Rovere, M. T., Pinna, G. D., Prpa, A., Maestri, R., Febo, O., et al. (1997). Arterial baroreflex modulation of heart rate in chronic heart failure. Clinical and hemodynamic correlates and prognostic implications. *Circulation* 96, 3450–3458. doi: 10.1161/01.cir.96.10.3450

Mrowka, R., Cimponeriu, L., Patzak, A., and Rosenblum, M. G. (2003). Directionality of coupling of physiological subsystems: age-related changes of cardiorespiratory interaction during different sleep stages in babies. *Am. J. Physiol. Regul. Integr. Comp. Physiol.* 285, R1395–R1401. doi: 10.1152/ajpregu.00373.2003

Mrowka, R., Patzak, A., and Rosenblum, M. G. (2000). Quantitative analysis of cardiorespiratory synchronization in infants. *Int. J. Bifurcation Chaos* 10, 2479–2488. doi: 10.1142/S0218127400001754

Nakamura, T., Adjei, T., Alqurashi, Y., Looney, D., Morrell, M. J., and Mandic, D. P. (2017). "Complexity science for sleep stage classification from EEG," in *2017 International Joint Conference on Neural Networks (IJCNN)* (Piscataway: IEEE), 4387–4394. doi: 10.1109/IJCNN.2017.7966411

Nakazato, T., Shikama, T., Toma, S., Nakajima, Y., and Masuda, Y. (1998). Nocturnal variation in human sympathetic baroreflex sensitivity. *J. Auton. Nerv. Syst.* 70, 32–37. doi: 10.1016/s0165-1838(98)00024-1

Natarajan, A., Pantelopoulos, A., Emir-Farinas, H., and Natarajan, P. (2020). Heart rate variability with photoplethysmography in 8 million individuals: a cross-sectional study. *Lancet Digit. Health* 2, E650–E657. doi: 10.1016/S2589-7500(20)30246-6

Noble, D. J., and Hochman, S. (2019). Hypothesis: pulmonary afferent activity patterns during slow, deep breathing contribute to the neural induction of physiological relaxation. *Front. Physiol.* 10:1176. doi: 10.3389/fphys.2019.01176

Oh, S. M., Choi, S. H., Kim, H. J., Park, K. S., and Lee, Y. J. (2019). The association between obstructive sleep apnea during REM sleep and autonomic dysfunction as measured by heart rate variability. *Sleep Breath.* 23, 865–871. doi: 10.1007/s11325-018-01779-y

O'Leary, D. S., and Woodbury, D. J. (1996). Role of cardiac output in mediating arterial blood pressure oscillations. *Am. J. Physiol.* 271, R641–R646. doi: 10.1152/ajpregu.1996.271.3.R641

Orini, M., Laguna, P., Mainardi, L., and Bailón, R. (2012). Assessment of the dynamic interactions between heart rate and arterial pressure by the cross time–frequency analysis. *Physiol. Meas.* 33, 315–331. doi: 10.1088/0967-3334/33/3/315

Osborn, J. W., Jacob, F., and Guzman, P. (2005). A neural set point for the long-term control of arterial pressure: beyond the arterial baroreceptor reflex. *Am. J. Physiol. Regul. Integr. Comp. Physiol.* 288, R846–R855. doi: 10.1152/ajpregu.00474.2004

Pagani, M., Somers, V., Furlan, R., Dell'Orto, S., Conway, J., Baselli, G., et al. (1988). Changes in autonomic regulation induced by physical training in mild hypertension. *Hypertension* 12, 600–610. doi: 10.1161/01.hyp.12.6.600

Palmero, H. A., Caeiro, T. F., Iosa, D. J., and Bas, J. (1981). Baroreceptor reflex sensitivity index derived from phase 4 of the Valsalva manoeuvre. *Hypertension* 3, II134–II137. doi: 10.1161/01.hyp.3.6_pt_2.ii-134

Parashar, R., Amir, M., Pakhare, A., Rathi, P., and Chaudhary, L. (2016). Age related changes in autonomic functions. *J. Clin. Diagn. Res.* 10, CC11–CC15. doi: 10.7860/JCDR/2016/16889.7497

Parati, G., Di Rienzo, M., Bertinieri, G., Pomidossi, G., Casadei, R., Groppelli, A., et al. (1988). Evaluation of the baroreceptor-heart rate reflex by 24-hour intraarterial blood pressure monitoring in humans. *Hypertension* 12, 214–222. doi: 10.1161/01.hyp.12.2.214

Parmeggiani, P. (1994). *The Autonomic Nervous System in Sleep. Principles and Practice of Sleep Medicine*, 2nd Edn. Philadelphia, PA: Saunders, doi: 10.1002/ppul.1065

Peter, J. H., Gassel, W., Mayer, J., Herres-Mayer, B., Penzel, T., Schneider, H., et al. (1989). Effects of cilazapril on hypertension, sleep, and apnea. *Am. J. Med.* 87, 72S–78S. doi: 10.1016/s0002-9343(89)80935-0

Pichot, V., Roche, F., Celle, S., Barthélémy, J. C., and Chouchou, F. (2016). HRV analysis: a free software for analyzing cardiac autonomic activity. *Front. Physiol.* 7:557. doi: 10.3389/fphys.2016.00557

Pietri, P., and Stefanadis, C. (2021). Cardiovascular aging and longevity: JACC State-of-the-Art review. *J. Am. Coll. Cardiol.* 77, 189–204. doi: 10.1016/j.jacc.2020.11.023

Pikovsky, A., Rosenblum, M., and Kurths, J. (2001). *Synchronization: À Universal Concept in Nonlinear Sciences*. New York, NY: Cambridge University Press.

Pinna, G. D., La Rovere, M. T., Maestri, R., Mortara, A., Bigger, J. T., and Schwartz, P. J. (2000). Comparison between invasive and noninvasive measurements of baroreflex sensitivity: implications from studies on risk stratification after a myocardial infarction. *Eur. Heart. J.* 18, 1522–1529. doi: 10.1053/euhj.1999.1948

Ponomarenko, V. I., Karavaev, A. S., Borovkova, E. I., Hramkov, A. N., Kiselev, A. R., Prokhorov, M. D., et al. (2021). Decrease of coherence between the respiration and parasympathetic control of the heart rate with aging. *Chaos* 31:073105. doi: 10.1063/5.0056624

Ponomarenko, V. I., Prokhorov, M. D., Karavaev, A. S., Kiselev, A. R., Gridnev, V. I., and Bezruchko, B. P. (2013). Synchronization of low-frequency oscillations in the cardiovascular system: application to medical diagnostics and treatment. *Eur. Phys. J. Spec. Top.* 222, 2687–2696. doi: 10.1140/epjst/e2013-02048-1

Prokhorov, M. D., Karavaev, A. S., Ishbulatov, Y. M., Ponomarenko, V. I., Kiselev, A. R., and Kurths, J. (2021). Interbeat interval variability versus frequency modulation of heart rate. *Phys. Rev. E.* 103:042404. doi: 10.1103/PhysRevE.103.042404

Prokhorov, M. D., Ponomarenko, V. I., Gridnev, V. I., Bodrov, M. B., and Bespyatov, A. B. (2003). Synchronization between main rhythmic processes in the human cardiovascular system. *Phys. Rev. E.* 68:041913. doi: 10.1103/PhysRevE.68.041913

Rechtschaffen, A., and Kales, A. (1968). *A Manual of Standardized Terminology, Techniques and Scoring System of Sleep Stages in Human Subjects. UCLA Brain Information Service*. Los Angeles: Brain Research Institute.

Ringwood, J. V., and Malpas, S. C. (2001). Slow oscillations in blood pressure via a nonlinear feedback model. *Am. J. Physiol. Regul. Integr. Comp. Physiol.* 280, R1105–R1115. doi: 10.1152/ajpregu.2001.280.4.R1105

Rosenblum, M., and Kurths, J. (1998). "Analysing synchronization phenomena from bivariate data by means of the hilbert transform," in *Nonlinear Analysis of Physiological Data*, eds H. Kantz, J. Kurths, and G. Mayer-Kress (Berlin: Springer), 91–99.

Schreiber, T., and Schmitz, A. (1996). Improved surrogate data for nonlinearity tests. *Phys. Rev. Lett.* 77, 635–638. doi: 10.1103/PhysRevLett.77.635

Schumann, A. Y., Bartsch, R. P., Penzel, T., Ivanov, P. C., and Kantelhardt, J. W. (2010). Aging effects on cardiac and respiratory dynamics in healthy subjects across sleep stages. *Sleep* 33, 943–955. doi: 10.1093/sleep/33.7.943

Shaffer, F., and Ginsberg, J. P. (2017). An overview of heart rate variability metrics and norms. *Front. Public. Health.* 5:258. doi: 10.3389/fpubh.2017.00258

Sharma, G., and Goodwin, J. (2006). Effect of aging on respiratory system physiology and immunology. *Clin. Interv. Aging* 1, 253–260. doi: 10.2147/ciia.2006.1.3.253

Shiogai, Y., Stefanovska, A., and McClintock, P. V. E. (2010). Nonlinear dynamics of cardiovascular ageing. *Phys. Rep.* 488, 51–110. doi: 10.1016/j.physrep.2009.12.003

Sleight, P., La Rovere, M. T., Mortara, A., Pinna, G., Maestri, R., Leuzzi, S., et al. (1995). Physiology and pathophysiology of heart rate and blood pressure variability in humans: is power spectral analysis largely an index of baroreflex gain? *Clin. Sci.* 88, 103–109. doi: 10.1042/cs0880103

Smyth, H. S., Sleight, P., and Pickering, G. W. (1969). Reflex regulation of arterial pressure during sleep in man: a quantitative method of assessing baroreflex sensitivity. *Circ. Res.* 24, 109–121. doi: 10.1161/01.res.24.1.109

Somers, V. K., Dyken, M. E., Mark, A. L., and Abboud, F. M. (1993). Sympathetic-nerve activity during sleep in normal subjects. *N. Engl. J. Med.* 328, 303–307. doi: 10.1056/NEJM199302043280502

Subramanian, S. K., Sharma, V. K., Arunachalam, V., Rajendran, R., and Gaur, A. (2019). Comparison of baroreflex sensitivity and cardiac autonomic function between adolescent athlete and non-athlete boys - a cross-sectional study. *Front. Physiol.* 10:1043. doi: 10.3389/fphys.2019.01043

Swenne, C. A. (2013). Baroreflex sensitivity: mechanisms and measurement. *Neth. Heart J.* 21, 58–60. doi: 10.1007/s12471-012-0346-y

Tan, C. O. (2013). Heart rate variability: are there complex patterns? *Front. Physiol.* 4:165. doi: 10.3389/fphys.2013.00165

Task Force of the European Society of Cardiology [TFESC] (1996). Heart rate variability: standards of measurement, physiological interpretation and clinical use. *Circulation* 3, 1043–1065. doi: 10.1161/01.cir.93.5.1043

Theiler, J., Eubank, S., Longtin, A., Galdrikian, B., and Farmer, J. D. (1992). Testing for nonlinearity in time series: the method of surrogate data. *Phys. D.* 58, 77–94. doi: 10.1016/0167-2789(92)90102-S

Tripathy, R. K., and Acharya, U. (2018). Use of features from RR-time series and EEG signals for automated classification of sleep stages in deep neural network framework. *Biocybern. Biomed. Eng.* 38, 890–902. doi: 10.1016/J.BBE.2018.05.005

Valente, M., Javorka, M., Porta, A., Bari, V., Krohova, J., Czippelova, B., et al. (2018). Univariate and multivariate conditional entropy measures for the characterization of short-term cardiovascular complexity under physiological stress. *Physiol. Meas.* 39:014002. doi: 10.1088/1361-6579/aa9a91

Van de Borne, P., Nguyen, H., Biston, P., Linkowski, P., and Degaute, J. P. (1994). Effects of wake and sleep stages on the 24-h autonomic control of blood pressure and heart rate in recumbent men. *Am. J. Physiol.* 266, H548–H554. doi: 10.1152/ajpheart.1994.266.2.H548

Van Roon, A. M., Mulder, L. J. M., Althaus, M., and Mulder, G. (2004). Introducing a baroreflex model for studying cardiovascular effects of mental workload. *Psychophysiology* 41, 961–981. doi: 10.1111/j.1469-8986.2004.00251.x

Vanneau, T., Quiquempoix, M., Trignol, A., Verdonk, C., van Beers, P., Sauvet, F., et al. (2021). Determination of the sleep–wake pattern and feasibility of NREM/REM discrimination using the non-invasive piezoelectric system in rats. *J. Sleep Res.* 30:e13373. doi: 10.1111/jsr.13373

Vanoli, E., Adamson, P. B., Lin, B., Pinna, G. D., Lazzara, R., and Orr, W. C. (1995). Heart rate variability during specific sleep stages. A comparison of healthy subjects with patients after myocardial infarction. *Circulation* 91, 1918–1922. doi: 10.1161/01.cir.91.7.1918

Wagner, C. D., and Persson, P. B. (1998). Chaos in the cardiovascular system: an update. *Cardiovasc. Res.* 40:257. doi: 10.1016/s0008-6363(98)00251-x

Wessel, N., Berg, K., Kraemer, J. F., Gapelyuk, A., Rietsch, K., Hauser, T., et al. (2020). Cardiac autonomic dysfunction and incidence of de novo atrial fibrillation: heart rate variability vs. heart rate complexity. *Front. Physiol.* 11:596844. doi: 10.3389/fphys.2020.596844

Young, B. E., Kaur, J., Vranish, J. R., Stephens, B. Y., Barbosa, T. C., Cloud, J. N., et al. (2020). Augmented resting beat-to-beat blood pressure variability in young, healthy, non-Hispanic black men. *Exp. Physiol.* 105, 1102–1110. doi: 10.1113/EP088535

Zemaityte, D., Varoneckas, G., and Sokolov, E. (1984). Heart rhythm control during sleep. *Psychophysiology* 21, 279–289. doi: 10.1111/j.1469-8986.1984.tb02935.x

Conflict of Interest: The authors declare that the research was conducted in the absence of any commercial or financial relationships that could be construed as a potential conflict of interest.

Publisher's Note: All claims expressed in this article are solely those of the authors and do not necessarily represent those of their affiliated organizations, or those of the publisher, the editors and the reviewers. Any product that may be evaluated in this article, or claim that may be made by its manufacturer, is not guaranteed or endorsed by the publisher.

frontiers in Neuroscience

ORIGINAL RESEARCH
published: 25 February 2022
doi: 10.3389/fnins.2022.833344

Effectiveness of Different Methods for Baroreflex Sensitivity Assessment in Determining the Severity of Cardiovascular Autonomic Neuropathy in Patients With Parkinson's Disease

Chih-Cheng Huang[1], Yun-Ru Lai[1], Chia-Yi Lien[1], Ben-Chung Cheng[2], Chia-Te Kung[3], Yi-Fang Chiang[1] and Cheng-Hsien Lu[1,4,5,6]**

[1] Department of Neurology, Kaohsiung Chang Gung Memorial Hospital, Chang Gung University College of Medicine, Kaohsiung, Taiwan, [2] Department of Internal Medicine, Kaohsiung Chang Gung Memorial Hospital, Chang Gung University College of Medicine, Kaohsiung, Taiwan, [3] Department of Emergency Medicine, Kaohsiung Chang Gung Memorial Hospital, Chang Gung University College of Medicine, Kaohsiung, Taiwan, [4] Center for Shockwave Medicine and Tissue Engineering, Kaohsiung Chang Gung Memorial Hospital, Chang Gung University College of Medicine, Kaohsiung, Taiwan, [5] Department of Biological Science, National Sun Yat-sen University, Kaohsiung, Taiwan, [6] Department of Neurology, Xiamen Chang Gung Memorial Hospital, Xiamen, China

OPEN ACCESS

Edited by:
Yue-Der Lin,
Feng Chia University, Taiwan

Reviewed by:
Iryna S. Palamarchuk,
University of Ottawa, Canada
Carlos C. Crestani,
São Paulo State University, Brazil

***Correspondence:**
Yun-Ru Lai
yunrulai@cgmh.org.tw;
yunru.lai@gmail.com
Cheng-Hsien Lu
chlu99@ms44.url.com.tw;
chlu99@adm.cgmh.org.tw

Specialty section:
This article was submitted to Autonomic Neuroscience, a section of the journal Frontiers in Neuroscience

Received: *11 December 2021*
Accepted: *18 January 2022*
Published: *25 February 2022*

Citation:
Huang C-C, Lai Y-R, Lien C-Y, Cheng B-C, Kung C-T, Chiang Y-F and Lu C-H (2022) Effectiveness of Different Methods for Baroreflex Sensitivity Assessment in Determining the Severity of Cardiovascular Autonomic Neuropathy in Patients With Parkinson's Disease. Front. Neurosci. 16:833344. doi: 10.3389/fnins.2022.833344

Background: Autonomic disorders are an important non-motor feature of Parkinson's disease (PD). Baroreflex sensitivity (BRS) is often used as an indicator of cardiovascular autonomic function, and it is clinically significant. Several different methods of BRS assessment have been described. We evaluated and compared the efficiency of several methods of BRS assessment for additional insight into the underlying physiology and the determination of its severity in patients with PD.

Materials and Methods: Eighty-five patients with PD underwent cardiovascular autonomic testing. The Composite Autonomic Scoring Scale (CASS) was used to grade the severity of autonomic impairment and to define the presence of cardiovascular autonomic neuropathy (CAN). BRS was assessed using the Valsalva maneuver (BRS_VM). In addition, spontaneous BRS was computed using the sequence method and the spectral method.

Results and Conclusion: There was considerable agreement between the different methods of BRS assessment. Nevertheless, BRS_VM exhibited a higher degree of correlation with cardiovascular autonomic function than spontaneous BRS indexes obtained by the sequence or spectral method. BRS_VM, rather than spontaneous BRS, also had a predictive value for the presence of CAN to the diagnostic criteria by CASS in patients with PD.

Keywords: baroreflex sensitivity, Valsalva maneuver, sequence method, spectral method, Parkinson's Disease

INTRODUCTION

Autonomic disorders have been recognized as an important non-motor feature of Parkinson's disease (PD) (Martinez-Martin et al., 2011; Kim et al., 2014). Several studies have demonstrated that patients with PD exhibit decreased baroreflex sensitivity (BRS) (Szili-Torok et al., 2001; Blaho et al., 2017). The pattern of autonomic impairment provides an important clue to differentiate patients with PD from those with multiple system atrophy (Kimpinski et al., 2012; Pavy-LeTraon et al., 2018). In patients with severe autonomic failure, adrenergic impairment and decreased BRS cause orthostatic hypotension, which has a considerable impact on the patient's quality of life. Furthermore, patients with PD have recently been found to have an increased risk of cardiovascular or cerebrovascular events (Alves et al., 2020; Park et al., 2020). The decreased BRS noted in patients with PD may be a contributing factor for the increased cardiovascular risk.

Baroreflex sensitivity (BRS) in humans can be assessed using several different methods (Parati et al., 2000). Generally, these methods are divided into two categories: In the first category, BRS is assessed in a laboratory setting using an external stimulus that triggers a change in the blood pressure (BP) and a subsequent change in the heart rate (HR). In the second category, BRS is determined using spontaneous oscillations of BP and HR without external interventions. There is no "gold standard" method for BRS evaluation, as different methods may describe different aspects of baroreflex modulation. Nevertheless, certain methods may be especially suitable under specific circumstances or can be more clinically significant than others for a particular group of patients.

There is a paucity of studies regarding the comparison of various methods of BRS assessment in patients with PD. This study aimed to evaluate BRS in patients with PD using three different methods and to compare the clinical relevance of each method. Our hypothesis is that it may provide additional insight into the underlying physiology to evaluate the diversity of various BRS assessments. Therefore, an optimal assessment can be chosen in a specific clinical context or for a certain group of patients.

PATIENTS AND METHODS

Study Design and Patient Selection

We prospectively evaluated patients with a definitive diagnosis of idiopathic PD according to the clinical diagnostic criteria and magnetic resonance image findings (Hughes et al., 1992; Heim et al., 2017). The exclusion criteria were as follows: (1) cognitive impairment leading to inability to follow our instructions; (2) a known history of cardiovascular or cerebrovascular events; (3) presence of cardiovascular autonomic neuropathy related to diabetes or other etiologies; and (4) presence of an implanted pacemaker or any type of arrhythmia that prevented BRS assessment. The Institutional Review Committee on Human Research of the hospital approved this study (IRB 201901802B0). All participants received verbal and written information about the purpose of the study and signed informed consent forms.

Clinical Assessment of Parkinson's Disease

The clinical assessments of PD were performed using the Hoehn and Yahr Scale (Hoehn and Yahr, 1967) and the Unified Parkinson's Disease Rating Scale (UPDRS) (Martinez-Martin et al., 1994), and took place during the "off" state, which was defined as 12 h or more after administration of the last dose of antiparkinsonian therapy. The age at disease onset, sex, body height, body weight, body mass index (BMI), disease duration, and levodopa dosage [expressed as Levodopa Equivalent Dose (LED)] (Tomlinson et al., 2010) were recorded for all participants. The autonomic symptoms profile of each patient was assessed using the Composite Autonomic Symptom Score 31 (COMPASS 31) questionnaire (Sletten et al., 2012), and the cognitive function was evaluated using the Cognitive Abilities Screening Instrument (CASI C v2.0).

Autonomic Function Testing

All participants underwent a standardized evaluation of cardiovascular autonomic function during the "off" state, including heart rate response to deep breathing (HRDB), the Valsalva maneuver (VM), and the head-up tilt test (Low, 2003). In addition, 5 min of resting ECG recording and continuous BP monitoring were performed in the interval between the VM and the head-up tilt test. To avoid the influence of depth and frequency of breathing on spontaneous BRS, the patients had 10 min of rest between the end of VM and the 5-min recording of HR and BP. As for the number of VM testing, we followed the standardization of autonomic testing recommended by Low (2003); VM was repeated until 2 reproducible responses were obtained. The mean value of BRS_VM from these repeated procedures was registered. To avoid potential variability due to circadian rhythms, all tests were performed between 9:00 a.m. and 12:00 p.m. Patients receiving medications known to cause orthostatic hypotension or otherwise affect testing results were asked to stop drug treatment for a period corresponding to five half-lives before testing, provided that it was not detrimental to their wellbeing.

The HR was recorded continuously using a standard three-lead ECG monitor (Ivy Biomedical, model 3000; Branford, CT, United States), and the BP was measured continuously using beat-to-beat photoplethysmographic recording (Finameter Pro, Ohmeda; Englewood, OH, United States). The Valsalva ratio (VR) and HRDB parameters were obtained using the WR Testworks software (WR Medical Electronics Company, Stillwater, MN, United States) and calculated as described by Low (2003). The severity of the patient's cardiovascular autonomic impairment was graded using the Composite Autonomic Scoring Scale (CASS) (Low, 1993). The patients

were considered to meet the definition of cardiovascular autonomic neuropathy (CAN) if they exhibited a minimum CASS score of one in both the cardiovagal and the adrenergic domains or a minimum score of two in a single domain; that is, when the CASS score was equal to or higher than two.

Baroreflex Sensitivity Assessment

The BRS was assessed using three different methods: the Valsalva maneuver (BRS_VM) in the laboratory, and the spontaneous BRS by sequence and spectral methods. BRS_VM was calculated by least-squares regression analysis from changes in HR and BP during the early phase II of the VM. In contrast, spontaneous BRS was computed from BP and HR records at rest, and then the BRS_seq and α-index (both at low frequency, α-LF, and in high frequency, α-HF) were obtained. The computation was performed using the Nevrokard^{TM} BRS software package (Nevrokard, Slovenia) according to a previously described criteria to estimate BRS_seq (Huang et al., 2020). For the spectral method, the oscillations of systolic BP and the RR interval were transformed to the frequency domain using fast Fourier transform. The spectral powers were divided into two frequency bands: LF (0.04–0.15 Hz) and HF (0.15–0.4 Hz). The BRS α-index was computed as the mean of the square roots of the ratios of the spectral powers of RRI to SBP in the LF and HF ranges (α-LF and α-HF, respectively) if the coherence between these two signals was > 0.5.

Statistical Analysis

Data are expressed as mean ± SD or median (interquartile range, IQR) for continuous variables and as median (IQR) for ordinal variables. Associations between the measurements were evaluated using the Pearson correlation test for normally distributed continuous variables or by the Spearman non-parametric test for continuous variables with skewness or ordinal variables. Furthermore, receiver operating characteristic (ROC) curves were generated for the BRS indexes that showed significant differences between the experimental groups for predicting the presence of CAN. The threshold for statistical significance was set at $p < 0.05$. All statistical analyses were conducted using IBM SPSS Statistics v23 statistical software (IBM, Redmond, WA, United States).

RESULTS

Demographic Data of Patients With Parkinson's Disease

The 85 patients recruited in this study included 42 men and 43 women. Of the 85 patients, ten exhibited suboptimal effort in the performance of VM, which prevented the computation of a valid CASS score. Of the remaining 75 patients, 35 had CAN and 40 did not. The demographic data per group are listed in **Table 1**. Their demographic data, as well as their functional status (UPDRS), LED, and medication

TABLE 1 | Baseline characteristics of enrolled subjects and controls.

	Controls (*n* = 22)	PD patients (*n* = 85)*		
		CAN (*n* = 35)	Non-CAN (*n* = 40)	Total (*n* = 85)
Age, years	66.6 ± 7.8	68.0 ± 8.7	63.3 ± 9.6	67.5 ± 9.7
Sex (men/women)	11/11	16/19	19/21	42/43
Height (m)	1.60 ± 0.10	1.58 ± 0.08	1.59 ± 0.07	1.59 ± 0.07
Body weight (kg)	63.0 ± 13.4	63.4 ± 10.4	62.9 ± 12.3	63.4 ± 11.3
Body mass index (kg/m^2)	24.3 ± 3.5	25.4 ± 4.2	24.7 ± 4.5	25.0 ± 4.2
Disease duration, years	–	6.0 ± 4.4	5.8 ± 4.8	5.5 ± 4.4
LED (mg/day)	–	918.3 ± 585.6	799.4 ± 600.1	828.4 ± 575.7
UPDRS total score$^{\alpha}$	–	31 [23, 37]	22.5 [15, 35.3]	27 [18, 37.5]
UPDRS I $^{\beta}$	–	2 [1, 3]	1 [0, 2]	2 [1, 3]
UPDRS II (ADL score) $^{\gamma}$	–	11 [7, 14]	7.5 [5, 13.8]	10 [5, 13]
UPDRS III (motor score) $^{\delta}$	–	18 [14, 25]	13.5 [9, 19]	16 [10.5, 22]
Cognitive abilities screening instrument	–	78.7 ± 17.5	89.3 ± 7.1	83.6 ± 13.9
Total weighted COMPASS 31 score	–	19.7 ± 11.8	14.0 ± 9.3	16.1 ± 10.6
Anti-Parkinsonian medications$^{\Phi}$				
Levodopa	–	34	34	75
Dopamine agonist (Pramipexole/Ropinirole)	–	23	30	56
MAO-B inhibitors (Selegiline/Rasagiline)	–	12	14	30
COMT inhibitors (Entacapone)	–	5	6	12
Amantadine	–	4	4	8

**Ten of the patients were unclassified due to a lack of a valid score of Composite Autonomic Scoring Scale. Φ = All the patients took more than one kind of anti-Parkinsonian medications.*

CAN, cardiovascular autonomic neuropathy; UPDRS, Unified Parkinson's Disease Rating Scale; LED, Levodopa equivalent dose, MAO-B, monoamine oxidase B, COMT, catechol-o-methyl-transferase; COMPASS, Composite Autonomic Symptom Scale.

α = "Total UPDRS" score is the combined sum of parts I, II, and III. β = I. Mentation, behavior, and mood. γ = II. Activities of daily living (ADL). δ = III. Motor examination.

information, are listed in **Table 1**. In addition, 22 age- and sex-matched subjects (11 men and 11 women) were selected from the control database of our autonomic laboratory. Their autonomic parameters are listed in **Table 2** as normal reference of our laboratory.

Comparison Between Patients With and Without Cardiovascular Autonomic Neuropathy

Table 2 shows the values for autonomic symptom profile (COMPASS 31 score), cardiovascular autonomic function (autonomic parameters and CASS score), and BRS indexes calculated by the different methods in patients with and without CAN. Among the COMPASS 31 scores, the orthostatic intolerance, bladder, and total weighted scores were significantly different between the two groups. All cardiovascular autonomic parameters and the CASS score, as well as the subscores, showed a significant difference between the two groups with the exception of BP change during head-up tilt, which appeared to be higher in the CAN group but did not reach statistical significance. Regarding the BRS indexes, significant differences between the groups were only observed in BRS_VM. Neither of the autonomic parameters showed significant difference when comparing the group of non-CAN with normal reference, but all of the autonomic parameters except the two α-indexes (α-LF and α-HF) showed significant difference when comparing the group of CAN with normal reference. (The statistical results of the comparison with normal reference are not listed in **Table 2**).

Correlation Analysis Between Composite Autonomic Scoring Scale and the Different Baroreflex Sensitivity Indexes

Table 3 shows the results of the correlations between CASS and the BRS indexes. BRS_VM exhibited significant correlations with the CASS score and with the subscores in both cardiovagal and adrenergic domains (**Figure 1**). BRS_seq exhibited significant correlations with the CASS score and cardiovagal subscore, but not with the adrenergic subscore. There was no significant correlation between the α-index and the CASS score. The correlation analysis also evaluated the relationship between each BRS index. The correlation between BRS_VM and α-LF was not significant. There were significant correlations among all the other BRS indexes.

Diagnostic Accuracy for Cardiovascular Autonomic Neuropathy Using Receiver Operating Characteristic Curve Analysis

The significant statistical analyses for predicting the presence of CAN using the ROC curve analysis are listed in **Table 4**. Only BRS_VM showed diagnostic accuracy for the presence of CAN ($p < 0.05$). The cutoff value for the presence of CAN in patients with PD was 1.25 (AUC = 0.76, $p < 0.0001$), and the sensitivity

TABLE 2 | Comparison of parameters of autonomic function and composite autonomic symptom scale 31 between PD with or without CAN.

	Normal reference (*n* = 22)	PD patients (*n* = 75)		
		CAN (*n* = 35)	Non-CAN (*n* = 40)	*p*-value
Composite autonomic symptom scale 31				
Orthostatic intolerance	0	1.7 ± 1.2	0.6 ± 0.4	0.01*
Vasomotor score	0	0.7 ± 0.3	0.7 ± 0.6	0.72
Secretomotor score	0	2.1 ± 1.5	2.0 ± 1.6	0.64
Gastrointestinal symptoms score	0	5.5 ± 3.5	5.1 ± 3.6	0.64
Bladder score	0	2.0 ± 1.7	1.3 ± 1.2	0.02*
Pupillomotor score	0	3.7 ± 2.7	4.5 ± 2.6	0.22
Total weighted COMPASS score	0	19.7 ± 11.8	14.0 ± 9.3	0.02*
Cardiovascular autonomic function				
Composite autonomic symptom scale	0	2.7 ± 1.0	0.5 ± 0.3	< 0.0001*
Adrenergic subscore	0	1.0 ± 0.8	0.5 ± 0.3	< 0.0001*
Cardiovagal subscore	0	1.7 ± 0.9	0.4 ± 0.2	< 0.0001*
Heart rate response to deep breathing (beats/min)	11.0 ± 4.6	5.1 ± 1.8	10.4 ± 4.9	< 0.0001*
Valsalva ratio	1.5 ± 0.2	1.3 ± 0.3	1.4 ± 0.2	0.02*
BP drop during head-up tilt (mmHg)	2.2 (–2.8, 9.5)	11.0 (3.0, 24.0)	5.0 (-1.0, 12.8)	0.08
Baroreflex sensitivity methods				
BRS_VM (ms/mmHg)	2.3 ± 1.5	1.3 ± 0.8	2.2 ± 1.3	0.001*
BRS_Seq (ms/mmHg)	8.0 ± 4.0	5.7 ± 2.6	6.5 ± 3.0	0.2
a-LF (ms/mmHg)	8.5 ± 4.5	8.4 ± 7.9	7.7 ± 4.6	0.72
α-HF (ms/mmHg)	11.0 ± 6.9	7.8 ± 5.5	12.1 ± 9.4	0.09

*Values are expressed as mean ± SD or median [interquartile range (IQR)], *p < 0.05 (the comparison is between groups of CAN and non-CAN).*
CAN, cardiovascular autonomic neuropathy; BP, blood pressure; BRS_VM, baroreflex sensitivity obtained by Valsalva maneuver; BRS_seq, baroreflex sensitivity obtained by sequence method; α-LF, α index in low frequency; α-HF, α index in high frequency.

TABLE 3 | Correlation analysis between CASS and different BRS indexes.

Spearman correlation	BRS_VM		BRS_Seq		a-LF		a-HF	
	r	*p*	*r*	*p*	*r*	*p*	*r*	*p*
Composite autonomic scoring scale	–0.52	< 0.0001*	–0.28	0.02*	–0.06	0.72	–0.37	0.01*
Adrenergic sub score	–0.41	0.001*	–0.11	0.34	–0.01	0.94	–0.24	0.12
Cardiovagal sub score	–0.43	< 0.0001*	–0.30	0.01*	–0.10	0.52	–0.35	0.02*
Different BRS indexes								
BRS_VM	–	–	0.279	0.024*	0.033	0.840	0.424	0.007*
BRS_seq			–	–	0.571	< 0.001*	0.936	< 0.001*
α-LF					–	–	0.492	0.001*
α-HF							–	–

** Indicates that p-value < 0.05.*
CASS, Composite autonomic scoring scale; BRS, baroreflex sensitivity; BRS_VM, baroreflex sensitivity obtained by Valsalva maneuver; BRS_seq, baroreflex sensitivity obtained by sequence method; α-LF, α index in low frequency; α-HF, α index in high frequency.

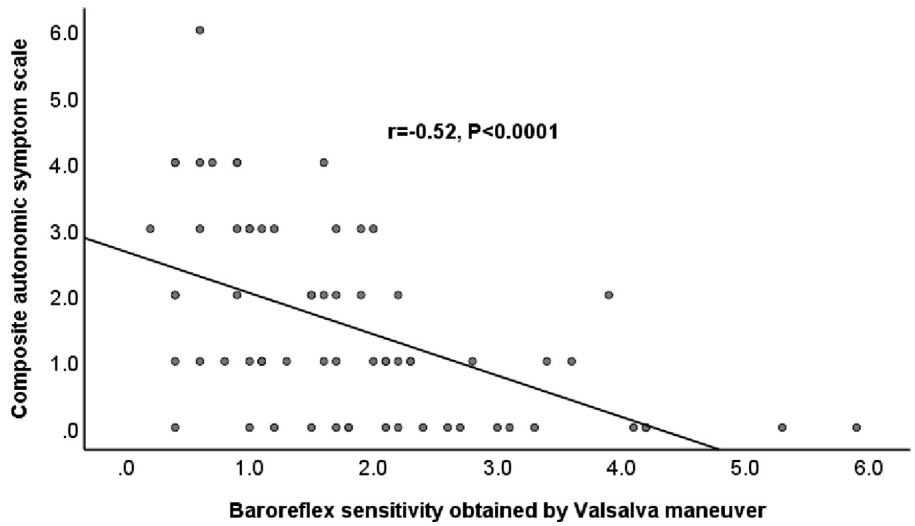

FIGURE 1 | Relationship between baroreflex sensitivity obtained by Valsalva maneuver and Composite Autonomic Scoring Scale in patients with Parkinson's disease.

TABLE 4 | Sensitivity, specificity, and area under the curve using receiver operating characteristic curve analysis for baroreflex sensitivity obtained by Valsalva maneuver in predicting cardiovascular autonomic neuropathy.

Significant parameters	Cutoff value	AUC (95% CI)	Sensitivity (%)	Specificity (%)	*p*-value
BRS_VM	1.25	0.76 (0.64–0.87)	74	60	< 0.0001*

**p < 0.01; ROC, receiver operating characteristic; BRS_VM, baroreflex sensitivity obtained by Valsalva maneuver; AUC, area under the curve.*

and specificity were 74% and 60%, respectively (**Figure 2** and **Table 4**).

DISCUSSION

Major Findings

Despite the remarkable agreement between the different methods for BRS assessment, BRS_VM had stronger correlation with CASS, which represents the severity of autonomic impairment, compared to spontaneous BRS indexes. BRS_VM also had a higher predictive value for the presence of CAN according to the diagnostic criteria by CASS in patients with PD than spontaneous BRS indexes.

Comparison of Different Baroreflex Sensitivity Assessments

To estimate BRS, the VM method explores the arterial baroreflex modulation of the heart through the quantification of tachycardia that occurs during the initial decrease in the BP at early phase II. An alternative method uses bradycardia during the subsequent increase in BP after the cessation of expiratory pressure (phase IV) (Goldstein et al., 1982). The former was selected because phase IV can be absent in patients with autonomic impairment

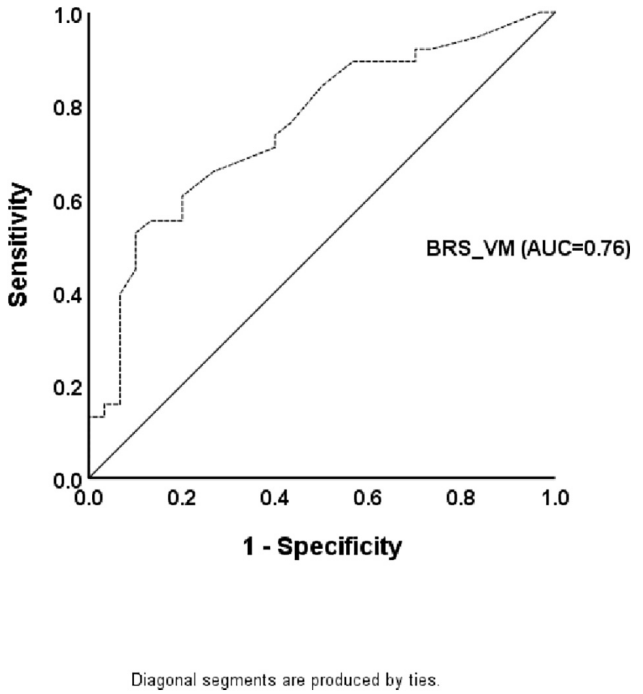

FIGURE 2 | The receiver operating characteristic curve for the presence of cardiovascular autonomic neuropathy in patients with Parkinson's disease. The diagnostic accuracy of baroreflex sensitivity obtained by the Valsalva maneuver is shown based on the receiver operating characteristic curve analysis.

such as the ones recruited for the present study (Sandroni et al., 1991). The disadvantage of BRS_VM is that the VM also triggers alterations in the chemoreceptor and cardiopulmonary receptor activity, which makes HR responses less specific. Specificity is also reduced by the concomitant stimulation of skeletal muscle receptors due to increased muscle tone during VM (Parati et al., 2000). Finally, active cooperation of the subjects being tested is required. This should be particularly taken into account in patients with PD, a certain proportion of whom fail to achieve the required effort due to motor or pulmonary dysfunction. This was the reason we did not manage to obtain valid CASS and BRS_VM data from ten of the patients that we had originally recruited. Spontaneous BRS techniques do not require any external intervention on the subject being tested, thus avoiding the aforementioned limitations. However, they still present some disadvantages. The sequence method is of limited use in patients with autonomic dysfunction such as the ones that participated in the present study because diminished BP fluctuations lead to a lack of a significant correlation with changes in the RR interval (Oka et al., 2003). The α-index is also unsuitable for these patients because of the small coherence between BP and HR (< 0.5). Our data showed no significant correlation between the α-index and the CASS score (**Table 3**), but the correlation was actually significant between α-HF and the CASS score in the subgroup of non-CAN (Spearman's rho = −0.550, $p = 0.005$). In other words, the correlation between CASS and α-HF was disrupted due to the existence of CAN. To sum up, spontaneous BRS may not be suitable to be used in patients with known autonomic impairment, such as the PD patients in this study.

There was a significant correlation between each of the BRS measures obtained by different techniques, but no correlation between BRS_VM and α-LF was identified. α-LF is influenced by additional factors such as Mayer waves in addition to baroreflex modulation (Julien, 2006; Silva et al., 2019). In subjects with intact autonomic function, baroreflex modulation is the key factor to determine α-LF. However, the influence from other factors becomes prominent in patients having autonomic impairment with reduced baroreflex modulation, such as the PD patients in our study. The reason may explain the lack of correlation between α-LF and BRS_VM in our patients. In contrast to our results that showed a significant correlation between BRS_VM and spontaneous BRS (except α-LF), the study by Yang et al. revealed a positive association between spontaneous sympathetic BRS and VM sympathetic BRS, but no correlation between spontaneous and VM cardiovagal BRS (Yang and Carter, 2013). We did not measure sympathetic BRS in the current study. The inconsistency in cardiovagal BRS may be due to different ages (much younger in Yang's study) and different characters (healthy subjects vs. patients with PD) of study subjects. Various BRS estimates are not interchangeable. A finding noted in a certain study cannot be applied to subjects with different context.

Baroreflex Sensitivity in Patients With Parkinson's Disease

Blunted BRS has been noted in previous reports (Szili-Torok et al., 2001; Blaho et al., 2017). Our data revealed that reduced BRS was noted in the CAN group but not in the non-CAN group. Furthermore, the significant difference was exhibited in BRS_VM and BRS_seq, but not in α-LF or α-HF. The finding supports the aforementioned notion that α-index is unsuitable to be used in these PD patients.

Study Limitations

There are some limitations to our study. First, we only had the database of the control group from our autonomic laboratory as normal reference for comparison. Although the case number was only 22, our normal reference of spontaneous BRS is similar to the one reported by Tank et al. (2000). Second, the study recruited only patients with comparatively better functions at a relatively early stage. We are uncertain whether our results can be applied to patients in advanced stages of PD. In addition, we only had early phase II for computing BRS_VM, and thus only tachycardia to BP decrease was assessed in the present study. BRS_VM can also be computed in phase IV to assess the function of bradycardia response to BP increase. As mentioned above, however, it was not done in the study because a certain part of our enrolled patients had absent phase IV due to adrenergic impairment. Finally, only three assessment methods for BRS were used in this study due to the laboratory settings and software availability. Further studies that include additional methods are required to comprehensively elucidate baroreflex modulation.

CONCLUSION

Our results showed considerable agreement between different methods for BRS assessment. Among them, BRS_VM had stronger correlation with CASS and was the only method that had a significant predictive value for the presence of CAN in patients with PD.

DATA AVAILABILITY STATEMENT

The raw data supporting the conclusions of this article will be made available by the authors, without undue reservation.

ETHICS STATEMENT

This study was conducted according to the guidelines of the Declaration of Helsinki, and approved by the Institutional Review Board of Chang Gung Medical Foundation (IRB 201901802B0). The patients/participants provided their written informed consent to participate in this study.

AUTHOR CONTRIBUTIONS

C-CH and C-HL conceptualization, formal analysis, and writing—review and editing. C-CH, Y-RL, and C-HL methodology. C-CH, Y-RL, C-YL, B-CC, C-TK, Y-FC, and C-HL investigation. C-CH writing—original draft preparation. C-HL resources, supervision, project administration, and funding acquisition. All authors have read and agreed to the published version of the manuscript.

FUNDING

This study was supported by grants from the Ministry of Science and Technology (MOST 109-2314-B-182A-079-MY3).

REFERENCES

Alves, M., Caldeira, D., Ferro, J. M., and Ferreira, J. J. (2020). Does Parkinson's disease increase the risk of cardiovascular events? A systematic review and meta-analysis. *Eur. J. Neurol.* 27, 288–296. doi: 10.1111/ene.14076

Blaho, A., Sutovsky, S., Valkovic, P., Siarnik, P., Sykora, M., and Turcani, P. (2017). Decreased baroreflex sensitivity in Parkinson's disease is associated with orthostatic hypotension. *J. Neurol. Sci.* 377, 207–211. doi: 10.1016/j.jns.2017.03.044

Goldstein, D. S., Horwitz, D., and Keiser, H. R. (1982). Comparison of techniques for measuring baroreflex sensitivity in man. *Circulation* 66, 432–439. doi: 10.1161/01.cir.66.2.432

Heim, B., Krismer, F., De Marzi, R., and Seppi, K. (2017). Magnetic resonance imaging for the diagnosis of Parkinson's disease. *J. Neural. Transm.* 124, 915–964. doi: 10.1007/s00702-017-1717-8

Hoehn, M. M., and Yahr, M. D. (1967). Parkinsonism: onset, progression and mortality. *Neurology* 17, 427–442. doi: 10.1212/wnl.17.5.427

Huang, C. C., Lai, Y. R., Wu, F. A., Kuo, N. Y., Tsai, Y. C., Cheng, B. C., et al. (2020). Simultaneously Improved Pulmonary and Cardiovascular Autonomic Function and Short-Term Functional Outcomes in Patients with Parkinson's Disease after Respiratory Muscle Training. *J. Clin. Med.* 9:316. doi: 10.3390/jcm9020316

Hughes, A. J., Daniel, S. E., Kilford, L., and Lees, A. J. (1992). Accuracy of clinical diagnosis of idiopathic Parkinson's disease: a clinico-pathological study of 100 cases. *J. Neurol. Neurosurg. Psychiatry* 55, 181–184. doi: 10.1136/jnnp.55.3.181

Julien, C. (2006). The enigma of Mayer waves: Facts and models. *Cardiovasc. Res.* 70, 12–21. doi: 10.1016/j.cardiores.2005.11.008

Kim, J. B., Kim, B. J., Koh, S. B., and Park, K. W. (2014). Autonomic dysfunction according to disease progression in Parkinson's disease. *Parkinsonism. Relat. Disord.* 20, 303–307. doi: 10.1016/j.parkreldis.2013.12.001

Kimpinski, K., Iodice, V., Burton, D. D., Camilleri, M., Mullan, B. P., Lipp, A., et al. (2012). The role of autonomic testing in the differentiation of Parkinson's disease from multiple system atrophy. *J. Neurol. Sci.* 317, 92–96. doi: 10.1016/j.jns.2012.02.023

Low, P. A. (1993). Composite autonomic scoring scale for laboratory quantification of generalized autonomic failure. *Mayo Clin. Proc.* 68, 748–752. doi: 10.1016/s0025-6196(12)60631-4

Low, P. A. (2003). Testing the autonomic nervous system. *Semin. Neurol.* 23, 407–421. doi: 10.1055/s-2004-817725

Martinez-Martin, P., Gil-Nagel, A., Gracia, L. M., Gomez, J. B., Martinez-Sarries, J., and Bermejo, F. (1994). Unified Parkinson's Disease Rating Scale characteristics and structure. The Cooperative Multicentric Group. *Mov. Disord.* 9, 76–83. doi: 10.1002/mds.870090112

Martinez-Martin, P., Rodriguez-Blazquez, C., Kurtis, M. M., Chaudhuri, K. R., and Group, N. V. (2011). The impact of non-motor symptoms on health-related quality of life of patients with Parkinson's disease. *Mov. Disord* 26, 399–406. doi: 10.1002/mds.23462

Oka, H., Mochio, S., Yoshioka, M., Morita, M., and Inoue, K. (2003). Evaluation of baroreflex sensitivity by the sequence method using blood pressure oscillations and R-R interval changes during deep respiration. *Eur. Neurol.* 50, 230–243. doi: 10.1159/000073865

Parati, G., Di Rienzo, M., and Mancia, G. (2000). How to measure baroreflex sensitivity: from the cardiovascular laboratory to daily life. *J. Hypertens* 18, 7–19.

Park, J. H., Kim, D. H., Park, Y. G., Kwon, D. Y., Choi, M., Jung, J. H., et al. (2020). Association of Parkinson Disease With Risk of Cardiovascular Disease and All-Cause Mortality: A Nationwide, Population-Based Cohort Study. *Circulation* 141, 1205–1207. doi: 10.1161/CIRCULATIONAHA.119.044948

Pavy-LeTraon, A., Brefel-Courbon, C., Dupouy, J., Ory-Magne, F., Rascol, O., and Senard, J. M. (2018). Combined cardiovascular and sweating autonomic testing to differentiate multiple system atrophy from Parkinson's disease. *Neurophysiol. Clin.* 48, 103–110. doi: 10.1016/j.neucli.2017.11.003

Sandroni, P., Benarroch, E. E., and Low, P. A. (1991). Pharmacological dissection of components of the Valsalva maneuver in adrenergic failure. *J. Appl. Physiol.* 71, 1563–1567. doi: 10.1152/jappl.1991.71.4.1563

Silva, L. E. V., Dias, D. P. M., da Silva, C. A. A., Salgado, H. C., and Fazan, R. Jr. (2019). Revisiting the Sequence Method for Baroreflex Analysis. *Front. Neurosci.* 13:17. doi: 10.3389/fnins.2019.00017

Sletten, D. M., Suarez, G. A., Low, P. A., Mandrekar, J., and Singer, W. (2012). COMPASS 31: a refined and abbreviated Composite Autonomic Symptom Score. *Mayo Clin. Proc.* 87, 1196–1201. doi: 10.1016/j.mayocp.2012.10.013

Szili-Torok, T., Kalman, J., Paprika, D., Dibo, G., Rozsa, Z., and Rudas, L. (2001). Depressed baroreflex sensitivity in patients with Alzheimer's and Parkinson's disease. *Neurobiol. Aging* 22, 435–438. doi: 10.1016/s0197-4580(01)00210-x

Tank, J., Baevski, R. M., Fender, A., Baevski, A. R., Graves, K. F., Ploewka, K., et al. (2000). Reference values of indices of spontaneous baroreceptor reflex sensitivity. *Am. J. Hypertens* 13, 268–275. doi: 10.1016/s0895-7061(99)00172-7

Tomlinson, C. L., Stowe, R., Patel, S., Rick, C., Gray, R., and Clarke, C. E. (2010). Systematic review of levodopa dose equivalency reporting in Parkinson's disease. *Mov. Disord.* 25, 2649–2653. doi: 10.1002/mds.23429

Yang, H., and Carter, J. R. (2013). Baroreflex sensitivity analysis: spontaneous methodology vs. Valsalva's maneuver. *Clin. Auton. Res.* 23, 133–139. doi: 10.1007/s10286-013-0195-9

Conflict of Interest: The authors declare that the research was conducted in the absence of any commercial or financial relationships that could be construed as a potential conflict of interest.

Publisher's Note: All claims expressed in this article are solely those of the authors and do not necessarily represent those of their affiliated organizations, or those of the publisher, the editors and the reviewers. Any product that may be evaluated in this article, or claim that may be made by its manufacturer, is not guaranteed or endorsed by the publisher.

frontiers | Frontiers in Neuroscience

ORIGINAL RESEARCH
published: 10 June 2022
doi: 10.3389/fnins.2022.812302

Advanced Cross-Correlation Function Application to Identify Arterial Baroreflex Sensitivity Variations From Healthy to Diabetes Mellitus

*Shoou-Jeng Yeh[1], Chi-Wen Lung[2,3], Yih-Kuen Jan[3] and Ben-Yi Liau[4]**

[1] Section of Neurology and Neurophysiology, Cheng-Ching General Hospital, Taichung, Taiwan, [2] Department of Creative Product Design, Asia University, Taichung, Taiwan, [3] Rehabilitation Engineering Laboratory, Kinesiology and Community Health, Computational Science and Engineering, University of Illinois at Urbana-Champaign, Champaign, IL, United States, [4] Department of Biomedical Engineering, Hungkuang University, Taichung, Taiwan

OPEN ACCESS

Edited by:
Yue-Der Lin,
Feng Chia University, Taiwan

Reviewed by:
Manpreet Kaur,
Vardhman Mahavir Medical College and Safdarjung Hospital, India
Vasile Urechie,
Vanderbilt University, United States

***Correspondence:**
Ben-Yi Liau
byliau@hk.edu.tw

Specialty section:
This article was submitted to Autonomic Neuroscience, a section of the journal Frontiers in Neuroscience

Received: *10 November 2021*
Accepted: *13 May 2022*
Published: *10 June 2022*

Citation:
Yeh S-J, Lung C-W, Jan Y-K and Liau B-Y (2022) Advanced Cross-Correlation Function Application to Identify Arterial Baroreflex Sensitivity Variations From Healthy to Diabetes Mellitus. Front. Neurosci. 16:812302. doi: 10.3389/fnins.2022.812302

Diabetes mellitus (DM) is a chronic disease characterized by elevated blood glucose levels, which leads over time to serious damage to the heart, blood vessels, eyes, kidneys, and nerves. DM is of two types–types 1 or 2. In type 1, there is a problem with insulin secretion, and in type 2–insulin resistance. About 463 million people worldwide have diabetes, and 80% of the majority live in low- and middle-income countries, and 1.5 million deaths are directly attributed to diabetes each year. Autonomic neuropathy (AN) is one of the common diabetic complications, leading to failure in blood pressure (BP) control and causing cardiovascular disease. Therefore, early detection of AN becomes crucial to optimize treatment. We propose an advanced cross-correlation function (ACCF) between BP and heart rate with suitable threshold parameters to analyze and detect early changes in baroreflex sensitivity (BRS) in DM with AN (DM+). We studied heart rate (HR) and systolic BP responses during tilt in 16 patients with diabetes mellitus only (DM−), 19 diabetes mellitus with autonomic dysfunction (DM+), and 10 healthy subjects. The ACCF analysis revealed that the healthy and DM groups had different filtered percentages of significant maximum cross-correlation function (CCF) value ($p < 0.05$), and the maximum CCF value after thresholds was significantly reduced during tilt in the DM+ group ($p < 0.05$). The maximum CCF index, a parameter for the phase between HR and BP, separated the healthy group from the DM groups ($p < 0.05$). Due to the maximum CCF index in DM groups being located in the positive range and significantly different from healthy ones, it could be speculated that BRS dysfunction in DM and AN could cause a phase change from lead to lag. ACCF could detect and separate DM+ from DM groups. This fact could represent an advantage of the ACCF algorithm. A common cross-correlation analysis was not easy to distinguish

between DM− and DM+. This pilot study demonstrates that ACCF analysis with suitable threshold parameters could explore hidden changes in baroreflex control in DM+ and DM−. Furthermore, the superiority of this ACCF algorithm is useful in distinguishing whether AN is present or not in DM.

Keywords: baroreflex sensitivity, diabetes mellitus, autonomic neuropathy, blood pressure, heart rate, advanced cross-correlation function

INTRODUCTION

Diabetes mellitus (DM) is a chronic disease with elevated blood sugar in the human body. The WHO team indicates that DM is a widespread and challenging health problem due to its high growth prevalence and impact on national economies. It was also revealed that 463 million adults have the condition globally and that it has been steadily increasing over the years (Gregg et al., 2021). Uncontrolled DM with increased blood sugar (hyperglycemia) causes serious damage to the heart, blood vessels, eyes, kidneys, and nerves. Diabetic autonomic neuropathy (DAN) is a common complication of diabetes that involves the autonomic nervous system. Because all the human body organs, including the cardiovascular system, are regulated by the parasympathetic and sympathetic divisions of the ANS (Vinik et al., 2003), patients with DAN would have a high risk of inducing renal failure, heart disease, stroke, blindness, and death.

The ANS controls and modulates blood pressure (BP) and heart rate (HR) interaction rapidly through arterial baroreflex. A negative feedback system buffers fluctuations to maintain HR and BP during varying conditions in daily life (Heusser et al., 2005; Robertson et al., 2012; Kaufmann et al., 2020). Cardiovascular variability and baroreflex effectiveness may be influenced by age, gender, reflex, humoral, behavioral, and environmental factors (Laitinen et al., 1998; Lanfranchi and Somers, 2002). Baroreflex measurement and assessment could be used as an index for circulatory regulation at the sinoatrial node (Lanfranchi and Somers, 2002; Jíra et al., 2006; La Rovere et al., 2008; Dutra-Marques et al., 2021; Heusser et al., 2021). A previous study reviewed approaches to measure baroreflex sensitivity (BRS), using the sequence method, cross-correlation method, cross-spectral method, synchronization index, cross multiscale entropy, joint symbolic dynamics, similarity index, etc., in DM. The study revealed that DM has baroreflex impairment with reduced baroreflex response and prolonged baroreflex (Javorka et al., 2011; Xiao et al., 2019; Cseh et al., 2020). Abnormal baroreflex function could indicate autonomic cardiovascular imbalance early (Ziegler et al., 2018; Cseh et al., 2020). Present BRS analysis methods based on HR and BP analysis might not be able to observe the sympathetic baroreflex component by its nature (Persson et al., 2001; Swenne, 2013; Kawada et al., 2021). Therefore, impaired baroreflex function could not always be detected due to this limitation or other reasons (Laude et al., 2004).

The cross-correlation function (CCF) estimates the relationship level between the two signals. It can be used to find hidden temporal similarities (Derrick and Thomas, 2004). This method has been applied to characterize autonomic and baroreflex control (Westerhof et al., 2004; Silvani et al., 2011). For instance, the method (cross-correlation BRS, xBRS) was applied to test EUROBAVAR data, including patients with a heart transplant and DAN. As a result, a different baroreflex delay was measured in patients compared with healthy subjects (Westerhof et al., 2004). Furthermore, CCF has been used successfully to evaluate cerebral autoregulation to find differences between healthy individuals and patients (Czosnyka et al., 1996; Steinmeier et al., 1996; Panerai et al., 2000, 1996; Chiu and Yeh, 2001). Recently, cross wavelet analysis was applied to follow BRS change in the time–frequency domain to understand sympathetic participation (de Boer and Karemaker, 2019). However, some non-stationary factors (e.g., weak baroreflex, frequent arrhythmias, respiratory, etc.) and unknown peripheral noise could affect the accuracy of the BRS estimation results. Therefore, a new baroreflex assessing procedure was needed to increase reliability (Persson et al., 2001; Swenne, 2013; Kawada et al., 2021; Pinheiro et al., 2021; Yamasaki et al., 2021). The purpose of this study is to propose an advanced cross-correlation function (ACCF) with suitable threshold parameters to reduce noise and inaccuracy in estimating baroreflex properties. We hypothesize that this approach (ACCF) can detect early changes in BRS in the DM group.

MATERIALS AND METHODS

Subjects and Measurement

In total, 35 age-matched patients with DM were enrolled in this study. There were 16 patients without autonomic neuropathy (AN) (DM−, 55.63 ± 15.49 years) and 19 patients with DM with AN (DM+, 65.87 ± 11.11 years). In addition, 10 healthy subjects (57.40 ± 8.41 years) were recruited. Medication was withdrawn during the study period. The AN was determined by the clinical autonomic reflex tests (R–R variation, Valsalva maneuver, and postural BP testing) (American Diabetes Association, 1992). The patients had no other cardiovascular disease and no significant BP difference ($p > 0.05$) among groups in the supine position. This study was approved by the Research Ethics Committee of Cheng-Ching General Hospital, Taiwan. Subjects were examined on a tilting table with a motor-driven change from horizontal supine to upright positions. Data acquisition was started after a 10 min relaxation period in the resting position. Then, the subject was head-up tilted to 75° within 4 s to induce BP fluctuation. A continuous arterial blood

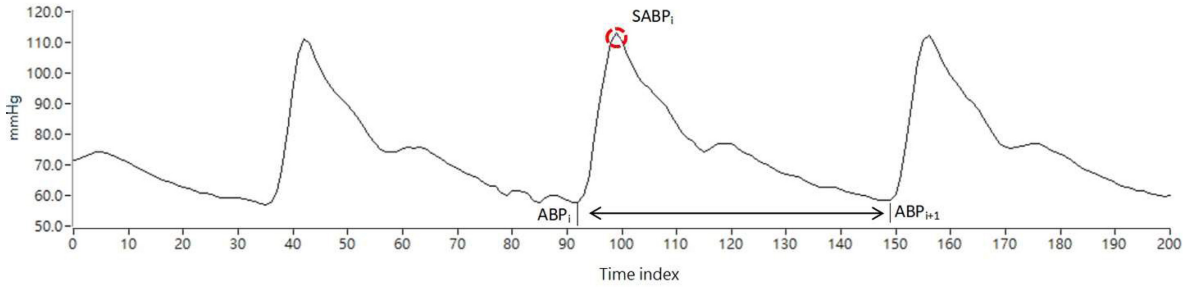

FIGURE 1 | Representation of the ABP signal, the red circle is the blood pressure wave peak.

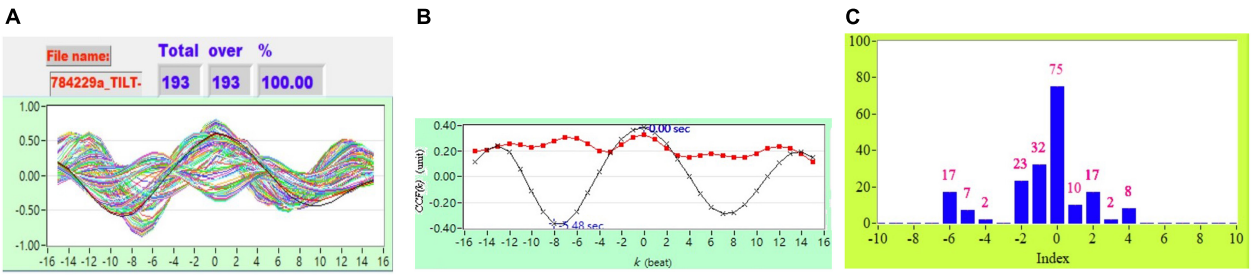

FIGURE 2 | (A) Representative plot of all *CCF* curves without thresholding, **(B)** mean *CCF* value (*x*) and SD (■), and **(C)** distribution bar chart of maximum *CCF* index during tilt in a healthy subject.

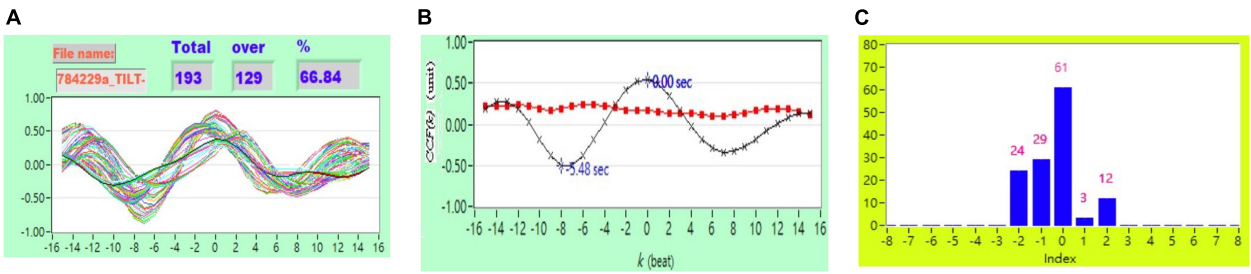

FIGURE 3 | (A) Representative plot of *CCF* curves with thresholding [$-5 \leqq k \leqq 5$ and $CCF(k) > 0$], **(B)** mean *CCF* value (*x*) and SD (■), and **(C)** distribution bar chart of maximum *CCF* index during tilt in a healthy subject.

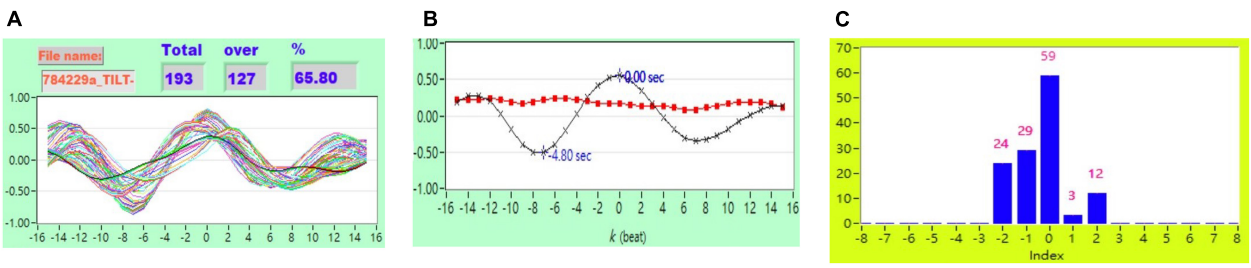

FIGURE 4 | (A) Representative plot of *CCF* curves with thresholding [$-5 \leqq k \leqq 5$ and $CCF(k) > 0.3$], **(B)** mean *CCF* value (*x*) and SD (■), and **(C)** distribution bar chart of maximum *CCF* index during tilt in a healthy subject.

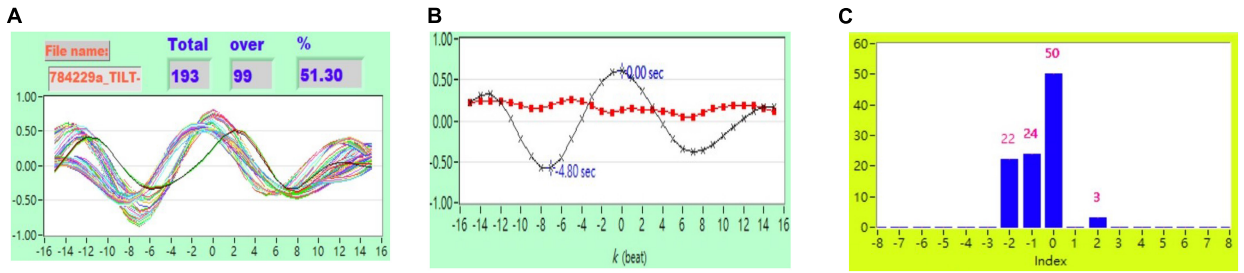

FIGURE 5 | (A) Representative plot of *CCF* curves with thresholding [$-5 \leqq k \leqq 5$ and $CCF(k) > 0.5$], **(B)** mean *CCF* value (x) and SD (■), and **(C)** distribution bar chart of maximum *CCF* index during tilt in a healthy subject.

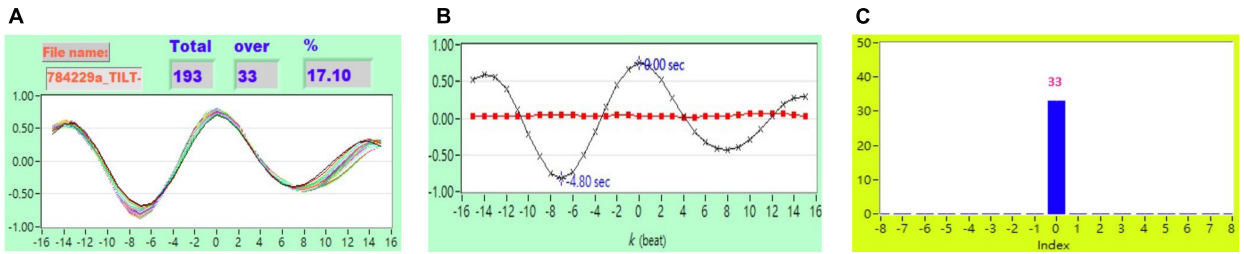

FIGURE 6 | (A) Representative plot of *CCF* curves with thresholding [$-5 \leqq k \leqq 5$ and $CCF(k) > 0.7$] **(B)** mean *CCF* value (x) and SD (■), and **(C)** distribution bar chart of maximum *CCF* index during tilt in a healthy subject.

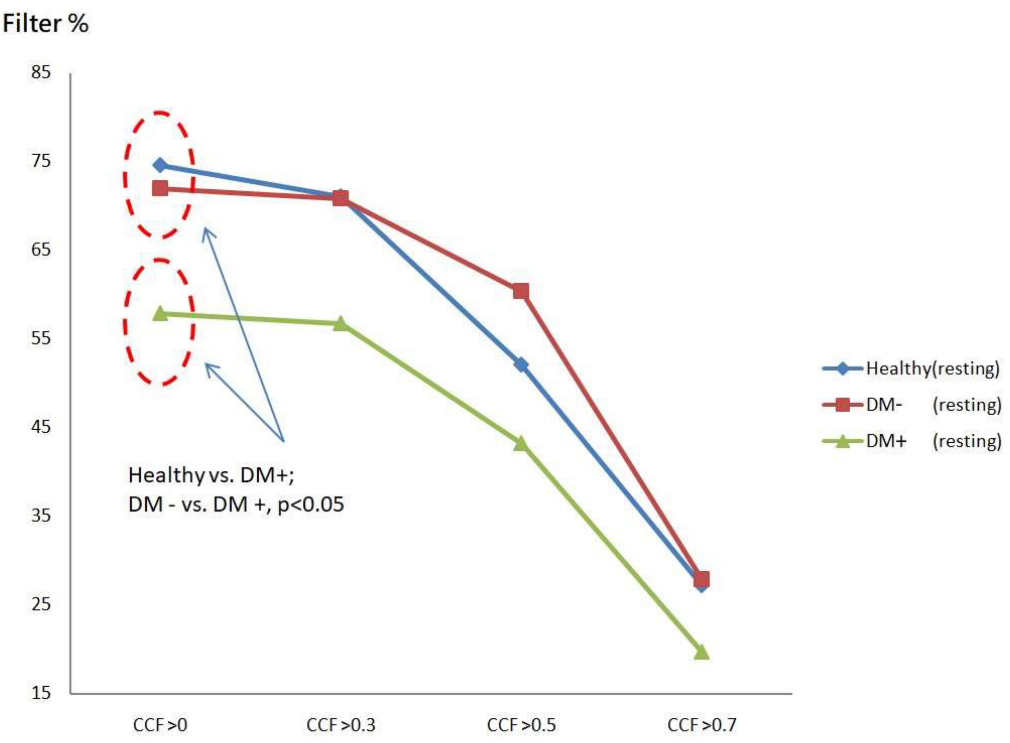

FIGURE 7 | The plot of filter % with different thresholds by *ACCF* results in the supine position. Filtered maximum *CCF* value (% to all *CCF* values) using the threshold $CCF > 0$, 0.3, 0.5, and 0.7 in resting position in healthy (blue), diabetes mellitus (DM–, red), and DM with autonomic neuropathy (DM+, green). Threshold $CCF > 0$ allowed to differentiate healthy, DM–, and DM+.

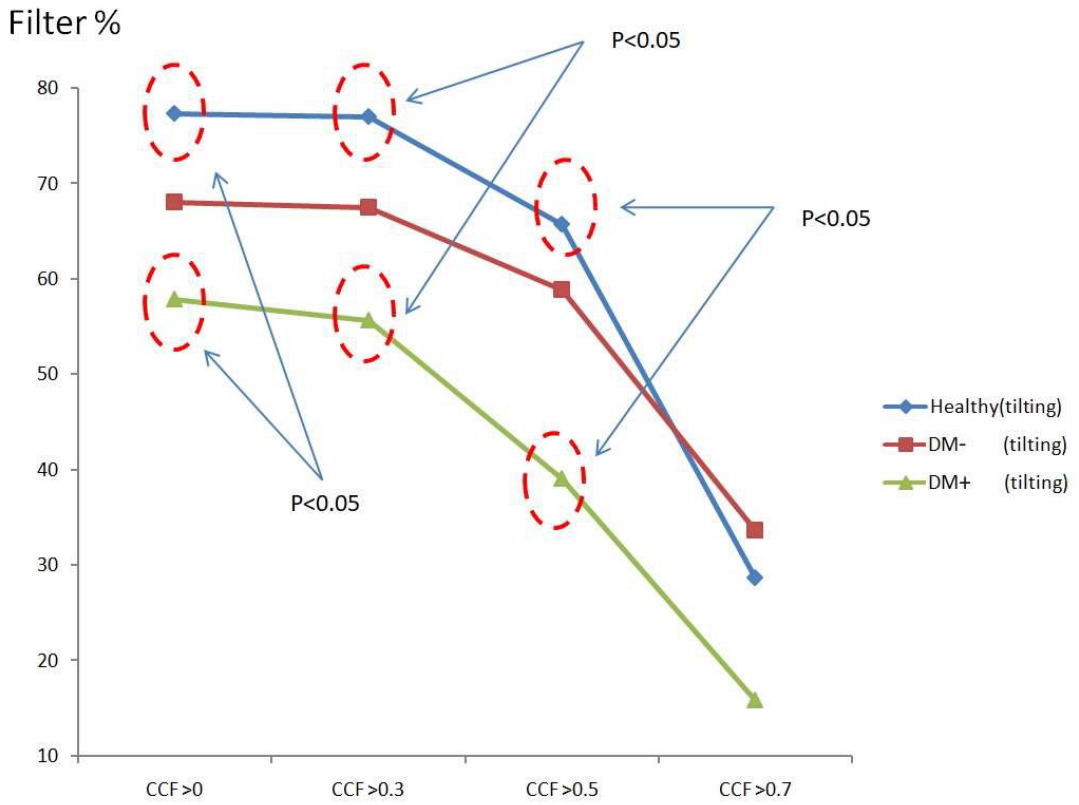

FIGURE 8 | The plot of filter % with different thresholds by *ACCF* results in a tilting position. *ACCF* results of tilt. Filtered maximum CCF value (% to all CCF values) using the threshold *CCF* > 0, 0.3, 0.5, and 0.7 in resting position in healthy (blue), diabetes mellitus (DM–, red), and DM with autonomic neuropathy (DM+, green). CCF thresholds of >0, >0.3, and >0.5 allowed for the differentiation of healthy and DM+ individuals.

pressure (ABP) signal was acquired at 60 Hz sample frequency for 5 min by Finapres (Model 2300, Ohmeda, Englewood, CO, United States) during supine and head-up tilt positions. Signals were analyzed with their own developed system using the software—LabVIEW language (Chiu and Yeh, 2001; Chiu et al., 2005).

Figure 1 shows the representation of the ABP signal. While the ABP pulse signal was acquired continuously by Finapres, SABPi (*i*th systolic arterial blood pressure) is the waveform peak through time index in the *i*th ABP pulse beat. Therefore, SABPi is the maximum BP value calculated by the *i*th pulse beat. The systolic arterial blood pressure (SABP) value was calculated using each pulse as follows:

$$\mathrm{SABP}_i = \max\left(\mathrm{ABP}_i,\ \mathrm{ABP}_{i+1}\right)$$

Simultaneously, systolic BP was aligned with the R–R interval, and instantaneous HR was derived from the point at which the systolic BP event occurred. In the previous studies, beat-to-beat BP and HR could be recorded by photoplethysmography. The accuracy of beat-to-beat non-invasive measurement *via* finger arterial pressure using Finpres was confirmed (Novak et al., 1994; Buclin et al., 1999).

Advanced Cross-Correlation Function Estimation

Cross-Correlation Function Estimation for Baroreflex Sensitivity

Cross-correlation is a method to assess the similarity degree of two series data sets. The cross-correlation function (CCF) could provide a measure of association between time-series signals (Derrick and Thomas, 2004). In this study, the SABP signal and the beat-to-beat HR signal as the input data for estimation. The relation and phase between the SABP and the HR signals can be used to evaluate the baroreflex function. The cross-correlation and phase between BP and HR depend on the autonomic baroreflex control. Therefore, it could explore changes in baroreflex mechanisms for health and disease.

Let the cross-correlation function be expressed as *CCF(k)*, *W* is the length of the window, *k* is the number of peak-to-peak displacement points, and *N* is the total signal length. Assume that the SABP and HR signals are represented as *f(n)* and *g(n)*, respectively. To assess the autonomic nervous system in specific frequency bands, *f(n)* and *g(n)* signals

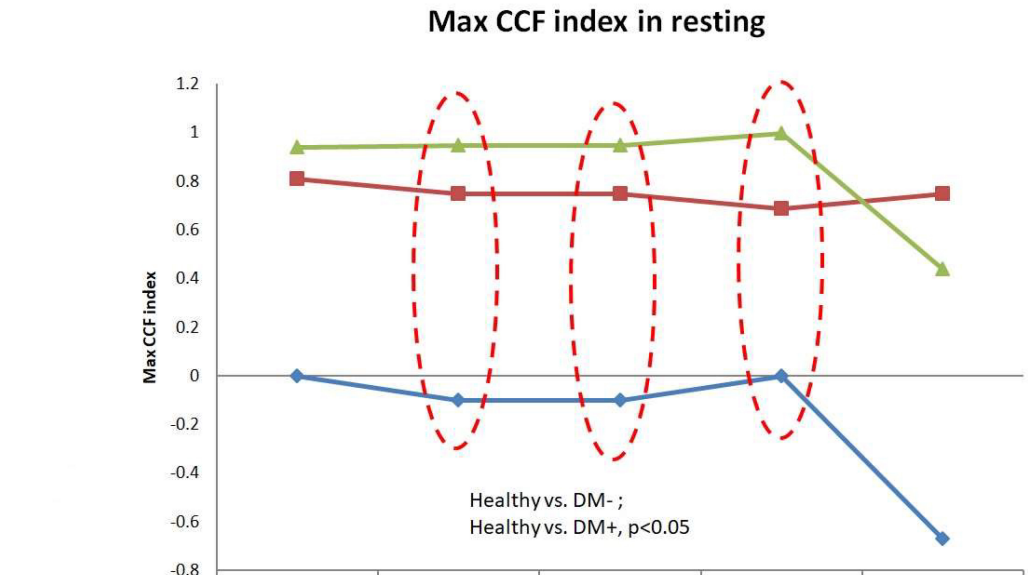

	no limitation	>0	>0.3	>0.5	>0.7
Healthy (resting)	0	-0.1	-0.1	0	-0.67
DM- (resting)	0.8125	0.75	0.75	0.69	0.75
DM+ (resting)	0.94	0.95	0.95	1	0.44

FIGURE 9 | The plot of the maximum *CCF* index with different thresholds by *ACCF* results in the supine position. *ACCF* phase analysis during resting supine. Filtered maximum CCF index in healthy (blue), diabetes mellitus (DM–, red), and DM with autonomic neuropathy (DM+, green). When the threshold setting was greater than 0, 0.3, and 0.5, the filtered maximum CCF index could significantly separate the healthy group from the DM– and DM+ group ($p < 0.05$). It also indicates that the phase between HR and BP was prolonged in DM.

were bandpass filtered in low frequency (LF) ranges before applying the CCF. Where the LF range is 0.07–0.15 Hz, assume that bandpass filtered $f(n)$ and $g(n)$ signals are $\hat{f}(n)$and $\hat{g}(n)$, respectively. The *CCF* between $\hat{f}(n)$and $\hat{g}(n)$ can be calculated as follows:

$$CCF_i(k) = \frac{R^i_{\hat{f}\hat{g}}(k)}{\left[R^i_{\hat{f}\hat{f}}(0)R^i_{\hat{g}\hat{g}}(0)\right]^{\frac{1}{2}}} \ldots k = 0, \ \pm 1, \ \pm 2, \cdots,$$
$$i = 1 \text{ to } N\text{–}W + 1 \ldots\ldots\ldots\ldots\ldots\ldots(1)$$

where $R^i_{\hat{f}\hat{g}}(k)$ is an estimation of the cross-covariance in the ith time window and defined as

$$R^i_{\hat{f}\hat{g}}(k) = \begin{cases} \frac{1}{W}\sum_{j=i}^{i+W} \hat{f}(j)\hat{g}(j+k), \ k = 0, \ 1, \ 2, \cdots \\ \frac{1}{W}\sum_{j=i}^{i+W} \hat{f}(j-k)\hat{g}(j), \ k = 0, \ -1, \ -2, \cdots \end{cases} \ldots\ldots\ldots\ldots\ldots\ldots(2)$$

$$\text{Also } R^i_{\hat{f}\hat{f}}(0) = \frac{1}{W}\sum_{j=i}^{i+W}[\hat{f}(j)]^2, \text{ and } R^i_{\hat{g}\hat{g}}(0) = \frac{1}{W}\sum_{j=i}^{i+W}[\hat{g}(j)]^2.$$

where N is the total number of cardiac cycles, W is the window width, and k is the time lag. In this study, $+k$ means that HR follows BP. $CCF_i(\cdot)$ is the outcome of *CCF* between $\hat{f}(n)$ and $\hat{g}(n)$ in the ith time window.

Advanced Cross-Correlation Function Estimation Using the Thresholding

As described in section "*Cross-Correlation Function* Estimation for Baroreflex Sensitivity," the original *CCF* estimation has $N = 256$, $W = 64$, and no other threshold following the *CCF* estimation. **Figure 1** shows typical 2D figures using the *CCF* estimation. Due to $i = 1$ to $N - W + 1$, there are 193 *CCF* curves in this study. A typical 2D representative figure is shown in **Figure 1**.

In *ACCF* estimation, we set thresholding parameters for k to improve some limitations and filter some noise to avoid a result bias. The thresholding was as follows:

Followed the *CCF* estimation, we set $N = 256$, $W = 64$, and $-5 \leqq k \leqq 5$.

The *ACCF* with thresholding between $\hat{f}(n)$and $\hat{g}(n)$ can be calculated as follows:

$$ACCF_i(k) = \frac{R^i_{\hat{f}\hat{g}}(k)}{\left[R^i_{\hat{f}\hat{f}}(0)R^i_{\hat{g}\hat{g}}(0)\right]^{\frac{1}{2}}} > threshold, k=0, \ +1, \ +2, \ +3, \ +4, \ +5 \ldots\ldots\ldots\ldots(3)$$

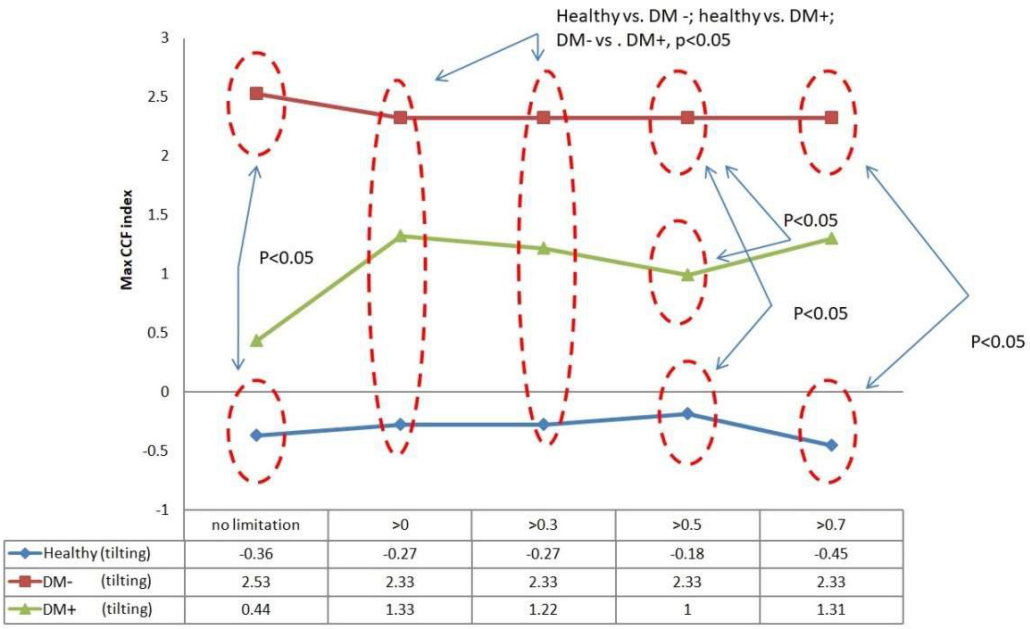

	no limitation	>0	>0.3	>0.5	>0.7
Healthy (tilting)	-0.36	-0.27	-0.27	-0.18	-0.45
DM- (tilting)	2.53	2.33	2.33	2.33	2.33
DM+ (tilting)	0.44	1.33	1.22	1	1.31

FIGURE 10 | The plot of the maximum *CCF* index with different thresholds by *ACCF* results in a tilting position. *ACCF* phase analysis during tilt. Filtered maximum *CCF* index in healthy (blue), diabetes mellitus (DM–, red), and DM with autonomic neuropathy (DM+, green). When the threshold setting was set greater than 0, 0.3, 0.5, and 0.7, the filtered maximum *CCF* index could significantly separate the healthy group from the DM– and DM+ groups ($p < 0.05$). In addition, the two DM groups could be separated ($p < 0.05$) when the threshold was set to 0, 0.3, and 0.5.

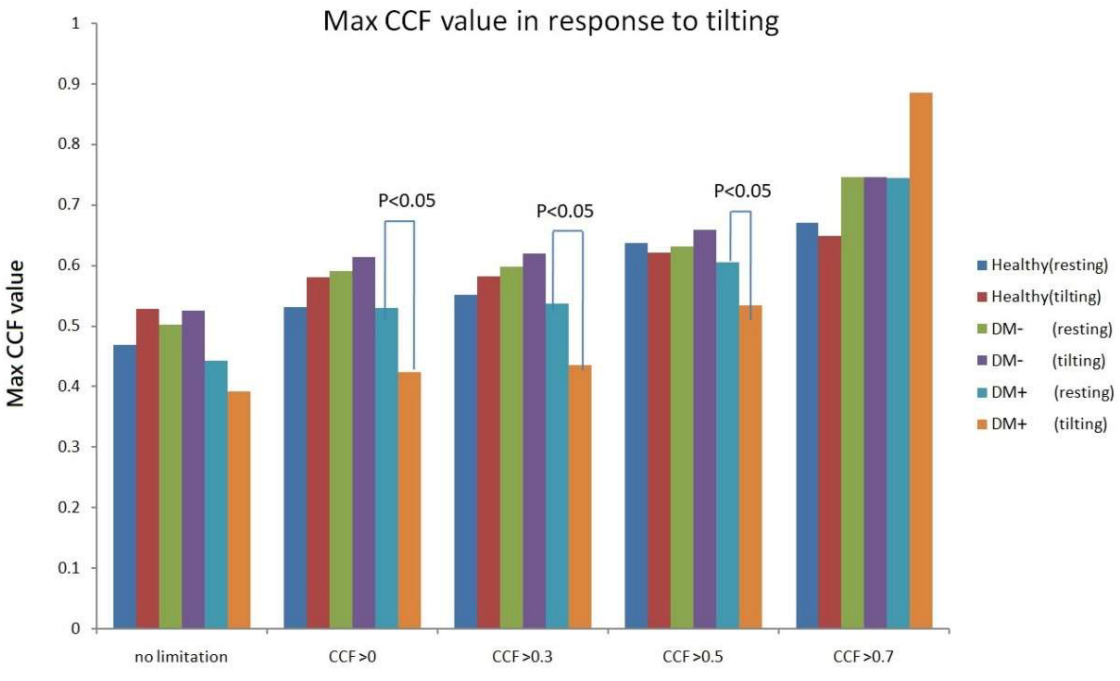

FIGURE 11 | Maximum *CCF* value response to tilt in healthy (red), diabetes mellitus (DM–, purple), and DM with autonomic neuropathy (DM+, orange) after thresholding of *CCF* > 0, 0.3, 0.5, and 0.7.

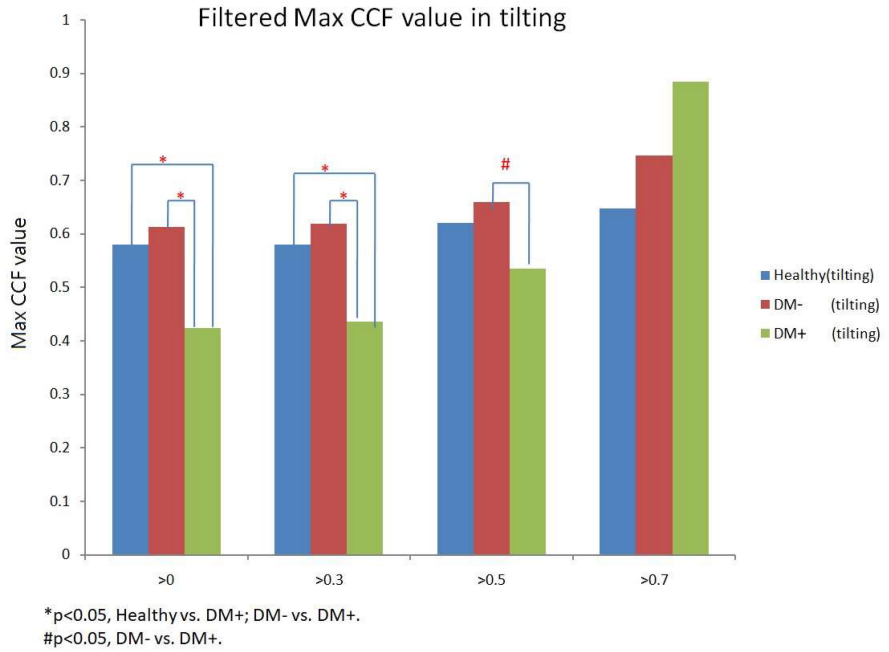

FIGURE 12 | The filtered maximum *CCF* value in healthy (blue), diabetes mellitus (DM–, red), and DM with autonomic neuropathy (DM+, green) using the threshold $CCF > 0$, 0.3, 0.5, and 0.7 during tilting position. The symbol "*" and "#" mean the *p*-value smaller than 0.05 in *t*-test.

where the threshold = 0, 0.3, 0.5, 0.7.

Figure 2 shows the representative plot of all *CCF* curves without threshold. **Figures 3–6** are the representative plot of all *CCF* curves with different thresholds, respectively.

RESULTS

The Filtered Proportion of Maximum *Cross-Correlation Function* Value

The filtered value was the proportion of *CCF* values that passed the threshold set for all *CCF* values without thresholds. **Figure 7** shows *ACCF* results for the supine position. The filtered value was higher in the healthy group than in the DM groups when the *CCF* threshold was set to be greater than 0 ($CCF > 0$). This threshold of $CCF > 0$ permits separating the healthy group from DM groups ($p < 0.05$) in the resting position. The two DM groups, DM− and DM+, also showed significantly different filtered values ($p < 0.05$). It revealed the effect of AN on DM that the relation level between BP and HR by the maximum *CCF* value. The filtered amount of *CCF* values in the DM+ group always keeps the lower percentage values at every threshold.

Figure 8 shows the *ACCF* results of tilt. The filtered value (% of all CCF values) was higher in the healthy than those in the DM+ group when the *CCF* threshold was set at $CCF > 0$, $CCF > 0.3$, and $CCF > 0.5$. The healthy group could be significantly separated from the DM+ group ($p < 0.05$).

The filtered *CCF* values tended to be lower with the higher threshold in healthy and DM groups using the threshold setting. In the DM+ group, the least filtered percentage of *CCF* values was always kept at every different threshold. It could show a more significant difference between the healthy group and DM+ group in an upright position.

Maximum Cross-Correlation Function Index With Threshold

Figure 9 shows the filtered maximum *CCF* index in the resting supine. When the threshold setting for maximum *CCF* value is greater than 0, 0.3, and 0.5, the filtered maximum *CCF* index could significantly separate the healthy group from the DM group ($p < 0.05$). It also indicated that the phase between HR and BP was prolonged in DM. In addition, the two DM groups could be separated significantly ($p < 0.05$) when the threshold was set to 0, 0.3, and 0.5.

Figure 10 shows the filtered maximum *CCF* index during tilt. The filtered maximum *CCF* index value was greater during the upright position when the threshold was set at greater than 0, 0.3, 0.5, and 0.7. The max *CCF* index could completely separate the healthy group from the DM ($p < 0.05$). In addition, the two DM groups could be separated ($p < 0.05$) when the threshold was set to 0, 0.3, and 0.5.

Comparison of Maximum Cross-Correlation Function Value in Response to Head-up Tilting

Figure 11 shows the estimated CCF value after filter during tilt. The results indicate that when the threshold for *CCF* was set greater than 0, 0.3, and 0.5, the estimate of maximum *CCF*

values of the DM+ group was reduced significantly ($p < 0.05$) in response to tilting, while *CCF* did not change in healthy.

Figure 12 shows the filtered maximum *CCF* value after thresholding during tilt position. When the threshold was greater than 0, 0.3, and 0.5, the maximum *CCF* values were significantly lower in DM+ ($p < 0.05$) than in the DM− group. Moreover, when the threshold was greater than 0 and 0.3, the maximum *CCF* values of DM+ were significantly lower ($p < 0.05$) than those in the healthy group. Thresholding $CCF > 0$, 0.3, and 0.5 during tilt distinguished between DM+ and DM−.

DISCUSSION

To the best of our knowledge, this is the first study to investigate baroreflex performance and differences using the *ACCF* to observe progress in baroreflex dysfunction from healthy to DAN. The thresholding for maximum CCF value showed that the DM+ group showed the least filtered percentage relative to all CCF values. In addition, the percentage of filtered value in the DM+ group was significantly different from the healthy group. That could indicate that the baroreflex function mediated the relationship between BP and HR is increased more than those in healthy and DM− groups. This difference could not be found using a common CCF analysis method without a threshold (**Figure 10**).

In addition, the maximum CCF value after thresholding is significantly reduced during tilt in the DM+ group. In clinical practice, AN diagnosis requires a series of complex tests. It is worth noting that during upright, maximum CCF values after thresholding were significantly different in the DM+ group from those in the healthy and DM− groups. This fact could represent an advantage of the ACCF algorithm to distinguish DM+ or DM−. We demonstrated that setting the threshold for maximum CCF value in the estimation process could differentiate between DM+ and healthy groups and even DM+ and DM− groups. It is known that the BRS is reduced in patients with DM and cannot counteract BP fluctuations effectively. Furthermore, patients with DM+ are unable to regulate their HR, blood vessel tone, and other parameters due to baroreflex dysfunction, which raises the risk of cardiovascular disease (Kuusela et al., 2002; Yu et al., 2011; Fuchs and Ehelton, 2020).

Furthermore, we could show that the phase between BP and HR, determined by the maximum *CCF* index in the *ACCF* estimation, is different in healthy and DM groups. A negative lag represents a phase-lead characteristic (BP leads HR) (Chiu and Yeh, 2001; Chiu et al., 2005). Recently, de Boer and Karemaker (2019) assessed BRS by cross wavelet analysis and head-up tilt. The results enabled the estimation of cross-spectra and derived quantities of BRS during time and frequency conditions. Some researchers assumed that baroreflex dysfunction causes a reduction of phase-lead to nearly zero time delay (Steinmeier et al., 1996). Our results confirm the previous support. In this study, **Figures 9**, **10** show the maximum *CCF* index of *ACCF* estimation results, which indicates the maximum *CCF* index in the healthy group, was in the negative range for both resting and tilting positions. Thus, the analysis results of the healthy and DM+ groups were confirmed by a previous report (Westerhof et al., 2004), and it may be standard for normal BRS function.

Interestingly, the maximum *CCF* index in DM groups was located in the positive range and was significantly different from those in the healthy group. We speculated that BRS dysfunction in DM and AN could cause a change from phase-lead to phase-lag. Furthermore, in line with previous studies, baroreflex response was reduced, and the delay was prolonged (Javorka et al., 2011; Xiao et al., 2019; Cseh et al., 2020), which supported the assumption. Therefore, we proposed an advanced cross-correlation function to estimate BRS in healthy and DM groups. Our results revealed that significant differences between the groups would be shown when the threshold setting for maximum CCF value was 0–0.5. It might be suggested that the proposed thresholding of maximum CCF from 0 to 0.5 improves the separation of DM+ and DM−.

CONCLUSION

Advanced CCF analysis with suitable thresholding improves the detection of changes in DM's BRS. The new method could explore hidden changes in circulatory system component characteristics and BRS performance and provide new insight and risk prediction in patients with DM.

DATA AVAILABILITY STATEMENT

The raw data supporting the conclusions of this article will be made available by the authors, without undue reservation.

ETHICS STATEMENT

The studies involving human participants were reviewed and approved by the Research Ethics Committee of Cheng-Ching General Hospital, Taiwan. The patients/participants provided their written informed consent to participate in this study.

AUTHOR CONTRIBUTIONS

B-YL and S-JY: conceptualization and methodology. B-YL and Y-KJ: formal analysis. B-YL, C-WL, and Y-KJ: writing. B-YL: project administration. All authors have read and agreed to the published version of the manuscript.

FUNDING

This work was supported by the Ministry of Science and Technology, Taiwan (MOST 110-2637-E-241-002) to B-YL and S-JY.

ACKNOWLEDGMENTS

We thank the National Science Council, Taiwan, ROC, for supporting this research under Contract No. MOST 110-2637-E-241-002.

REFERENCES

American Diabetes Association (1992). Proceedings of a consensus development conference on standardized measures in diabetic neuropathy: autonomic nervous system testing. *Diabetes Care* 15(Suppl. 3), 1095–1103.

Buclin, T., Buchwalder-Csajka, C., Brunner, H. R., and Biollaz, J. (1999). Evaluation of noninvasive blood pressure recording by photoplethysmography in clinical studies using angiotensin challenges. *Br. J. Clin. Pharmacol.* 48, 586–593. doi: 10.1046/j.1365-2125.1999.00049.x

Chiu, C. C., and Yeh, S. J. (2001). Assessment of cerebral autoregulation using time-domain cross-correlation analysis. *Comput. Biol. Med.* 31, 471–480.

Chiu, C. C., Yeh, S. J., and Liau, B. Y. (2005). Assessment of cerebral autoregulation dynamics in diabetics using time-domain cross-correlation analysis. *J. Med. Bio. Eng.* 25, 53–59.

Cseh, D., Climie, R. E., Offredo, L., Guibout, C., Thomas, F., Zanoli, L., et al. (2020). Type 2 diabetes mellitus is independently associated with decreased neural baroreflex sensitivity: the paris prospective study III. *Arterioscler. Thromb. Vasc. Biol.* 40, 1420–1428.

Czosnyka, M., Smielewski, P., Kirkpatrick, P., Menon, D. K., and Pickard, J. D. (1996). Monitoring of cerebral autoregulation in head-injured patients. *Stroke* 27, 1829–1834. doi: 10.1161/01.str.27.10.1829

de Boer, R. W., and Karemaker, J. M. (2019). Cross-wavelet time-frequency analysis reveals sympathetic contribution to baroreflex sensitivity as cause of variable phase delay between blood pressure and heart rate. *Front. Neurosci.* 13:694. doi: 10.3389/fnins.2019.00694

Derrick, T. R., and Thomas, J. M. (2004). "Time series analysis: the cross-correlation function," in *Innovative Analyses of Human Movement*, ed. N. Stergiou (Champaign IL: Human Kinetics Publishers), 189–205.

Dutra-Marques, A. C., Rodrigues, S., Cepeda, F. X., Toschi-Dias, E., Rondon, E., Carvalho, J. C., et al. (2021). Exaggerated exercise blood pressure as a marker of baroreflex dysfunction in normotensive metabolic syndrome patients. *Front. Neurosci.* 15:680195. doi: 10.3389/fnins.2021.680195

Fuchs, F. D., and Ehelton, P. K. (2020). High blood pressure and cardiovascular disease. *Hypertension* 75, 285–292.

Gregg, E., Buckley, J., Ali, M., Davies, J., Flood, D., Griffiths, B., et al. (2021). *Improving Health Outcomes of People with Diabetes Mellitus: Target Setting to Reduce the Global Burden of Diabetes Mellitus by 2030*. Geneva: WHO technical document.

Heusser, K., Heusser, R., Jordan, J., Urechie, V., Diedrich, A., and Tank, J. (2021). Baroreflex curve fitting using a WYSIWYG boltzmann sigmoidal equation. *Front. Neurosci.* 15:697582. doi: 10.3389/fnins.2021.697582

Heusser, K., Tank, J., Luft, F. C., and Jordan, J. (2005). Baroreflex failure. *Hypertension.* 2005, 834–839.

Javorka, M., Lazarova, Z., Tonhajzerova, I., Turianikova, Z., Honzikova, N., Fiser, B., et al. (2011). Baroreflex analysis in diabetes mellitus: linear and nonlinear approaches. *Med. Biol. Eng. Comput.* 49, 279–288.

Jíra, M., Závodná, E., Honzíková, N., Nováková, Z., and Fiser, B. (2006). Baroreflex sensitivity as an individual characteristic feature. *Physiol. Res.* 55, 349–351. doi: 10.33549/physiolres.930814

Kaufmann, H., Norcliffe-Kaufmann, L., and Palma, J. A. (2020). Baroreflex dysfunction. *New Engl. J. Med.* 382, 163–178.

Kawada, T., Saku, K., and Miyamoto, T. (2021). Closed-loop identification of baroreflex properties in the frequency domain. *Front. Neurosci.* 15:694512. doi: 10.3389/fnins.2021.694512

Kuusela, T. A., Jartti, T. T., Tahvanainen, K. U. O., and Kaila, T. J. (2002). Nonlinear methods of biosignal analysis in assessing terbutaline-induced heart rate and blood pressure changes. *Am. J. Physiol. Heart Circ. Physiol.* 282, H773–H781. doi: 10.1152/ajpheart.00559.2001

La Rovere, M. T., Pinna, G. D., and Raczak, G. (2008). Baroreflex sensitivity: measurement and clinical implications. *Ann. Noninvasive Electrocardiol.* 13, 191–207. doi: 10.1111/j.1542-474X.2008.00219.x

Laitinen, T., Hartikainen, J., Vanninen, E., Niskanen, L., Geelen, G., and Länsimies, E. (1998). Age and gender dependency of baroreflex sensitivity in healthy subjects. *J. Appl. Physiol.* 84, 576–583. doi: 10.1152/jappl.1998.84.2.576

Lanfranchi, P. A., and Somers, V. K. (2002). Arterial baroreflex function and cardiovascular variability: interactions and implications. *Am. J. Physiol. Regul. Integr. Comp. Physiol.* 283, R815–R826. doi: 10.1152/ajpregu.00051.2002

Laude, D., Elghozi, J. L., Girard, A., Bellard, E., Bouhaddi, M., Castiglioni, P., et al. (2004). Comparison of various techniques used to estimate spontaneous baroreflex sensitivity (the EuroBaVar study). *Am. J. Physiol. Regul. Integr. Comp. Physiol.* 286, R226–R231. doi: 10.1152/ajpregu.00709.2002

Novak, V., Novak, P., and Schondorf, R. (1994). Accuracy of beat-to-beat noninvasive measurement of finger arterial pressure using the finapres: a spectral analysis approach. *J. Clin. Monitor.* 10, 118–126. doi: 10.1007/BF02886824

Panerai, R. B., Kelsall, A. W., Rennie, J. M., and Evans, D. H. (1996). Analysis of cerebral blood flow autoregulation in neonates. *IEEE Trans. Biomed. Eng.* 43, 779–788. doi: 10.1109/10.508541

Panerai, R. B., Simpson, D. M., Deverson, S. T., Mahony, P., Hayes, P., and Evans, D. H. (2000). Multivariate dynamic analysis of cerebral blood flow regulation in humans. *IEEE Trans. Biomed. Eng.* 47, 419–423. doi: 10.1109/10.827312

Persson, P. B., DiRienzo, M., Castiglioni, P., Cerutti, C., Pagani, M., Honzikova, N., et al. (2001). Time versus frequency domain techniques for assessing baroreflex sensitivity. *J. Hypertens.* 19, 1699–1705. doi: 10.1097/00004872-200110000-00001

Pinheiro, A., Vianna, L. C., and Carmo, J. C. (2021). Noiseless variable-pressure neck chamber device to assess the carotid baroreflex function. *Front. Physiol* 11:613311. doi: 10.389/fphys.2020.613311

Robertson, D., Diedrich, A., and Chapleau, M. W. (2012). Editorial on arterial baroreflex issue. *Auton. Neurosci. Basic Clin.* 172, 1–3.

Silvani, A., Magosso, E., Bastianini, S., Lenzi, P., and Ursino, M. (2011). Mathematical modeling of cardiovascular coupling: central autonomic commands and baroreflex control. *Auton. Neurosci. Basic Clin.* 162, 66–71. doi: 10.1016/j.autneu.2011.04.003

Steinmeier, R., Bauhuf, C., Hübner, U., Bauer, R. D., Fahlbusch, R., Laumer, R., et al. (1996). Slow rhythmic oscillations of blood pressure, intracranial pressure, microcirculation, and cerebral oxygenation. *Dyn. Interrelation Time Course Hum. Stroke* 27, 2236–2243. doi: 10.1161/01.str.27.12.2236

Swenne, C. A. (2013). Baroreflex sensitivity: mechanisms and measurement. *Neth. Heart J.* 21, 58–60. doi: 10.1007/s12471-012-0346-y

Vinik, A. I., Maser, R. E., Mitchell, B. D., and Freeman, R. (2003). Diabetic autonomic neuropathy. *Diabetes care* 26, 1553–1579.

Westerhof, B. E., Gisolf, J., Stok, W. J., Wesseling, K. H., and Karemaker, J. M. (2004). Time-domain cross-correlation baroreflex sensitivity: performance on the EUROBAVAR data set. *J. Hypertens.* 22, 1371–1380. doi: 10.1097/01.hjh.0000125439.28861.ed

Xiao, M.-X., Lu, C.-H., Ta, N., Jiang, W.-W., Tang, X.-J., and Wu, H.-T. (2019). Application of a speedy modified entropy method in assessing the complexity of baroreflex sensitivity for age-controlled healthy and diabetic subjects. *Entropy* 21:894.

Yamasaki, F., Sato, T., Sato, K., and Diedrich, A. (2021). Analytic and integrative framework for understanding human sympathetic arterial baroreflex function: equilibrium diagram of arterial pressure and plasma norepinephrine level. *Front. Neurosci.* 15:707345. doi: 10.3389/fnins.2021.707345

Yu, J. G., Zhou, R. R., and Cai, G. J. (2011). From hypertension to stroke: mechanisms and potential prevention strategies. *CNS Neurosci. Ther.* 17, 577–584. doi: 10.1111/j.1755-5949.2011.00264.x

Ziegler, D., Strom, A., Kupriyanova, Y., Bierwagen, A., Bönhof, G. J., Bódis, K., et al. (2018). Association of lower cardiovagal tone and baroreflex sensitivity with higher liver fat content early in type 2 diabetes. *J. Clin. Endocrinol. Metab.* 103, 1130–1138. doi: 10.1210/jc.2017-02294

Conflict of Interest: The authors declare that the research was conducted in the absence of any commercial or financial relationships that could be construed as a potential conflict of interest.

Advantages of publishing in Frontiers

OPEN ACCESS
Articles are free to read for greatest visibility and readership

FAST PUBLICATION
Around 90 days from submission to decision

HIGH QUALITY PEER-REVIEW
Rigorous, collaborative, and constructive peer-review

TRANSPARENT PEER-REVIEW
Editors and reviewers acknowledged by name on published articles

Frontiers
Avenue du Tribunal-Fédéral 34
1005 Lausanne | Switzerland

Visit us: www.frontiersin.org
Contact us: frontiersin.org/about/contact

REPRODUCIBILITY OF RESEARCH
Support open data and methods to enhance research reproducibility

DIGITAL PUBLISHING
Articles designed for optimal readership across devices

FOLLOW US
@frontiersin

IMPACT METRICS
Advanced article metrics track visibility across digital media

EXTENSIVE PROMOTION
Marketing and promotion of impactful research

LOOP RESEARCH NETWORK
Our network increases your article's readership